Flow and transport in saturated and unsaturated fractured porous media: Development of particle-based modeling approaches.

Dissertation zur Erlangung des
mathematisch-naturwissenschaftlichen Doktorgrades
"Doctor rerum naturalium"
der Georg-August-Universität Göttingen

vorgelegt von
Jannes Kordilla
aus Göttingen
Göttingen, 2014

Betreuungsausschuss

Prof. Dr. M. Sauter
Dr. T. Geyer
Prof. Dr. A. Tartakovsky

Mitglieder der Prüfungskommission

Referent/in: Prof. Dr. M. Sauter
Korreferent/in: Prof. Dr. A. Tartakovsky

Weitere Mitglieder der Prüfungskommission

Dr. T. Geyer
Prof. Dr. T. Graf
PD Dr. E. Holzbecher
Prof. Dr. T. Ptak

Tag der mündlichen Prüfung: 23.06.2014

Abstract. The main objective of this thesis is the development of particle-based flow and transport models to assist in the characterization of small-scale flow features and provide insight into the complex flow and transport dynamics on core- and fracture scales. Based on the evaluation of the simulation of flow in a fractured karst aquifer using a double continuum model and the Richards equation to describe unsaturated flow, the fundamental weaknesses of the approach are identified and new innovative methods are presented to capture the underlying preferential flow and transport features. The simulation of flow and transport in unsaturated fractured aquifers is extremely challenging due to the multitude of scales involved in the description of geometrical features, which often restrict the definition of a global representative elementary volume. Furthermore the hydraulic characteristics of a fractured aquifer can often only be obtained from integral approaches such as pumping and slug tests, spring discharge analyses and tracer tests in order to constrain the hydraulic parameter space. *Double-continuum models* provide a well-balanced approach in terms of the required field information and the resulting predictive modeling capacity. The first part of this thesis deals with the simulation of a fractured karst aquifer with a double-continuum model, where flow is governed by the Richards equation, van Genuchten parameters and inter-continua exchange is controlled by a linear exchange term. The steep recessions following a recharge event are the characteristic feature of karst springs and can be very well reproduced by the model. The secondary conduit continuum acts as the main connection to the spring and receives varying amounts of discharge from the fractured matrix system depending on the head difference. In order to avoid the simulation of rapid recharge through the unsaturated zone of the conduit continuum, the respective recharge boundary has been added to the bottom of the conduit continuum, essentially creating a bypass. A general drawback of the double-continuum approach has been the ambiguity of model results. The dualistic parameter space in combination with parameters that are difficult to determine, provokes the existence of several well calibrated systems, as demonstrated by extensive multidimensional sensitivity analyses. Especially in karst aquifers the vertical rapid recharge flow features, such as dissolution shafts and wide fractures or fault systems, contribute to the fastest components of the travel time spectrum and cannot be adequately represented by common volume effective modeling approaches, such as the Richards equation and van Genuchten relationships. Therefore the main part of the thesis is devoted to the development of two *Smoothed Particle Hydrodynamics (SPH)* codes to provide innovative numerical tools for the particle based simulation of small-scale free-surface flow and transport. SPH models rely on a Eulerian description of a flow field governed by the Navier-Stokes equation with particles moving according to classical Newton mechanics. The meshfree modeling approach allows a flexible treatment of the highly dynamic boundaries encountered on unsaturated fractures and porous media. A free-surface SPH model including the effect of surface tension has been employed to simulate droplet and film flow on smooth and rough fracture surfaces. A wide range of wetting conditions and Reynolds numbers is covered to obtain a set of characteristic dimensionless parameters. The model is shown to satisfy general scaling laws and dewetting dynamics governed by critical-state contact angle behavior. The generation of adsorbed films on initially dry surfaces is delineated and prewetted surfaces are shown to increase the velocities of droplets, thus highlighting the importance of co-existing flow modes. Several types of macroroughness are implemented to demonstrate the decline of droplet velocities compared to smooth surfaces. In order to bridge the gap between the macroscopic continuum description of the Navier-Stokes equation and the underlying atomistic effects described by statistical mechanics, a *mesoscopic SPH model* has been developed. This new discretization of the fully-coupled Landau-Lifshitz-Navier-Stokes and advection-diffusion equations allows to simulate advective flow and transport including the effects of fluctuating hydrodynamics which can dynamically adapt to the model scale. The combination of classical Fickian diffusion and thermodynamic fluctuations is described by an effective diffusion coefficient. Various numerical experiments show the accuracy of the model and wavenumber divergencies of interface concentration fields agree with recent laboratory experiments.

Kurzfassung. Das Ziel der vorliegenden Arbeit ist die Entwicklung von partikelbasierenden Strömungs- und Transportmodellen zur Charakterisierung von kleinskaligen Strömungsprozessen in gesättigten und ungesättigten Poren- und Kluftsystemen. Aufgrund der unzureichenden Prozessbeschreibung von ungesättigter Strömung in Doppelkontinuummodellen mittels der Richardsgleichung und van Genuchten Parametern werden innovative Methoden präsentiert um die zugrunde liegenden hochdynamischen Strömungs- und Transportprozesse zu erfassen.

Die Simulation von Strömung und Transport in ungesättigten geklüfteten Aquiferen bildet immer noch ein höchst anspruchsvolles Aufgabenfeld aufgrund von skalenübergreifenden Diskontinuitäten, welche oftmals die Definition eines globalen repräsentativen Einheitsvolumens nicht zulassen. Des Weiteren können die hydraulischen Eigenschaften und potentiellen Parameterräume von geklüfteten Aquiferen oftmals nur durch integrale Ansätze, wie z.B. Pump- und Slugtests, Zeitreihenanalysen von Quellschüttungen und Tracertests ermittelt werden. *Doppelkontinuummodelle* bieten hierfür einen ausgewogenen Ansatz hinsichtlich der erforderlichen Felddaten und der resultierenden prädiktiven Modellqualität. Der erste Teil dieser Arbeit evaluiert den Doppelkontinuumansatz, welcher die Simulation von Strömung mittels der Richardsgleichung und van Genuchten Parametern in zwei, durch einen linearen Austauschterm gekoppelten, Kontinua ermöglicht. Ganglinien von Karstquellen weisen eine charakteristischen steilen Abfall nach Niederschlagsereignissen auf, der durch das Modell erfolgreich reproduziert werden kann. Das Röhrensystem bildet die hydraulische Brücke zur Karstquelle und nimmt potentialabhängige Wassermengen des geklüfteten Matrixsystems auf. Um die Simulation von schneller Grundwasserinfiltration durch das Röhrenkontinuum innerhalb der ungesättigten Zone zu vermeiden wurde die entsprechende Randbedingung an die untere Grenze des Kontinuums gesetzt. Ein genereller Nachteil des Doppelkontinuumsansatz ist die potentielle Mehrdeutigkeit von Modellergebnissen. Der duale Parameterraum in Kombination mit schwierig zu ermittelnden Parametern, führt zur Existenz von mehr als einem kalibrierten Modell, wie durch mehrdimensionale Sensitivitätsanalysen aufgezeigt wird.

Insbesondere in Karstaquiferen bilden Diskontinuitäten, wie z.B. Lösungsdolinen, Klüfte und Störungssysteme, bevorzugte hydraulische Elemente für schnelle vertikale Grundwasserneubildungsprozesse, die oftmals nicht durch volumeneffektive Modellansätze erfasst werden können. Der Hauptteil dieser Arbeit befasst sich daher mit der Entwicklung von zwei *Smoothed Particle Hydrodynamics (SPH)* Modellen um ein adäquates numerisches Werkzeug zur partikelbasierenden Simulation von kleinskaligen Strömungen mit freien Oberflächen und Transportprozessen bereitzustellen. SPH Modelle ermöglichen eine Eulersche Beschreibung eines Strömungsfelds auf Basis der Navier-Stokes Gleichung und Partikelbewegung mittels klassischer Newtonscher Mechanik. Der gitterlose Modellansatz ermöglicht flexible Simulationen von hochdynamischen Phasengrenzen in ungesättigten Klüften und Porenräumen. Das erste *SPH Modell* wird eingesetzt um durch Oberflächenspannung dominierte Tropfen- und Filmströmungen auf glatten und rauhen Kluftoberflächen zu simulieren. Charakteristische dimensionslose Kennzahlen werden über einen weiten Bereich von Benetzungswinkeln und Reynoldszahlen bestimmt. Modellergebnisse weisen einen hervorragende Übereinstimmung mit dimensionslosen Skalierungsfunktionen auf und kritische Kontaktwinkel folgen der zu erwartenden Entnetzungsdynamik. Die Entstehung von adsorbierten Filmen auf trockenen Oberflächen wird für einen breiten Parameterraum bestimmt. Des Weiteren wird der Einfluss von befeuchteten Oberflächen auf die Geschwindigkeitszunahme von Tropfenströmung aufgezeigt und so die Bedeutung der Koexistenz verschiedener Strömungsmodi gezeigt. Der Effekt von Oberflächenrauhigkeit auf Tropfenströmung wird für verschiedene Rauhigkeiten ermittelt und eine deutliche Geschwindigkeitsabnahme demonstriert.

Um die makroskopische Kontinuumsbeschreibung der Navier-Stokes Gleichung und atomistische Effekte eines klassischen Partikelsystems der statistischen Mechanik zu kombinieren wurde ein zweites *mesoskopisches SPH Modell* entwickelt. Diese neue Diskretisation der vollständig gekoppelten Landau-Lifshitz-Navier-Stokes und Advektions- Diffusionsgleichung ermöglicht die Simulation von Strömung und Transport bei gleichzeitiger Berücksichtigung von Fluktuationsdynamiken, welche sich korrekt der Systemskala anpassen. Die Verbindung von klassischer Fickscher Diffusion und thermodynamischen Fluktuationen wird hierbei durch einen effektiven Diffusionskoeffizienten beschrieben. Numerische Experimente zeigen die Präzision des Modells. Grenzflächen zwischen zwei Fluiden unterschiedlicher Konzentration weisen eine korrekte Wellenzahldivergenz entsprechend aktuellen Laborergebnissen auf.

Acknowledgement. I would like to express my gratitude to all the people that have been supporting me financially or emotionally throughout the course of my PhD. Prof. Dr. M. Sauter is thanked for his scientific guidance, generous financial support and encouraging words during the inevitable periods of frustration and little progress. Despite the uncertain outcome of my research, he supported me to pursue my own scientific interests without limiting my creativity and curiosity which has been one of the most demanding, yet also most rewarding experience of the past years.

I would like to thank Dr. T. Geyer for his financial support and supervision of my work. His constructive criticism and continuous support have been of vital importance for the success of this work. Our field trips have been a welcoming distraction from my numerical work and helped me to stay in touch with the (unfortunately) complex hydrologic reality of unsaturated aquifers.

My particular thanks go to Prof. Dr. A. Tartakovsky who has been an excellent host during my research visits at the Pacific Northwest National Laboratory (PNNL). His playful, yet rigorous scientific approach helped me to push my limits, overcome fears and enabled me to pursue my interest in programming. His financial support allowed me to visit PNNL in 2013 for several months.

I appreciate the work of the additional committee members Prof. Dr. T. Ptak, PD Dr. E. Holzbecher and Prof. Dr. T. Graf who read my thesis and acted as referees during my defense. I would also like to thank Prof. Dr. I. Neuweiler who agreed to evaluate my thesis as an external reviewer under time pressure.

Dr. W. Pan is thanked for her constructive discussions about numerical modeling of fluctuating hydrodynamics and support during the preparation of our manuscript.

I am grateful for the financial support by the German Academic Exchange Service (DAAD) for my first and second research visit abroad. Being able to travel and establish cooperations with international scientists has been an extremely important part of my development as a researcher.

Beka is thanked for her ongoing reliable administrative support and the countless prepared documents and contracts.

I am indebted to my friends and colleagues at the Department of Applied Geosciences in Göttingen who shared the ups and downs during our PhD time, in particular: my office mate Joanna for the occasional cheer up and Lebanese coffee, Sebastian for Franken-wisdom and festival visits and Markus for our sporadic summer Willi-resets.

During all of my three research visits the whole PNNL staff has been very welcoming and made my stay a pleasant experience. My special thanks go to Trish who took care of all administrative tasks and Mike who took care of all IT related issues. Exploring the US culture and keeping the life-work balance wouldn't have been possible without the people I met in Richland, the guesthouse and at PNNL. In no particular order my thanks go to Ayoub and his wife, my office colleagues Avik, Selim, Kobe, Don, Christina and Laurentio, my guesthouse neighbors Pietro, Jasper, Max and Tom, and finally Karan and Niru. Special thanks go to the family of Prof. Dr. Tartakovsky, Guzele and Masha for their hospitality and delicious dinners.

Last but not least my deepest thanks go to my Family and friends who were my biggest source of emotional support: My mother and my stepfather for their continuous encouragement and financial support and Ariane for her patience.

Table of Contents

List of Figures

List of Tables

List of Listings

1 | Introduction

1.1 Motivation and background

Understanding of flow and transport in porous fractured media is of importance for water supply, mining, tunneling, the location of potential repositories (EVANS & RASMUSSEN, 1991), subsurface storage, and the development of geothermal reservoirs in hard rock regions (FLINT et al., 2001) and is possibly one of the main challenges in hydrogeological research. The migration of contaminants from radioactive waste disposals has been triggering significant research efforts, particularly to gain a deeper understanding of vertical flow and transport processes through the unsaturated zone of fractured aquifers (NICHOLL et al., 1994; NRC, 1996). In this context, unsaturated flow in porous fractured rocks has been identified as one of the most critical processes that affect the sensitivity of an aquifer or repository to rapid infiltration and control the overall vulnerability of the system (WANG & NARASIMHAN, 1993). Especially in karst aquifers, which provide further pathways for rapid infiltration, such as vertical dissolution shafts, and in addition a highly conductive conduit systems in the saturated zone, very high transport velocities have been observed (GEYER et al., 2008; SAUTER, 1992).

Fractured rocks are characterized by a wide spectrum of discontinuities spanning in their geometrical and hydraulic properties across several spatial scales. The occurrence of these discontinuities might lead to (1) preferential flow pathways considerably reducing the travel time of water through geological media (NIMMO, 2012; SU et al., 2000) and (2) flow barriers in the sub-surface causing flow diversion (GHEZZEHEI, 2005). Unsaturated flow

in fractured rocks differs strongly from flow in unsaturated porous media and therefore classical Darcy continuum approaches generally do not apply. While a number of approaches have been developed for the simulation of saturated fracture flow, only few attempts have been made to develop models that are able to quantitatively describe discrete unsaturated fracture flow processes (NIMMO, 2010; NRC, 2001) and in general *"the processes affecting flow in unsaturated fractured rock are not well understood so far"* (SINGHAL & GUPTA, 2010). Current approaches are often transferred from local scale soil investigations to fractured rock hydraulics (LU & KWICKLIS, 2012; ZHANG et al., 2004). However, the scale of heterogeneities in soils and fractured rocks differ significantly from each other, resulting in different dominant flow processes. This concerns in particular gravity driven free surface flow dynamics, which are of major interest for the prediction of flow velocities and water travel time distributions in fractured rocks. Recent works of TOKUNAGA & WAN (1997) and TOKUNAGA et al. (2000) gave experimental insight into fracture surface flow dynamics and highlighted the importance of free surface film flow. To incorporate this preferential flow mechanism, source-responsive film-flow models (MIRUS & NIMMO, 2013; NIMMO, 2007; NIMMO, 2010) based on a laminar flow description have been developed. These models can capture the fast nature of the flow as well as the highly dynamic reaction of the flow to changes in the input signal, i.e. the recharge dynamics. It is remarkable to note that flow velocities obtained from these approaches (up to several $\mathrm{mm\,s^{-1}}$) have been classified as "fast" to distinguish them from the average flow velocities described by the Richards' equation (RICHARDS, 1931) and common hydraulic property functions (van GENUCHTEN, 1980), which yield 10–100 $\times$ lower average wetting front velocities (GERMANN & HENSEL, 2006). However, recent experimental (DRAGILA & WEISBROD, 2004b; JI et al., 2006; NICHOLL & GLASS, 2005; SU et al., 2004) and theoretical investigations (DRAGILA & WEISBROD, 2004a; DRAGILA & WHEATCRAFT, 2001; GERMANN et al., 2007; GHEZZEHEI, 2004; OR & GHEZZEHEI, 2006) suggest the existence of even faster flow modes, such as droplets, rivulets and wavy films, which may occur on fracture surfaces and result in velocities of up to $1.5\,\mathrm{m\,s^{-1}}$ (DRAGILA

& WEISBROD, 2003).

Due to the flow intermittency, highly dynamic interphases and nonlinear flow dynamics, potential models need to fulfill a multitude of challenging requirements in order to properly resolve the complex flow dynamics in unsaturated fractures. The characterization of transport processes requires even more sophisticated approaches. Due to the strong hydraulic contrast between porous matrix and fracture, advective and diffusive transport processes have to be considered simultaneously for a consistent quantification.

1.2 Objectives and approaches

The results of this thesis are intended to enhance the process understanding of unsaturated flow and transport dynamics and provide robust numerical techniques for their quantitative and qualitative simulations.

The main objectives of this thesis are:

- The evaluation of the simulation of unsaturated flow in fractured karst aquifers with a double-continuum model.
- The characterization of small-scale flow and transport processes that are related to the rapid flow spectrum dominated by unsaturated flow in fractures and the adjacent porous matrix.
- The development of a mechanistic approach to simulate free-surface flow dynamics including the effects of surface tension. The model will be employed to investigate droplet and film flow on fracture surfaces, obtain dimensionless parameter sets, delineate general flow regimes and study the effect of surface roughness on average flow velocities.
- The development of a model capable of simulating advective and diffusive transport enhanced by stochastic fluctuations. The model is intended to complement the study of fracture surface flow dynamics and provide a tool for a deeper understanding of flow and transport processes across the fracture matrix interface. The effect of molecular stresses and fluxes on the macrosopic diffusion dynamics will be studied for miscible fluid interfaces under various dynamic conditions.

Despite the urgent need for advanced modeling tools for the characterization of unsaturated fracture flow dynamics the application to field scale problems still requires adequate upscaled models. On one hand this is due to the generally limited amount of field data, which restricts the use of complex models and on the other hand computational performance still limits the degree of detail for catchment scale simulations. Hence, a double-continuum model is employed to simulate flow in a fractured karst aquifer, where flow is governed by Richards' equation (RICHARDS, 1931) and unsaturated hydraulic properties are evaluated according to the van Genuchten model (van GENUCHTEN, 1980) with a first-order exchange coefficient describing the continuum coupling (GERKE & VAN GENUCHTEN, 1993). The approach is evaluated in terms of applicability and the ambiguity of the results is critically discussed. Limitations in the process description of rapid unsaturated flow in fractures, shafts and faults using the van Genuchten permeability relations are identified.

To investigate the small scale flow and transport features, that are disguised by the continuum description and thus reduce the respective physical parameters in the double-continuum model to pure calibration parameters, two Smoothed Particle Hydrodynamics (SPH) models are developed. The first SPH model is developed to investigate the importance of droplet and film flow as a rapid flow component and demonstrate the applicability of the approach to obtain dimensionless parameters for upscaled semi-analytical models over a wide range of wetting conditions and Reynolds numbers.

The second SPH model allows to bridge the gap between atomistic, mesoscopic, and macrosocopic view of transport processes. By coupling the advective-diffusion equations with the Landau-Lifshitz-Navier-Stokes equations (LANDAU & LIFSHITZ, 1987) the model allows to characterize a system by means of an effective diffusion coefficient consisting of a Fickian contribution, random stresses and random fluxes.

1.3 Format of the thesis

Chapter 2 describes various attempts to characterize unsaturated flow and transport in fractured aquifers. A brief introduction to the concept of scales is given and scale dependant investigation techniques are presented. In addition to the empirical methods the chapter also examines mathematical models and various numerical techniques for flow and transport in unsaturated and saturated fractures rocks. Due to the cumulative nature of the thesis references are given after each chapter.

Chapter 3 gives an overview of the employed SPH codes and their key elements. In particular this includes the general code flow, the most important algorithms and the MPI parallelization of the stochastic SPH code. The chapter can be read in conjunction with the respective Chapters 5 and 6, which give a more mathematical description of the employed SPH codes.

Chapters 4 to 6 represent the main research work of this thesis. Chapters 4 and 5 have been accepted for publications in peer-reviewed journals and Chapter 6 has been submitted to a peer-reviewed journal.

Chapter 4 deals with the catchment scale simulation of saturated and unsaturated flow in a fractured karst aquifer using a double continuum approach. The model presented in this chapter has been mainly set up during my Diploma thesis. The whole manuscript has been written during the course of this dissertation and the final model has been set up during the review process.

Chapter 5 presents an SPH model to investigate free surface flow on smooth and rough fractures surfaces. The code base has been originally developed by TARTAKOVSKY & MEAKIN (2005) and was used as a basis for all my modifications and enhancements. This includes rewriting of input and output routines, creation of geometries, replacement of the pairwise interaction kernel, computation of the surface tension, fluid pressures and all relevant flow data.

Chapter 6 provides a fully coupled SPH model for the Landau-Lifshitz-Navier-Stokes and advection-diffusion equations to simulate flow and transport. The whole code has been written by myself based on the model de-

veloped in Chapter 5. Code snippets for the evaluation of tracer moments have been taken from TARTAKOVSKY et al. (2009).

Chapter 7 gives a comprehensive conclusion with regard to the objectives of the thesis and suggestions for future research are provided.

1.4 References

DRAGILA, M. I. & WEISBROD, N. (2004a): 'Flow in Menisci Corners of Capillary Rivulets'. *Vadose Zone Journal*, vol. **3**: pp. 1439–1442 (cit. on p. 2).

– (2004b): 'Fluid motion through an unsaturated fracture junction'. *Water Resources Research*, vol. **40**: pp. 1–11 (cit. on p. 2).

– (2003): 'Parameters affecting maximum fluid transport in large aperture fractures'. *Advances in Water Resources*, vol. **26**: pp. 1219–1228 (cit. on p. 2).

DRAGILA, M. I. & WHEATCRAFT, S. (2001): 'Free-surface films'. *Conceptual Models of Flow and Transport in the Fractured Vadose Zone*. National Academies Press: pp. 217–241 (cit. on p. 2).

EVANS, D. D. & RASMUSSEN, T. C. (1991): *Unsaturated Flow and Transport Through Fractured Rock Related to High-level Waste Repositories: Final Report–phase III*. Tech. rep. Washington: Office of Nuclear Regulatory Research (cit. on p. 1).

FLINT, A. L., FLINT, L. E., BODVARSSON, G. S., KWICKLIS, E. M. & FABRYKA-MARTIN, J. (2001): 'Evolution of the conceptual model of unsaturated zone hydrology at Yucca Mountain, Nevada'. *Journal of Hydrology*, vol. **247**(1-2): pp. 1–30 (cit. on p. 1).

GENUCHTEN, M. T. van (1980): 'A Closed-form Equation for Predicting the Hydraulic Conductivity of Unsaturated Soils'. *Soil Science Society of America Journal*, vol. **44**(5): pp. 892–898 (cit. on pp. 2, 4).

GERKE, H. H. & VAN GENUCHTEN, M. (1993): 'Evaluation of a first-order water transfer term for variably saturated dual-porosity flow models'. *Water Resources Research*, vol. **29**: pp. 1225–1225 (cit. on p. 4).

GERMANN, P. F., HELBLING, A. & VADILONGA, T. (2007): 'Rivulet Approach to Rates of Preferential Infiltration'. *Vadose Zone Journal*, vol. **6**(2): pp. 207–220 (cit. on p. 2).

GERMANN, P. F. & HENSEL, D. (2006): 'Poiseuille Flow Geometry Inferred from Velocities of Wetting Fronts in Soils'. *Vadose Zone Journal*, vol. **5**(3): p. 867 (cit. on p. 2).

Geyer, T., Birk, S., Liedl, R. & Sauter, M. (2008): 'Quantification of temporal distribution of recharge in karst systems from spring hydrographs'. *Journal of Hydrology*, vol. **348**(3-4): pp. 452–463 (cit. on p. 1).

Ghezzehei, T. A. (2004): 'Constraints for flow regimes on smooth fracture surfaces'. *Water Resources Research*, vol. **40**: pp. 1–14 (cit. on p. 2).

– (2005): 'Flow diversion around cavities in fractured media'. *Water Resources Research*, vol. **41**: pp. 1–5 (cit. on p. 1).

Ji, S.-H., Nicholl, M. J., Glass, R. J. & Lee, K.-K. (2006): 'Influence of simple fracture intersections with differing aperture on density-driven immiscible flow: Wetting versus nonwetting flows'. *Water Resources Research*, vol. **42**: pp. 1–10 (cit. on p. 2).

Landau, L. D. & Lifshitz, E. M. (1987): *Fluid Mechanics: Volume 6 (Course Of Theoretical Physics)*. Butterworth-Heinemann (cit. on p. 4).

Lu, Z. & Kwicklis, E. M. (2012): 'Numerical Evaluation of Effective Unsaturated Hydraulic Properties of Fractured Rocks using a Stochastic Continuum Approach'. *Vadose Zone Journal*, vol. **11**(4) (cit. on p. 2).

Mirus, B. B. & Nimmo, J. R. (2013): 'Balancing practicality and hydrologic realism: A parsimonious approach for simulating rapid groundwater recharge via unsaturated-zone preferential flow'. *Water Resources Research*, vol. **49**(3): pp. 1458–1465 (cit. on p. 2).

Nicholl, M. J. & Glass, R. J. (2005): 'Infiltration into an Analog Fracture'. *Vadose Zone Journal*, vol. **4**(4): p. 1123 (cit. on p. 2).

Nicholl, M. J., Glass, R. J. & Wheatcraft, S. (1994): 'Gravity-driven infiltration instability in initially dry nonhorizontal fractures'. *Water Resources Research*, vol. **30**(9): pp. 2533–2546 (cit. on p. 1).

Nimmo, J. R. (2012): 'Preferential flow occurs in unsaturated conditions'. *Hydrological Processes*, vol. **26**(5): pp. 786–789 (cit. on p. 1).

– (2007): 'Simple predictions of maximum transport rate in unsaturated soil and rock'. *Water Resources Research*, vol. **43**(5) (cit. on p. 2).

– (2010): 'Theory for Source-Responsive and Free-Surface Film Modeling of Unsaturated Flow'. *Vadose Zone Journal*, vol. **9**(2): p. 295 (cit. on p. 2).

NRC (2001): *Conceptual Models of Flow and Transport in the Fractured Vadose Zone*. Washington D.C.: National Academy Press: p. 374 (cit. on p. 2).

– (1996): *Rock Fractures and Fluid Flow: Contemporary Understanding and Applications*. Washington D.C.: National Academy Press: p. 551 (cit. on p. 1).

Or, D. & Ghezzehei, T. A. (2006): 'Traveling liquid bridges in unsaturated fractured porous media'. *Transport in Porous Media*, vol. **68**(1): pp. 129–151 (cit. on p. 2).

Richards, L. A. (1931): 'Capillary Conduction of Liquids Through Porous Mediums'. *Physics*, vol. **1**(5): pp. 318–333 (cit. on pp. 2, 4).

Sauter, M. (1992): *Quantification and Forecasting of Regional Groundwater Flow and Transport in a Karst Aquifer (Gallusquelle, Malm, SW. Germany)*. Tübinger Geowissenschaftliche Arbeiten: p. 150 (cit. on p. 1).

Singhal, B. B. & Gupta, R. P. (2010): *Applied Hydrogeology of Fractured Rocks*. Springer: p. 408 (cit. on p. 2).

Su, G. W., Geller, J. T., Hunt, J. R. & Pruess, K. (2004): 'Small-Scale Features of Gravity-Driven Flow in Unsaturated Fractures'. *Vadose Zone Journal*, vol. **3**(2): pp. 592–601 (cit. on p. 2).

Su, G. W., Geller, J. T., Pruess, K. & Hunt, J. R. (2000): 'Overview of Preferential Flow in Unsaturated Fractures'. *Geophysical Monograph Series*. 122nd ed. Vol. 122. American Geophysical Union (cit. on p. 1).

Tartakovsky, A. & Meakin, P. (2005): 'Simulation of Unsaturated Flow in Complex Fractures Using Smoothed Particle Hydrodynamics'. *Vadose Zone Journal*, vol. **4**(3): pp. 848–855 (cit. on p. 5).

Tartakovsky, A., Tartakovsky, G. & Scheibe, T. (2009): 'Effects of incomplete mixing on multicomponent reactive transport'. *Advances in Water Resources*, vol. **32**(11): pp. 1674–1679 (cit. on p. 6).

Tokunaga, T. K. & Wan, J. (1997): 'Water film flow along fracture surfaces of porous rock'. *Water Resources Research*, vol. **33**(6): p. 1287 (cit. on p. 2).

Tokunaga, T. K., Wan, J. & Sutton, S. R. (2000): 'Transient film flow on rough fracture surfaces'. *Water Resources Research*, vol. **36**(7): pp. 1737–1746 (cit. on p. 2).

Wang, J. & Narasimhan, T. (1993): 'Unsaturated flow in fractured porous media'. *Flow and contaminant transport in fractured rock*. Ed. by J. Bear,

C.-F. Tsang & G. De Marsily. San Diego: Academic Press. Chap. 7: pp. 325–394 (cit. on p. 1).

Zhang, K., Wu, Y.-S., Bodvarsson, G. S. & Liu, H.-H. (2004): 'Flow Focusing in Unsaturated Fracture Networks: A Numerical Investigation'. *Vadose Zone Journal*, vol. 3(2): pp. 624–633 (cit. on p. 2).

2 | General Overview

2.1 Heterogeneities in fractured hardrocks

The presence of discontinuities in the porous rock matrix is what sets fractured hard rock systems apart from other porous media. The development of discontinuities in hard rocks defines the complexity of the fractured flow system (SINGHAL & GUPTA, 2010). This process depends strongly on the parent rock. Sedimentary hard rocks commonly exhibit primary bedding or layering that may act as an effective pathway for water flow. Metamorphic rocks often display foliation features due to parallel-planar alignment of mineral grains as a result of recrystallization during metamorphism. The partial loss of cohesion by mechanical stress introduces single fractures. Highly interconnected discrete fractures are described as fracture zones. Depending on the degree of interconnectivity, these fractures may lead to a local increase in hydraulic conductivity.Typical measures for characterization of single fractures and fracture zones on field scale are orientation, dip, length, fracture area, density, spacing, interconnectivity, persistence, roughness and aperture.

2.2 Scale concepts

Process understanding and development of mathematical models require an appropriate conceptual model that involves system compartments at the level of scale investigations. The term "scale" describes a dimensional spectrum of a system (e.g., characteristic length, time) being analyzed with respect to process and parameterization (FAYBISHENKO, 2003). Scaling is based on theoretical or phenomenological relationships between micro-

and macroscale properties that remove redundant microscale information (WOOD, 2009). Scaling of unsaturated flow in porous media is often based on the analysis of local unsaturated zone parameters (e.g. water retention and unsaturated hydraulic conductivity; MILLER et al., 1997) to derive field-scale average parameters. Governing flow equations in unsaturated porous media (e.g., RICHARDS, 1931) usually employ volume-effective parameters. The REV (representative elementary volume; BEAR, 1972) serves as a basic concept in material characterization to define equivalent parameters. The size of an REV may be scale-dependent since the dominating processes and geometrical features of a system may not behave scale-invariant. To account for flow processes observed on various scales, FAYBISHENKO et al. (2001) introduced the concept of a hierarchy of scales for the investigation of fractured rocks (see Fig. 2.1). The core scale allows specific experiments for detailed investigations of flow and transport processes in individual fractures and the porous matrix. The small scale includes a volume of rock and intersecting fractures. Experiments at this scale can be used, for example, for the interpretation of fracture-matrix interactions. The volume of rock involving all types of fractures, fracture boundaries on the top and the bottom of a rock unit are intermediate-scale components. A sequence of different rock units containing large fractures is the objective of large-scale investigations.

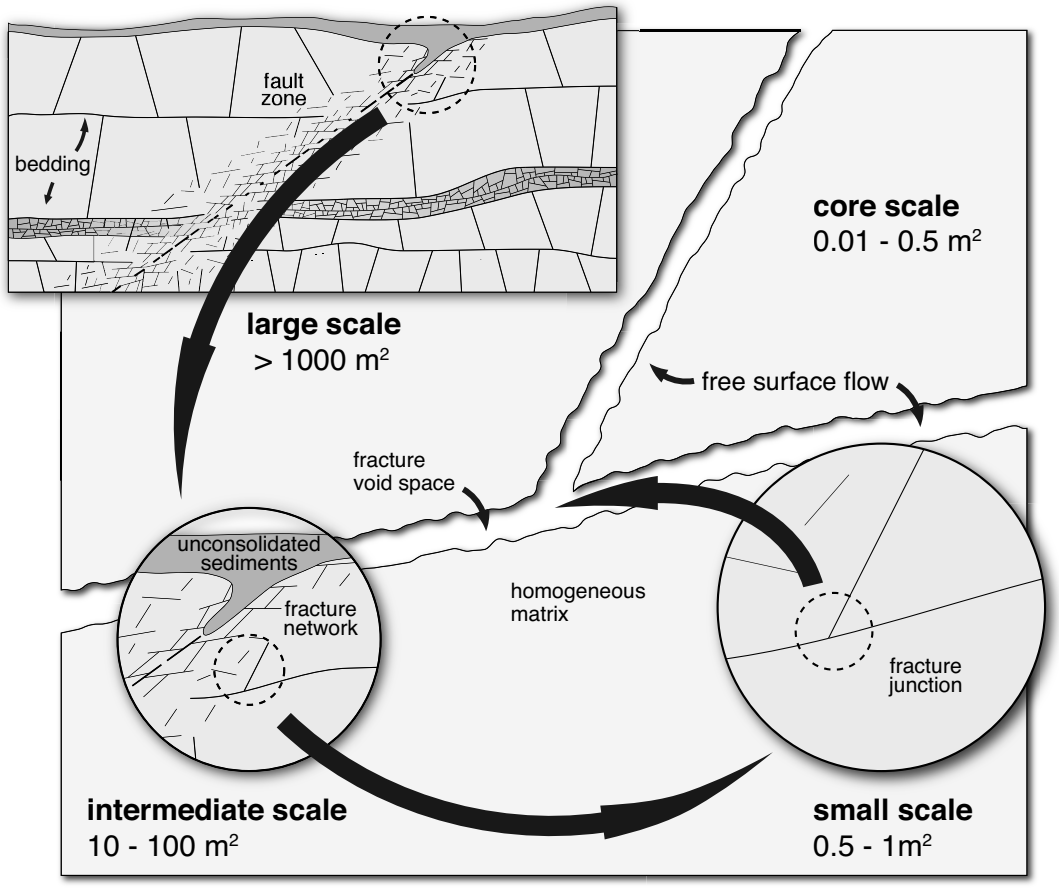

FIG. 2.1. Scales encountered in the unsaturated zone in fractured rocks. Modified from FAYBISHENKO et al. (2000).

2.3 Laboratory and field experiments

2.3.1 Laboratory experiments

Investigations of unsaturated fracture flow in laboratory experiments have been carried out by various authors and are usually limited to core and small scale. Only a few investigations exist which systematically describe the influence of fracture surface characteristics (e.g. asperities, roughness, wetting) on flow dynamics in the unsaturated zone. Because laboratory scale experiments are usually limited to simple geometries and solid-fluid

configurations, the results commonly require non-dimensionalization procedure to allow universal applicability. A common laboratory approach in the characterization of unsaturated fracture flow has been the analogue fracture experiment. Common experimental setups include: (1) textured glass plates forming a small aperture single fracture element (GLASS & NICHOLL, 1996; NICHOLL & GLASS, 2005; SU et al., 2001); (2) large aperture surfaces with a free surface (BENSON, 2001; TOKUNAGA & WAN, 2001; TOKUNAGA & WAN, 1997; TOKUNAGA et al., 2000); and (3) broken glass fractures with low aperture and width, i.e. no transversal fluid flow can occur (DRAGILA & WEISBROD, 2004a; DRAGILA & WEISBROD, 2004b; SU et al., 2004). While the first setup was successful in describing the influence of transversal flow and fingering effects, it neglects the effect of imbibition that occurs due to a finite matrix porosity. As shown by TOKUNAGA & WAN (2001) free-surface film flow on fractures (second setup) depends to a large degree on the porosity and pore size distribution of the sample often not considered in synthetic fracture experiments. The third experimental setup mainly focuses on rapid flow regimes such as droplets, rivulets and falling films. However, they fail to capture the influence of adsorbed films on porous surfaces, i.e., they are commonly covering only non- or partial-wetting conditions. The latter experiments can be considered closely related to research into contact line dynamics, which play a major role in the flow processes on surfaces. Laboratory studies of droplets have shown the complex behavior under static (BIKERMAN, 1950; FURMIDGE, 1962) and quasi-transient conditions, i.e. at the onset of movement (DUSSAN & CHOW, 1983; ELSHERBINI & JACOBI, 2004; ELSHERBINI & JACOBI, 2006). Recent experiments by PODGORSKI et al. (2001) and LE GRAND et al. (2005) have shown that transient flow dynamics are more complex when droplets begin to change their aspect ratio. As shown by PODGORSKI et al. (2001), dimensionless scaling laws can be employed to quantify droplet velocities for arbitrary fluid-solid combinations. Percolation experiments using fractured rock samples and comparable materials under laboratory conditions were conducted by NICHOLL & GLASS (2005). The authors studied the occurrence of gravity driven fingering within an individual fracture, which has substan-

tial influence on infiltration mechanism. Information about the fracture network for numerical simulations and comparison to field data can be either obtained from surface mapping of fractures or by excavation. The latter technique has been employed, for example, by GLASS et al. (2002) in combination with dyed water to obtain the flow-effective three-dimensional fracture network.

2.3.2 Field experiments

As reviewed by NIMMO (2012), various authors observed the importance of rapid preferential flow under unsaturated conditions during field experiments. The spatial scale of the field experimental investigations ranges from a few cubic meters up to whole catchment size. In contrast to analog laboratory experiments, the detailed geometry of the flow system is usually not known. Several methods exist for in-situ monitoring of water potentials and water content in porous media. The application of these methods to fractured rocks is a challenge because of strong measurement artifacts related to probe installation. Additionally, these methods are applicable to a limited degree to the characterization of flow along discrete elements. Local measurements of water potentials in unsaturated media are typically made with tensiometers and thermocouple psychrometers (e.g., EVANS et al., 2001; SALVE, 2005; SCHNEEBELI et al., 1995). However, tensiometer techniques do not provide adequate three-dimensional resolution of the fracture and matrix capillary to determine exchange between both flow systems (FAIRLEY et al., 2000). Geophysical methods give additional spatial information of rock water content. The application of time domain reflectometry (TDR) probes in partially saturated rocks is described by SAKAKI & RAJARAM (2006). Geophysical non-destructive methods for the measurement of water content are, for example, neutron and gamma-ray tomography (CHENG et al., 2012; HAINSWORTH & AYLMORE, 1983; JUNG et al., 2012). Time-lapse electrical resistivity tomography was employed by ARORA & AHMED (2011) to characterize percolation of water through a fractured granite. The authors found a good correlation between water content and resistivity and showed that fractures in the unsaturated zone act as preferential pathways.

Percolation and tracer experiments provide an estimate for the movement of the wetting front, arrival times and recovered volumes of water through unsaturated fractured rock zones (LANGE et al., 2010). The interpretation of field tracer experiments is still challenging, because of limited access to observation points in the unsaturated zone of hard rocks. Local observation points for investigations are caves, mining shafts, tunnels or boreholes for water and tracer monitoring.

2.4 Mathematical models

Mathematical models constitute important tools for process simulation and scale continuous characterization of a hydrogeological system. In general, numerical and analytical approaches can be distinguished. Analytical approaches are essential for comparison and initial verification of numerical models. With early models, it was believed that unsaturated fracture flow requires a saturated rock matrix. However, in field studies (e.g. Yucca Mountain), observed percolation rates were higher than simulated percolation rates indicating the existence of localized unsaturated fracture flow (FLINT et al., 2001). The models may fail when film flow processes dominate unsaturated fracture flow (ROSSI & NIMMO, 1994; SHOKRI et al., 2010). This shortcoming might be adjusted empirically by (1) the introduction of additional parameters to existing hydraulic conductivity functions for multimodal pore space distributions (DURNER, 1994; ROSS & SMETTEM, 1993, see also Fig. 2.3, dual porosity model) and (2) the coexistence of capillary and thin film flow (LEBEAU & KONRAD, 2010; PETERS & DURNER, 2008). Recent studies by NIMMO (2010) and MIRUS & NIMMO (2013) introduced the concept of source-responsive free-surface models which assume the existence of a continuous film through the unsaturated zone governed by laminar flow dynamics. *However, the importance of gravity driven free surface flow in fractured rocks cannot be addressed with these modeling approaches. Unsaturated flow, especially in wide aperture fractures, can extend beyond the characteristic thicknesses of thin films and is governed by small-scale physics with wetting and dewetting dynamics controlling the complex three-phase (solid-fluid-air) contact line dynamics.*

2.4.1 Analytical models

Finding analytical expressions to quantify flow in unsaturated fractures represents a challenge due to the occurrence of several highly dynamic flow regimes (see Fig. 2.2) and flow intermittency.

Adsorbed films

Adsorbed film flow has been identified as an important flow feature on fracture surfaces by TOKUNAGA & WAN (1997) with average flow velocities of $3 \times 10^{-7}\,\mathrm{m\,s^{-1}}$. It has been widely accepted as a fast flow mechanism to draw the contrast to capillary dominated flow in the porous matrix, which can be several orders of magnitude slower. However, much faster flow regimes exist (for velocities of up to $1.5\,\mathrm{m\,s^{-1}}$) which contribute to the rapid flow spectrum, ranging from droplets, over rivulets to falling films. Various (semi-) analytical solutions exist for these distinct flow regimes. These solutions are commonly restricted to steady-state conditions, certain geometries and do not cover all flow regimes or coexistence of flow modes.

Droplets

Droplet flow (also termed slug flow by some authors for flow in narrow fractures) has been investigated by numerous authors. Solutions for stationary shapes of sessile droplets (GOMBA & HOMSY, 2009; KRASOVITSKI & MARMUR, 2005) and transient dynamics including breakup mechanisms (e.g., GHEZZEHEI & OR, 2005; HASSEINE et al., 2011; LUNATI & OR, 2009) exist. A common approach for quantifying droplet dynamics for arbitrary fluid-solid configurations is to find dimensionless scaling laws based on empirical experiments as shown by ELSHERBINI & JACOBI (2004) and PODGORSKI et al. (2001). For example, PODGORSKI et al. (2001) have found a general linear relationship between Bond number and Capillary number unique for every fluid-solid configuration. Contact angle models have been proposed, e.g., by COX (1986), VOINOV (1976) and BLAKE & RUSCHAK (1997). In recent experiments LE GRAND et al. (2005) could delineate important shape transitions based on capillary numbers and give implications for the onset of Landau-Levich films for very low contact angles.

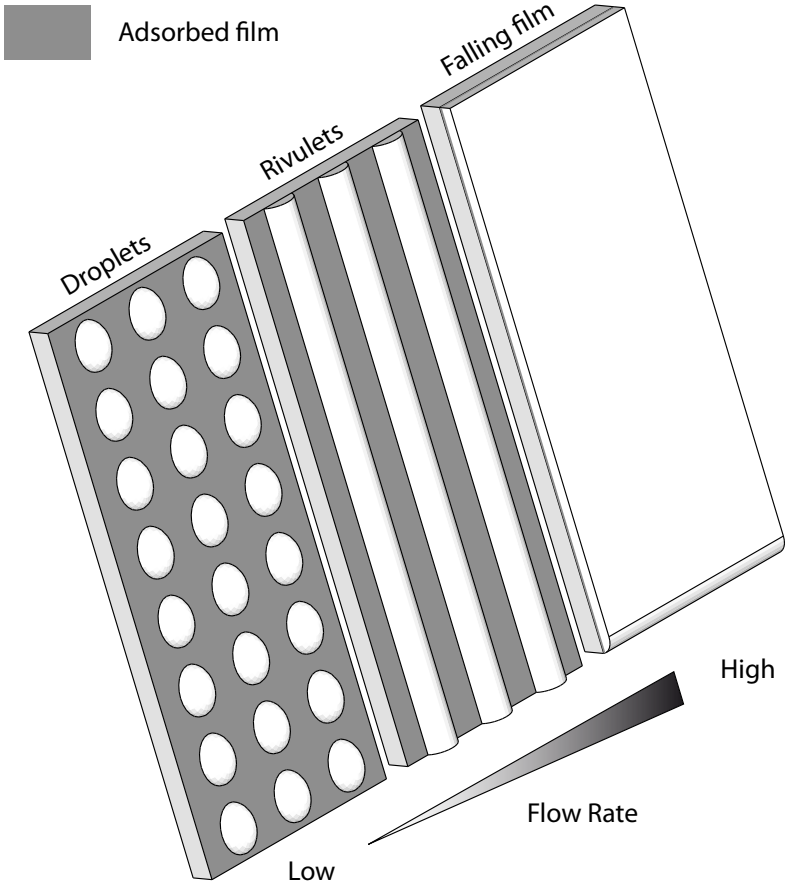

FIG. 2.2. Concepts of flow regimes on wide aperture fractures. Modified from GHEZZEHEI (2004).

Rivulets

Rivulet flow occurs if flow rates are high enough to prevent an early breakup into droplets. Solutions for rivulet flow between two parallel plates were provided for example by DRAGILA & WEISBROD (2003) and DRAGILA & WEISBROD (2004a) using a combination of parabolic Poiseuille and semiparabolic Stokes models. Critical flow rates for snapping, i.e. breakup, are given in terms of minimum volumetric flow rates accommodated in corners of the rivulet core governed by semiparabolic free-surface Stokes flow. Rivulets

on wide aperture fractures have been described in GHEZZEHEI (2004) using expression for uniform falling films following TOWELL & ROTHFELD (1966). GERMANN et al. (2007) demonstrated how rivulet flow can be incorporated into a moisture model to simulate preferential flow in soils.

Free-surface films

Free-surface films (turbulent falling films) can be considered the most unlikely form of unsaturated flow, only occuring during heavy infiltration events if excess water is running down along the fully wetted fracture surface. The hydrodynamic theory was partially described by NUSSELT (1916) under assumption of fully laminar flow. However, for Reynolds numbers larger than 20 surface waves and ripples may develop which travel at much higher velocity than films (CHU & DUKLER, 1974; DRAGILA & WHEATCRAFT, 2001; DROSOS et al., 2004; PATNAIK & PEREZ-BLANCO, 1996). According to GHEZZEHEI (2004) the Nusselt film flow description may however be extended to Reynolds numbers up to 200 as low amplitude surface waves are not significantly higher than the mean laminar film thickness. A film flow model for free-surface flows including the effect of undulating surface waves of differing amplitude has been proposed by DRAGILA & WHEATCRAFT (2001) who point out the importance of traveling waves for the overall effectiveness of film flow. The model requires Reynolds numbers and Celerety numbers (surface velocity normalized to film thickness) as input parameters and is therefore not suited for predictive modeling.

A promising semi-analytical approach to combine models for some of the mentioned flow regimes has been proposed by GHEZZEHEI (2004). The author provides a general framework and unified dimensionless description of several flow regimes on dry wide aperture fractures based on the findings of PODGORSKI et al. (2001). The semi-analytical model takes into account droplets, rivulets and falling films and delineates the occurrence of these distinct rapid surface flow regimes for steady-state conditions based on an energy minimization principle. Adsorbed films and porous matrix interaction are not included in the solution and the necessary dimensionless scaling parameters required as model input are difficult to obtain from

laboratory experiments.

2.4.2 Numerical models

Numerical models for unsaturated flow can be distinguished by the type of numerical discretization of the governing partial differential equations into (1) grid-based models and (2) meshless models. Theoretically, both model types describe heterogeneities in flow systems on different scales.

Grid based models

The simulation of flow in heterogeneous media on large scales has been described by single continuum, multi continuum and discrete modeling approaches (TEUTSCH & SAUTER, 1991). The approaches differ strongly in their capability to represent heterogeneities, their practical applicability and the investigation effort required for model parameterization (see Fig. 2.3). The application of continuum models involves several assumptions and approximations, as single continuum porous medium models do not describe the dual nature of fractured rock systems. They require existence of a representative elementary volume (REV), which is not realistic for flow in fractured rocks on small scale. Continuum approaches coupled with simple bypass functions provide a possibility to avoid the mechanistic simulation of unsaturated fracture flow. These approaches have been applied to field scale flow problems but are limited in their predictability (DOUMMAR et al., 2012). Saturated and unsaturated simulations of dual flow systems on large scales without detailed information about the system geometry was shown by MCLAREN et al. (2000) and KORDILLA et al. (2012) by applying the Richards equation and a first-order exchange term (GERKE & VAN GENUCHTEN, 1993) to account for transfer of water between macropores (or fracture) and soil (or rock). The solution of the Richards equation requires the water retention function and the hydraulic conductivity function, which can be formulated by a variety of mathematical expressions. Fracture continuum parameters are calibrated to sustain fracture flow in the presence of an unsaturated rock matrix. These parameters however do not have a physical meaning and cannot be determined experimentally. The

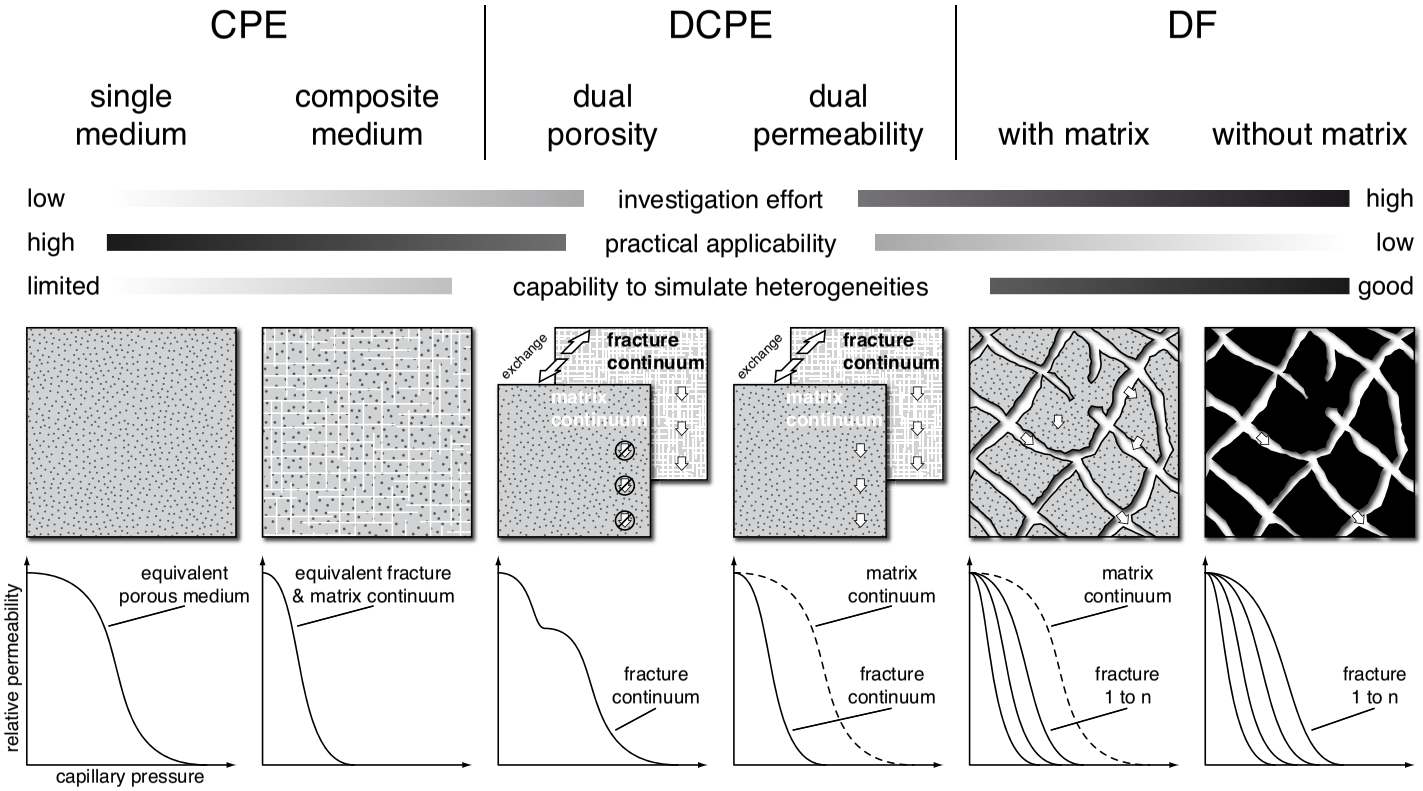

FIG. 2.3. Classification scheme for conceptual models of flow in fractured rocks and their characteristic relative permeability curves. CPE (continuum porous equivalent), DCPE (double continuum porous equivalent, DF (discrete fracture). Compiled after (NRC, 2001; TEUTSCH & SAUTER, 1991).

fracture geometry is not adequately described either and preferential flow along fractures may be highly nonlinear and driven by the gravitational instability of denser water invading a less dense air phase (PRUESS et al., 1999). The application of continuum models for simulation of unsaturated flow require that a representative elementary volume (REV) can be defined and is usually based on the Richards equation. A better geometrical representation of a fracture system and therefore the physical flow process can be achieved by discrete modeling approaches (EVANS & RASMUSSEN, 1991; KWICKLIS & HEALY, 1993; ZHANG et al., 2004, see Fig. 2.3, DF). Different laws of motion can be applied for fracture flow to consider different flow regimes. A disadvantage of discrete models is that the amount of fractures in large-scale systems exceeds by far computational capacities and that geometry of all individual discontinuities must be known a priori or described by employing statistical parameters (BONNET et al., 2001; GUERRIERO et al., 2010; LONG et al., 1982; SMITH & SCHWARTZ, 1984). Therefore, discrete models are rarely applied in field studies (JEANNIN, 2001; JEANNIN & MARÉCHAL, 1995; ZHANG et al., 2004) and are mainly used for the simulation of small-scale problems to explain specific types of flow process phenomena. A promising approach to deal with fractured systems has been proposed by LIU et al. (1998) and LIU & BODVARSSON (2003). The active fracture model (AFM) assumes that only a portion of connected fractures contributes to the overall conductivity of the fracture-matrix system, which is governed by (modified) van Genuchten relation permeability relations. To relate the amount of active fractures in the system to the effective saturation a simple power law is employed where the γ exponent is an intrinsic property of the fracture system and can be determined by inverse modeling. As noted by LIU & BODVARSSON (2003) the AFM approach assumes a homogeneous flow field and further research is needed to incorporate improved permeability relationships for the highly dynamic flow regimes encountered in fractures. *This is the basic incentive for the development of mechanistic modeling approaches presented in this thesis: Small-scale numerical investigations are essential to provide a detailed understanding of unsaturated flow processes in fractured media and the influence of system*

complexity on the flow dynamics.

Meshless Models

In contrast to grid-based methods, meshless modeling approaches rely on a particle based (Eulerian or Lagrangian) description of a field, which offers a versatile treatment of highly dynamic interfaces and complex geometries. The necessity for complex front-tracking algorithms to detect moving phase boundaries is eliminated because the mobile particles themselves are used to represent geometry and serve as discretization points to solve the governing equations. Gridless particle methods can be classified regarding their ability to resolve scale-dependent physics and therefore are suited for different spatio-temporal resolutions (DZWINEL et al., 2003). This hierarchical framework spanning several spatial scales arises mainly from computational limitations. Theoretically methods like Molecular Dynamics (MD, ALDER & WAINWRIGHT, 1959) can describe flow processes on all scales. However, reasonably sized simulation domains of porous fractured media would be far beyond computational capabilities, even for state of the art High-Performance-Computing facilities. Alternative meso- and macroscale methods such as Dissipative Particle Dynamics (DPD, HOOGERBRUGGE & KOELMAN, 1992) and Smoothed Particle Hydrodynamics (SPH, GINGOLD & MONAGHAN, 1977; LUCY, 1977) can be regarded as up-scaled formulations of MD models (HOOVER et al., 1994) for which the particle interactions are governed by stochastic or continuum descriptions, allowing for a much coarser temporal and spatial discretization (see Fig. 2.4). All models outlined above represent a liquid or solid by point masses whose motion is determined by simply integrating equations of Newtonian particle dynamics. Regarding the size of the particles and the resolved time scales, classical **MD** models allow the closest approximation to the atomistic physics of a system. Computationally feasible domain sizes are in the range of 10^{-14} m to 10^{-9} m with simulated time spans of 10^{-14} s to 10^{-3} s (DZWINEL et al., 2003). MD models have been employed to study a variety of phenomena such as fluid flow (KOPLIK et al., 1988), semiconductors (KRESSE & HAFNER, 1993) or protein and DNA structures (KARPLUS & PETSKO, 1990).

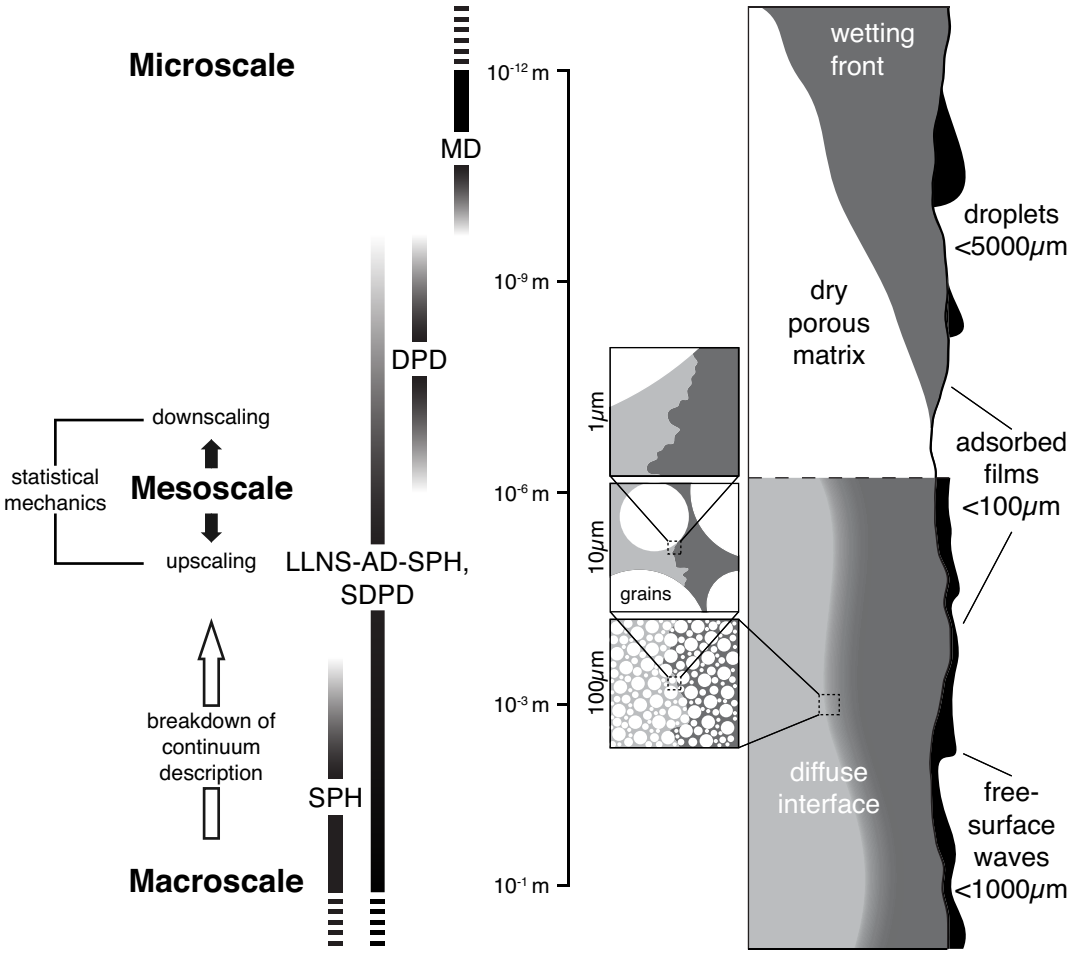

FIG. 2.4. Characteristic scales encountered in unsaturated fracture flow and scale hierarchy of particle techniques. SPH: smoothed particle hydrodynamics; SDPD: smoothed dissipative particle dynamics; LLNS-AD-SPH: Landau-Lifshitz-Navier-Stokes advection-diffusion SPH; DPD: dissipative particle dynamics; MD: molecular dynamics. Information compiled from (DRAGILA & WEISBROD, 2003; DRAGILA & WHEATCRAFT, 2001; DZWINEL et al., 1999; DZWINEL et al., 2003; ESPAÑOL & REVENGA, 2003; TOKUNAGA & WAN, 2001; TOKUNAGA & WAN, 1997).

Particle forces in MD are obtained via pairwise and/or multibody interactions

$$\mathbf{F}_i = m_i \frac{d\mathbf{v}_i}{dt} = \sum_j F^{C_2}(\mathbf{r}_i,\mathbf{r}_j) + \sum_j \sum_k F^{C_3}(\mathbf{r}_i,\mathbf{r}_j,\mathbf{r}_k) + \cdots, \tag{2.1}$$

where

$$\frac{d\mathbf{r}_i}{dt} = \mathbf{v}_i, \tag{2.2}$$

m_i, $\mathbf{v}_i$ and $\mathbf{r}_i$ are the mass, velocity and position of atom i, dt is the time step, F^{C_2} is a conservative pairwise interparticle force and F^{C_3} a three-body force (PLIMPTON, 1995). Depending on the problem type multibody forces of higher order have to be considered, though in most problems these can be neglected leaving only the computationally efficient pairwise F^{C_2} term. A common form for the pairwise potential is the Lennard-Jones potential (JONES, 1924)

$$\phi(r) = 4\varepsilon \left[\left(\frac{\sigma}{r}\right)^{12} - \left(\frac{\sigma}{r}\right)^{6} \right] = 4\varepsilon \left[\left(\frac{\sigma}{r_c}\right)^{12} - \left(\frac{\sigma}{r_c}\right)^{6} \right], \tag{2.3}$$

where r is the interparticle distance, σ is the distance at which the potential is zero, ε controls the attractive strength of the potential. For computational reasons a truncated potential with a cut-off distance $r_c = 2.5\sigma$ (comparable to the weighting length h of the SPH kernel or cutoff radius r_c in DPD models, see below) is often employed (see Fig. 2.5). The force between each particle pair (i.e., an attractive or repulsive force) can then be obtained as

$$F^{C_2}(\mathbf{r}_i,\mathbf{r}_j) = \frac{\partial \phi(r)}{\partial r} \frac{\mathbf{r}_{ij}}{r_{ij}}, \tag{2.4}$$

where $r = |\mathbf{r}_i - \mathbf{r}_j|$ and particles are advanced in time using an appropriate time stepping scheme. In order to obtain the macroscopic system properties, such as temperature or pressure, the temporal and spatial averages of

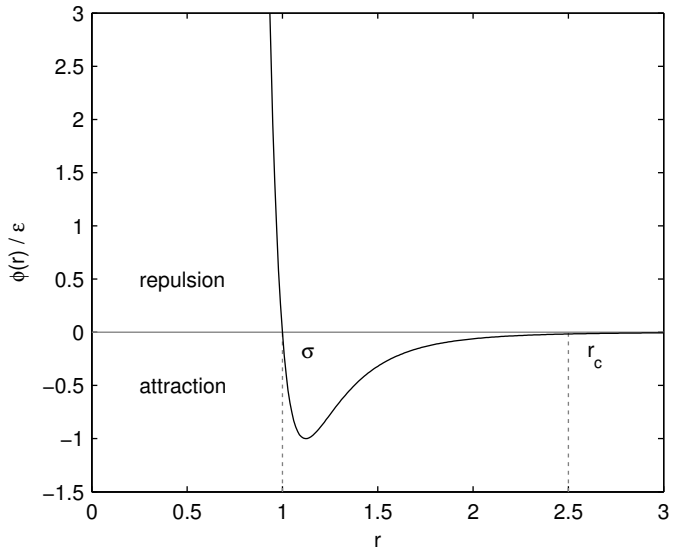

FIG. 2.5. Lennard-Jones potential for an MD model with $\varepsilon = -1$, $\sigma = 1$ and a common cut-off radius at $r_c = 2.5\sigma$.

statistical functions of particle motions have to be computed by means of kinetic theory (BOLTZMANN, 1872; MAXWELL, 1867, see also Chapter 6).

Despite their ability to preserve molecular details, MD models are computationally still extremely demanding and larger scale processes cannot be simulated (DZWINEL et al., 1999). As an alternative method **DPD** has been introduced by HOOGERBRUGGE & KOELMAN (1992), ESPAÑOL (1995) and GROOT & WARREN (1997), which can be thought of as a coarse-grained MD system, where particles represent clusters of merged atoms or molecules. Spatial and time scales covered by DPD are only slightly higher than for MD models and it is possible to derive the Navier-Stokes equation and a continuum viscosity for large scale coarse-grained models (FLEKKØY & COVENEY, 1999; FÜCHSLIN et al., 2007).

DPD models have been used to solve a wide range of small-scale problems such as flow of colloidial suspensions (BIAN et al., 2012; BOEK et al., 1997), elastic behavior of lipid membranes (LI et al., 2004), droplet and contact line dynamics (HUANG & MEAKIN, 2008; HUANG et al., 2009; KONG & YANG,

2006) and multiphase flow (TIWARI & ABRAHAM, 2006). Further studies have focussed on flow dynamics in microchannels (KUMAR et al., 2009; LIU et al., 2007b) and fractures (LIU et al., 2007a; MEAKIN & TARTAKOVSKY, 2009).

Particles (or clusters) in classical DPD interact via conservative forces (as in MD models) and fluctuating and dissipative interparticle forces that reflect the lost internal degrees of freedom and upscaled molecular properties:

$$\mathbf{F}_{ij} = \sum_{i \neq j} \mathbf{F}_{ij}^{C} + \sum_{i \neq j} \mathbf{F}_{ij}^{D} + \sum_{i \neq j} \mathbf{F}_{ij}^{R}, \tag{2.5}$$

where $F(\mathbf{r}_i,\mathbf{r}_j) = \mathbf{F}_{ij}$ and the forces are:

$$\mathbf{F}_{ij}^{C} = a w_{ij}^{C} \mathbf{e}_{ij} \qquad \text{(conservative force)} \tag{2.6}$$

$$\mathbf{F}_{ij}^{D} = -\gamma (w_{ij}^{R})^2 (\mathbf{e}_{ij} \cdot \mathbf{v}_{ij}) \mathbf{e}_{ij} \qquad \text{(dissipative force)} \tag{2.7}$$

$$\mathbf{F}_{ij}^{R} = \sigma w_{ij}^{R} \xi_{ij} (\Delta t)^{-1/2} \mathbf{e}_{ij} \qquad \text{(random force)} \tag{2.8}$$

Here $\mathbf{e}_{ij} = \mathbf{r}_{ij}/r_{ij}$ with $\mathbf{r}_i - \mathbf{r}_j = |\mathbf{r}_{ij}|$, a is the magnitude of the weighting function $w_{ij} = w(r_{ij})$, γ is a friction coefficient, σ controls the amplitude of the random noise, Δt is the time step and ξ_{ij} is a random number from a normal distribution with a unit variance and vanishing mean. The weighting function for the conservative force can assume various shapes including $w^C = 1 - r/r_c$ and $w^D = (w^R)^2 = (1 - r/r_c)^2$ (see Fig. 2.6 and LIU et al., 2007a). In the case of multiphase problems it should also consist of an attractive and repulsive part. The fluctuation-disspiation theorem (ESPAÑOL, 1995) relates the dissipative (viscous) forces to the thermal fluctuations, such that a thermal equilibrium can be established (i.e. stochastic kicks on the particles are on average fully dissipated). For a quadratic relationship between the dissipative and the random weighting function the following fluctuation-dissipation relation established a thermal equilibrium at a tem-

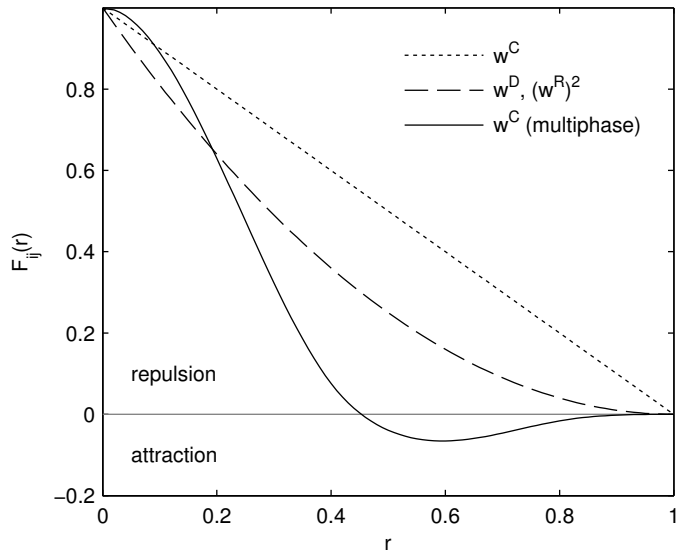

FIG. 2.6. Common forms of the conservative, dissipative and random force weighting in DPD models. For multiphase problems (e.g. coexistence of gas and liquid phase) a conservative force with attractive and repulsive parts is employed.

perature T (FÜCHSLIN et al., 2007):

$$2k_B T\gamma w_{ij}^D = \sigma^2 \left(w_{ij}^R\right)^2, \tag{2.9}$$

such that

$$\sigma^2 = 2k_B T\gamma, \tag{2.10}$$

where k_B is the Boltzmann constant. Early forms of DPD models suffered from two major problems: (1) They relied on conservative forces and therefore did not allow the implementation of a problem specific equation of state and (2) the physical scale of the model could not be defined, thus making them a poor choice for the simulation of Newtonian fluids (ESPAÑOL, 2005). Approaches such as thermodynamically consistent DPD (TC-DPD, SERRANO & ESPAÑOL, 2001) and smoothed dissipative particle dynamics

(SDPD, Español & Revenga, 2003) have since been introduced to achieve a deeper coupling of macro- and microscale hydrodynamics and relate DPD particles to physical volumes and intrinsic properties such as pressure and density. The former technique proved to be difficult to implement in three dimensions, as it relies on an underlying Voronoi grid where the required dynamic tessellation is computationally too expensive. A general drawback of DPD models are the high computation times when compared to SPH models. On scales where thermodynamic fluctuations can be neglected computation times of SPH models are orders of magnitude faster due to the time step constraints that microscopic fluctuations impose on the model (Filipovic et al., 2009). The **SPH** method shares some features with DPD, that is, it employs particles to discretize the simulation domain and particles interact through a weighting function. However, in contrast to classical DPD which relies on a stochastic description of collision forces, the particle acceleration in SPH is computed from a pressure gradient, which depends on the density obtained through multi-body particle interactions. Having its roots in astronomy and the simulation of protostar formations (Lucy, 1977) the distinction between the physical and numerical meaning of the term "particle" becomes readily apparent. In fluid dynamics the SPH method is used to discretize the Navier-Stokes equation, where particles represent finite volumes of matter whose accelerations are evolved in time following the momentum conservation for an incompressible system

$$\frac{D\boldsymbol{v}}{Dt} = -\frac{1}{\rho}\boldsymbol{\nabla} P + \frac{\mu}{\rho}\nabla^2\boldsymbol{v} + \boldsymbol{g} \tag{2.11}$$

and the continuity equation

$$\frac{d\rho}{dt} = -\rho\,(\nabla \cdot \mathrm{v}) \tag{2.12}$$

where P is the pressure, ρ the density, μ the viscosity and $\mathbf{g}$ the gravitational acceleration. Therefore SPH assumes a continuum description of the flow field a priori and can be classified as a macroscopic technique in its classical form. However, as will be also shown in this thesis (see Chapters 5

and 6), the effects of underlying atomistic physics can be incorporated in order to bridge the gap between macroscopic and microscopic physics. For more details about the theoretical background and the computational implementation the reader is referred to Chapter 3 and the introductions of Chapters 5 and 6).

SPH has been applied to a variety of studies in astronomy (Chakrabarti & Molteni, 1993; Gingold & Monaghan, 1977; Lucy, 1977; Monaghan & Price, 2004) and more general shock problems (Børve et al., 2001; Monaghan & Gingold, 1983). Engineering type problems such as dam breaks (Colagrossi & Landrini, 2003), coastal wave dynamics (Monaghan & Kos, 1999) and ship hull dynamics on open water bodies (Maruzewski et al., 2010) could be successfully simulated. In environmental and geoscientific reasearch fields SPH has been applied to large-scale flow problems such as lava flow (Hérault et al., 2011), landslide and mudflow dynamics (Laigle et al., 2007; McDougall & Hungr, 2004) and icesheet modeling (Pan et al., 2012).

The application of SPH to porescale dynamics has been triggering a lot of research efforts to cope with the distinct physical phenomena that dominate flow and transport processes at such scales. The inclusion of surface tension via pairwise particle interaction forces in the Navier-Stokes flow description (Morris, 2000; Nugent & Posch, 2000; Tartakovsky & Meakin, 2005b) was one of the prerequisites to simulate small scale free surface flows (Jiang et al., 2010; Sigalotti et al., 2006). Subsequent studies showed the flexibility of the approach to resolve complex geometries and simulate flow in rough and smooth fractures under various wetting conditions (Kordilla et al., 2013; Tartakovsky & Meakin, 2005a; Tartakovsky & Meakin, 2005c). Analogous to the discretization of the Navier-Stokes equation, SPH discretizations of the advection-diffusion equation (Gouet-Kaplan et al., 2009; Hu & Adams, 2006; Monaghan & Kocharyan, 1995; Tartakovsky et al., 2009a; Tartakovsky & Meakin, 2006; Tartakovsky et al., 2007b) and advection-diffusion-reaction equation (Meakin & Tartakovsky, 2009; Tartakovsky et al., 2007a; Tartakovsky et al., 2009b) have been presented to solve a wide range of multiphase problems.

Geometrical features of porous media and their effect on hydrodynamic dispersion have been investigated, e.g. by ZHU & FOX (2002), ZHU & FOX (2001), and ZHU et al. (1999).

Keeping the notation of Eqs. (2.1) and (2.5) the total force exerted on an SPH particle can consist of up to five components

$$\mathbf{F}_i = \sum_{i \neq j} \mathbf{F}_{ij}^P + \sum_{i \neq j} \mathbf{F}_{ij}^D + \mathbf{F}_i^G + \sum_{i \neq j} \mathbf{F}_{ij}^I + \sum_{i \neq j} \mathbf{F}_{ij}^R, \tag{2.13}$$

where

$$\mathbf{F}_{ij}^P = m_j m_i \left(\frac{P_j}{\rho_j^2} + \frac{P_i}{\rho_i^2} \right) \mathbf{e}_{ij} \frac{dW(r_{ij},h)}{dr_{ij}} \qquad \text{(pressure-gradient force)} \tag{2.14}$$

$$\mathbf{F}_{ij}^D = 2\mu m_j m_i \frac{\boldsymbol{v}_{ij}}{\rho_i \rho_j r_{ij}} \frac{dW(r_{ij},h)}{dr_{ij}} \qquad \text{(dissipative viscous force)} \tag{2.15}$$

$$\mathbf{F}_{ij}^G = m_i \mathbf{g} \qquad \text{(gravitational body force)} \tag{2.16}$$

$$\mathbf{F}_{ij}^I = \frac{1}{m_i} \boldsymbol{F}_{ij} \qquad \text{(pairwise interaction force)} \tag{2.17}$$

$$\mathbf{F}_{ij}^R = \left(s_j \frac{m_j^2}{\rho_j^2} + s_i \frac{m_i^2}{\rho_i^2} \right) \mathbf{e}_{ij} \frac{dW(r_{ij},h)}{dr_{ij}} \qquad \text{(random force).} \tag{2.18}$$

The pressure-gradient force has been derived by MONAGHAN (1982) who casted it in its symmetric form that fully conserves linear momentum. In opposite to MD or classical DPD a continuum space discretization in SPH is given in terms of a mass distribution m_j at position $\mathbf{r}_i$ with fluid density approximated by

$$\rho_i = \sum_{j=1}^{N} m_j W(\boldsymbol{r}_i - \boldsymbol{r}_j, h). \tag{2.19}$$

or more general for any field variable $f(\mathbf{r})$ defined on a continuum space its spatial averages and gradient can be obtained as

$$\begin{aligned}\langle f(\boldsymbol{r})\rangle &= \sum_{j=1}^{N} f(\boldsymbol{r}_j) W(|\boldsymbol{r}-\boldsymbol{r}_j|,h)\Delta V_j \qquad (2.20)\\ &= \sum_{j=1}^{N} f(\boldsymbol{r}_j) W(|\boldsymbol{r}-\boldsymbol{r}_j|,h)\frac{m_j}{\rho_j}\\ \langle \nabla f(\boldsymbol{r})\rangle &= \sum_{j=1}^{N} f(\mathbf{r}_j) \nabla W(|\boldsymbol{r}-\boldsymbol{r}_j|,h)\frac{m_j}{\rho_j}. \qquad (2.21)\end{aligned}$$

The weighting kernel employed in SPH generally assumes a hat like shape and, in order to assign a volume to each particle, the kernel is normalized such that

$$\int d\mathbf{r} W(\mathbf{r}) = 1. \qquad (2.22)$$

and one can obtain the number density n_i (the inverse of the volume V_i occupied by each particle)

$$n_i = \frac{1}{V_i} = \sum_j W(|\boldsymbol{r}-\boldsymbol{r}_j|,h) \qquad (2.23)$$

or similarly the mass density as in Eq. (2.19). The pressure is obtained from a problem dependent equation of state and in fluid dynamics often assumes a simple form such as $P_i = c_0^2\rho_i$, where the speed of sound c_0 controls the compressibility of the system. Dissipative forces in SPH are explicitly implemented by prescribing a dynamic viscosity term μ and various discretizations of the viscous stress in Eq. (2.11) have been proposed. Most forms, such as the one of Morris (1997) for incompressible fluids, approximate the second order viscosity term by a combination of first order derivatives in the SPH discretization. This way a computationally expensive nested summation can be avoided (Watkins et al., 1996). The pairwise interaction weighting function can have similar properties and form as shown

in Fig. 2.6 (multiphase), but should always consist of a short-range attractive and long-rang repulsive part to create surface tension (KORDILLA et al., 2013; TARTAKOVSKY & MEAKIN, 2005b).

The random force (Eq. 2.18) is implemented similar to the symmetric pressure gradient, where the magnitude of the random stress is related to the viscous dissipation via the fluctuation-disspiation theorem (ESPAÑOL, 1995) and the form of the stress follows from the Landau-Lifshitz-Navier-Stokes equations (LANDAU & LIFSHITZ, 1987). The correct scaling of the stress with the inverse of the particle volume (see Chapter 6) essentially converts the macrocsopic SPH model into a truly mesoscopic model which dynamically adjusts the underlying microscopic fluctuations while preserving the continuum dynamics of the macroscopic Navier-Stokes equations.

2.5 References

ALDER, B. J. & WAINWRIGHT, T. E. (1959): 'Studies in Molecular Dynamics. I. General Method'. *Journal of Chemical Physics*, vol. **31**(2): p. 459 (cit. on p. 23).

ARORA, T. & AHMED, S. (2011): 'Characterization of recharge through complex vadose zone of a granitic aquifer by time-lapse electrical resistivity tomography'. *Journal of Applied Geophysics*, vol. **73**(1): pp. 35–44 (cit. on p. 15).

BEAR, J. (1972): *Dynamics of fluids in porous media*. Courier Dover Publications (cit. on p. 12).

BENSON, D. A. (2001): 'A model of water streaking down a wall'. *Water Resources Research*, vol. **37**(2): p. 427 (cit. on p. 14).

BIAN, X., LITVINOV, S., QIAN, R., ELLERO, M. & ADAMS, N. A. (2012): 'Multiscale modeling of particle in suspension with smoothed dissipative particle dynamics'. *Physics of Fluids*, vol. **24**(1): p. 012002 (cit. on p. 26).

BIKERMAN, J. (1950): 'Sliding of drops from surfaces of different roughnesses'. *Journal of Colloid Science*, vol. **5**(4): pp. 349–359 (cit. on p. 14).

BLAKE, T. & RUSCHAK, K. (1997): 'Wetting: static and dynamic contact lines'. *Liquid film coating*. Springer (cit. on p. 17).

BOEK, E. S., COVENEY, P., LEKKERKERKER, H. N. W. & SCHOOT, P. van der (1997): 'Simulating the rheology of dense colloidal suspensions using dissipative particle dynamics'. *Physical Review E*, vol. **55**(3): pp. 3124–3133 (cit. on p. 26).

BOLTZMANN, L. (1872): 'Weitere Studien über das Wärmegleichgewicht unter Gasmolekülen'. *Akademie der Wissenschaften, Mathematische-Natur-wissenschaftliche Klasse*, vol. **66**(3): pp. 275–370 (cit. on p. 26).

BONNET, E., BOUR, O., ODLING, N. E., DAVY, P., MAIN, I., COWIE, P. & BERKOWITZ, B. (2001): 'Scaling of fracture systems in geological media'. *American Geophysical Union*, vol. **39**(3): pp. 347–383 (cit. on p. 22).

BØRVE, S., OMANG, M. & TRULSEN, J. (2001): 'Regularized smoothed particle hydrodynamics : a new approach to simulating magnetohydrodynamic shocks'. *The Astrophysical Journal*, vol. **1**: pp. 82–93 (cit. on p. 30).

Chakrabarti, S. & Molteni, D. (1993): 'Smoothed particle hydrodynamics confronts theory: Formation of standing shocks in accretion disks and winds around black holes'. *The Astrophysical Journal*, vol. **417**: pp. 671–676 (cit. on p. 30).

Cheng, C. L., Kang, M., Perfect, E., Voisin, S., Horita, J., Bilheux, H. Z., Warren, J. M., Jacobson, D. L. & Hussey, D. S. (2012): 'Average Soil Water Retention Curves Measured by Neutron Radiography'. *Soil Science Society of America Journal*, vol. **76**(4): p. 1184 (cit. on p. 15).

Chu, K. & Dukler, A. (1974): 'Statistical characteristics of thin, wavy films: Part II. Studies of the substrate and its wave structure'. *American Institute of Chemical Engineers Journal*, vol. **20**(4): pp. 695–706 (cit. on p. 19).

Colagrossi, A. & Landrini, M. (2003): 'Numerical simulation of interfacial flows by smoothed particle hydrodynamics'. *Journal of Computational Physics*, vol. **191**: p. 448 (cit. on p. 30).

Cox, R. (1986): 'The dynamics of the spreading of liquids on a solid surface. Part 1. Viscous flow'. *Journal of Fluid Mechanics*, vol. **168**(1): pp. 169–194 (cit. on p. 17).

Doummar, J., Sauter, M. & Geyer, T. (2012): 'Simulation of flow processes in a large scale karst system with an integrated catchment model (Mike She) Identification of relevant parameters influencing spring discharge'. *Journal of Hydrology*, vol. **426-427**: pp. 112–123 (cit. on p. 20).

Dragila, M. I. & Weisbrod, N. (2004a): 'Flow in Menisci Corners of Capillary Rivulets'. *Vadose Zone Journal*, vol. **3**: pp. 1439–1442 (cit. on pp. 14, 18).

– (2004b): 'Fluid motion through an unsaturated fracture junction'. *Water Resources Research*, vol. **40**: pp. 1–11 (cit. on p. 14).

– (2003): 'Parameters affecting maximum fluid transport in large aperture fractures'. *Advances in Water Resources*, vol. **26**: pp. 1219–1228 (cit. on pp. 18, 24).

Dragila, M. I. & Wheatcraft, S. (2001): 'Free-surface films'. *Conceptual Models of Flow and Transport in the Fractured Vadose Zone*. National Academies Press: pp. 217–241 (cit. on pp. 19, 24).

Drosos, E., Paras, S. & Karabelas, A. (2004): 'Characteristics of developing free falling films at intermediate Reynolds and high Kapitza numbers'.

International Journal of Multiphase Flow, vol. **30**(7-8): pp. 853–876 (cit. on p. 19).

Durner, W. (1994): 'Hydraulic conductivity estimation for soils with heterogeneous pore structure'. *Water Resources Research*, vol. **30**(2): p. 211 (cit. on p. 16).

Dussan, E. B. & Chow, R. T.-P. (1983): 'On the ability of drops or bubbles to stick to non-horizontal surfaces of solids'. *Journal of Fluid Mechanics*, vol. **137**: pp. 1–29 (cit. on p. 14).

Dzwinel, W., Alda, W. & Yuen, D. (1999): 'Cross-Scale Numerical Simulations Using Discrete Particle Models'. *Molecular Simulation*, vol. **22**(6): pp. 397–418 (cit. on pp. 24, 26).

Dzwinel, W., Yuen, D. & Boryczko, K. (2003): 'Bridging diverse physical scales with the discrete-particle paradigm in modeling colloidal dynamics with mesoscopic features'. *Chemical Engineering Science*, vol. **61**(7): pp. 2169–2185 (cit. on pp. 23, 24).

ElSherbini, A. I. & Jacobi, A. M. (2004): 'Liquid drops on vertical and inclined surfaces; I. An experimental study of drop geometry.' *Journal of Colloid and Interface Science*, vol. **273**(2): pp. 556–65 (cit. on pp. 14, 17).

– (2006): 'Retention forces and contact angles for critical liquid drops on non-horizontal surfaces.' *Journal of Colloid and Interface Science*, vol. **299**(2): pp. 841–9 (cit. on p. 14).

Español, P. (2005): 'Dissipative Particle Dynamics'. *Handbook of Materials Modeling*. Ed. by S. Yip. Chap. 8.6: pp. 2503–2512 (cit. on p. 28).

– (1995): 'Hydrodynamics from dissipative particle dynamics'. *Physical Review E*, vol. **52**(2): pp. 1734–1742 (cit. on pp. 26, 27, 33).

Español, P. & Revenga, M. (2003): 'Smoothed dissipative particle dynamics'. *Physical Review E*, vol. **67**(2): pp. 1–12 (cit. on pp. 24, 29).

Evans, D. D. & Rasmussen, T. C. (1991): *Unsaturated Flow and Transport Through Fractured Rock Related to High-level Waste Repositories: Final Report–phase III*. Tech. rep. Washington: Office of Nuclear Regulatory Research (cit. on p. 22).

Evans, D.D., Rasmussen, T.C., Todd, C. & J., N.T. (2001): 'Flow and Transport Through Unsaturated Fractured Rock'. *Geophysical Monograph Series*, vol. **42**: p. 201 (cit. on p. 15).

Fairley, J.P., Podgorney, R.K. & Wood, T.R. (2000): 'Unsaturated Flow through a Small FractureMatrix Network: Part 2. Uncertainty in Modeling Flow Processes'. *Vadose Zone Journal*, vol. **3**: pp. 101–108 (cit. on p. 15).

Faybishenko, B. (2003): 'On the physics of unstable infiltration, seepage, and gravity drainage in partially saturated tuffs'. *Journal of Contaminant Hydrology*, vol. **62-63**: pp. 63–87 (cit. on p. 11).

Faybishenko, B., Witherspoon, P.A., Doughty, C., Geller, J., Wood, T.R. & R., P. (2001): 'Multi-scale investigations of liquid flow in a fractured basalt vadose zone'. *Flow and Transport Through Unsaturated Fractured Rock*. Ed. by D. Evans, T. Nicholson & T. Rassmusen. Wiley Online Library: pp. 161–182 (cit. on p. 12).

Faybishenko, B., Witherspoon, P. & Benson, S. (2000): *Dynamics of fluids in fractured rock*. American Geophysical Union (cit. on p. 13).

Filipovic, N., Ivanovic, M. & Kojic, M. (2009): 'A comparative numerical study between dissipative particle dynamics and smoothed particle hydrodynamics when applied to simple unsteady flows in microfluidics'. *Physical Review E*, vol. **7**: pp. 227–235 (cit. on p. 29).

Flekkøy, E. & Coveney, P. (1999): 'From Molecular Dynamics to Dissipative Particle Dynamics'. *Physical Review Letters*, vol. **83**(9): pp. 1775–1778 (cit. on p. 26).

Flint, A.L., Flint, L.E., Bodvarsson, G.S., Kwicklis, E.M. & Fabryka-Martin, J. (2001): 'Evolution of the conceptual model of unsaturated zone hydrology at Yucca Mountain, Nevada'. *Journal of Hydrology*, vol. **247**(1-2): pp. 1–30 (cit. on p. 16).

Füchslin, R.M., Fellermann, H., Eriksson, A. & Ziock, H.-J. (2007): 'Coarse-Graining and Scaling in Dissipative Particle Dynamics'. *The Journal of Chemical Physics*, vol.: p. 8 (cit. on pp. 26, 28).

Furmidge, C. (1962): 'Studies at phase interfaces. I. The sliding of liquid drops on solid surfaces and a theory for spray retention'. *Journal of Colloid Science*, vol. **17**(4): pp. 309–324 (cit. on p. 14).

Gerke, H. H. & Van Genuchten, M. (1993): 'Evaluation of a first-order water transfer term for variably saturated dual-porosity flow models'. *Water Resources Research*, vol. **29**: pp. 1225–1225 (cit. on p. 20).

Germann, P. F., Helbling, A. & Vadilonga, T. (2007): 'Rivulet Approach to Rates of Preferential Infiltration'. *Vadose Zone Journal*, vol. **6**(2): pp. 207–220 (cit. on p. 19).

Ghezzehei, T. A. (2004): 'Constraints for flow regimes on smooth fracture surfaces'. *Water Resources Research*, vol. **40**: pp. 1–14 (cit. on pp. 18, 19).

Ghezzehei, T. A. & Or, D. (2005): 'Liquid fragmentation and intermittent flow regimes in unsaturated fractured media'. *Water Resources Research*, vol. **41**(12): pp. 1–10 (cit. on p. 17).

Gingold, R. A. & Monaghan, J. J. (1977): 'Smoothed particle hydrodynamics: theory and application to non-spherical stars'. *Mon. Not. R. Astron. Soc.* Vol. **181**: pp. 375–389 (cit. on pp. 23, 30).

Glass, R. J. & Nicholl, M. J. (1996): 'Physics of gravity fingering of immiscible fluids within porous media: An overview of current understanding and selected complicating factors'. *Geoderma*, vol. **70**(2-4): pp. 133–163 (cit. on p. 14).

Glass, R. J., Nicholl, M. J., Ramirez, A. L. & Daily, W. D. (2002): 'Liquid phase structure within an unsaturated fracture network beneath a surface infiltration event: Field experiment'. *Water Resources Research*, vol. **38**(10): pages (cit. on p. 15).

Gomba, J. M. & Homsy, G. M. (2009): 'Analytical solutions for partially wetting two-dimensional droplets.' *Langmuir : the ACS journal of surfaces and colloids*, vol. **25**(10): pp. 5684–91 (cit. on p. 17).

Gouet-Kaplan, M., Tartakovsky, A. & Berkowitz, B. (2009): 'Simulation of the interplay between resident and infiltrating water in partially saturated porous media'. *Water Resources Research*, vol. **45**(5): pp. 1–9 (cit. on p. 30).

Groot, R. D. & Warren, P. B. (1997): 'Dissipative particle dynamics: Bridging the gap between atomistic and mesoscopic simulation'. *Journal of Chemical Physics*, vol. **107**(11): pp. 4423–4435 (cit. on p. 26).

Guerriero, V., Iannace, A., Mazzoli, S., Parente, M., Vitale, S. & Giorgioni, M. (2010): 'Quantifying uncertainties in multi-scale studies of fractured reservoir analogues: Implemented statistical analysis of scan line data from carbonate rocks'. *Journal of Structural Geology*, vol. **32**(9): pp. 1271–1278 (cit. on p. 22).

Hainsworth, J.M. & Aylmore, L. (1983): 'The use of computer assisted tomography to determine spatial distribution of soil water content'. *Australian Journal of Soil Research*, vol. **21**(4): p. 435 (cit. on p. 15).

Hasseine, A., Bellagoun, A. & Bart, H.-J. (2011): 'Analytical solution of the droplet breakup equation by the Adomian decomposition method'. *Applied Mathematics and Computation*, vol. **218**(5): pp. 2249–2258 (cit. on p. 17).

Hérault, A., Bilotta, G. & Vicari, A. (2011): 'Numerical simulation of lava flow using a GPU SPH model'. *Annals of Geophysics*, vol. **54**(5): pp. 600–620 (cit. on p. 30).

Hoogerbrugge, P. & Koelman, J. (1992): 'Simulating microscopic hydrodynamic phenomena with dissipative particle dynamics'. *Europhys. Lett.* Vol. **19**(June): pp. 155–160 (cit. on pp. 23, 26).

Hoover, W.G., Pierce, T.G., Hoover, C.G., Shugart, J.O., Stein, C.M. & Edwards, A.L. (1994): 'Molecular Dynamics , Smoothed-Particle Applied Mechanics , and Irreversibility'. *Computers & Mathematics with Applications*, vol. **28**(10): pp. 155–174 (cit. on p. 23).

Hu, X.Y. & Adams, N.A. (2006): 'A multi-phase SPH method for macroscopic and mesoscopic flows'. *Journal of Computational Physics*, vol. **213**: p. 844 (cit. on p. 30).

Huang, H. & Meakin, P. (2008): 'Three-dimensional simulation of liquid drop dynamics within unsaturated vertical Hele-Shaw cells'. *Water Resources Research*, vol. **44**(3): W03411 (cit. on p. 26).

Huang, J.J., Shu, C. & Chew, Y.T. (2009): 'Lattice Boltzmann study of droplet motion inside a grooved channel'. *Physics of Fluids*, vol. **21**: pp. 1–11 (cit. on p. 26).

Jeannin, P.Y. (2001): 'Modeling flow in phreatic and epiphreatic karst conduits'. *Water Resources Research*, vol. **37**(2): pp. 191–200 (cit. on p. 22).

Jeannin, P.Y. & Maréchal, J.C. (1995): 'Lois de pertes de charge dans les conduits karstiques: base théorique et observations'. *Bull. Hydrogéol., Neuchâtel*, vol. **14**: pp. 149–176 (cit. on p. 22).

Jiang, T., Ouyang, J., Yang, B. & Ren, J. (2010): 'The SPH method for simulating a viscoelastic drop impact and spreading on an inclined plate'. *Computational Mechanics*, vol. **45**(6): pp. 573–583 (cit. on p. 30).

Jones, J.E. (1924): 'On the Determination of Molecular Fields. II. From the Equation of State of a Gas'. *Proceedings of the Royal Society A: Mathematical, Physical and Engineering Sciences*, vol. **106**(738): pp. 463–477 (cit. on p. 25).

Jung, S.Y., Lim, S. & Lee, S.J. (2012): 'Investigation of water seepage through porous media using X-ray imaging technique'. *Journal of Hydrology*, vol. **452-453**: pp. 83–89 (cit. on p. 15).

Karplus, M. & Petsko, G. (1990): 'Molecular dynamics simulations in biology'. *Nature*, vol. **347**(6294): pp. 631–639 (cit. on p. 23).

Kong, B. & Yang, X. (2006): 'Dissipative particle dynamics simulation of contact angle hysteresis on a patterned solid/air composite surface.' *Langmuir*, vol. **22**(5): pp. 2065–73 (cit. on p. 26).

Koplik, J., Banavar, J. & Willemsen, J. (1988): 'Molecular dynamics of Poiseuille flow and moving contact lines'. *Physical Review Letters*, vol. **60**(13): pp. 1282–1286 (cit. on p. 23).

Kordilla, J., Sauter, M., Reimann, T. & Geyer, T. (2012): 'Simulation of saturated and unsaturated flow in karst systems at catchment scale using a double continuum approach'. *Hydrology and Earth System Sciences*, vol. **16**(10): pp. 3909–3923 (cit. on p. 20).

Kordilla, J., Tartakovsky, A. & Geyer, T. (2013): 'A Smoothed Particle Hydrodynamics model for droplet and film flow on smooth and rough fracture surfaces'. *Advances in Water Resources*, vol. **59**: pp. 1–14 (cit. on pp. 30, 33).

Krasovitski, B. & Marmur, A. (2005): 'Drops down the hill: theoretical study of limiting contact angles and the hysteresis range on a tilted plate'. *Langmuir*, vol. (21): pp. 3881–3885 (cit. on p. 17).

Kresse, G. & Hafner, J. (1993): 'Ab initio molecular dynamics for liquid metals'. *Physical Review B*, vol. **47**(1): pp. 558–561 (cit. on p. 23).

Kumar, A., Asako, Y., Abu-nada, E., Krafczyk, M. & Faghri, M. (2009): 'From dissipative particle dynamics scales to physical scales: a coarse-graining study for water flow in microchannel'. *Microfluid Nanofluid*, vol. **7**: pp. 467–477 (cit. on p. 27).

Kwicklis, E. & Healy, R. (1993): 'Numerical investigation of Steady Liquid Water Flow in a Variably Saturated Fracture Network'. *Water Resources Research*, vol. **29**(12): pp. 4091–4102 (cit. on p. 22).

Laigle, D., Lachamp, P. & Naaim, M. (2007): 'SPH-based numerical investigation of mudflow and other complex fluid flow interactions with structures'. *Computational Geosciences*, vol. **11**(4): pp. 297–306 (cit. on p. 30).

Landau, L.D. & Lifshitz, E.M. (1987): *Fluid Mechanics: Volume 6 (Course Of Theoretical Physics)*. Butterworth-Heinemann (cit. on p. 33).

Lange, J., Arbel, Y., Grodek, T. & Greenbaum, N. (2010): 'Water percolation process studies in a Mediterranean karst area'. *Hydrological Processes*, vol. **24**(13): pp. 1866–1879 (cit. on p. 16).

Le Grand, N., Daerr, A. & Limat, L. (2005): 'Shape and motion of drops sliding down an inclined plane'. *Journal of Fluid Mechanics*, vol. **541**: p. 293 (cit. on pp. 14, 17).

Lebeau, M. & Konrad, J.-M. (2010): 'A new capillary and thin film flow model for predicting the hydraulic conductivity of unsaturated porous media'. *Water Resources Research*, vol. **46**(12): pp. 1–15 (cit. on p. 16).

Li, D.-W., Liu, X.Y. & Feng, Y.P. (2004): 'Bond-Angle-Potential-Dependent Dissipative Particle Dynamics Simulation and Lipid Inverted Phase'. *The Journal of Physical Chemistry B*, vol. **108**(30): pp. 11206–11213 (cit. on p. 26).

Liu, H. & Bodvarsson, G.S. (2003): 'Upscaling of constitutive relations in unsaturated heterogeneous tuff matrix'. *Journal of Hydrology*, vol. **276**: pp. 198–209 (cit. on p. 22).

Liu, H.-H., Doughty, C. & Bodvarsson, G.S. (1998): 'An active fracture model for unsaturated flow and transport in fractured rocks'. *Water Resources Research*, vol. **34**(10): pp. 2633–2646 (cit. on p. 22).

Liu, M., Meakin, P. & Huang, H. (2007a): 'Dissipative particle dynamics simulation of fluid motion through an unsaturated fracture and fracture junction'. *Journal of Computational Physics*, vol. **222**: pp. 110–130 (cit. on p. 27).

– (2007b): 'Dissipative particle dynamics simulation of multiphase fluid flow in microchannels and microchannel networks'. *Physics of Fluids*, vol. **19**: pp. 1–11 (cit. on p. 27).

Long, J. C. S., Remer, J. S., Wilson, C. R. & Witherspoon, P. A. (1982): 'Porous media equivalents for networks of discontinuous fractures'. *Water Resources Research*, vol. **18**(3): pp. 645–658 (cit. on p. 22).

Lucy, L. B. (1977): 'A numerical approach to the testing of the fission hypothesis'. *Astronomical Journal*, vol. **82**(12): pp. 1013–1024 (cit. on pp. 23, 29, 30).

Lunati, I. & Or, D. (2009): 'Gravity-driven slug motion in capillary tubes'. *Physics of Fluids*, vol. **21**(5): p. 052003 (cit. on p. 17).

Maruzewski, P., Le Touzé, D., Oger, G. & Avellan, F. (2010): 'SPH high-performance computing simulations of rigid solids impacting the free-surface of water'. *Journal of Hydraulic ...* Vol. **47**: pp. 126–134 (cit. on p. 30).

Maxwell, J. (1867): 'On the Dynamical Theory of Gases'. *Philosophical Transactions of the Royal Society of London*, vol. **157**(1867): pp. 49–88 (cit. on p. 26).

McDougall, S. & Hungr, O. (2004): 'A model for the analysis of rapid landslide motion across three-dimensional terrain'. *Canadian Geotechnical Journal*, vol. **1097**: pp. 1084–1097 (cit. on p. 30).

Mclaren, R. G., Forsyth, P. A., Sudicky, E. A., Vanderkwaak, J. E., Schwartz, F. W. & Kessler, J. H. (2000): 'Flow and transport in fractured tuff at Yucca Mountain: numerical experiments on fast preferential flow mechanisms'. *Journal of Contaminant Hydrology*, vol. **43**: pp. 211–238 (cit. on p. 20).

Meakin, P. & Tartakovsky, A. (2009): 'Modeling and simulation of pore-scale multiphase fluid flow and reactive transport in fractured and porous media'. *Reviews of Geophysics*, vol. (47): pp. 1–47 (cit. on pp. 27, 30).

MILLER, S., BAAFI, E. & SCHOFIELD, N. (1997): 'Geostatistical simulation for upscaling field measurements of unsaturated hydraulic conductivity'. *Geostatistics Wollongong*, vol. **96**: pp. 1098–1111 (cit. on p. 12).

MIRUS, B.B. & NIMMO, J.R. (2013): 'Balancing practicality and hydrologic realism: A parsimonious approach for simulating rapid groundwater recharge via unsaturated-zone preferential flow'. *Water Resources Research*, vol. **49**(3): pp. 1458–1465 (cit. on p. 16).

MONAGHAN, J.J. (1982): 'Why particle methods work'. *SIAM: SIAM Journal on Scientific Computing*, vol. **3**(4): pp. 422–433 (cit. on p. 31).

MONAGHAN, J.J. & GINGOLD, R. (1983): 'Shock Simulation by the Particle method SPH'. *Journal of Computational Physics*, vol. **389**: pp. 374–389 (cit. on p. 30).

MONAGHAN, J.J. & KOCHARYAN, A. (1995): 'SPH simulation of multi-phase flow'. *Computer Physics Communications*, vol. **87**: pp. 225–235 (cit. on p. 30).

MONAGHAN, J.J. & KOS, A. (1999): 'Solitary waves on a Cretan beach'. *Journal of Waterway, Port, Coastal, and Ocean Engineering*, vol. (June): pp. 145–154 (cit. on p. 30).

MONAGHAN, J.J. & PRICE, D.J. (2004): 'Toy stars in one dimension'. *Monthly Notices of the Royal Astronomical Society*, vol. **350**(4): pp. 1449–1456 (cit. on p. 30).

MORRIS, J.P. (1997): 'Modeling Low Reynolds Number Incompressible Flows Using SPH'. *Journal of Computational Physics*, vol. **136**(1): pp. 214–226 (cit. on p. 32).

– (2000): 'Simulating surface tension with smoothed particle hydrodynamics'. *International Journal for Numerical Methods in Fluids*, vol. **33**: pp. 333–353 (cit. on p. 30).

NICHOLL, M.J. & GLASS, R.J. (2005): 'Infiltration into an Analog Fracture'. *Vadose Zone Journal*, vol. **4**(4): p. 1123 (cit. on p. 14).

NIMMO, J.R. (2012): 'Preferential flow occurs in unsaturated conditions'. *Hydrological Processes*, vol. **26**(5): pp. 786–789 (cit. on p. 15).

– (2010): 'Theory for Source-Responsive and Free-Surface Film Modeling of Unsaturated Flow'. *Vadose Zone Journal*, vol. **9**(2): p. 295 (cit. on p. 16).

NRC (2001): *Conceptual Models of Flow and Transport in the Fractured Vadose Zone*. Washington D.C.: National Academy Press: p. 374 (cit. on p. 21).

NUGENT, S. & POSCH, H. A. (2000): 'Liquid drops and surface tension with smoothed particle applied mechanics'. *Physical Review E*, vol. **62**(4): pp. 4968–4975 (cit. on p. 30).

NUSSELT, W. (1916): 'Die Oberflächenkondensation des Wasserdampfes'. *Zeitschrift des Vereins Deutscher Ingenieure*, vol. **60**: pp. 541–546 (cit. on p. 19).

PAN, W., TARTAKOVSKY, A. & MONAGHAN, J. J. (2012): 'A smoothed-particle hydrodynamics model for ice-sheet and ice-shelf dynamics'. *Journal of Glaciology*, vol. **58**(208): pp. 216–222 (cit. on p. 30).

PATNAIK, V. & PEREZ-BLANCO, H. (1996): 'Roll waves in falling films: an approximate treatment of the velocity field'. *International journal of heat and fluid flow*, vol. **17**(1): pp. 63–70 (cit. on p. 19).

PETERS, A. & DURNER, W. (2008): 'A simple model for describing hydraulic conductivity in unsaturated porous media accounting for film and capillary flow'. *Water Resources Research*, vol. **44**(11): pp. 1–11 (cit. on p. 16).

PLIMPTON, S. (1995): 'Fast parallel algorithms for short-range molecular dynamics'. *Journal of Computational Physics*, vol. **117**(1): pp. 1–19 (cit. on p. 25).

PODGORSKI, T., FLESSELLES, J.-M. & LIMAT, L. (2001): 'Corners, Cusps, and Pearls in Running Drops'. *Physical Review Letters*, vol. **87**(3): p. 036102 (cit. on pp. 14, 17, 19).

PRUESS, K., FAYBISHENKO, B. & BODVARSSON, G. S. (1999): 'Alternative concepts and approaches for modeling flow and transport in thick unsaturated zones of fractured rocks'. *Science*, vol.: pp. 281–322 (cit. on p. 22).

RICHARDS, L. A. (1931): 'Capillary Conduction of Liquids Through Porous Mediums'. *Physics*, vol. **1**(5): pp. 318–333 (cit. on p. 12).

ROSS, P. J. & SMETTEM, K. R. J. (1993): 'Describing soil hydraulic properties with sums of simple functions'. *Soil Science Society of America Journal*, vol. **57**(1): pp. 26–26 (cit. on p. 16).

Rossi, C. & Nimmo, J.R. (1994): 'Modeling of soil water retention from saturation to oven dryness'. *Water Resources Research*, vol. **30**(3): pp. 701–708 (cit. on p. 16).

Sakaki, T. & Rajaram, H. (2006): 'Performance of different types of time domain reflectometry probes for water content measurement in partially saturated rocks'. *Water Resources Research*, vol. **42**(7): pp. 1–15 (cit. on p. 15).

Salve, R. (2005): 'Observations of preferential flow during a liquid release experiment in fractured welded tuffs'. *Water Resources Research*, vol. **41**(9): pp. 1–14 (cit. on p. 15).

Schneebeli, M., Flühler, H. & Gimmi, T. (1995): 'Measurements of Water Potential and Water Content in Unsaturated Cystalline Rock'. *Water Resources Research*, vol. **31**(8): pp. 1837–1843 (cit. on p. 15).

Serrano, M. & Español, P. (2001): 'Thermodynamically consistent mesoscopic fluid particle model'. *Physical Review E*, vol. **64**(4): p. 046115 (cit. on p. 28).

Shokri, N., Lehmann, P. & Or, D. (2010): 'Liquid-phase continuity and solute concentration dynamics during evaporation from porous media: Pore-scale processes near vaporization surface'. *Physical Review E*, vol. **81**(4): p. 046308 (cit. on p. 16).

Sigalotti, L.D.G., Daza, J. & Donoso, A. (2006): 'Modelling free surface flows with smoothed particle hydrodynamics'. *Condensed Matter Physics*, vol. **9**(2): pp. 359–366 (cit. on p. 30).

Singhal, B.B. & Gupta, R.P. (2010): *Applied Hydrogeology of Fractured Rocks*. Springer: p. 408 (cit. on p. 11).

Smith, L. & Schwartz, F.W. (1984): 'An Analysis of the Influence of Fracture Geometry on Mass Transport in Fractured Media'. *Water Resources Research*, vol. **20**(9): pp. 1241–1252 (cit. on p. 22).

Su, G.W., Geller, J.T., Pruess, K. & Hunt, J.R. (2001): 'Solute transport along preferential flow paths in unsaturated fractures'. *Water Resources Research*, vol. **37**(10): pp. 2481–2491 (cit. on p. 14).

Su, G. W., Geller, J. T., Hunt, J. R. & Pruess, K. (2004): 'Small-Scale Features of Gravity-Driven Flow in Unsaturated Fractures'. *Vadose Zone Journal*, vol. **3**(2): pp. 592–601 (cit. on p. 14).

Tartakovsky, A., Ferris, K. F. & Meakin, P. (2009a): 'Lagrangian particle model for multiphase flows'. *Computer Physics Communications*, vol. **180**(10): pp. 1874–1881 (cit. on p. 30).

Tartakovsky, A. & Meakin, P. (2005a): 'A smoothed particle hydrodynamics model for miscible flow in three-dimensional fractures and the two-dimensional Rayleigh-Taylor instability'. *Journal of Computational Physics*, vol. **207**: pp. 610–624 (cit. on p. 30).

– (2005b): 'Modeling of surface tension and contact angles with smoothed particle hydrodynamics'. *Physical Review E*, vol. **72**: p. 026301 (cit. on pp. 30, 33).

– (2006): 'Pore scale modeling of immiscible and miscible fluid flows using smoothed particle hydrodynamics'. *Advances in Water Resources*, vol. **29**(10): pp. 1464–1478 (cit. on p. 30).

– (2005c): 'Simulation of Unsaturated Flow in Complex Fractures Using Smoothed Particle Hydrodynamics'. *Vadose Zone Journal*, vol. **4**(3): pp. 848–855 (cit. on p. 30).

Tartakovsky, A., Meakin, P., Scheibe, T. D. & Eichler West, R. (2007a): 'Simulations of reactive transport and precipitation with smoothed particle hydrodynamics'. *Journal of Computational Physics*, vol. **222**(2): pp. 654–672 (cit. on p. 30).

Tartakovsky, A., Tartakovsky, G. & Scheibe, T. (2009b): 'Effects of incomplete mixing on multicomponent reactive transport'. *Advances in Water Resources*, vol. **32**(11): pp. 1674–1679 (cit. on p. 30).

Tartakovsky, A., Ward, A. L. & Meakin, P. (2007b): 'Pore-scale simulations of drainage of heterogeneous and anisotropic porous media'. *Physics of Fluids*, vol. **19**(10): p. 103301 (cit. on p. 30).

Teutsch, G. & Sauter, M. (1991): 'Groundwater modeling in karst terranes: Scale effects, data acquisition and field validation'. *Proc. Third Conf. Hydrogeology, Ecology, Monitoring, and Management of Ground Water in Karst Terranes, Nashville, TN*: pp. 17–35 (cit. on pp. 20, 21).

Tiwari, A. & Abraham, J. (2006): 'Dissipative-particle-dynamics model for two-phase flows'. *Physical Review E*, vol. **74**(5): p. 056701 (cit. on p. 27).

Tokunaga, T.K. & Wan, J. (2001): 'Surface-zone flow along unsaturated rock fractures'. *Water Resources Research*, vol. **37**(2): p. 287 (cit. on pp. 14, 24).

– (1997): 'Water film flow along fracture surfaces of porous rock'. *Water Resources Research*, vol. **33**(6): p. 1287 (cit. on pp. 14, 17, 24).

Tokunaga, T.K., Wan, J. & Sutton, S.R. (2000): 'Transient film flow on rough fracture surfaces'. *Water Resources Research*, vol. **36**(7): pp. 1737–1746 (cit. on p. 14).

Towell, G. & Rothfeld, L. (1966): 'Hydrodynamics of rivulet flow'. *American Institute of Chemical Engineers Journal*, vol. **12**(5): pp. 972–980 (cit. on p. 19).

Voinov, O. (1976): 'Hydrodynamics of wetting'. *Fluid Dynamics*, vol. **11**(5): pp. 714–721 (cit. on p. 17).

Watkins, S., Bhattal, A., Francis, N., Turner, J. & Whitworth, A. (1996): 'A new prescription for viscosity in Smoothed Particle Hydrodynamics'. *Astronomy and Astrophysics Supplement Series*, vol. **119**: pp. 177–187 (cit. on p. 32).

Wood, B.D. (2009): 'The role of scaling laws in upscaling'. *Advances in Water Resources*, vol. **32**(5): pp. 723–736 (cit. on p. 12).

Zhang, K., Wu, Y.-S., Bodvarsson, G.S. & Liu, H.-H. (2004): 'Flow Focusing in Unsaturated Fracture Networks: A Numerical Investigation'. *Vadose Zone Journal*, vol. **3**(2): pp. 624–633 (cit. on p. 22).

Zhu, Y.I. & Fox, P.J. (2002): 'Simulation of Pore-Scale Dispersion in Periodic Porous Media Using Smoothed Particle Hydrodynamics'. *Journal of Computational Physics*, vol. **182**(2): pp. 622–645 (cit. on p. 31).

– (2001): 'Smoothed Particle Hydrodynamics Model for Diffusion through Porous Media'. *Transport in Porous Media*, vol. **43**: pp. 441–471 (cit. on p. 31).

Zhu, Y.I., Fox, P.J. & Morris, J.P. (1999): 'A pore-scale numerical model for flow through porous media'. *International Journal for Numerical and Analytical Methods in Geomechanics*, vol. **23**: pp. 881–904 (cit. on p. 31).

3 | Methods

The intention of this chapter is to give an in depth overview of the SPH codes used in the studies described in Chapters 5 and 6. Some of the technical details are not suitable for publication in a journal, however, they may serve as a (short) manual and alleviate subsequent development and usage of the codes. Due to the strict time step constraints and necessary higher resolution for convergence studies it was inevitable to parallelize the stochastic SPH code (see Chapter 6). Therefore the MPI[1] (Message Passing Interface) implementation is also described in the following. The code runs without use of external libraries making it readily usable on most platforms with a functional MPI and Fortran installation. The only exception is the efficient binary output format which requires compilation of the free TecIO[2] libraries and linking with the SPH code.

The HydroGeoSphere model that was used to simulate unsaturated flow in a karst system (see Chapter 4) has not been modified and its code is not publicly available. In addition to the description in Chapter 4 further information can be found on the official Aquanty[3] website or in Therrien et al. (2008).

3.1 SPH code

The three-dimensional SPH code is entirely written in Fortran and can be compiled with any opensource or commercial compiler compliant with the

1 www.mpi-forum.org
2 www.tecplot.com
3 www.aquanty.com

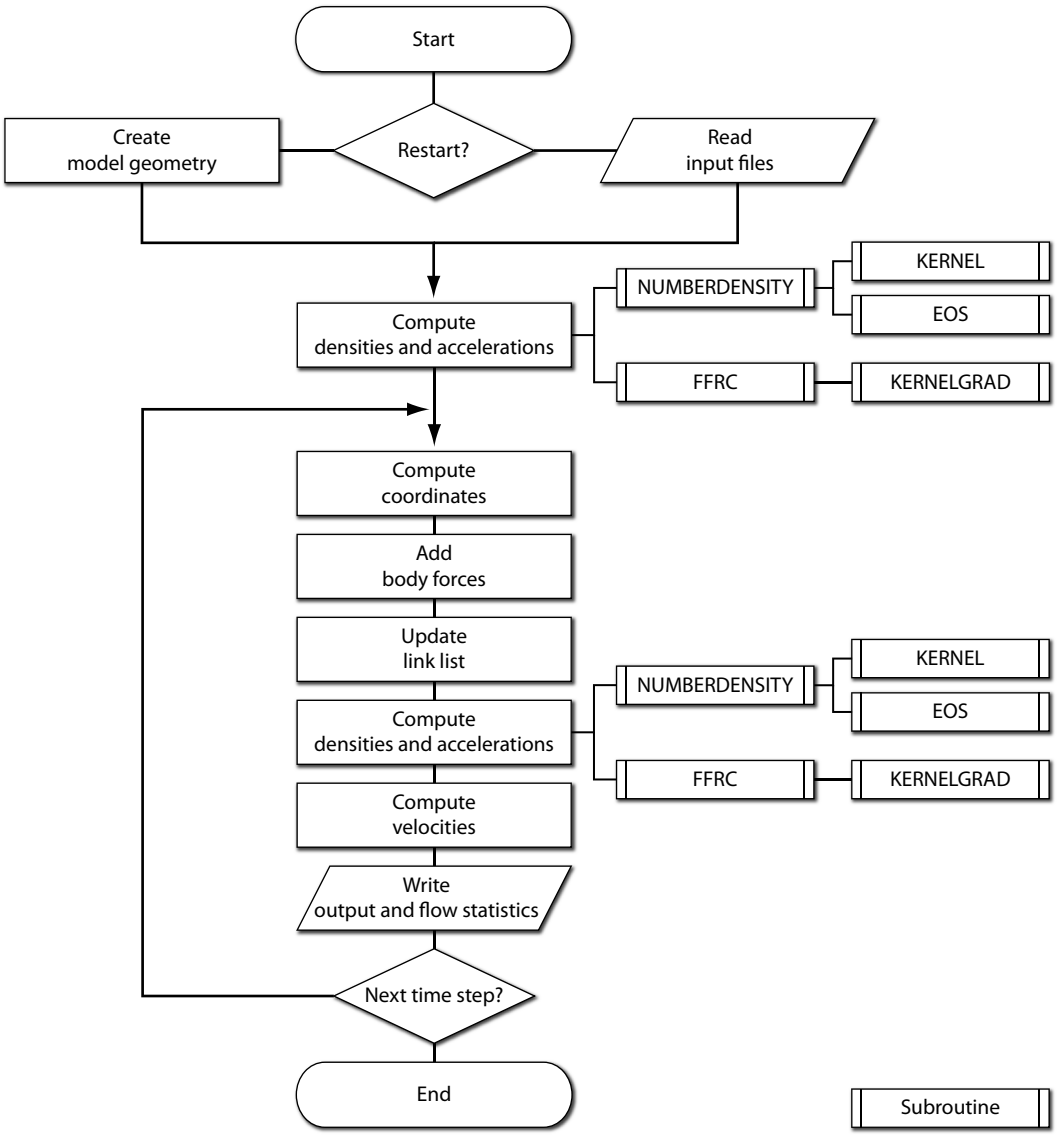

FIG. 3.1. Flowchart of the three-dimensional free-surface SPH code used in Chapter 5.

Fortran90 standard. For the sake of clarity all visual examples are two-dimensional. The transfer to three dimensions is straightforward and in most cases requires only adding an additional array. Here a brief introduction to the SPH method is given to elucidate the general codeflow, however, the detailed theoretical descriptions can be found in Chapter 5 (free surface flow code) and Chapter 6 (stochastic MPI code).

In the SPH method a problem domain is formed by particles, which do not possess any connection as opposed to meshbased methods, such as Finite-Element or Finite-Difference methods. Note that the term "particle" should not be confused with "molecule" or "atom". Depending on the type of problem particles rather represent a finite portion of the domain, each with physical material properties. In the case of fluid dynamics these are commonly the mass, density, pressure and velocity. Since SPH is a Lagrangian method the discretization points (i.e. the particles) move with the material, in contrast to Eulerian methods, where the material moves across a spatially fixed grid.

The key characteristic of SPH is the integral representation of an arbitrary continuous field function multiplied by a smoothing kernel, which is approximated by a discrete number of particles. The kernel function (also smoothing or weighting function) essentially creates an area of influence for each particle to obtain a smoothed field property by a summation over all interacting particles. By definition the kernel has a finite size and its integration yields one (Eq. 2.22). Spatial derivatives of a function can simply be obtained in terms of the function values and Eq. (2.21).

Since particles need to be related to physical properties, it is convenient to replace the differentials in the integral representation over the domain by the quotient of mass and density. With this form of the particle approximation a discretization of the Navier-Stokes equation

$$\frac{D\boldsymbol{v}}{Dt} = -\frac{1}{\rho}\boldsymbol{\nabla} P + \frac{\mu}{\rho}\nabla^2\boldsymbol{v} + \boldsymbol{g} \tag{3.1}$$

can be obtained. Starting with an initial particle field the first step is to compute the particle densities (see Fig. 3.1) and obtain the corresponding

pressure of each particle using a suitable equation of state (EOS). In the absence of gravitational acceleration this gradient (i.e., the first term on the RHS of Eq. 3.1) is the main driving force creating a particle acceleration. Note that on a perfectly regular grid the system initially is in an equilibrium and hence no acceleration due to pressure gradients will occur. After computing the viscosity term which dissipates system energy (i.e. decreases the acceleration) the particle coordinates are updated for the first time marking the beginning of the main loop. Here gravitational acceleration is added, new densities and accelerations are computed and velocities are updated using an explicit time stepping scheme. This is repeated until the desired time is reached.

The descriptions in the following subsections will roughly follow the general codeflow as can be seen in Fig. 3.1 and cover the most important aspects of the codes and their numerical implementation.

3.1.1 Model geometry

In the following the most important variables for the model geometry are explained assuming a rectangular flow domain of size 4 h in terms of the SPH smoothing length and a number density of nine. In this example a typical Poiseuille flow problem consisting of two parallel plates and fluid flow in between is set up. Boundaries are assumed to be impermeable in y-direction and periodic in x-direction, that is, fluid particles are allowed to cross the boundary and enter on the opposite side or interact with particles across the boundary (see Fig. 3.2). Listing 3.1 shows the corresponding code. Depending on the desired number density (i.e., the number of particles within an area of 1 h^2 in a two-dimensional problem) particles are placed on a regular lattice considering the offset to account for the periodic boundaries (lines 8-14). Here `nddp` refers to the integer domain size (4) and `anddp` to the corresponding real numbered size 4.0. In the next step particles are assigned either a fluid type (`itype(i)=1`) or boundary type (`itype(i)=0`), where `npart` is the total particle number. Boundary particles are static (i.e., $v = 0$) but contribute to the density evolution. Therefore they usually prevent penetration of fluid particles into the wall due to the increasing

Listing 3.1. Setup of a model geometry.

```
coord      = 0.d0
itype      = 0
l          = 0
ndensity   = 9
p_per_h    = real(ndensity)**(1.0d0/2.0d0)
pspacing_x = int(p_per_h) * nddp1
pspacing_y = int(p_per_h) * nddp2

do i=1,pspacing_x
do j=1,pspacing_y
  coord(2,l) = real(j)*(anddp2/pspacing_y)-((anddp2/pspacing_y)*0.5d0)
  coord(1,l) = real(i)*(anddp1/pspacing_x)-((anddp1/pspacing_x)*0.5d0)
  l = l+1
end do
end do

!##### Assign fluid (1) or boundary type (0)
npart = l
nwall = 0
do i=1,npart
  itype(i) = 1
  if(coord(2,i).le.1.0d0.or.coord(2,i).ge.3.0d0) then
    itype(i) = 0
    nwall = nwall + 1
  endif
end do
nfluid = npart - nwall
```

Listing 3.2. Calculation of particle distance for periodic boundaries.

```
dx = coord(1,iic) - coord(1,i)
dy = coord(2,iic) - coord(2,i)

if(dx>anddh1) dx = dx -anddp1
if(dy>anddh2) dy = dy -anddp2
if(dx<anddhm1) dx = anddp1 + dx
if(dy<anddhm2) dy = anddp2 + dy
```

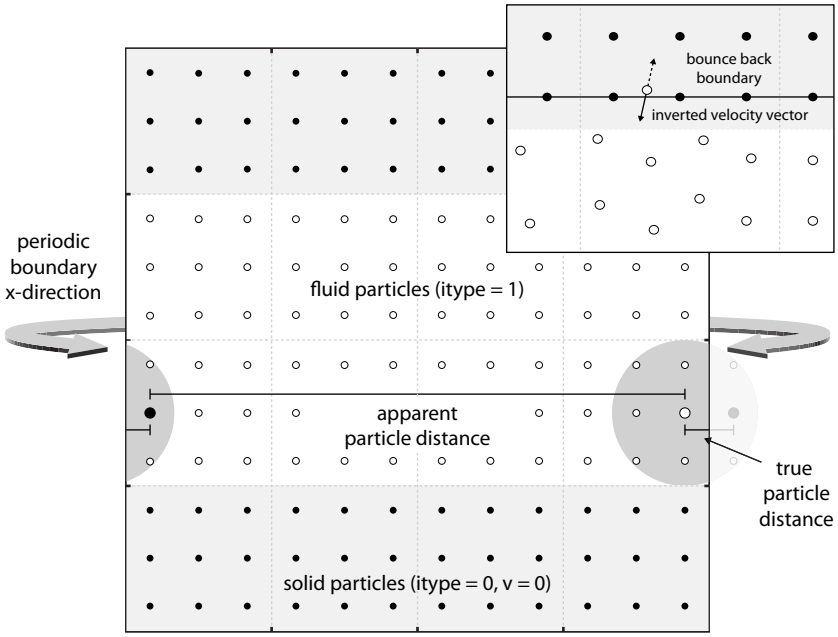

FIG. 3.2. Types of boundary conditions and general regular grid setup for a classic Poiseuille flow problem with periodic boundaries in y-direction. Grid cells have size 1 h and the grey circle is the range of the smoothing function (1 h). Particles interact across periodic boundary conditions, where true particle distances are determined according to Listing 3.2. Velocity vectors are inverted in case a particle penetrates the bounce back boundary.

pressure which drives fluid particles away from the boundary. In case fluid particles still cross the wall boundary (see Fig. 3.2, inset) their velocity vectors are simply inverted (bounce back boundary). Listing 3.2 shows the determination of particle distances and treatment of periodic boundaries. Here `anddh` and `anddm` correspond to the positive or negative half of the flow domain. After the apparent distances have been determined (lines 1-2) the true distance can be evaluated in case a periodic boundary has been detected in between two particles (lines 4-7)

3.1.2 Link-list approach

Even though the SPH technique relies on freely moving particles as discretization points to solve governing equations, for numerical efficiency the particle system is supported by underlying grid cells. Together with

Listing 3.3. Updating the link-list.

```
icc = 0
do i = 1,npart
  ixx = coord(1,i)
  iyy = coord(2,i)
  izz = coord(3,i)
  iic = icc(ixx,iyy,izz)
  icc(ixx,iyy,izz) = i

  if(iic==0) then
    ll(i) = 0
  else
    ll(i) = iic
  end if
end do
```

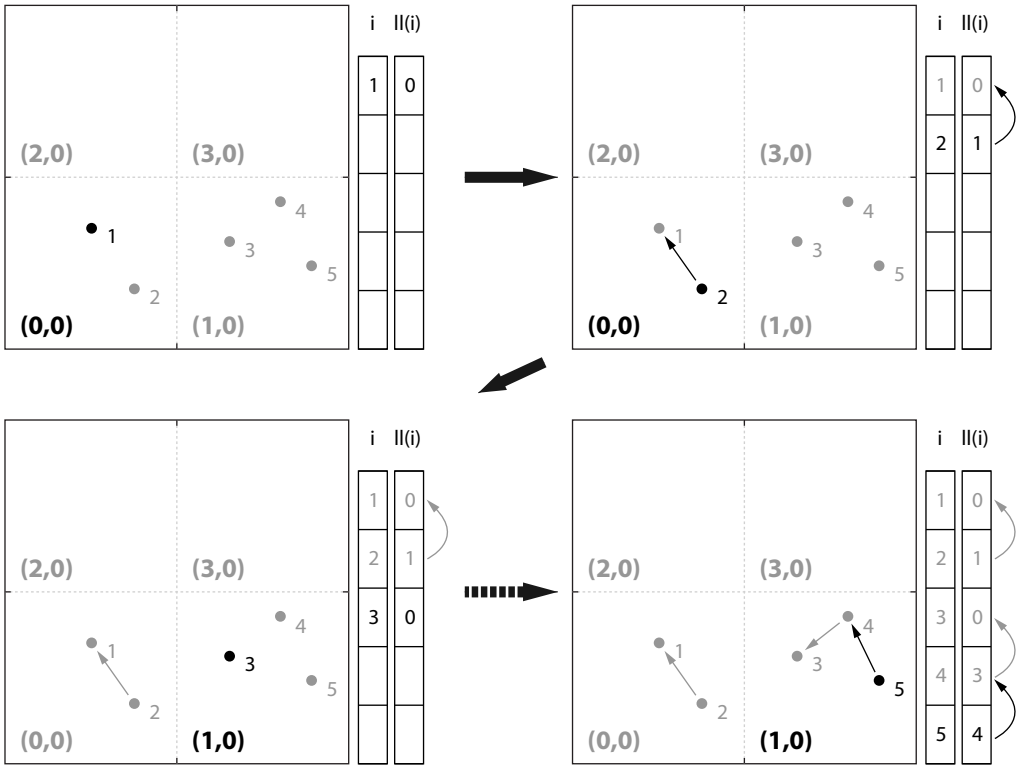

FIG. 3.3. Generation of a link-list. Numbers in brackets denote the position in the `icc` array, i.e. the the grid cell. Columns show the particle index (left) and corresponding entry in the link-list `ll` array.

a link-list they allow to easily identify particles residing in the same grid cell without the need of looping through the whole particle array to find potential neighbors. This helps to dramatically decrease computation time within nested loops (see Section 3.1.3).

Here all important elements for the creation of the link-list are described. The `icc` array has three dimensions of size equal to the maximum domain size in each direction (eight in this example). It creates an underlying grid with cell sizes 1 h, which essentially helps to assign particles to the grid cell that they temporarily reside in. In opposite to most other arrays which are allocated in a way that array indexing starts at 1, in this case the array allocation is explicitly given as `icc(0:ndd1,0:ndd2,0:ndd3)` (e.g. indexing from 0 to 7). This is necessary to properly determine each particle's cell based on its coordinates as follows (see Listing 3.3). Before updating the link-list all elements of the `icc` array are reset to zero. In the next step we loop over all particles and assign each component of a particles coordinate (real type) to the integer variables `ixx`, `iyy` and `izz`. Due to the datatype mismatch the coordinate components get truncated (e.g. `coord(1,i)=0.9` to `ixx=0`), thus assigning the particle to the correct subgrid element. The following process (lines 6-13) will create the link-list:

1. The variable `iic` stores the index of the previous particle that has been found in the cell of the current particle or will be assigned zero if the current particle is the first one detected in the cell (line 6).
2. The current cell, defined by the three-dimensional `icc` array, stores the index `i` of the current particle (line 7) and at at the end of the loop the maximum particle index.
3. The link-list array `ll(i)` of size `npart` stores either the value zero (current particle is the first one in the cell) or the particle index of the previous particle that has been detected in the same cell (line 9-13).

Figure 3.3 gives a schematic overview of the link list approach for a simple two-dimensional system with five particles and only two occupied cells. It should be noted that the same example also applies for a system where

the particle indices appear completely disordered (e.g. particle 5 and 1 are located in cell zero), the only difference being that particles residing in the same cell might not appear in ascending order in the link-list array but will still be linked to each other in a unidirectional fashion.

3.1.3 NUMBERDENSITY and FFRC subroutine

The NUMBERDENSITY and FFRC subroutine both depend on a properly set up link-list to enable efficient computation of multibody interactions between the particles. Both subroutines share the same basic structure, namely a nested loop over all particles, which is optimized by using the link-list to reduce the number particle pairs that are checked for a possible interaction. Fig. 3.4 shows the general structure of the NUMBERDENSITY and FFRC subroutine and Fig. 3.5 a two-dimensional sample domain to illustrate the behavior of the algorithm. The corresponding sample code for a two-dimensional system is shown in Listing 3.4.

Similar to setting up the link-list (see Section 3.1.2) the outermost loop cycles through all particles and initially determines the underlying grid cell of particle `i` (lines 1-5). In the next step the algorithm sweeps over all cells (including the particle cell) adjacent to the particle cell to search for possible particle interactions (lines 6-9). Due to the fixed smoothing length of 1 h the grid size can also be set to unity and therefore reduce the maximum area (or volume in three dimensions) to be checked (see Fig. 3.5). The innermost parts of the code (lines 10-30) first check if there are any particles except particle `i` within the cell and then determine the highest particle index `iic=icc(ii,jj)` of the cell as assigned during the link-list update (see Section 3.1.2). For distances smaller than the interaction range of the kernel the KERNEL and/or KERNELGRAD functions are invoked to compute the weighted contribution $W(r_{ij},h)$ resp. $\nabla W(r_{ij},h)$ of the interaction between particle `i` and `iic` (excluding selfinteractions, i.e. `iic=/i`). At this point (lines 20-29) the link-list is employed to efficiently track all particles residing within the current cell starting at particle `iic`. Until reaching `ll(iic)=0` the particle `iic` is constantly reassigned the predecessing particle index ll(iic) via the link-list. As before, particle interactions are only

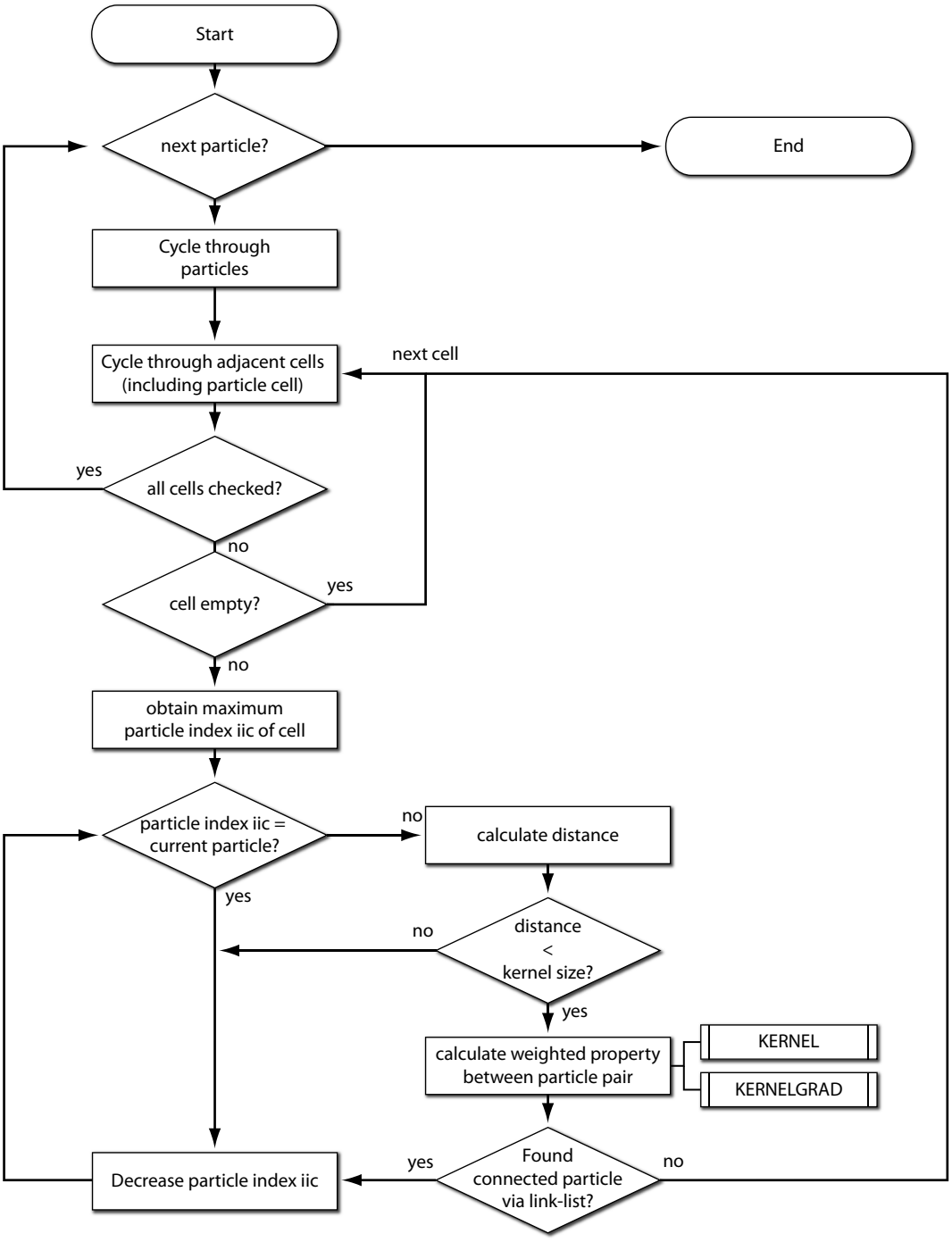

FIG. 3.4. Flowchart for the FFRC and NUMBERDENSITY subroutine to calculate accelerations. Both subroutines call either the KERNEL and/or the KERNELGRAD function to obtain the respective weighted property (density,acceleration etc.) through the multibody interactions.

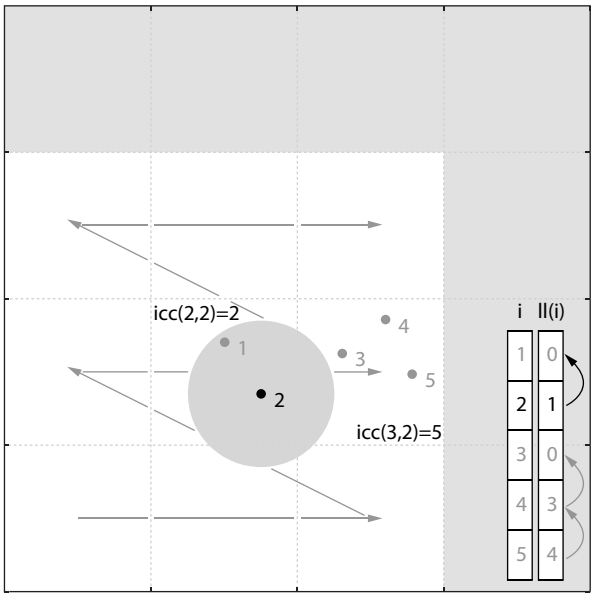

FIG. 3.5. Two-dimensional sample domain illustrating the efficient grid sweeping to reduce potential particle interactions. Here only white cells are screened for possible interactions with particle 2, where gray arrows denote the sweep direction. Final interactions with particle 2 are only calculated for particles lying within the kernel range (circle). The value of the `icc` array is used as a starting point to efficiently track all particles within each cell via the link-list in reverse index oder.

computed for distances smaller 1 h and selfinteractions are excluded.

3.1.4 KERNEL, KERNELGRAD and EOS function

The KERNEL function is called from the NUMBERDENSITY subroutine and the KERNELGRAD from the FFRC subroutine (see Fig. 3.1) for each interacting particle pair. In addition, the NUMBERDENSITY subroutine also calls the EOS function to determine the pressure for particle `i` once all particle interactions have been evaluated for the particle density. The KERNEL and KERNELGRAD function evaluate the weighting function for each particle distance smaller than 1 h. In this work a quintic spline kernel is employed which is composed of three piecewise quintic polynomials each of size `ra=1/3` (see Fig. 3.6). Depending on the particle distance the respective polynomial is evaluated and returned by the function (see Listing 3.5). The KERNELGRAD

Listing 3.4. Two-dimensional form of the FFRC and NUMBERDENSITY subroutine with its basic core features.

```
do i=1,npart
  xx = coord(1,i)
  yy = coord(2,i)
  ixx = xx
  iyy = yy
  do ix=-1,1
  do iy=-1,1
  ii = ixx + ix
  jj = iyy + iy
    if(icc(ii,jj)/=0) then
    iic = icc(ii,jj)
      if(iic=/i) then
      !calculate distance
        if(distance<1) then
          !calculate weighted property and sum contribution from all
          !interactions
        end
      end

      do while (ll(iic)/=0)
      iic = ll(iic)
        if(iic/=i) then
        !calculate distance
          if(distance<1) then
          !calculate weighted property and sum contribution from all
          !interactions
          end
        end
      end do
    end if
  end do
  end do
end do
```

function simply evaluates the corresponding derivatives.

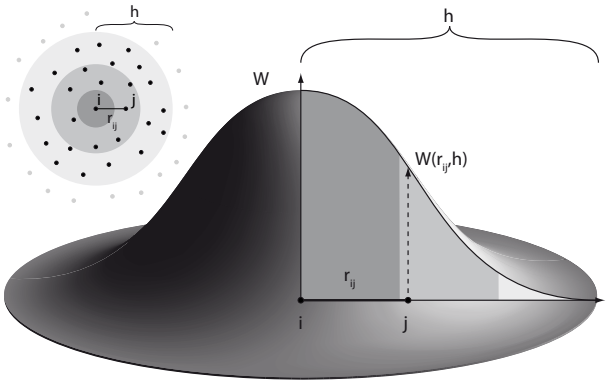

FIG. 3.6. Sample kernel W for a two-dimensional system with a circular support domain of length h and value $W(r_{ij},h)$ between particle i and j. A particle property for particle i is obtained by a kernel weighted summation over all particles j within the interaction range of particle i, where r_{ij} is the distance between both particles. Shaded grey areas represent the piecewise quintic polynomials used in this work (see Listing 3.5).

Listing 3.5. KERNEL function for a quintic spline kernel. Arguments are the particle distance dd, the normalization constant a and the kernel range ra.

```
weight = 0.0d0
if(dd.le.ra) then
  weight = weight + a*((3.0d0-dd/h)**5.0d0
                      - 6.0d0*(2.0d0-dd/ra)**5.0d0
                      + 15.0d0*(1.0d0-dd/ra)**5.d0)
else if(dd.le.2.0d0*ra) then
  weight = weight + a*((3.0d0-dd/ra)**5.0d0
                      - 6.0d0*(2.0d0-dd/ra)**5.0d0)
else if(dd.le.3.0d0*ra) then
  weight = weight + a*(3.0d0-dd/ra)**5.0d0
end if
```

3.2 Parallel stochastic SPH code

The stochastic SPH code has been developed based on the code described in Section 3.1.

3.2.1 MPI implementation

Here the most important changes regarding the MPI implementation are highlighted. Figure 3.7 gives on overview of the code and the parts which have been parallelized or where additional MPI directives where needed. To provide some illustrative examples a simulation consisting of 12 particles running on four processors is assumed. During execution of the parallelized code the computationally intensive tasks, such as nested loops over all particle arrays in the `NUMBERDENSITY` or `FFRC` subroutines, are split up such that each process will handle only a subrange of the arrays. However, it should be noted that each process stores global particle arrays of size 12 in its own memory space whose subranges have to be updated at certain times by combining the subarray data from all other processes and therefore homogenizing the global arrays of all processes. This is necessary if a task such as the density calculation in the `NUMBERDENSITY` subroutine requires particle information from particles residing on a different processor.

To set up the MPI system some additional variables are introduced and the Fortran MPI header file (`mpif.h`) has to be included (see Listing 3.6). Here `myid` is a unique identifier for each process (i.e. to distinguish processes on each of the four processors in our example), `numprocs` is the total number of processes, `j1` and `jm` replace the loop ranges (e.g. `i=1,npart`) to handle a subrange `i=j1,jm` on a specific process and `npart1` denotes the maximum particle number on each process. Errors in the MPI communicators are stored in the variable `ierr`. The arrays `cnt`, `dsp` and `gather` are needed update the global arrays with the help of MPI communicators once a parallel computation has been carried out, where `cnt` and `dsp` have a size equal to the number of processes and the size of `gather` equals the total particle number.

Listing 3.7 shows how the indices of the array subranges and the total number of particles (in this case 3 on each) are determined on each process.

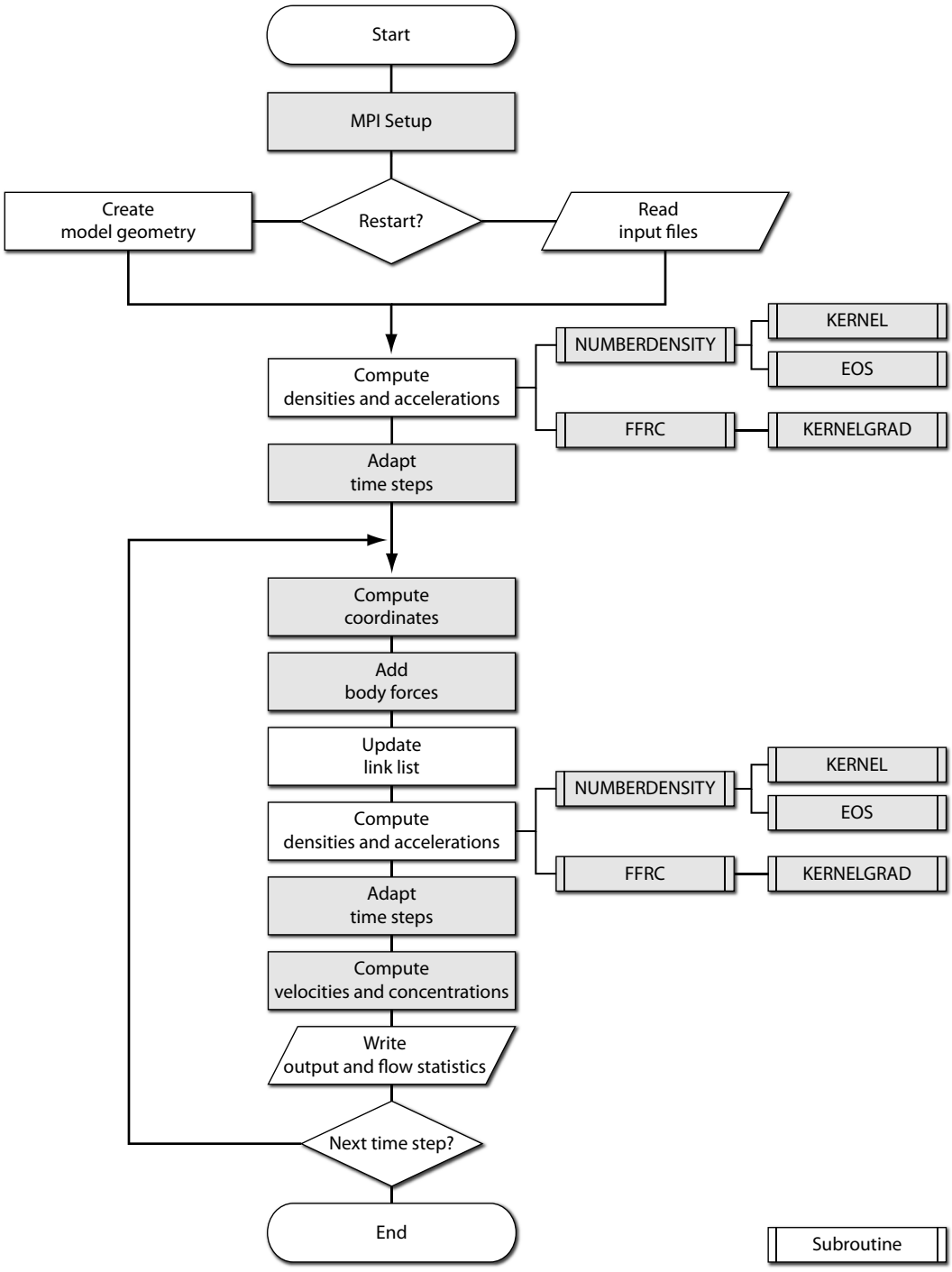

FIG. 3.7. Flowchart for the parallel stochastic SPH code used in Chapter 6. Gray processes and subroutines were parallelized or needed additional MPI directives (adaptive time stepping, see Listing 3.9).

Listing 3.6. MPI setup and additional variables.

```
1  PROGRAM stochasticsph
2  USE IFPORT
3  implicit none
4  EXTERNAL eos
5  INCLUDE 'tecio.f90'
6  INCLUDE 'mpif.h'
7
8  integer*4 :: myid, numprocs, j1, jm, npart1, ierror
9  integer*4 :: cnt(:), dsp(:)
10 real*8    :: gather(:)
11
12 CALL MPI_INIT(ierror)
13 CALL MPI_COMM_RANK(MPI_COMM_WORLD,myid,ierror)
14 CALL MPI_COMM_SIZE(MPI_COMM_WORLD,numprocs,ierror)
```

Consequently the ranges would be `j1=1` and `jm=3` on the first processor (`myid=0`) and `j1=10` and `jm=12` on the last processor (`myid=3`). In order to make this information globally available `MPI_ALLGATHER` is called on each process (see Listing 3.8). Its arguments are the send buffer `npart1`, the send count (one) and its MPI data type, the receiving buffer `cnt`, the number of elements to receive (one) and the receiving MPI data type, the communicator and the error handle. In this example (see Fig. 3.8, left subfigure) the `cnt` array on each process would finally consist of four entries, each denoting the number of particles on the respective processor.

To update the `density` and `pressure` array after a call of the `NUMBER-DENSITY` subroutine on each process the `MPI_ALLGATHERV` command is issued. It allows for various sizes of the sending buffer and more control over the placement in the receving buffer. The main difference to the `MPI_ALLGATHER` command is the usage of the `dsp` array which holds information about the displacement of the sent data on each process relative to the global array. As an example, updating the `density` array (see Listing 3.8 and Fig. 3.8) requires (on each process) the buffer starting address `density(j1)`, the total particle number `npart1` and its data type `MPI_REAL8`, the receiving array `density`, the number of elements to receive (`cnt`, previously determined by `MPI_ALLGATHER`), their displacement in the global

Listing 3.7. Determine start and end index on each process and the total number of particles.

```
if (myid.eq.0) then
  j1 = 1
else
  j1 = (npart/numprocs)*myid+1
endif

if (myid.eq.(numprocs-1)) then
  jm = npart
else
  jm = (npart/numprocs)*(myid+1)
endif
npart1 = jm-j1+1
```

array (`dsp`) with the data type and again the MPI communicator and error handle.

After calling the FFRC subroutine the adaptive time step algorithm requires information about the minimum particle distance and maximum acceleration across all processes to compute a new step size. The minimum particle distances and maximum accelerations are simply computed within the FFRC subroutine and stored in the `ddmin` and `vforcemax` variables in-

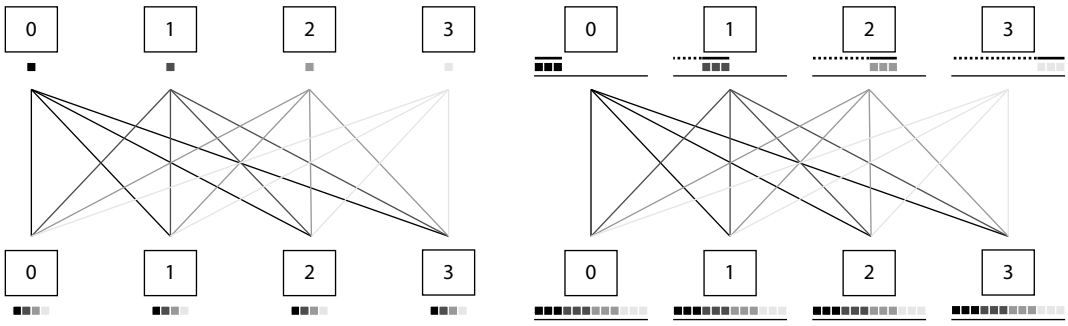

FIG. 3.8. MPI commands used to update global variables (left) or arrays (right) of each process represented by big squares with process id (`myid`). Lower row represents the updated state. Symbols below process id: Small squares - data elements, bold lines - size of send buffer (`npart1`), dotted lines - displacement (`dsp`), thin lines - global array size (`npart`).

Listing 3.8. Collect particle count from each process (MPI_ALLGATHER), store it in global count array and compute necessary displacement on each process. To update the global arrays MPI_ALLGATHERV is issued.

```
CALL MPI_ALLGATHER(npart1,1,MPI_INTEGER,cnt,1,MPI_INTEGER,MPI_COMM_WORLD
                   ,ierror)

dsp(1) = 0
do i = 2,numprocs
  dsp(i) = dsp(i-1)+cnt(i-1)
end do

CALL MPI_ALLGATHERV(density(j1),npart1,MPI_REAL8,density,cnt,dsp
                    ,MPI_REAL8,MPI_COMM_WORLD,ierror)
```

dependently on each process. In order to find the global minimum and maximum the MPI_ALLREDUCE command is used (see Listing 3.9). Similar to the MPI_ALLGATHER command information from each processor is broadcasted to all other processes and made globally accessible via the variables ddmin_global and vforcemax_global. However, here a boolean operation or summation is applied to all local data elements before passing it to the global variable. As an example, to find the minimum particle distance the routine takes as input arguments the sending buffer ddmin, the global receiving buffer ddmin_global, the element count, the MPI datatype, the desired reduction method (finding the minimum, i.e. MPI_MIN) and the

Listing 3.9. MPI reduction for the adaptive time stepping.

```
CALL MPI_ALLREDUCE(ddmin, ddmin_global, 1, MPI_REAL8, MPI_MIN
                   ,MPI_COMM_WORLD, ierror)
CALL MPI_ALLREDUCE(vforcemax, vforcemax_global, 1, MPI_REAL8, MPI_MAX
                   ,MPI_COMM_WORLD, ierror)

t_cond1 = 0.25d0*ddmin_global/c0
t_cond2 = 0.25d0*dsqrt(ddmin_global/vforcemax_global)
t_cond3 = 0.125d0*(ddmin_global**2.0d0)*(massdensity/mu)
tstep   = tstep_reduction*MIN(t_cond1,t_cond2,t_cond3)
tstep2  = tstep*tstep/2.0d00
tsteph  = 0.50d00*tstep
```

communicator and error handle. This way all `ddmin` values accross the processes are compared and the minimum is passed to the global variable.

Before going the first time into the main loop a seed for the pseudorandom number generator is set with a single call to the intrinsic subroutine `RANDOM_SEED(PUT=123456789)` (see Listing 3.10). This will yield the exact same constant seed on all processes and thus allows for easier debugging. At the beginning of each time step nine arrays of random numbers of size `npart` are generated with a call to the intrinsic subroutine `RANDOM_NUMBER` and passed to the `FFRC` subroutine. The resulting numbers are uniformly distributed between -1 and 1 with a unity variance. Due to the constant seed they are equal across all processes and allow for proper momentum conservation when being used in the `FFRC` subroutine. A truly random seed can be simply implemented by fetching the system clock for example, however, this will require additional MPI communication to broadcast only one random seed to all processes in order to obtain the same random number arrays on all processes. Within the main program most computationally intensive loops (see Fig. 3.7) have been parallelized by replacing the whole particle range with the respective subrange `j1` and `jm` (see Listing 3.7). As an example the calculation of velocity is carried out as can be seen in Listing 3.11. It should be noted that the `MPI_ALLGATHERV`, which has to be called afterwards, only accepts starting buffer addresses of vectors but not matrices. Therefore each vectorial component has to be temporarily written to the gather array which can then be used to homogenize the global veloc-

Listing 3.10. Random number generation (only one array shown).

```
seed = 1234567891815
CALL RANDOM_SEED(PUT=seed)

##### Start of main lopp

do i=1,npart
  CALL RANDOM_NUMBER(rnumber)
  randomarray1(i)=((rnumber*(-2.0d0))+1.0)*dsqrt(3.0d00)
enddo
```

Listing 3.11. Loop parallelization.

```
do i = j1,jm
  do j = 1,3
    velocity(j,i) = velocity(j,i) + tsteph*(vforce(j,i) + vnext(j,i))
    vforce(j,i) = vnext(j,i)
  enddo
enddo
```

ity array (see Listing 3.12). Finally, before the program is terminated all processes call MPI_FINALIZE to ensure that the communicators are properly closed.

Listing 3.12. Creation of gather arrays.

```
do i=j1,jm
  gather(i) = velocity(1,i)
end do

CALL MPI_ALLGATHERV(gather(j1),npart1,MPI_REAL8,velocity(1,:),cnt,dsp
                    ,MPI_REAL8,MPI_COMM_WORLD,ierror)
```

3.3 References

THERRIEN, R., MCLAREN, R. G., SUDICKY, E. & PANDAY, S. (2008): 'HydroGeoSphere: A three-dimensional numerical model describing fully-integrated subsurface and surface flow and solute transport'. *Manual (Draft), HydroGeoLogic Inc., Herndon, VA*, vol. (cit. on p. 49).

4 | Simulation of saturated and unsaturated flow in karst systems at catchment scale using a double continuum approach*

Kordilla, J.[1], Sauter, M.[1], Reimann, T.[2], Geyer, T.[1]

[1]Geoscientific Centre, University of Göttingen, Göttingen, Germany
[2]Institute for Groundwater Management, TU Dresden, Dresden, Germany

* Kordilla, J., Sauter, M., Reimann, T., Geyer, T. (2012): Simulation of saturated and unsaturated flow in karst systems at catchment scale using a double continuum approach. *Hydrology and Earth System Sciences*, **16**(10), pp. 39093923.

Abstract. The objective of this work is the simulation of saturated and unsaturated flow in a karstified aquifer using a double continuum approach. The HydroGeoSphere code (THERRIEN et al., 2008) is employed to simulate spring discharge with the Richards equations and van Genuchten parameters to represent flow in the (1) fractured matrix and (2) conduit continuum coupled by a linear exchange term. Rapid vertical small-scale flow processes in the unsaturated conduit continuum are accounted for by applying recharge boundary conditions at the bottom of the saturated model domain. An extensive sensitivity analysis is performed on single parameters as well as parameter combinations. The transient hydraulic response of the karst spring is strongly controlled by the matrix porosity as well as the van Genuchten parameters of the unsaturated matrix, which determine the head dependent inter-continuum water transfer when the conduits are draining the matrix. Sensitivities of parameter combinations partially reveal a non-linear dependence over the parameter space. This can be observed for parameters not belonging to the same continuum as well as combinations, which involve the exchange parameter, showing that results of the double continuum model may depict a certain degree of ambiguity. The application of van Genuchten parameters for simulation of unsaturated flow in karst systems is critically discussed.

4.1 Introduction

Discharge dynamics in karst aquifers are determined by superposition of several effects: (1) water infiltration into soil, (2) water percolation through the unsaturated zone, (3) groundwater flow in highly conductive karst conduits and interaction with (4) groundwater flow in the low-conductive fissured and fractured rock matrix. These different effects, without even having considered the variability of precipitation and evapotranspiration, are a result of the particular properties of the individual compartments: soil-epikarstic zone, vadose zone, and phreatic zone. Each of these compartments is, in turn, characterized by two coupled flow systems: a highly permeable one with low storage and a less permeable one with high storage. Therefore, different individual (rapid, slow) flow components with characteristic temporal distributions are induced. Accordingly, the final spring discharge is then a function of the individual flow contributions of each of these compartments (SMART & HOBBS, 1986), which makes the inverse analysis of spring discharge a major challenge, requiring elaborate modeling tools and a large spectrum of data to constrain the model. The simulation of coupled saturated and unsaturated flow is still a challenge in hydrogeology in particular in fractured (THERRIEN & SUDICKY, 1996) and karstified systems (REIMANN et al., 2011a). This is predominantly a result of the data scarcity respecting the hydraulic parameter field of real karst systems. Therefore, flow in karst systems is often simulated with lumped parameter modeling approaches, which translate precipitation signals to discharge hydrographs by applying simple transfer functions (DREISS, 1989). Generally, this type of approach is appropriate for situations in which predicted system states are expected to range between already observed events. The simulation of natural karst systems with distributed parameter models is reported only in a few studies (e.g. HILL & POLYAK, 2010; JEANNIN, 2001). However, distributive modeling approaches incorporate flow laws and, therefore, are adequate for the process based simulation of karst hydraulics (e.g. BIRK et al., 2006; REIMANN et al., 2011b) and transport problems (e.g. BIRK et al., 2005; DREYBRODT et al., 2005).

TEUTSCH & SAUTER (1991) demonstrate in how far the different mathematical model approaches are suitable for different types of problems (flow, transport, regional, local). An approach that takes into account the limited information about aquifer geometry and still allows the simulation of the dynamics of the karst system at an event basis, i.e. considers the dual flow behavior of karst systems is the double continuum approach (e.g. SAUTER et al., 2006; TEUTSCH & SAUTER, 1991). The approach was introduced by BARENBLATT et al. (1960) and applied for simulation of karst hydraulics on catchment scale by TEUTSCH (1988) and SAUTER (1992). It yields equations for simulation of slow and diffuse flow in the fissured matrix and the discrete rapid underground drainage by solution conduits in karst systems. Here, we want to assess the relative importance of individual factors and parameter combinations on the discharge behavior of a karst spring without detailed knowledge about the hydraulic parameter field of an aquifer system. This type of information is of major importance to focus characterization efforts in catchment based karst studies. Furthermore, the importance of infiltration dynamics, i.e. the temporal distribution of the rapid and the slow flow component on the discharge dynamics is to be determined. We employ the integrated saturated-unsaturated double-continuum approach HydroGeoSphere (THERRIEN et al., 2008) to simulate recharge and discharge dynamics in a karst aquifer with a thick unsaturated zone. Flow simulations are based on the Richards' equation and respective parameters are described via the van Genuchten parametric model. Given that the van Genuchten parameters have been developed for porous media on REV scales, parameters obtained for the large scale conduit system are pure calibration parameters without physical meaning in nature. Furthermore, the Richards equation is not able to express the highly nonlinear flow regime observed in unsaturated fractured rocks, for example, rivulet flow (DRAGILA & WEISBROD, 2004b; GERMANN et al., 2007). The application and limitations of the approach for flow simulation in karst systems are discussed. A comprehensive parameter study was conducted in order to elucidate sensitive and important model parameters as well as parameter dependencies, and to reduce the model ambiguity to assist in focused karst characterization.

4.2 Methods

4.2.1 Modeling approach

The application of the double-continuum approach requires two sets of flow equations, one for the matrix (primary) and one for the conduit (secondary) continuum, solved consecutively at the same node and coupled with an exchange term that defines the hydraulic interface and controls the inter-continuum exchange flow. The applied HydroGeoSphere model (THERRIEN et al., 2008) is a non-commercial code available to the interested user under http://hydrogeosphere.org/. The model has been extensively used for various studies involving dual porosities such as MCLAREN et al. (2000), ROSENBOM et al. (2009) and SCHWARTZ et al. (2010). The governing equation in the applied model is the Richards equation (RICHARDS, 1931), which is slightly modified to account for inter-continuum water exchange:

$$-\nabla w_m(q_m) + \Gamma_{ex} \pm R_m = w_m \frac{\partial}{\partial t}(\theta_{sm} S_{wm}) \tag{4.1}$$

$$-\nabla w_c(q_c) + \Gamma_{ex} \pm R_c = w_c \frac{\partial}{\partial t}(\theta_{sc} S_{wc}), \tag{4.2}$$

where w_m and w_c are the volumetric fractions of each continuum of the total porosity, such that $w_m = 1.0 - w_c$. S_{wm} and S_{wc} are the water saturations of the respective continuum and R_m and R_c denote a volumetric fluid flux per unit volume (source/sink term) for each continuum. The saturated water content of the matrix and conduit system are assumed equal to the effective matrix porosity θ_{sm} and conduit porosity θ_{sc} and are related to the water content of the matrix θ_m and of the conduit θ_c according to

$$\theta_m = S_{wm}\theta_{sm} \tag{4.3}$$

$$\theta_c = S_{wc}\theta_{sc} \tag{4.4}$$

The conduit and total porosity are given as

$$\theta_{total} = \theta_{sm}(1 - w_c) + \theta_{sc} w_c = \theta_{sm}(w_m) + \theta_{sc} w_c. \tag{4.5}$$

i.e. the whole simulation domain consists of nodes with primary porosity θ_{sm} with a volumetric fraction of $w_m = 1.0 - w_c$ and secondary porosity θ_{sc} with a volumetric fraction of w_c. Given that the local conduit porosity is chosen to be 1.0 and that both continua cover the whole domain the overall conduit porosity can simply be evaluated as:

$$\theta_{sc} \triangleq \theta_{sc(local)} w_c. \tag{4.6}$$

The fluxes q_m and q_c are obtained from

$$q_m = -K_m k_{rm} \nabla(\psi_m + z) \tag{4.7}$$

$$q_c = -K_c k_{rc} \nabla(\psi_c + z), \tag{4.8}$$

where K_m and K_c denote hydraulic conductivity, ψ_m and ψ_c are the pressure heads in each continuum and z is the elevation head. In the unsaturated zone, the relative permeabilities k_{rm}, k_{rc} and k_{ri} (interface) depend on the water saturation which in turn is related to the pressure head according to van GENUCHTEN (1980):

$$S_{wm} = S_{wrm} + (1 - S_{wrm}) \left[1 + |\alpha_m \psi_m|^{n_m}\right]^{-m_m} \tag{4.9}$$

$$S_{wc} = S_{wrc} + (1 - S_{wrc}) \left[1 + |\alpha_c \psi_c|^{n_c}\right]^{-m_c} \tag{4.10}$$

$$S_{wi} = S_{wri} + (1 - S_{wri}) \left[1 + |\alpha_i \psi_m|^{n_i}\right]^{-m_i} \tag{4.11}$$

for $\psi < 0$, where S_{wrm}, S_{wrc} and S_{wri} are the residual saturations, α_m, α_c and α_i denote the inverse air-entry pressure head, n_m, n_c and n_i are the pore-size distribution indices of each continuum and the interface. Note that the evaluation of the interface relative conductivity is based on the pressure head of the matrix. In the saturated zone where $\psi \geq 0$ the saturations are

$S_{wm} = S_{wc} = S_{wi} = 1$. The relative permeability is given by:

$$k_{rm}(S_{wm}) = S_{em}^{(lp)} \left[1 - \left(1 - S_{em}^{1/m_m}\right)^{m_m}\right]^2 \tag{4.12}$$

$$k_{rc}(S_{wc}) = S_{ec}^{(lp)} \left[1 - \left(1 - S_{ec}^{1/m_c}\right)^{m_c}\right]^2 \tag{4.13}$$

$$k_{ri}(S_{wi}) = S_{ei}^{(lp)} \left[1 - \left(1 - S_{ei}^{1/m_i}\right)^{m_i}\right]^2 \tag{4.14}$$

with l_p being the pore connectivity parameter (equals 0.5 after MUALEM, 1976), S_e the effective saturation

$$S_{em} = \frac{S_{wm} - S_{wrm}}{1 - S_{wrm}} \tag{4.15}$$

$$S_{ec} = \frac{S_{wc} - S_{wrc}}{1 - S_{wrc}} \tag{4.16}$$

$$S_{ei} = \frac{S_{wi} - S_{wri}}{1 - S_{wri}} \tag{4.17}$$

and m is defined as:

$$m_m = 1 - \frac{1}{n_m} \tag{4.18}$$

$$m_c = 1 - \frac{1}{n_c} \tag{4.19}$$

$$m_i = 1 - \frac{1}{n_i} \tag{4.20}$$

for $n > 1$. In the saturated zone the storage terms on the right-hand side of Eq. (4.1) and Eq. (4.2) are replaced by:

$$S_{wm} S_{sm} \frac{\partial \psi_m}{\partial t} + \theta_{sm} \frac{\partial S_{wm}}{\partial t} \tag{4.21}$$

$$S_{wc} S_{sc} \frac{\partial \psi_c}{\partial t} + \theta_{sc} \frac{\partial S_{wc}}{\partial t}, \tag{4.22}$$

where S_{sm} and S_{sc} are the specific storage coefficients. Water release by compaction of the porous medium is neglected in the unsaturated zone.

The term Γ_{ex} in Eq. (4.1) and Eq. (4.2) describes the volumetric fluid exchange rate per unit volume between primary and secondary continuum and is given as:

$$\Gamma_{ex} = \alpha_{ex} K_i k_{ri} (\psi_c - \psi_m), \tag{4.23}$$

where K_i is the hydraulic conductivity of the interface (e.g. sediments) and k_{ri} the relative interface permeability (Barenblatt et al., 1960). The exchange parameter α_{ex} is determined by calibration and defined as (Gerke & Van Genuchten, 1993):

$$\alpha_{ex} = \frac{\beta}{\alpha^2} \gamma_w, \tag{4.24}$$

where β is a geometry factor (3 for rectangular matrix blocks, 15 for spheres), a is the distance between the center of a matrix block and the adjacent fracture or conduit and γ_w is an empirical coefficient usually set to 0.4. As mentioned in the introduction the van Genuchten approach, adopted in HydroGeoSphere does not apply to fractured and karstified rock materials. The highly heterogeneous flow field and preferential flow paths associated with such media and the consequently greater size of an REV compared to porous media are rendering the parameter determination by laboratory experiments impractical. Still, the van Genuchten parameters reflect properties of an unsaturated porous material and can be considered as an adequate parameter set to describe transient infiltration processes if they are treated as calibration parameters in order to upscale from the Darcy-scale averaging volume to the field scale.

4.2.2 Sensitivity analysis

An extensive sensitivity analysis is performed to determine the influence of the calibrated parameters on the computed flow. The root-mean-square error (RMSE) is chosen to rate the accuracy of fit and calculate deviations

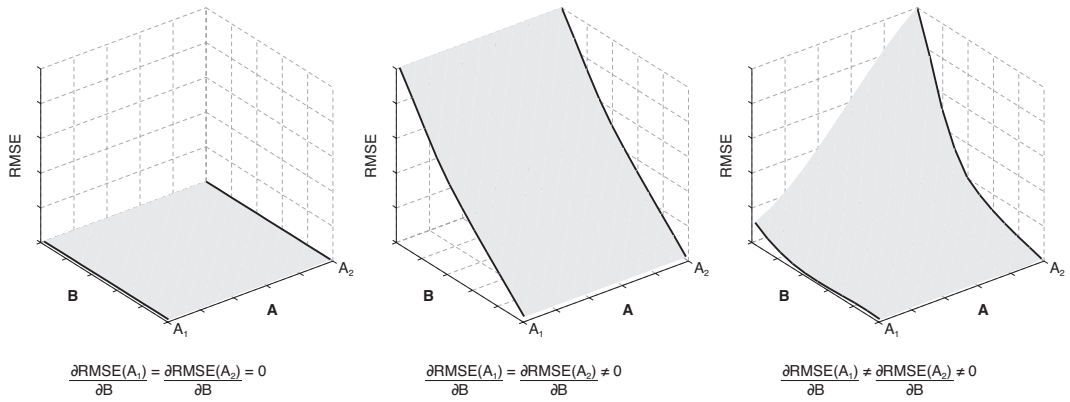

FIG. 4.1. Examples for inter-parameter dependencies. From left to right: (1) both parameters insensitive, (2) both parameters sensitive with linear dependency, (3) both parameters sensitive but non-linear dependency.

from the calibrated model. The RMSE is defined as (BAMBERG et al., 2007):

$$RMSE = \sqrt{\frac{1}{n}\sum_{i=1}^{n}(m_i - f_i)^2}, \tag{4.25}$$

where n is the total number of data points, m_i denotes the simulated spring discharge derived by the sensitivity analyses and f_i is the calibrated model value. For sensitivity analyses the RMSE has been evaluated using daily data and documented parameter ranges were employed if possible. However, for some variables, in particular the van Genuchten parameters for the unsaturated zone of hard rocks, only few data and estimates can be found in the literature, e.g. WEISS (1987), SAUTER (1992), CONTRACTOR & JENSON (2000) and ROULIER et al. (2006). Consequently, the sensitivity of these parameters was determined systematically to evaluate the degree of ambiguity of the model. Depending on field observations parameter ranges were varied on linear or log-scale. Parameter spaces were assigned to cover at least the reported values from field experiments. In order to provide a further quantitative comparison recession coefficients are given for one important recharge event during March 1988 (α_1) and the following recession until

beginning of April 1988 (α_2). Due to the complex flow model it is likely that some parameters do not show a linear correlation and sometimes the simulated discharge curve is only influenced by specific parameter combinations. The final analysis of parameter sensitivity on an idealized example is subdivided into: (1) insensitive parameters, (2) one sensitive parameter and (3) both parameters are sensitive (see Fig. 4.1, from left to right). In the latter case parameter A may be more sensitive for a certain range of parameter B. Given a constant parameter B_n and B_{n+dn} where n denotes the parameter value and dn a change in the parameter the parameter combination is refered to as non-linear if the change in RMSE over the whole range of parameter A is different for B_n and B_{n+dn} that is if

$$f(A,B_n) \neq f(A,B_{n+dn}) \tag{4.26}$$

This case is particularly important if a properly calibrated model can be achieved for two different parameter combinations where at least one parameter is a pure calibration parameter, i.e. its range is difficult to estimate by field observations. Therefore, more than 1000 model runs were performed and the influence of parameter combinations on the simulated discharge curve analyzed.

4.3 Case study

4.3.1 Description of the field site

The HydroGeoSphere model is employed to simulate flow in the catchment area of the Gallusquelle spring from February 1988 to January 1990. The Gallusquelle spring is situated in Southwest Germany on the Swabian Alb, a northeast-southwest striking Jurassic carbonate plateau. The catchment area has been studied extensively by several authors including aquifer characterization (Birk et al., 2005; Sauter, 1992), speleology (Abel et al., 2002; Gwinner, 1976), and flow processes (Geyer et al., 2008). The size of the catchment is about 45 km^2. It is delineated by a water divide in the northwest and the River Fehla in the northeast (see Fig. 4.2). In the south the catchment is bounded by the northeastern fault zone of the Hohenzollern-

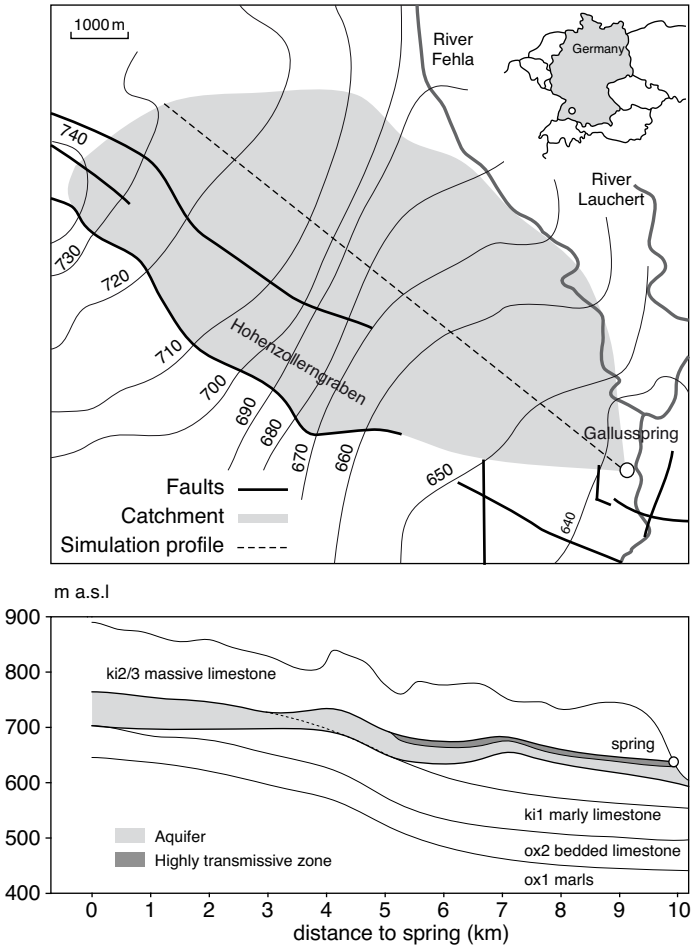

FIG. 4.2. Gallusquelle catchment and crosssection used for the simulation.

graben, which was found to be impermeable by tunneling works in the 1960's. After SAUTER (1992) the base of the aquifer is formed by Kimmeridge marls (ki1). With a 70 m to 90 m thickness, this unit is rather consistent in the northwestern parts of the project area and consists of calcareous marls and occasional limestone intercalations. In the southeastern area no borehole information about the lower boundary of the unit are available. The uppermost catchment is made up of a sequence of Kimmeridgian limestones (ki2-5) from which the majority is developed as algal-sponge facies

and, therefore, belongs to the "Unterer Massenkalk" or "Oberer Massenkalk". The largest part of the catchment comprises limestones belonging to the "Unterer Massenkalk" (ki2 and ki3). The whole Jurassic sequence dips south-east at an angle of 1.2 degrees.

4.3.2 Geometry of the flow model

Based on the geological model, a vertical two-dimensional model domain of the catchment area was set up. The length of the domain is 10 km with a vertical thickness of 225 m. It reflects a cross section parallel to the direction of flow in the Gallusquelle catchment (see Fig. 4.2, lower figure). The model domain is represented by two continua reflecting flow in the low permeability fissured matrix (*matrix continuum*) and the highly permeable conduits (*conduit continuum*). The top of the model domain is set to 775 m a.s.l., which is an average elevation between ca. 910 m a.s.l. in the north-western part of the catchment and ca. 640 m a.s.l. in the south-eastern catchment and higher than the maximum groundwater head in the catchment. Every continuum is spatially discretized into 50 columns with a length of 200 m a.s.l. and a width of 1 m and 44 layers with a thickness of 5 m.

4.3.3 Boundary conditions

The lateral sides of the matrix continuum and of the conduit continuum, as well as the top of the conduit continuum are defined as no flow boundaries (see Fig. 4.3). A constant head boundary is applied to the right side of the conduit continuum at 634 m a.s.l. to represent the spring and allow discharge. A specified flux boundary is set at the top of the matrix continuum to account for diffuse recharge. Daily data of total recharge was estimated by GEYER (2008) for the simulation period on the Gallusquelle catchment. The applied water balance approach accounts for canopy storage, snow storage and soil-moisture storage before water entering the bedrock. A second specified flux boundary is set on the bottom of the whole conduit continuum to add rapid recharge in the aquifer. The location of the boundary condition considers that the transit time of the rapid recharge component through the unsaturated zone is below one day (GEYER et al.,

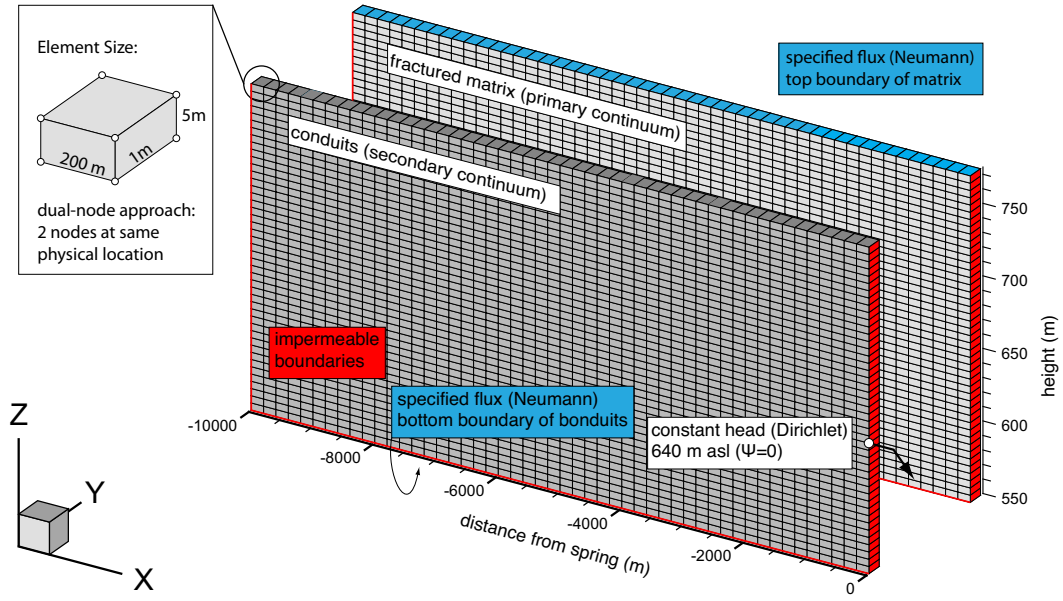

FIG. 4.3. Model grid of the two-dimensional model. A constant head boundary is applied at 640 m in the second continuum. Recharge is applied along the top boundary in both continuas. Every node in the primary continuum has its counterpart in the secondary continuum at the same physical location.

2008) and, therefore, negligible with regard to the daily time steps. The simulation of rapid water percolation from the top of the conduit continuum to the groundwater surface is physically not possible with the van Genuchten approach, because it does not consider gravity driven flow processes like film and droplet flow. The initial head distribution for transient discharge simulations is computed with a steady state simulation. The applied total recharge for the simulation is 1.5 mm d^{-1}, which corresponds to the average recharge across the catchment area during the year 1988. Ten percent of the total recharge is employed as rapid recharge component at the bottom of the conduit continuum. The amount is in the range of the rapid recharge component estimated by SAUTER (1997) from event analysis using oxygen isotopes in precipitation and Gallusquelle spring water to differentiate between different flow components.

4.3.4 Parameterization

For the model calibration, known parameters are only varied within reasonable ranges that agree with actual field observations (Tab. 4.2). Unknown model parameters are investigated by an extensive sensitivity analysis. The specific storage coefficients for matrix and conduits are negligible since the aquifer is unconfined; hence, water released due to compaction in the saturated zone is irrelevant. As there are no documented values for the hydraulic properties of the interface available, the van Genuchten parameters α_i, n_i, S_{wri} and the interface hydraulic conductivity K_i were set to values equal to the surrounding fissured matrix. Accordingly, inter-continuum water exchange is solely controlled by adjusting the exchange parameter α_{ex}. Model calibration is accomplished by fitting the observed and simulated discharge curves. Finally, the flow model contains 21 adjustable parameters for the fissured matrix and the conduit continuum.

4.4 Results and discussion

4.4.1 Model calibration

The calibrated model shows a good fit with most of the specific characteristics of the discharge hydrograph during the period between Feb./16th/1988 and Jan./20th/1990 (see Fig. 4.4). Please note that the discharge has been normalized to the catchment area (45 km^2). Calibrated values for all varied parameters are comparable to values documented in the literature (Tab. 4.2). The observed discharge curve shows less sharp peaks and is smoother than the simulated curve. Sauter (1992) did get a comparable fit with a double continuum model for the saturated zone. The author did apply a function for the transfer of water from the soil zone to the groundwater surface, which is not necessary for our model. During the time period investigated, two strong discharge events occurred, caused by major snowmelts which are refered to as first and second peak (see Fig. 4.4). The discharged water volume agrees well with the simulated data during the time period of the first peak. During the second discharge event (second peak) the simulated peak height is overestimated. It is not possible to change the relative

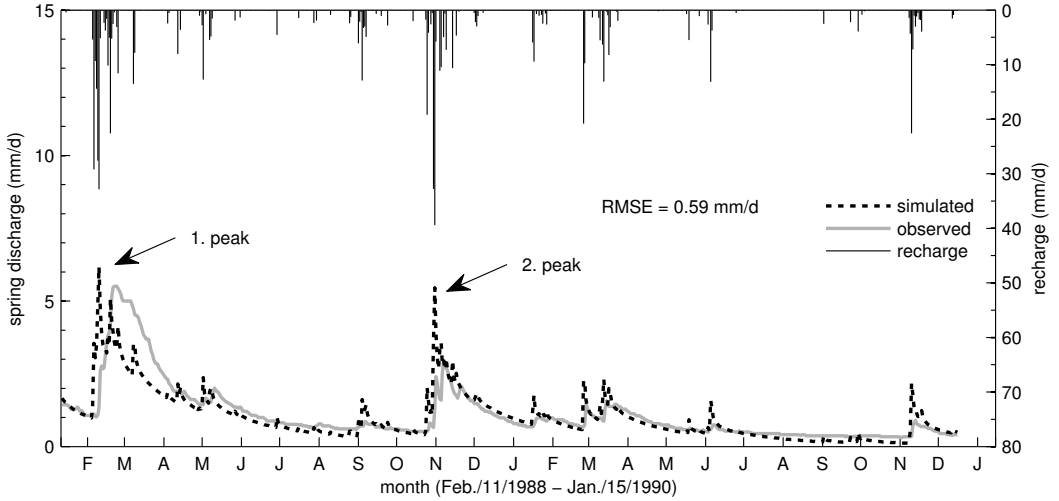

FIG. 4.4. The calibrated curve shows an acceptable fit. The secondary peak height is overestimated by the model. The first recharge event (first peak) reaches the spring too early. Recession curve slopes show a good overall correlation.

peak height difference between the first and second peak with the available calibration parameters. The recession curve slopes after discharge events show a good fit, except during low flow conditions between July and October 1989. This behavior could be attributed to the simplified geometry of the numerical model, which does not include the documented slightly inclined aquifer base and the geometry of different karstified zones in the karst system. The hydraulic heads in the matrix continuum and the conduit continuum are nearly identical during the simulation period with a difference of a few centimeters. Above the water table the matrix saturation drops to 0.35 near the surface (see Fig. 4.5). Flow paths in the unsaturated matrix continuum and conduit continuum are slightly inclined towards the spring, whereas flow in the saturated zone is laterally oriented towards the outlet, i.e. the karst spring. The flow paths of the unsaturated matrix continuum, which would be expected to be vertical for such a large scale porous medium, are caused by the strong influence of the conduit continuum, which imposes a strong hydraulic gradient all over the matrix

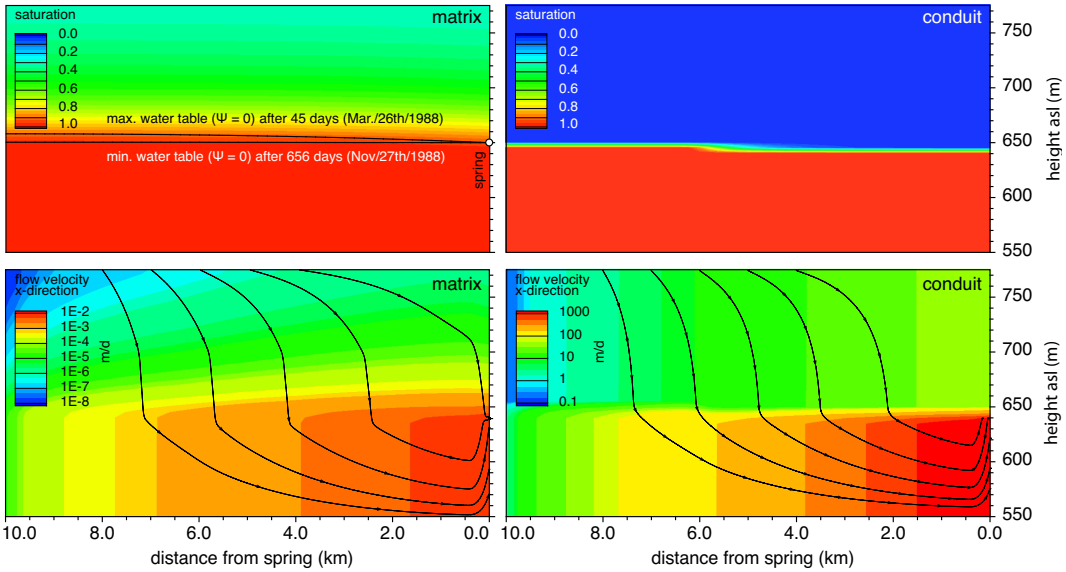

FIG. 4.5. Results of the transient flow model (Mar./26th/1988). Shown water tables apply for both continua as the height is nearly equal and differs 1 cm at most. The van Genuchten parameter α_m leads to a strong difference between the continua. The capillary rise is more pronounced in the matrix system, where saturation is ca. 0.35 near the surface. Saturation in the conduit system is lower than 0.1 above the water table and below 0.0001 near the surface. Flow velocities (only x-direction vector, note the different scaling for matrix and conduits) are apparently higher in the conduit continuum.

continuum. This behavior cannot be prevented unless the secondary continuum would be restricted to cover only the saturated zone. However, this is not an adequate solution considering the transient behavior of the system, i.e. the variation of water levels within both continua. The saturation in the conduit continuum is close to zero and has a very sharp transition along the water table. In this model, unsaturated flow in the conduits is also calibrated by the k_{rminc} parameter (minimum relative permeability of the conduits). Without this parameter, the relative permeability of the conduit continuum is a function of the residual saturation, i.e., setting of k_{rminc} simply overrides Eq. (4.13). This is the case for most of the unsaturated conduit continuum, where saturation declines very quickly (below 0.05) above

the water table for the given van Genuchten parameters. Therefore, with the applied van Genuchten parameters only, water flow in the unsaturated conduit continuum is extremely small such that exchange from the matrix into the conduit system is nearly completely prevented and a proper model calibration is impossible due to numerical insufficiencies. However, TOKUNAGA & WAN (1997) showed that gravity driven film flow processes occur on unsaturated fracture walls, which contribute to water percolation along surfaces and may act as an interface from the conduit system to the matrix system, thus giving a physical meaning to the k_{rminc} parameter. As the original van Genuchten model relies on a uni-modal distribution of the pore space the hydraulic response of such flow processes cannot be expected to be resolved by the model. Attempts to refine the original van Genuchten approach and include hydraulic features of fractures into a continuum model have been made for example by ROSS & SMETTEM (1993), DURNER (1994) and BROUYÈRE (2006) by constructing a continuous bi-modal retention curve. An important role for the water exchange in the double continuum approach plays the exchange parameter α_{ex}. It determines the ability of water to move in and out of the conduit continuum and lumps geometrical and hydraulic properties of the karst matrix system. The surface-volume ratio, for example, is higher for a dendritic system than for a single conduit with the same conduit volume. The exchange parameter in the calibrated model is set to a high value such that it does not act as an additional barrier for water transfer between both continua and water transfer is mainly controlled by the hydraulic properties of the two continua.

4.5 Sensitivity analysis

4.5.1 Single variation of hydraulic parameters for saturated flow conditions

Tab. (4.1) gives an overview of the recession coefficients and RMSE values obtained for the sensitive parameters. A parameter has been discarded as insensitive if the maximum RMSE is below $0.05\,\mathrm{mm\,d^{-1}}$. The recession co-

efficients have been measured at the first strong recharge event beginning of March 1988 (α_1) and during the low flow recession beginning of April 1988 (α_2). The calibrated values are $\alpha_1 = 0.23$ and $\alpha_2 = 0.03$ which is close to what has been reported by Sauter (1989) for a conduit dominated recession ($\alpha = 0.25$) for the same recharge event. Figure 4.6 (upper two graphs) shows the computed spring discharge for several model runs with varying hydraulic conductivity K_c and porosity θ_c in the conduit continuum. These parameters strongly influence the simulated spring discharge. Figure 4.7 (upper two graphs) additionally shows the respective recession coefficients. An increased conduit conductivity K_c results in higher α_1 recession coefficients and lower base flow levels indicated by the strong decrease of α_2. A decreased conduit conductivity K_c favors a slow recession and decreases α_1 to 0.06 which according to Sauter (1989) already indicates a mixed system (fractured matrix + conduits) response. Discharge peaks are broadened and the base flow is higher. In case the conduit drains the matrix system an increase of K_c enhances the exchange process between matrix and conduits by decreasing the hydraulic gradient in the conduit continuum and consequently increasing the hydraulic gradient between matrix and conduits. The conduit porosity θ_{sc} follows a similar pattern, i.e., an increase will enhance the exchange process, however, the impact on the discharge curves is far less pronounced within the given ranges and both recession coefficients are all in the same order of magnitude indicating a conduit dominated recession. A contrasting behavior is observed by a variation in matrix porosity θ_{sm}. With an increase in the parameter the water transfer between the continua during recharge events is decreased because of the lower head difference between conduit and matrix and the discharge curve is smoothened accordingly (see Fig. 4.6). The recession coefficient α_1 and α_2 are consequently slightly lower while for a very low matrix porosity of 1.2 % it is apparent that recessions coefficients represent a strongly conduit dominated system $\alpha_1 = 0.33$ and $\alpha_2 = 0.066$. K_m displays a low sensitivity within the given parameter range which can be attributed to the high exchange parameter of the calibrated model of $\alpha_{ex} = 1.0$. The high value leads to an immediate equalization of heads between conduit and matrix

such that water will not be restrained within the matrix system when total heads are slightly higher than within the conduit system. The matrix system always depends on the hydraulic state of the conduit continuum, which discharges water rapidly to the spring. However, in a three-dimensional karst system, flow velocities within the matrix will be little influenced by the conduit system with increasing distance to the conduit. The exchange parameter α_{ex} is sensitive only for strong reductions on the order of three to four magnitudes. A reduction to 0.001 lowers the peak height of both main peaks while decreasing recession curve slopes α_1 to 0.06 and slightly increasing base levels. Further reduction to 0.0001 drastically decreases peak heights and increases the base levels. The resulting α_2 coefficients are very low (0.002) and recharge events show no more pronounced peaks. An exchange reduction to 0.1 or 0.01 has no significant influence on the discharge curves, which indicates a sensitive interval between 0.001 and 0.0001.

4.5.2 Single variation of unsaturated zone parameters

Variations of the sensitive van Genuchten parameters for the vadose zone are shown in Fig. (4.8) and the corresponding recession coefficients in Fig. (4.9). The decrease of α_m and n_m results in a strong rise of peak heights and increase of recession slopes ($\alpha_1 = 0.36$ and 0.26 respectively). The influence of the van Genuchten α_m parameter on the discharge curve is connected to the inter-continuum water exchange process. Lowering the parameter increases the capillary rise, i.e. the matrix has higher saturation (and relative permeability) above the water table. Consequently the increased permeability leads to a stronger and earlier exchange of water from the matrix into the conduit continuum, such that recharge events affect spring discharge a lot earlier (pronounced event peaks). The opposite can be observed for a value of 0.365 where the saturation fringe declines very quickly with lower saturations above the water table. This reduces the main exchange interface to a smaller area above the water table. Thus during high recharge events, peak heights are reduced since water will remain longer in the matrix continuum and the α_2 recession coefficient becomes

Table 4.1. RMSE values and recession coefficients for all sensitive parameters. Parameters with a maximum RMSE below 0.05 mm d^{-1} have been considered as insensitive. Subscript m and c denote the matrix resp. the conduit continuum. Bold numbers denote the calibrated value.

Parameter	Value	Recess. coeff. (d^{-1})		RMSE (mm d^{-1})
		α_1	α_2	
K_c	100	0.26	0.160	1.329
	10	**0.23**	**0.030**	-
	1	0.06	0.015	0.645
θ_{sc}	0.00029	0.29	0.033	0.188
	0.00023	**0.23**	**0.030**	-
	0.00014	0.23	0.026	0.108
θ_{sm}	0.102	0.33	0.066	0.318
	0.042	**0.23**	**0.030**	-
	0.012	0.19	0.023	0.317
α_{ex}	**1.0**	**0.23**	**0.033**	-
	0.001	0.06	0.030	0.231
	0.0001	0.36	0.002	0.555
α_m	0.365	0.28	0.025	0.329
	0.0365	**0.23**	**0.030**	-
	0.00365	0.36	0.122	1.285
n_m	2.23	0.31	0.029	0.064
	1.83	**0.23**	**0.300**	-
	1.23	0.26	0.049	0.563
S_{wrm}	0.6	0.29	0.050	0.54
	0.3	0.32	0.034	0.142
	0.05	**0.23**	**0.030**	-
k_{rminc}	0.8	0.32	0.040	0.334
	0.05	**0.23**	**0.030**	-
	0.01	0.16	0.031	0.068

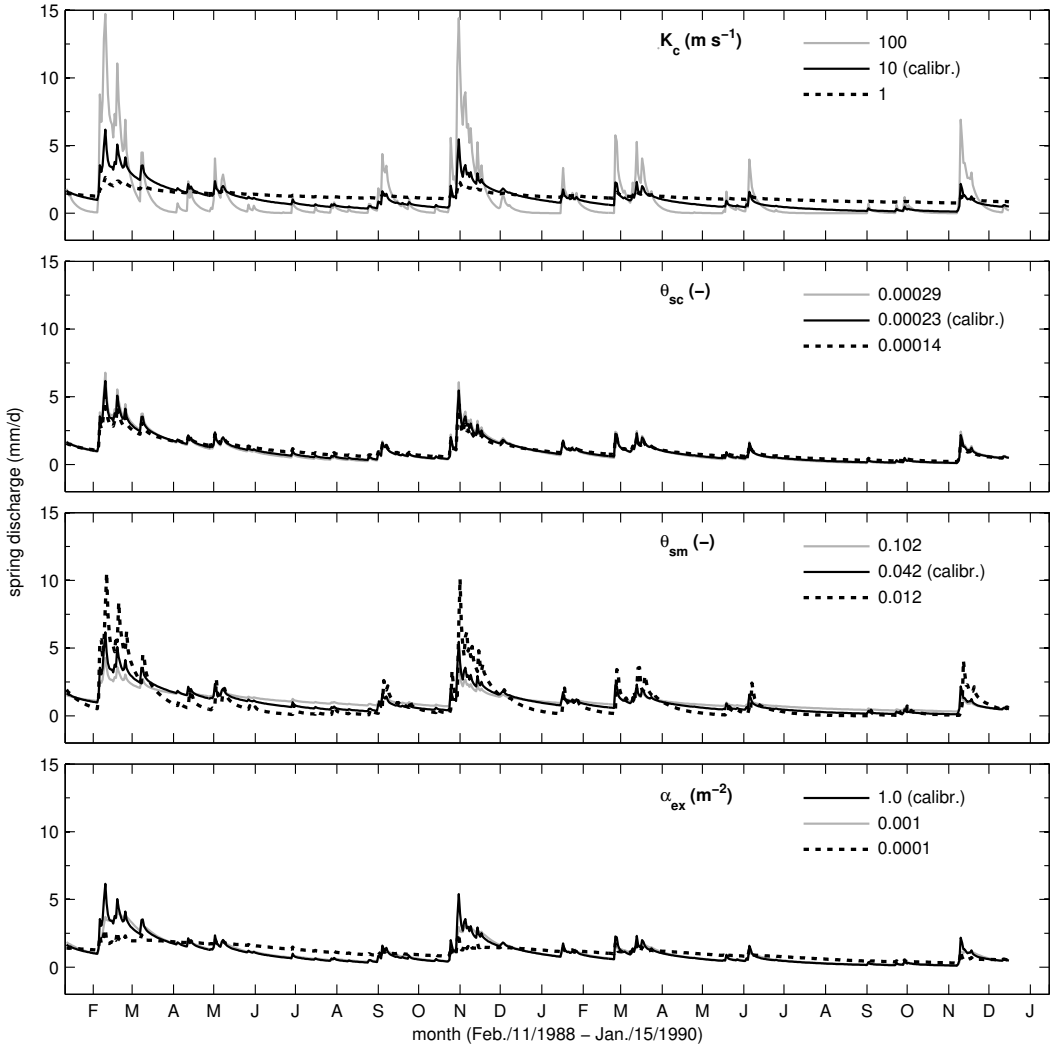

FIG. 4.6. Variation of hydraulic parameters (K_c, θ_{sc}, θ_{sm}) and the exchange parameter (α_{ex}).

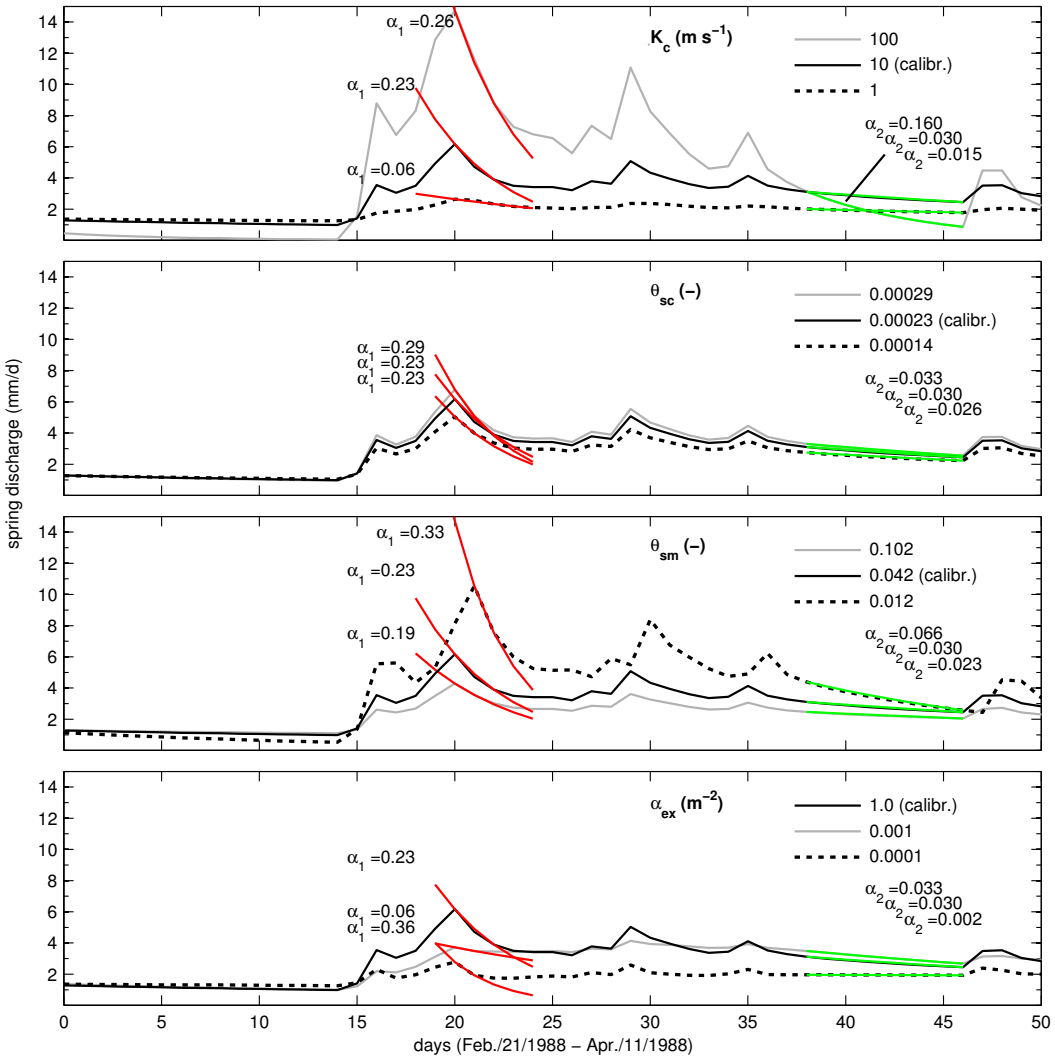

FIG. 4.7. Variation of hydraulic parameters (K_c, θ_{sc}, θ_{sm}) and the exchange parameter (α_{ex}).

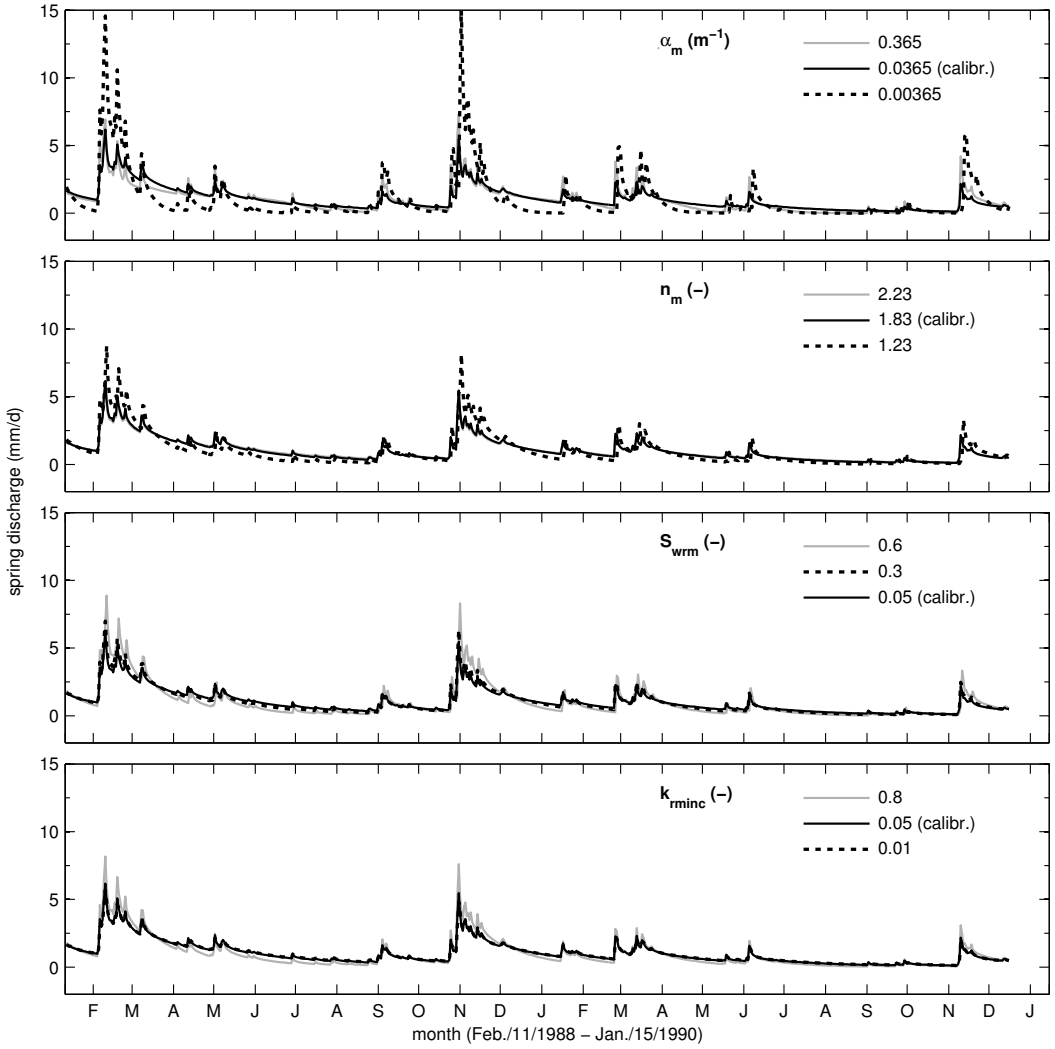

FIG. 4.8. Variation of the van Genuchten Parameters (α_m, n_m, S_{wrm}, k_{rminc}).

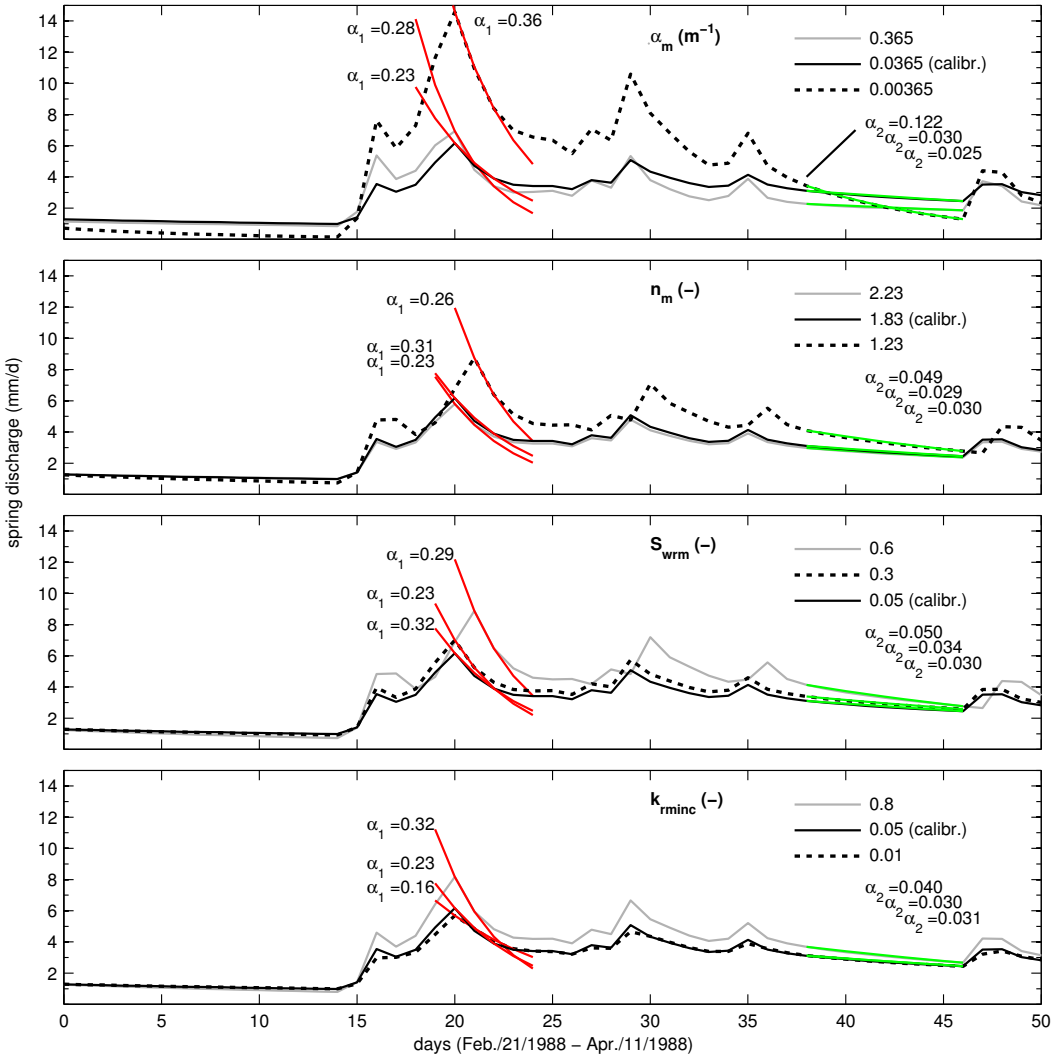

FIG. 4.9. Variation of the van Genuchten Parameters (α_m, n_m, S_{wrm}, k_{rminc}).

Table 4.2. Estimated values for the flow model derived from the model calibration and value ranges reported in the literature. Subscript m and c denote the matrix resp. the conduit continuum.

Parameter	Unit	Value	Literature Values	Reference[2]
K_c	(m/s)	10.0	3.0 - 10.0	1
K_m	(m/s)	2.9×10^{-6}	1.0×10^{-6} - 1.0×10^{-4}	1
θ_{sc}[1]	(-)	0.00023	0.00016 - 0.00064	1
θ_{sm}	(-)	0.042	0.007 - 0.025, >0.0 - 0.12	1,2
α_{ex}	(m^{-2})	1.0	-	-
Q	(%)	90	-	-
α_m	(m^{-1})	0.0365	0.0365, 0.0328 - 0.623	3,4
n_m	(-)	1.83	1.83, 0.01 - 3.0	3,4
S_{wrm}	(-)	0.05	0.01 - 0.05	4
α_c	(-)	5.1	5.1	3
n_c	(-)	2.56	2.56	3
S_{wrc}	(-)	0.0	-	-
k_{rminc}	(-)	0.05	-	-

[1]The local conduit continuum porosity is 1.0 i.e. $w_c\theta_{sc(local)} = \theta_{total} - w_m\theta_{sm}$ implicitly gives the total conduit porosity such that $\theta_{sc} \triangleq w_c\theta_{sc(local)}$. The total porosity is $\theta_{total} = 0.0422$.

[2]References: 1 - SAUTER (1992); 2 - WEISS (1987); 3 - ROULIER et al. (2006); 4 - CONTRACTOR & JENSON (2000).

slightly lower (0.025) reflecting the delayed discharge via the conduit system. The van Genuchten parameter n_m can be considered insensitive compared to α_m. The conduit van Genuchten parameters α_c and n_c are as well insensitive for the shown simulations. In the range of chosen values, the conduits do not produce a strong capillary rise, i.e. the unsaturated zone above the conduit water table always displays a sharp transition from saturated to strongly unsaturated. As mentioned earlier the application of the van Genuchten parameters to a highly conductive and discrete flow system such as a conduit implies a general abstraction of the physically based van Genuchten parameter set in order to create an upscaled continuum sys-

tem with a characteristic infiltration behavior and travel time distribution as well as an exchange interface in the unsaturated zone. In this work the exchange process in the unsaturated zone can be controlled by the α_c parameter in order to increase the capillary rise in the conduit continuum and enhance inter-continuum water transfer. However, such an approach also introduces a spatial information (i.e. the thickness of the conduit capillary fringe in vertical direction) which is not known in real karst systems. As described before the k_{rminc} parameter is used instead to maintain a constant water exchange in the unsaturated zone independent of the hydraulic state of the conduit system if saturations are too low. The residual water saturation of the matrix S_{wrm} and the minimum relative permeability of the conduits k_{rminc} both show a similar behavior regarding parameter variations. Increasing the parameters yields an enhanced exchange from the matrix to the conduit continuum due to a higher relative conductivity. Consequently recharge events are transmitted faster to the model outlet, i.e. the spring.

4.5.3 Combined parameter variations

The above presented sensitivity analyses imply only one single parameter varied at a time. However, a further important observation is that certain parameter combinations may show non-linear behavior with respect to their sensitivity, i.e. the influence of one parameter on the RMSE is not linear over the whole range of a second parameter. Tab. (4.3) shows maximum RMSE obtained for each parameter combination and if a non-linear relationship can be observed (bold RMSE values). For example, the simultaneous variation of the matrix van Genuchten parameter α_m and the conduit conductivity K_c displays a pronounced sensitivity for low α_m values (Fig. 4.10). While for the calibrated α_m value of $0.0365\,\mathrm{m}^{-1}$ the conduit conductivity K_c is almost insensitive in the range of $1\,\mathrm{m\,s}^{-1}$ to $10\,\mathrm{m\,s}^{-1}$ a lower α_m value of $0.003\,65\,\mathrm{m}^{-1}$ yields a high RMSE of $1.6\,\mathrm{mm\,d}^{-1}$ already at a K_c value of $10\,\mathrm{m\,s}^{-1}$, i.e. $\partial\mathrm{RMSE}(\alpha_m = 0.00365)/\partial K_c$ is much higher. A similar behavior can be shown for a combination of matrix porosity θ_{sm} and the conduit conductivity where lower porosities yield higher RMSE values with an increase

Table 4.3. Parameter combinations used for the sensitivity analyses and highest RMSE (mm d) observed. Bold RMSE values denote a non-linear inter-parameter dependence.

	Range													
	Low	High	K_c	K_m	θ_{sc}	θ_{sm}	α_{ex}	Q	α_m	n_m	S_{wrm}	α_c	n_c	S_{wrc}	k_{rminc}
K_c	1.0	100.0	–												
K_m	2.89×10^{-7}	2.89×10^{-4}	1.34	–											
θ_{sc}	1.40×10^{-4}	2.90×10^{-4}	1.48	0.19	–										
θ_{sm}	0.022	0.102	**2.23**	0.83	0.89	–									
α_{ex}	1.00×10^{-4}	1.0	**1.33**	0.56	0.61	**0.77**	–								
Q	30	95	1.33	0.06	0.23	0.77	0.57	–							
α_m	0.365×10^{-5}	3.65	**3.20**	···	···	···	1.29	···	–						
n_m	1.23	2.23	···	···	···	···	0.58	···	1.58	–					
S_{wrm}	0.05	0.6	···	···	···	···	···	···	1.87	···	–				
α_c	3.1	8.1	···	···	···	···	0.56	···	···	···	···	–			
n_c	2.16	3.16	···	···	···	···	0.56	···	···	0.56	···	0.25	–		
S_{wrc}	0.0	0.4	···	···	···	···	0.56	···	···	···	···	0.01	···	–	
k_{rminc}	0.01	0.8	···	···	···	···	0.56	···	···	···	···	0.33	···	···	–

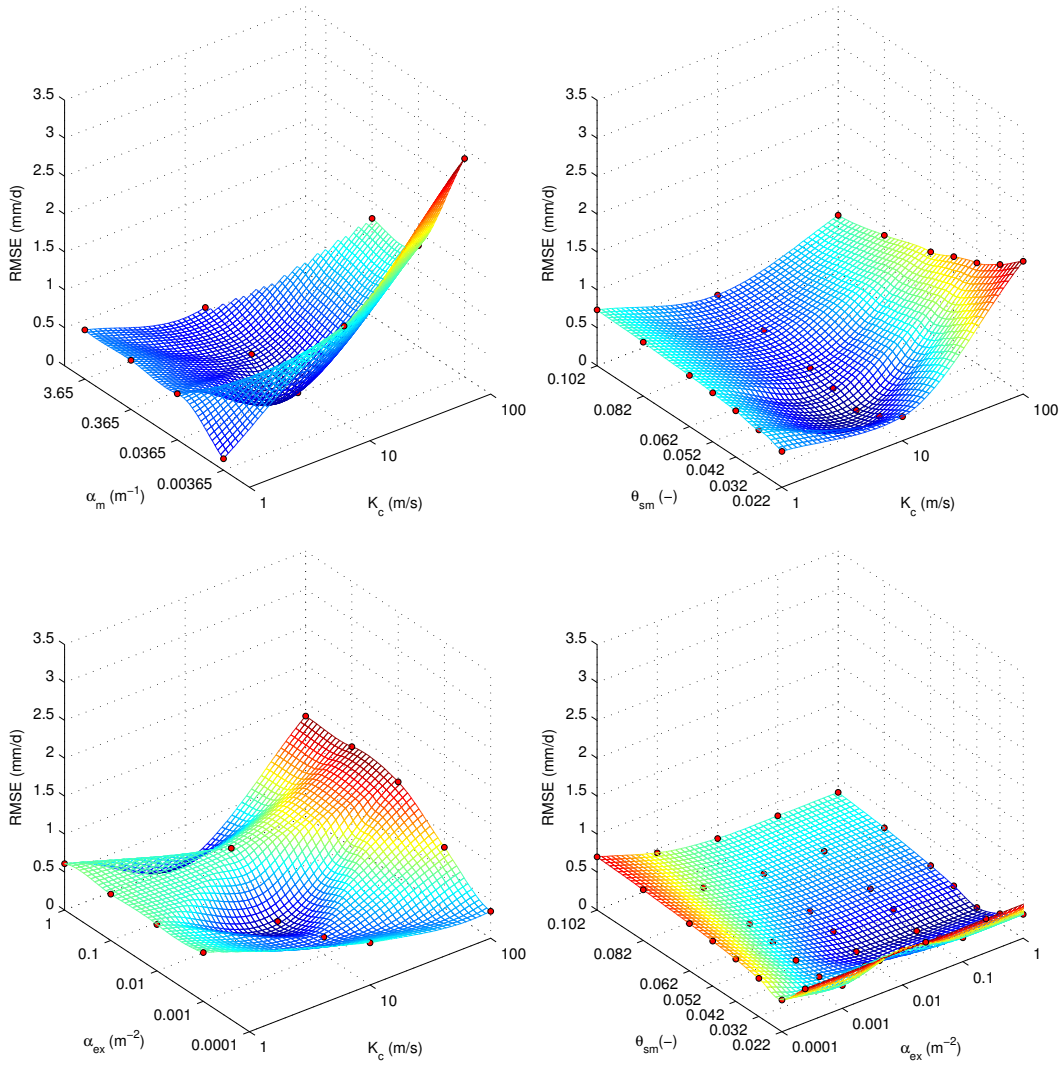

FIG. 4.10. Sensitivity matrices showing nonlinear inter-parameter dependencies.

in conduit conductivity to 100 m s^{-1} whereas for rather high matrix porosities of 0.102 the increase in RMSE is less pronounced. The conduit conductivity K_c exhibits a higher sensitivity for the calibrated exchange parameter α_{ex} = 1.0 (see Fig. 4.10) such that a high conductivity value (100 m s^{-1}) results in RMSE values of ca. 1.4 mm d^{-1} while for a lower exchange parameter the same conductivity yields a deviation of only 0.4 mm d^{-1}. The exchange parameter has a higher sensitivity for high conductivity values of the conduit system while it is nearly insensitive for low values (1 m s^{-1}). In sum, the variation of the exchange parameter influences the discharge curve depending on the combination with other parameters. This behavior can also be observed for the combination of matrix porosity θ_{sm} and exchange parameter α_{ex}. Here the exchange parameter has a higher sensitivity for matrix porosities between 0.032 and 0.102 while at the lower limit (0.012 - 0.022) this sensitivity vanishes.

4.6 Conclusion

The applied vertical two-dimensional double continuum approach is successfully employed to simulate the discharge behavior of the karst system Gallusquelle for a period of two years. Because of the high amount of model parameters of the saturated-unsaturated flow model, a comprehensive sensitivity analysis was performed. The analysis shows that the simulated discharge curve displays high sensitivity to a variation of a number of model parameters. The sensitivity study demonstrates that the simulation of karst hydraulics requires strong a-priori knowledge about parameter ranges to reduce ambiguity of the model. However, especially for the conduit continuum, only little about physical parameters is known and further research is needed. Physical parameters of the saturated fissured matrix can be obtained from field experiments on the scale of a representative elementary volume. Furthermore, the analysis shows that the sensitivity of a parameter depends to a large degree on the other calibrated model parameters. Therefore, sensitivity analyses should simultaneously take into account parameters of both continua in order to detect deviations from a linear behavior if both parameters are sensitive. It also means that

conclusions about parameter sensitivity change from model to model and are not simply transferable. The fissured matrix porosity as well as van Genuchten parameters of the matrix continuum are the most important parameters for an appropriate flow simulation. The conduit system drains the fissured matrix and can, due to its high hydraulic conductivity, effectively discharge varying quantities of water transferred from the matrix continuum. The van Genuchten parameters of the fissured matrix are the most crucial property in terms of sensitivity, uncertainty and model limitations. The exchange process between matrix and conduit continuum is mainly controlled by differences in hydraulic properties. The α_{ex} parameter was set to a rather high value during the calibration, i.e. exchange is not limited by a too low exchange coefficient. According to GERKE & VAN GENUCHTEN (1993) the parameter is defined to express the interface connectivity on a rather small scale, e.g. between a porous medium and macropores. On catchment scale it might implicitly correspond to the type of karst system (i.e. karstified layers vs. karst conduits). The choice of a two-dimensional dual-continuum model for simulation of flow in karst systems leads to certain advantages and limitations. Considering the lack of information for most karst spring catchments the dual-continuum approach provides an efficient way to lump its geometrical features, i.e. only limited informations about the conduit geometry and rapid recharge area are necessary. However, lateral flow dynamics between the localized conduits and the matrix system are not considered and water table fluctuations in a continuum only represent the volume-averaged dynamics of the whole system. Vertical two-dimensional modeling approaches are therefore more appropriate for the simulation of karstified layers than for the simulation of local karst conduit systems embedded in a fissured matrix. Furthermore the vertical two-dimensional approach neglects the lateral geometry of a spring catchment, e.g. reduction of cross-sectional area of the matrix contiunuum towards a karst spring, which might affect the discharge behavior. The unified simulation of the saturated and unsaturated matrix and conduit continuum using the Richards equation is limited valid regarding the underlying physical process description. The application of the Richards

equation for the matrix continuum can be considered as suitable at large scale (e.g. KAUFMANN, 2003). But at this scale, van Genuchten parameters cannot be measured and become calibration parameters. A clear limitation is the loss of the physical meaning of the Richards equation for the conduit continuum. Flow through localized karst conduits might be highly transient, i.e. the application of open channel flow approaches would be appropriate (REIMANN et al., 2011a). However, these approaches increase the number of calibration parameters and require additional knowledge about the geometry of a karst conduit system. Additionally, flow in unsaturated karst features (e.g. vertical shafts) is not controlled by matrix potential and capillary forces but rather flow processes dominated by gravitational forces such as film flow (TOKUNAGA & WAN, 1997; TOKUNAGA et al., 2000), turbulent film flow (GHEZZEHEI, 2004), droplet flow (DOE, 2001; DRAGILA & WEISBROD, 2004a) and rivulet flow (DRAGILA & WEISBROD, 2004b; SU et al., 2001; SU et al., 2004). In order to be able to apply the vertical dual continuum approach, boundary conditions were modified and rapid recharge was directly injected at the bottom of the saturated conduit continuum. This abstraction clearly reduces the predictive capability of the applied approach.

Acknowledgements

This work was funded by the Deutsche Forschungsgemeinschaft (DFG; German Research Foundation) under grants no. GE 2173/2-2 and SA 501/24-1. Careful reviews of the manuscript by the editor and two anonymous reviewers are gratefully acknowledged. We would also like to thank Dr. Thomas Graf and Dr. Rob McLaren for their advice.

4.7 References

ABEL, T., SAUTER, M. & HINDERER, M. (2002): 'Karst genesis of the Swabian Alb, south Germany, since the Pliocene'. *Acta Geol. Pol.* Vol. **52**(1): pp. 43–54 (cit. on p. 81).

BAMBERG, G., BAUR, F. & KRAPP, M. (2007): *Statistik*. München: Oldenbourg: p. 342 (cit. on p. 80).

BARENBLATT, G. I., ZHELTOV, I. P. & KOCHINA, I. N. (1960): 'Basic Concepts in the Theory of Seepage of Homogenous Liquids in Fissured Rocks Strata'. *Journal of Applied Mathematics and Mechanics*, vol. **24**: pp. 1286–1303 (cit. on pp. 75, 79).

BIRK, S., GEYER, T., LIEDL, R. & SAUTER, M. (2005): 'Process-Based Interpretation of Tracer Tests in Carbonate Aquifers'. *Ground Water*, vol. **43**(3): pp. 381–388 (cit. on pp. 74, 81).

BIRK, S., LIEDL, R. & SAUTER, M. (2006): 'Karst spring responses examined by process-based modeling.' *Ground Water*, vol. **44**(6): pp. 832–836 (cit. on p. 74).

BROUYÈRE, S. (2006): 'Modelling the migration of contaminants through variably saturated dual-porosity, dual-permeability chalk'. *Journal of Contaminant Hydrology*, vol. **82**: pp. 195–219 (cit. on p. 88).

CONTRACTOR, D. N. & JENSON, J. W. (2000): 'Simulated effect of vadose infiltration on water levels in the Northern Guam Lens Aquifer'. *Journal of Hydrology*, vol. **229**: pp. 232–254 (cit. on pp. 80, 96).

DOE, T. (2001): 'What do drops do? Surface wetting and network geometry effects on vadose-zone fracture flow'. *Conceptual models of flow and transport in the fractured vadose zone*. Washington D.C.: National Academy Press. Chap. 8: pp. 243–270 (cit. on p. 102).

DRAGILA, M. I. & WEISBROD, N. (2004a): 'Flow in Menisci Corners of Capillary Rivulets'. *Vadose Zone Journal*, vol. **3**: pp. 1439–1442 (cit. on p. 102).

– (2004b): 'Fluid motion through an unsaturated fracture junction'. *Water Resources Research*, vol. **40**: pp. 1–11 (cit. on pp. 75, 102).

Dreiss, S. J. (1989): 'Regional scale transport in a karst aquifer: 1. Component separation of spring flow hydrographs'. *Water Resources Research*, vol. **25**(1): pp. 117–125 (cit. on p. 74).

Dreybrodt, W., Gabrovek, F. & Romanov, D. (2005): *Processes of a Speleogenessis : A Modeling Approach*. Ljubljana: Karst Research Institute at ZRC SAZU, ZRC Publishing (cit. on p. 74).

Durner, W. (1994): 'Hydraulic conductivity estimation for soils with heterogeneous pore structure'. *Water Resources Research*, vol. **30**(2): p. 211 (cit. on p. 88).

Genuchten, M. T. van (1980): 'A Closed-form Equation for Predicting the Hydraulic Conductivity of Unsaturated Soils'. *Soil Science Society of America Journal*, vol. **44**(5): pp. 892–898 (cit. on p. 77).

Gerke, H. H. & Van Genuchten, M. (1993): 'Evaluation of a first-order water transfer term for variably saturated dual-porosity flow models'. *Water Resources Research*, vol. **29**: pp. 1225–1225 (cit. on pp. 79, 101).

Germann, P. F., Helbling, A. & Vadilonga, T. (2007): 'Rivulet Approach to Rates of Preferential Infiltration'. *Vadose Zone Journal*, vol. **6**(2): pp. 207–220 (cit. on p. 75).

Geyer, T. (2008): 'Process-based characterisation of flow and transport in karst aquifers at catchment scale'. PhD thesis. University of Göttingen: p. 103 (cit. on p. 83).

Geyer, T., Birk, S., Liedl, R. & Sauter, M. (2008): 'Quantification of temporal distribution of recharge in karst systems from spring hydrographs'. *Journal of Hydrology*, vol. **348**(3-4): pp. 452–463 (cit. on pp. 81, 83).

Ghezzehei, T. A. (2004): 'Constraints for flow regimes on smooth fracture surfaces'. *Water Resources Research*, vol. **40**: pp. 1–14 (cit. on p. 102).

Gwinner, M. P. (1976): *Origin of the Upper Jurassic limestones of the Swabian Alb (Southwest Germany)*. E. Schweizerbart (cit. on p. 81).

Hill, C. & Polyak, V. (2010): 'Karst hydrology of Grand Canyon, Arizona, USA'. *Journal of Hydrology*, vol. **390**(3-4): pp. 169–181 (cit. on p. 74).

Jeannin, P. Y. (2001): 'Modeling flow in phreatic and epiphreatic karst conduits'. *Water Resources Research*, vol. **37**(2): pp. 191–200 (cit. on p. 74).

KAUFMANN, G. (2003): 'Modelling unsaturated ow in an evolving karst aquifer'. *Journal of Hydrology*, vol. **276**: pp. 53–70 (cit. on p. 102).

MCLAREN, R. G., FORSYTH, P. A., SUDICKY, E. A., VANDERKWAAK, J. E., SCHWARTZ, F. W. & KESSLER, J. H. (2000): 'Flow and transport in fractured tuff at Yucca Mountain: numerical experiments on fast preferential flow mechanisms'. *Journal of Contaminant Hydrology*, vol. **43**: pp. 211–238 (cit. on p. 76).

MUALEM, Y. (1976): 'A new model for predicting the hydraulic conductivity of unsaturated porous media'. *Water Resources Research*, vol. **12**(3): pp. 513–522 (cit. on p. 78).

REIMANN, T., GEYER, T., SHOEMAKER, W. B., LIEDL, R. & SAUTER, M. (2011a): 'Effects of dynamically variable saturation and matrix-conduit coupling of flow in karst aquifers'. *Water Resources Research*, vol. **47**(11): pp. 1–19 (cit. on pp. 74, 102).

REIMANN, T., REHRL, C., SHOEMAKER, W. B., GEYER, T. & BIRK, S. (2011b): 'The significance of turbulent flow representation in single-continuum models'. *Water Resources Research*, vol. **47**(9): pp. 1–15 (cit. on p. 74).

RICHARDS, L. A. (1931): 'Capillary Conduction of Liquids Through Porous Mediums'. *Physics*, vol. **1**(5): pp. 318–333 (cit. on p. 76).

ROSENBOM, A., THERRIEN, R. & REFSGAARD, J. (2009): 'Numerical analysis of water and solute transport in variably-saturated fractured clayey till'. *Journal of Contaminant Hydrology*, vol. **104**(1-4): pp. 137–152 (cit. on p. 76).

ROSS, P. J. & SMETTEM, K. R. J. (1993): 'Describing soil hydraulic properties with sums of simple functions'. *Soil Science Society of America Journal*, vol. **57**(1): pp. 26–26 (cit. on p. 88).

ROULIER, S., BARAN, N., MOUVET, C., STENEMO, F., MORVAN, X., ALBRECHTSEN, H.-J., CLAUSEN, L. & JARVIS, N. (2006): 'Controls on atrazine leaching through a soil-unsaturated fractured limestone sequence at Brévilles, France.' *Journal of Contaminant Hydrology*, vol. **84**(1-2): pp. 81–105 (cit. on pp. 80, 96).

SAUTER, M. (1997): 'Differentiation of flow components in a karst aquifer using the δ^{18}O signature'. *Tracer Hydrology*. Ed. by A. KRANJC. Balkema: pp. 435–441 (cit. on p. 84).

– (1992): *Quantification and Forecasting of Regional Groundwater Flow and Transport in a Karst Aquifer (Gallusquelle, Malm, SW. Germany)*. Tübinger Geowissenschaftliche Arbeiten: p. 150 (cit. on pp. 75, 80–82, 96).

SAUTER, M., GEYER, T., KOVACS, A. & TEUTSCH, G. (2006): 'Modellierung der Hydraulik von Karstgrundwasserleitern Eine Übersicht'. *Grundwasser*, vol. **3**: pp. 143–156 (cit. on p. 75).

SCHWARTZ, F., SUDICKY, E. & MCLAREN, R. G. (2010): 'Ambiguous hydraulic heads and C^{14} activities in transient regional flow'. *Ground Water*, vol. **48**(3): pp. 366–379 (cit. on p. 76).

SMART, P. L. & HOBBS, S. L. (1986): 'Characterisation of carbonate aquifers: A conceptual base'. *Proceedings of the Environmental Problems in Karst Terranes and Their Solutions Conference, Bowling Green, Ky. Published by NWWA*: pp. 17–31 (cit. on p. 74).

SU, G. W., GELLER, J. T., PRUESS, K. & HUNT, J. R. (2001): 'Solute transport along preferential flow paths in unsaturated fractures'. *Water Resources Research*, vol. **37**(10): pp. 2481–2491 (cit. on p. 102).

SU, G. W., GELLER, J. T., HUNT, J. R. & PRUESS, K. (2004): 'Small-Scale Features of Gravity-Driven Flow in Unsaturated Fractures'. *Vadose Zone Journal*, vol. **3**(2): pp. 592–601 (cit. on p. 102).

TEUTSCH, G. (1988): 'Grundwassermodelle im Karst: Praktische Ansätze am Beispiel zweier Einzugsgebiete im Tiefen und Seichten Malmkarst der Schwäbischen Alb'. PhD thesis. Universität Tübingen (cit. on p. 75).

TEUTSCH, G. & SAUTER, M. (1991): 'Groundwater modeling in karst terranes: Scale effects, data acquisition and field validation'. *Proc. Third Conf. Hydrogeology, Ecology, Monitoring, and Management of Ground Water in Karst Terranes, Nashville, TN*: pp. 17–35 (cit. on p. 75).

THERRIEN, R., MCLAREN, R. G., SUDICKY, E. & PANDAY, S. (2008): 'HydroGeoSphere: A three-dimensional numerical model describing fully-integrated subsurface and surface flow and solute transport'. *Manual (Draft), HydroGeoLogic Inc., Herndon, VA*, vol. (cit. on pp. 73, 75, 76).

THERRIEN, R. & SUDICKY, E. A. (1996): 'Three-dimensional analysis of variably-saturated flow and solute transport in discretely-fractured porous media'. *Journal of Contaminant Hydrology*, vol. **3542**(95): pp. 1–44 (cit. on p. 74).

TOKUNAGA, T. K. & WAN, J. (1997): 'Water film flow along fracture surfaces of porous rock'. *Water Resources Research*, vol. **33**(6): p. 1287 (cit. on pp. 88, 102).

TOKUNAGA, T. K., WAN, J. & SUTTON, S. R. (2000): 'Transient film flow on rough fracture surfaces'. *Water Resources Research*, vol. **36**(7): pp. 1737–1746 (cit. on p. 102).

WEISS, E. G. (1987): 'Porositäten, Permeabilitäten und Verkarstungserscheinungen im mittleren und oberen Malm der südlichen Frankenalb'. PhD thesis. Universität Erlangen (cit. on pp. 80, 96).

5 | A Smoothed Particle Hydrodynamics model for droplet and film flow on smooth and rough fracture surfaces*

Kordilla, J.[1], Tartakovsky, A.M.[2], Geyer, T.[1]

[1]Geoscientific Centre, University of Göttingen, Göttingen, Germany
[2]Computational Mathematics Group, Pacific Northwest National Laboratory, Richland, USA

* Kordilla, J., Tartakovsky, A.M. & Geyer, T., (2013): A Smoothed Particle Hydrodynamics model for droplet and film flow on smooth and rough fracture surfaces. *Advances in Water Resources*, **59**, pp. 114.

Abstract. Flow on fracture surfaces has been identified by many authors as an important flow process in unsaturated fractured rock formations. Given the complexity of flow dynamics on such small scales, robust numerical methods have to be employed in order to capture the highly dynamic interfaces and flow intermittency. In this work we use a three-dimensional multiphase Smoothed Particle Hydrodynamics (SPH) model to simulate surface tension dominated flow on smooth fracture surfaces. We model droplet and film flow over a wide range of contact angles and Reynolds numbers encountered in such flows on rock surfaces. We validate our model via comparison with existing empirical and semi-analyical solutions for droplet flow. We use the SPH model to investigate the occurrence of adsorbed trailing films left behind droplets under various flow conditions and its importance for the flow dynamics when films and droplets coexist. It is shown that flow velocities are higher on prewetted surfaces covered by a thin film which is qualitatively attributed to the enhanced dynamic wetting and dewetting at the trailing and advancing contact lines. Finally, we demonstrate that the SPH model can be used to to study flow on rough surfaces.

5.1 Introduction

Understanding physics of fast flow through unsaturated fractured rocks, is important for management of groundwater resources and prediction of repository performance in hard rock regions (Evans & Rasmussen, 1991; Singhal & Gupta, 2010). The uncertainties range from process understanding at local scale to that of hydraulic understanding of regional fault zones (Mclaren et al., 2000). Simulation of unsaturated flow in hard rocks represents a challenge due to highly non-linear free-surface flow dynamics and the complexity of interactions between flow in a fracture and the surrounding matrix. Hard rock formations contain fractures and other discontinuities with varying spatial parameters including orientation, density and aperture distributions (Singhal & Gupta, 2010). Volumetric flow rates of water in unsaturated fractures may differ by several orders of magnitude from flow rates through the porous rock matrix. In sites where the rock matrix has a small permeability, fractures may provide the primary pathways for percolation of water to the phreatic zone (Evans et al., 2001). In this case, classical modeling approaches (van Genuchten, 1980; Mualem, 1976) for unsaturated flow in porous media may not be accurate for flow in fractured rocks. Recent laboratory experiments of Tokunaga & Wan (1997) and Tokunaga et al. (2000) have shown that film flow contributes significantly to the overall unsaturated flow in fractured rocks. Depending on the matric potential, i.e., the saturation of the matrix, films with thickness up to 70 µm and average flow velocity of $3 \times 10^{-7}\,\mathrm{m\,s^{-1}}$ may develop on fracture surfaces providing an efficient preferential pathway for laminar flow. Even faster flow velocities on fracture surfaces may develop due to the presence of droplets (Doe, 2001; Dragila & Weisbrod, 2003), continuous rivulets (Dragila & Weisbrod, 2004a; Dragila & Weisbrod, 2004b; Germann et al., 2007; Su et al., 2001; Su et al., 2004) and falling (turbulent) films (Ghezzehei, 2004). As noted by Doe (2001) and Ghezzehei (2004) these flow regimes may coexist with adsorbed films, however their influence on the faster flow regimes such as droplets has not been investigated by these authors and is also part of this work. Flow rates during transitions

between droplets, rivulets and falling films can range significantly in magnitude, and have been investigated by GHEZZEHEI (2004) using an energy minimization principle. The approach is partially based on the findings of PODGORSKI et al. (2001). The authors investigated droplet flow on inclined surfaces and proposed a dimensionless linear scaling law to quantify flow velocities and provide a general framework and a unified dimensionless description of such flow processes. In order to apply the scaling to arbitrary fluid-substrate systems GHEZZEHEI (2004) introduced a dimensionless scaling parameter. In this study, we employ this scaling law in a quantitative study of droplet flow on dry and wet fracture surfaces. Given the complexity of the small-scale flow dynamics and the heterogenous nature of fractured rock surfaces, numerical models provide a significant addition to laboratory experiments and analytical solutions to investigate these systems. Models have to resolve the highly dynamic fluid interfaces as well as boundary geometries. Traditional grid-based methods, such as Finite-Element or Volume of Fluid (HIRT & NICHOLS, 1981; HUANG & MEAKIN, 2008) methods, in general require complex and computationally demanding interface tracking schemes. Furthermore, these methods have to rely on empirical boundary conditions specifying dynamic receding and advancing contact angles as a function of velocity. Lagrangian particle methods offer a versatile treatment of multiphase flows in domains with a complex geometry. In particle methods, there is no need for front-tracking algorithms to detect a moving interface as it moves with the particles. In addition particle methods are rigorously Galileian invariant as particle interactions only depend on relative differences in positions and velocities of the interacting particles. Furthermore, particle methods exactly conserves mass, energy and momentum due to antisymmetric particle-particle forces. Depending on the form of forces acting between particles, particle methods can model fluid flow on different spatio-temporal scales. Molecular Dynamics (MD) is able to accurately model multiphase fluid flow on a molecular scale but modeling flow in a reasonably-sized porous domain or fracture is far out of reach of modern MD codes, even in state-of the-art High-Performance computing facilities. Smoothed Particle Hydrodynamics (SPH, GINGOLD &

MONAGHAN, 1977; LUCY, 1977) can be seen as upscaled formulations of MD in which particles represent fluid volumes and forces acting between particles of the same fluid phase are obtained from a meshless discetization of the Navier-Stokes equations (HOOVER et al., 1994). Due to the similarity to MD, the surface tension and static and dynamic contact angles can be modeled via molecular-like pair-wise interaction forces (TARTAKOVSKY & MEAKIN, 2005b). Making these forces "soft", i.e., creating forces that have a finite magnitude for small (and zero) distances between a pair of particles, allows the SPH multiphase model to simulate flow on hydrodynamics time and length scales. A critical review of various numerical methods for multiphase flows in porous and fractured media can be found in MEAKIN & TARTAKOVSKY (2009). Application of SPH for modeling flow in porous media has been demonstrated by, amongst others, HOLMES et al. (2011), HOLMES et al. (2000), TARTAKOVSKY et al. (2009a), and TARTAKOVSKY & MEAKIN (2006). In this work we use a SPH model to study free-surface fluid flow on smooth and rough wide aperture fractures, i.e., flow bounded by a single fracture surface. This SPH model has been used before to study multiphase and free surface flows (TARTAKOVSKY & MEAKIN, 2005b; TARTAKOVSKY & MEAKIN, 2005c; TARTAKOVSKY et al., 2009b; TARTAKOVSKY et al., 2007), but has not been rigorously validated for three-dimensional free-surface flow dominated by capillary forces. We demonstrate that the SPH method of TARTAKOVSKY & MEAKIN (2005b) can be applied to model dynamics of droplets on dry surfaces. Our simulations show how wetted surfaces naturally arise from droplet wetting dynamics and demonstrate the effect of prewetted surfaces on droplet flow. The objectives of this work are: (1) the verification of the SPH model with existing empirical and semi-analytical solutions; (2) the investigation of droplet wetting behavior on initially dry surfaces for a wide range of wetting conditions; and (3) the study of transient droplet flow on fracture surfaces covered by adsorbed films using the SPH model. To ensure numerical accuracy of the SPH simulations, the effect of resolution on static contact angles is investigated. Contact angle hysteresis for droplets in a critical state, i.e., at the verge of movement, is simulated and compared to laboratory data of ELSHERBINI &

JACOBI (2004) and ELSHERBINI & JACOBI (2006). Transient droplet flow is verified using the dimensionless linear scaling of PODGORSKI et al. (2001). The formation of adsorbed films emitted from droplets on initially dry fracture surfaces and their influence on droplet flow is investigated. The effect of surface roughness on flow velocities is demonstrated.

5.2 Method

In the following we give a brief description of the SPH method and the governing equations. More detailed derivations and approximations involved in the SPH method can be found for example in MONAGHAN (1982) and TARTAKOVSKY & MEAKIN (2005b). To derive a SPH discretization of the Navier-Stokes equations, one can start with the definition of the Dirac δ function

$$f(\boldsymbol{r}) = \int_{\Omega} f(\boldsymbol{r}')\delta(\boldsymbol{r}-\boldsymbol{r}')d\boldsymbol{r}', \tag{5.1}$$

where $f(\boldsymbol{r})$ is a continuous function defined on a domain Ω and $\boldsymbol{r}$ is the position vector. In SPH, for computational reasons, the δ function is replaced with a smooth, bell-shaped kernel function W (MONAGHAN, 1982) that produces a smoothed approximation $\langle f(\mathbf{r})\rangle$ of $f(\mathbf{r})$:

$$\langle f(\boldsymbol{r})\rangle = \int_{\Omega} f(\boldsymbol{r}')W(|\boldsymbol{r}-\boldsymbol{r}'|,h)d\boldsymbol{r}'. \tag{5.2}$$

For the sake of simplicity we drop the angular brackets denoting the approximation in the following. The kernel $W(|\boldsymbol{r}-\boldsymbol{r}'|,h)$ satisfies the normalization condition

$$\int_{\Omega} W(|\boldsymbol{r}-\boldsymbol{r}'|,h)d\boldsymbol{r}' = 1 \tag{5.3}$$

and has a compact support h such that $W(r,h) = 0$ for $r > h$. In the generalized limit of $h \to 0$, the following condition is satisfied:

$$\lim_{h\to 0} W(|\boldsymbol{r} - \boldsymbol{r}'|,h) = \delta(\boldsymbol{r} - \boldsymbol{r}'). \tag{5.4}$$

We use a fourth-order weighting function W (TARTAKOVSKY & MEAKIN, 2005a):

$$W(|\boldsymbol{r}|,h) = \alpha_k \begin{cases} (3q)^5 - 6\,(2q)^5 + 15\,(1q)^5 & 0 \le |\boldsymbol{r}| < \frac{1}{3}\ h \\ (3q)^5 - 6\,(2q)^5 & \frac{1}{3}h \le |\boldsymbol{r}| < \frac{2}{3}\ h \\ (3q)^5 & \frac{2}{3}h \le |\boldsymbol{r}| < \quad h \\ 0 & |\boldsymbol{r}| > \quad h, \end{cases} \tag{5.5}$$

where $\alpha_k = 81/(359\pi h^3)$ and $q = 1 - 3|\boldsymbol{r}|/(qh)$. Eq. (6.10) can be approximated as

$$f(\boldsymbol{r}) = \sum_{j=1}^{N} f(\boldsymbol{r}_j) W(|\boldsymbol{r} - \boldsymbol{r}_j|,h) \Delta V_j, \tag{5.6}$$

where the domain space is discretized with a set of N particles. If $f(\mathbf{r})$ is a scalar or vector property of a fluid (e.g. fluid density or velocity), then we replace the finite volume ΔV_j by m_j/ρ_j (m_j and ρ_j are the mass and mass density of a fluid carried by particle j) and obtain a general SPH approximation for f and its gradient in terms of the values f at points $\boldsymbol{r_j}$, $f_j = f(\boldsymbol{r_j})$,

$$f(\boldsymbol{r}) = \sum_{j=1}^{N} m_j \frac{f_j}{\rho_j} W(|\boldsymbol{r} - \boldsymbol{r}_j|,h), \tag{5.7}$$

and

$$\boldsymbol{\nabla} f(\boldsymbol{r}) = \sum_{j=1}^{N} m_j \frac{f_j}{\rho_j} \boldsymbol{\nabla} W(|\boldsymbol{r} - \boldsymbol{r}_j|,h), \tag{5.8}$$

where $\nabla W(|\boldsymbol{r} - \boldsymbol{r}_j|,h)$ is computed analytically. Flow of each fluid phase is governed by the continuity equation,

$$\frac{d\rho}{dt} = -\rho\,(\nabla \cdot \mathrm{v}) \tag{5.9}$$

and the momentum conservation equation

$$\frac{d\boldsymbol{v}}{dt} = -\frac{1}{\rho}\nabla P + \frac{\mu}{\rho}\nabla^2\boldsymbol{v} + \boldsymbol{g}, \tag{5.10}$$

subject to the Young-Laplace boundary conditions at the fluid-fluid interface

$$(P_n - P_w)\mathbf{n} = (\boldsymbol{\tau}_n - \boldsymbol{\tau}_w)\cdot\mathbf{n} + S\sigma\mathbf{n} \tag{5.11}$$

and, under static conditions, the Young equation at the fluid-fluid-solid interface,

$$T_{nw}\cos\theta_0 + T_{sw} = T_{sn}, \tag{5.12}$$

where $\boldsymbol{v}$ is the velocity, $\boldsymbol{\tau} = \left[\mu(\nabla\mathbf{v} + \nabla\mathbf{v}^{\mathrm{T}})\right]$ is the viscous stress tensor, ρ is the density, μ is the viscosity, and P is the pressure of the corresponding fluid phase. The subscripts n and w denote the non-wetting and wetting phases, correspondingly; S is the curvature of the interface and σ is the surface tension. The normal vector $\mathbf{n}$ is pointed from the non-wetting phase. The coefficients T_{nw}, T_{sw}, and T_{sn} are the specific interfacial energy between non-wetting, wetting and solid phases. The static contact angle θ_0 is a constant parameter for a given fluid-fluid-solid system. Under dynamic conditions, approximate models, such as creeping flow and lubrication flow (Huh & Scriven, 1971), and phenomenological models (de Gennes, 1985; Tanner, 1979) are used to relate the contact angle to local velocities or stresses. Using Eqs. (5.7) and (6.15), the Navier-Stokes Eqs. (6.1) and (6.2) subject to the boundary conditions (5.11) and (5.12) can be discretized as (Gingold & Monaghan, 1982; Morris, 1997; Tartakovsky & Meakin,

2005b):

$$\frac{d\boldsymbol{v}_i}{dt} = -\sum_{j=1}^{N} m_j \left(\frac{P_j}{\rho_j^2} + \frac{P_i}{\rho_i^2}\right) \frac{\mathbf{r}_{ij}}{r_{ij}} \frac{dW(r_{ij},h)}{dr_{ij}} + 2\mu \sum_{j=1}^{N} m_j \frac{\boldsymbol{v}_{ij}}{\rho_i \rho_j r_{ij}} \frac{dW(r_{ij},h)}{dr_{ij}} + \boldsymbol{g}_{sph} + \frac{1}{m_i} \sum_{j=1}^{N} \boldsymbol{F}_{ij}, \tag{5.13}$$

and

$$\frac{d\boldsymbol{r}_i}{dt} = \boldsymbol{v}_i, \tag{5.14}$$

where $\boldsymbol{v}_i$ is the particle velocity, t is the time, P_i and μ are the fluid pressure and viscosity at $\boldsymbol{r}_i$, $r_{ij} = |\boldsymbol{r}_{ij}|$, $\boldsymbol{r}_{ij} = \boldsymbol{r}_i - \boldsymbol{r}_j$, and $\boldsymbol{v}_{ij} = \boldsymbol{v}_i - \boldsymbol{v}_j$. For computational efficiency we set h and the mass of the SPH particles m_i to unity. A common link-list approach with an underlying square-lattice of size h is used to rapidly locate all particles within the interaction range h. All variables in the SPH model are given in consistent model units. Particle-particle interaction forces $\boldsymbol{F}_{ij}$ are added to the SPH momentum conservation equations to generate surface tension (Tartakovsky & Meakin, 2005b). The exact form of this force is not very important as long as it is anti-symmetric and short range repulsive, long range attractive, and is zero for a distance between particles i and j greater than h. In this work we construct $\boldsymbol{F}_{ij}$ following Liu et al. (2006) who employed this type of interaction force in DPD models. The function consists of two superposed kernel functions $W_1(r_{ij}) = W(r_{ij},h_1)$ and $W_2(r_{ij}) = W(r_{ij},h_2)$,

$$\boldsymbol{F}_{ij} = \begin{cases} s\left(AW_1(r_{ij},h_1)\frac{\boldsymbol{r}_{ij}}{r_{ij}} + BW_2(r_{ij},h_2)\frac{\boldsymbol{r}_{ij}}{r_{ij}}\right) & r_{ij} \le h \\ 0 & r_{ij} > h, \end{cases} \tag{5.15}$$

where $A = 2.0$, $h_1 = 0.8$, $B = -1.0$ and $h_2 = 1.0$. The resulting force is smooth and continuous with short-range repulsive and long-range attractive parts as seen in Fig. 5.1. The parameter s controls the interaction

strength and has values s_{sf} (solid-fluid) and s_{ff} (fluid-fluid). Other forms of the interaction force have been used for example by TARTAKOVSKY & MEAKIN (2005b) who employed a cosine function. Regardless of the specific form of $\boldsymbol{F}_{ij}$, the combined effect of the pair-wise forces on any particle away from the fluid/fluid interface is near zero. $\boldsymbol{F}_{ij}$ generates a total force acting on particles in the direction normal to the interface. In such, the SPH model is similar to the Continuous Surface Force method (BRACKBILL et al., 1992) for solving the Navier-Stokes equations subject to the Young-Laplace boundary condition at the fluid-fluid interface. The density ρ can be obtained from the general field approximation (Eq. 5.7) with $f_j = \rho_j$ as,

$$\rho_i = \sum_{j=1}^{N} m_j W(\boldsymbol{r}_i - \boldsymbol{r}_j, h). \tag{5.16}$$

The system of SPH equations is finally closed by a van der Waals equation

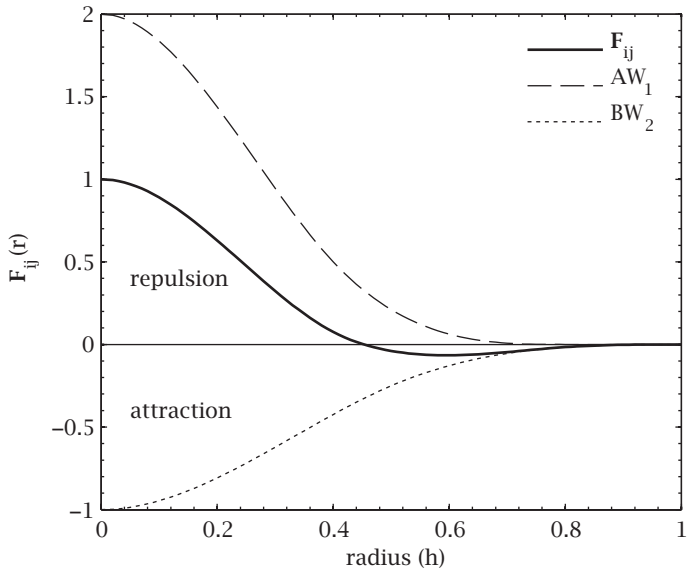

FIG. 5.1. The interaction potential consists of two superimposed cubic spline functions W_1 and W_2 with parameters A and B following LIU et al. (2006).

of state:

$$P = \frac{\rho(k_b T/m)}{1-\rho(b/m)} - \frac{a}{m}\rho^2, \tag{5.17}$$

where k_b is the Boltzmann constant, m is the mass of an SPH particle, T is the temperature and a and b are the van der Waals constants. Values for the constants are $k_b T = 1.6$, $a = 3.0$ and $b = 1/3$. The SPH Eqs. (6.17) and (6.20) are integrated using a "velocity-Verlet" time stepping algorithm (ALLEN & TILDESLEY, 1989):

$$\boldsymbol{r}_i(t+\Delta t) = \boldsymbol{r}_i(t) + \Delta t \boldsymbol{v}_i(t) + 0.5\Delta t^2 \boldsymbol{a}_i(t) \tag{5.18}$$

$$\boldsymbol{v}_i(t+\Delta t) = \boldsymbol{v}_i(t) + 0.5\Delta t \left[\boldsymbol{a}_i(t) + \boldsymbol{a}_i(t+\Delta t)\right]. \tag{5.19}$$

At each time step the density is evaluated using Eq. (6.16), the pressure is obtained from Eq. (6.21) and finally the acceleration is calculated from Eq. (6.17). Stability of the solution is ensured by the following time step constraints (TARTAKOVSKY & MEAKIN, 2005b):

$$\Delta t \leq 0.25 \min_i \left(\frac{h}{3|\boldsymbol{v}_i|}\right) \tag{5.20}$$

$$\Delta t \leq 0.25 \min_i \left(\sqrt{\frac{h}{3|\boldsymbol{a}_i|}}\right) \tag{5.21}$$

$$\Delta t \leq \min_i \left(\frac{\rho_i h^2}{9\mu}\right), \tag{5.22}$$

where $|\cdot|$ is the magnitude of a vector. The model is initialized by placing particles randomly inside the simulation domain until the desired number density is reached. The random particle positions may lead to spurious velocities and noisy results. To avoid this, the model is equilibrated by evolving particle positions according to Eqs. (6.30 – 6.33) with $s_{ij} = 0$ and $\boldsymbol{g}_{sph} = 0$, subject to periodic boundary conditions. A higher viscosity is used at this step for (dissipative) viscous forces to quickly dampen velocity fluctuations. In this study, we assume that the flow of the liquid phase is not affected by the gas phase and solve the Navier-Stokes equations for the

liquid phase only (i.e., SPH particles are only used to discretize liquid and solid phases). Here we model droplet flow on inclined solid surfaces that form an angle α with the horizontal direction. To simplify the implementation of the SPH model, without loss of generality, we assume that the solid surface is horizontal and the body force acts at the angle $90^\circ - \alpha$ to the horizontal direction:

$$\boldsymbol{g}_{sph} = g \begin{pmatrix} cos\left(90^\circ - \alpha\frac{\pi}{180^\circ}\right) \\ 0 \\ -sin\left(90^\circ - \alpha\frac{\pi}{180^\circ}\right) \end{pmatrix}. \tag{5.23}$$

The final model setup consists of identifying liquid and boundary particles and removing particles from the gas phase. The summations in Eqs. (6.17) and (6.16) are over both liquid and boundary particles within the distance h from particle i. We assign the fluid viscosity to boundary particles, with the velocity of the boundary particles being zero. The viscous interaction between liquid and boundary particles generate no-slip boundary conditions and the repulsive components of the $\boldsymbol{F}_{ij}$ force and the force resulting from the discretization of the pressure gradient produce the no-flow boundary condition. It should be noted that solid surfaces are not shown in some figures for reasons of clarity.

5.3 Model Calibration

5.3.1 Surface Tension

In our SPH model surface tension is not prescribed explicitly. It arises from the particle interaction forces and, for given A, B, h_1 and h_2, the surface tension depends on s_{ff}. Here we set the fluid-fluid interaction parameter to $s_{ff} = 0.05$. A liquid droplet in a gas phase is simulated in zero gravity and the surface tension is obtained from the Young-Laplace law:

$$\sigma_{sph} = \frac{R_{eq}}{2}\Delta P, \tag{5.24}$$

where R_{eq} is the droplet radius and ΔP is a difference in pressure inside and outside of the droplet. Since we do not explicitly model the air phase, the pressure outside of the bubble is zero and ΔP is equal to the liquid pressure $\overline{P}$ inside the bubble. It should be noted that the employed EOS results in attractive and repulsive forces (these forces are combined in the first term on the right-hand-side of Eq. (6.17), TARTAKOVSKY et al., 2009a), but for problems with free-surfaces the attractive forces are not strong enough to generate surface tension (e.g. to form stable fluid bubbles). The addition of the $\boldsymbol{F}_{ij}$ forces is needed to create surface tension, which generates additional pressure. A total fluid pressure within a volume V_r with radius r_v can be found from the virial theorem as shown by TARTAKOVSKY & MEAKIN (2005b) and ALLEN & TILDESLEY (1989):

$$\overline{P} = \frac{1}{2dV_r} \sum_i \sum_j \boldsymbol{r}_{ij} \boldsymbol{f}_{ij} = \frac{1}{8r_v^3} \sum_i \sum_j \boldsymbol{r}_{ij} \boldsymbol{f}_{ij}, \tag{5.25}$$

where $d = 3$ in a three-dimensional system and $\boldsymbol{f}_{ij} = m_i d\boldsymbol{v}_i/dt$. In the double summations, the first summation is over all particles within distance r_v from the center of the droplet. The second summation is over all SPH particles. Since the range of the forces $\mathbf{f}_{ij}$ is equal to h, only particles within the distance $r_v + h$ should be considered in the second summation. To exclude the boundary effect, we set $r_v = R_{eq} - h$. Droplets are equilibrated using a higher viscosity such that droplet oscillations are quickly dampened and $\overline{P}$ can be determined. As the contribution of the viscous force to $\boldsymbol{f}_{ij}$ is zero at equilibrium conditions the resulting pressure $\overline{P}$ is independent of viscous forces and, hence, the prescribed model viscosity. Surface tension obtained from the simulations of droplets of different sizes is nearly constant as can be seen in Fig. 5.2. However, if droplet radii are close to h, our results deviate slightly from the Young-Laplace law due to an insufficient numerical resolution. All simulations shown in this paper use an interaction force of $s_{ff} = 0.05$ which yields a surface tension of $\sigma_{sph} = 0.25$ (in SPH model units) that was calculated as a half of the slope of the linear part of the curve in Fig. 5.2.

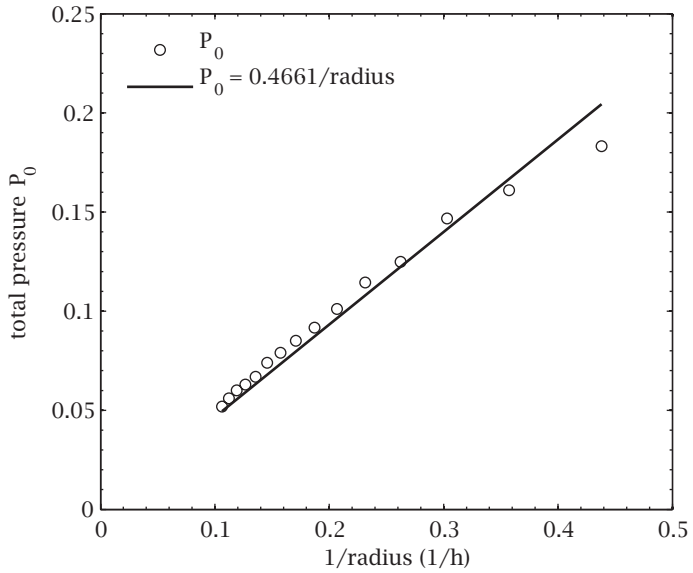

FIG. 5.2. Surface tension and pressure for various droplet sizes, $\boldsymbol{g}_{sph} = 0$, $s_{ff} = 0.05$.

5.3.2 Static Contact Angles

For given A, B, h_1, h_2 and s_{ff}, the contact angle depends on s_{fs}. Here we study numerically the dependance of the static contact angle on s_{fs} and resolution of the SPH model. This is done by simulating the behavior of a droplet that is slowly brought into contact with a flat surface. Under static conditions, this system can be described by the dimensionless Bond number,

$$Bo = \frac{\rho g V^{2/3}}{\sigma}, \tag{5.26}$$

where V is the volume of a droplet. In this study we consider droplets with $Bo = 1$. This corresponds to a water droplet with a volume of $V = 20.86\,\mathrm{m}^3$. In the simulations described in this section, the density has an average value of $\rho_{sph} = 39.2$ in the model units. The characteristic size of the droplet is in the range $V^{2/3} = 8.15 - 88.95\,h^2$, depending on the resolution. The surface tension is set to $\sigma_{sph} = 0.25$. The gravitational acceleration is

adjusted to the change in volume (numerical resolution) in order to keep the Bond number constant and ranges between $\boldsymbol{g}_{sph} = 0.000782 - 0.0000717$. All parameters are given in SPH model units. To study the dependence of the static contact angle on s_{sf}, we discretize the droplet with 20390 particles that corresponds to the characteristic size of the droplet of $V^{2/3} = 60.44\,h^2$. The simulation domain has dimensions of $x = 32\,h$, $y = 32\,h$ and $z = 16\,h$ with a layer of solid particles of thickness $1\,h$. Droplets are initially equilibrated in the absence of gravity. Gravitational acceleration and solid-fluid interaction force are then gradually increased up to the prescribed values of $\boldsymbol{g}_{sph} = 0.0001139$ and $s_{sf} = 0.05$, which corresponds to $Bo = 1.0$. We then decrease the interaction force ($s_{sf} = 0.05, 0.04, ...0.01, 0.005, 0.001$) in order to determine the dependence of the contact angle on s_{sf}. Contact angles are measured "visually" once a stationary state is reached (see Fig. 5.3) by determination of the three-phase contact line and the best fitting tangent (Kwok et al., 1997). As droplets may not be perfectly axisymmetric, two orthogonal cross-sections are extracted and the mean is taken from four measurements (one on each side of a cross-section). We also fitted a third-order polynomial to the particle hull. Knowing the polynomial, the contact angle at the base of the droplet can be determined analytically. This method may be more reproducible, though depending on the discretization, it may lead to high deviations as surfaces are not perfectly smooth due to their particle nature. In order to investigate the influence of the resolution on the static contact angle we use nine droplet radii ranging from $R_{eq} = 1.77\,h$ (902 particles) to $R_{eq} = 5.85\,h$ (77993 particles) while keeping

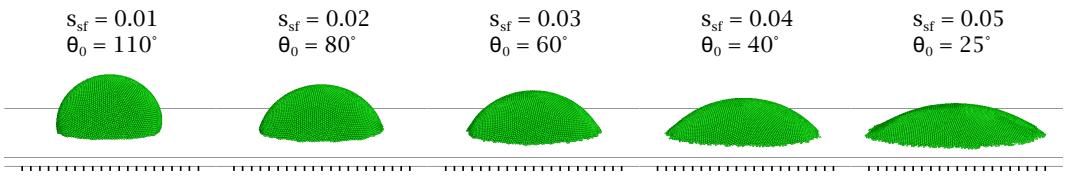

FIG. 5.3. Static contact angles for different fluid-solid interactions strengths s_{sf}. Shown droplets have an equilibrated radius of $R_{eq} = 5.85$ h and $Bo = 1.0$. Tick marks have 1 h spacing.

the Bond number constant at $Bo = 1.0$. Figure 5.4 shows the resulting static contact angles for each droplet discretization and all fluid-solid interaction forces. Contact angles of droplets with higher resolution are closer to the mean values, however, as there is no systematic deviation from the mean at lower resolutions we conclude that the scatter of data is only a result of the measurement and not of numerical origin. Figure 5.5 shows the static contact angles for each strength of the interaction force s_{sf} and the standard deviation. Simulations are restricted to static contact angles between about 110° and 25° corresponding to $s_{sf} = 0.01$ and $s_{sf} = 0.05$.

It should be noted that for very high values of the solid-fluid interaction force ($s_{sf} > 0.05$, i.e., very low contact angles) the droplet wedges may not be adequately resolved depending on the chosen discretization leading to an improper macroscopic appearance of contact angles.

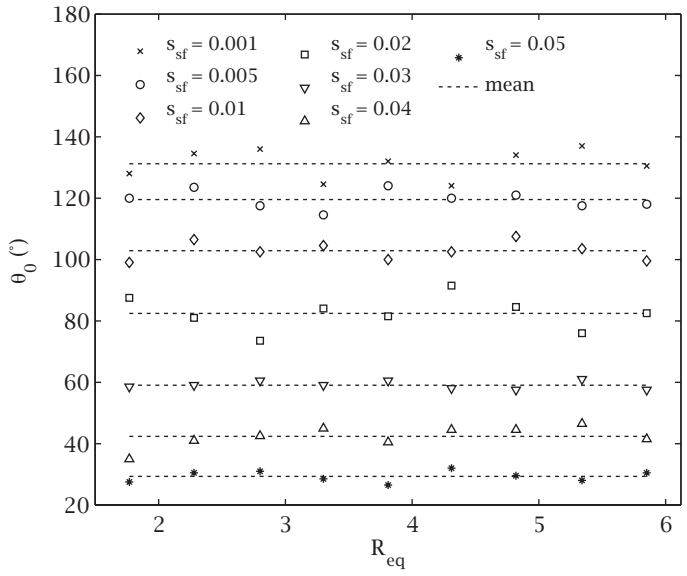

FIG. 5.4. Static contact angles for different droplet resolutions and their mean values.

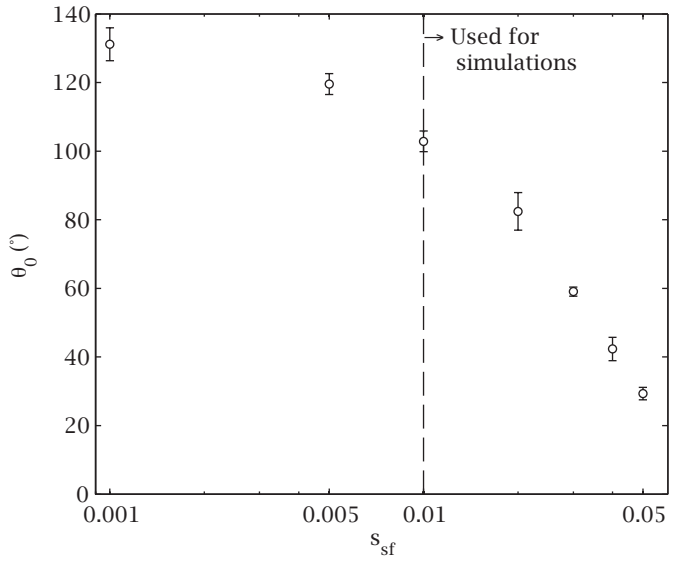

FIG. 5.5. Mean static contact angles for varying interaction force s_{sf} and standard deviation. $Bo = 1.0$ for all radii.

5.4 Verification of Droplet Flow on Dry Surfaces

Transient droplet dynamics on surfaces have been investigated by numerous authors using laboratory experiments (BIKERMAN, 1950; ELSHERBINI & JACOBI, 2004; ELSHERBINI & JACOBI, 2006; FURMIDGE, 1962; PODGORSKI et al., 2001), theoretical methods (DUSSAN & CHOW, 1983; LE GRAND et al., 2005), and numerical models (HUANG et al., 2009; JIANG et al., 2010; MOGNETTI et al., 2010). In the following, we show that our model agrees with empirical and semi-analytical solutions and thus can be consistently calibrated for a wide range of fluid-substrate configurations.

5.4.1 Critical Contact Angles

Here we investigate droplets in a critical state, i.e., at the onset of a sliding motion on an inclined plate. Under dynamic conditions, two contact angles can be identified: the advancing contact angle θ_A, the contact angle at the drop front perpendicular to the direction of motion; and the receding contact angle θ_R, the contact angle at the drop's rear. The dynamic contact angles at a critical state have been studied by, amongst others, ELSHERBINI

& JACOBI (2004) and ELSHERBINI & JACOBI (2006). Their results suggest that droplets on the verge of sliding exhibit a general relation between contact angles and Bond number independent of the static contact angle. ELSHERBINI & JACOBI (2004) examined the dynamic contact angles around the perimeter of the drop and showed that at the critical state the maximum angle θ_{max} is equal to the advancing contact angle ($\theta_{max} \approx \theta_A$) and the minimum angle θ_{min} is equal to the receding contact angle ($\theta_{min} \approx \theta_R$) for all investigated fluid-substrate combinations and Bond numbers ranging from 0.0 to 3.0. These findings are in accordance with results of MACDOUGALL & OCKRENT (1942) and TSUKADA et al. (1982). Here the Bond number is defined as

$$Bo' = \frac{\rho g (2R)^2}{\sigma} \sin(\alpha), \tag{5.27}$$

where α is the inclination angle of the surface measured from the horizontal. Based on laboratory experiments ELSHERBINI & JACOBI (2004) and ELSHERBINI & JACOBI (2006) proposed a general non-linear (quadratic) relation between $\theta_{min}/\theta_{max}$ and Bo':

$$\frac{\theta_{min}}{\theta_{max}} = 0.01 Bo'^2 - 0.155 Bo' + 0.97. \tag{5.28}$$

For the numerical experiment we use several fluid-substrate configurations by varying static contact angles. This is done by varying s_{sf} from 0.0 to 0.05. In these simulations, the drop sizes range from $R_{eq} = 1.77$ to 5.85, resulting in $Bo' = 0.14 - 2.8$. Gravitational acceleration is set to $\boldsymbol{g}_{sph} = 0.000164$, average density is $\rho_{sph} = 39.2$ and surface tension $\sigma_{sph} = 0.25$. Similar to the determination of static contact angles, the droplets are equilibrated by setting $\boldsymbol{g}_{sph} = 0.0$ and then slowly placed on a horizontal surface by increasing the gravitational acceleration. When the height of the droplets becomes constant (the droplets reached an equilibrium on a flat surface), we start increasing the surface inclination by one degree every 150 time steps giving the drop enough time to adjust. The receding and advancing contact angle are measured when droplet movement of the receding and advancing

contact line sets on, i.e., at the critical state. Figure 5.6 shows a droplet with radius $R_{eq} = 4.82\,h$ and four different static contact angles between 60° and 110° (s_{sf} = 0.01,0.02,0.025,0.03) in its critical state. Our results are in a good agreement with the findings of ELSHERBINI & JACOBI (2004) as shown in Fig. 5.7. Most of our numerical results are within the margin of error of the experimental measurements in ELSHERBINI & JACOBI (2004). A slight deviation can be observed for very high Bond numbers above 2.0. We believe that this may be a result of: (1) the error introduced when measuring the contact angles in our simulations; and (2) an insufficient discretization of the droplet wedges at low contact angles (i.e., high solid-fluid interaction forces) that are necessary to achieve a critical state at such high inclination angles (i.e., Bond numbers).

5.4.2 Dimensionless Scaling

Transient droplet flow on subhorizontal surfaces can be extremely complex. However, as shown by PODGORSKI et al. (2001) a general scaling law can be applied in order to quantify droplet flow dynamics within a certain range of conditions. Based on laboratory experiments using silicon oils and deion-

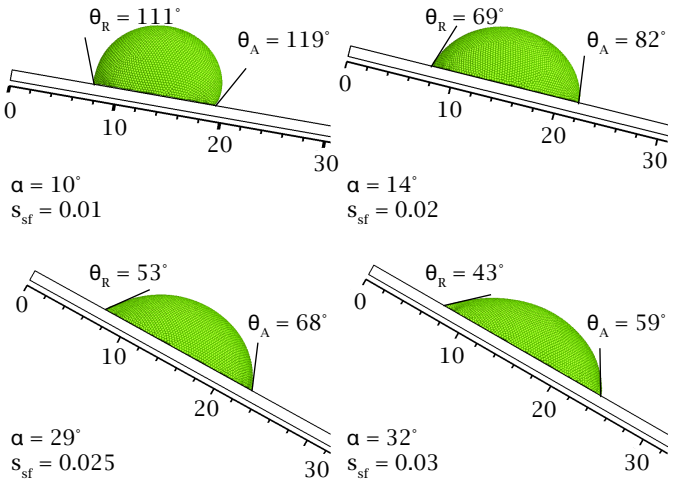

FIG. 5.6. Advancing and receding contact angles for droplets in a critical state. All shown droplets have the same equilibrated radius of 4.82 h (Bo = 1.02) and static contact angles between 60° and 110°.

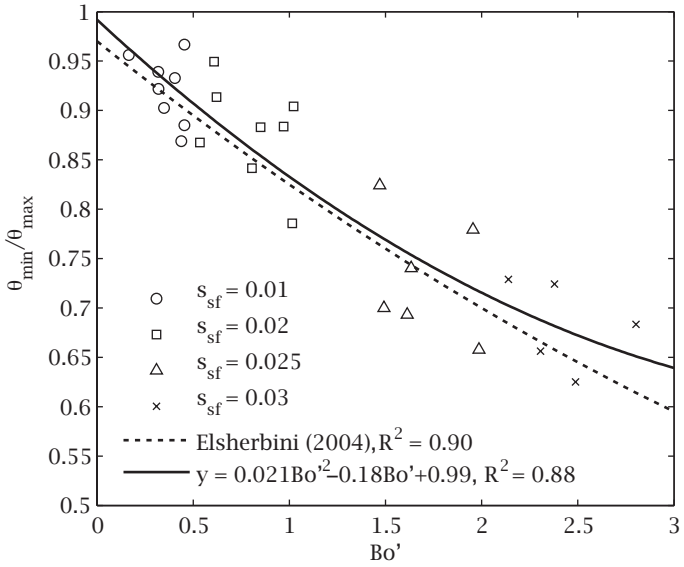

FIG. 5.7. $\theta_{min}/\theta_{max}$ ratios for Bond numbers between 0.0 and 3.0 and several fluid-solid interaction strengths s_{sf}. Note that Bo' is defined according to Eq. (5.27). Contact angle measurement are estimated to yield an error of $\pm 5°$.

ized water as well as several substrates, PODGORSKI et al. (2001) proposed a linear scaling law that relies on a force balance:

$$Ca \sim Bo \sin(\alpha) - \Delta_\theta, \tag{5.29}$$

where the capillary number is defined as

$$Ca = \mu v / \sigma, \tag{5.30}$$

with v being the droplet velocity, α is the surface inclination angle measured from the horizontal and Δ_θ is a perimeter-averaged projection factor of the surface tension. In order to apply the scaling to various static contact angles in our numerical experiments, we follow GHEZZEHEI (2004) to define a proportionality constant γ such that Eq. (5.29) becomes

$$Ca = \gamma\, Bo \sin(\alpha) - \Delta_\theta \tag{5.31}$$

and γ and Δ_θ can be determined as empirical constants unique for a given static contact angle. The model domain used for transient droplet flow has dimensions $x = 128\,h$, $y = 64\,h$ and $z = 16\,h$ which corresponds to $(45.7 \times 22.8 \times 5.7)\,\mathrm{mm}^3$ in SI units. Periodic boundary conditions are used in the x- and y-directions. The model is set up analogous to a typical laboratory experiment for measurements of contact angles. After a droplet equilibrates on a surface with prescribed inclination for the desired interaction force ($s_{sf} = 0.01, 0.02 ... 0.05$), gravitational acceleration is gradually increased until the prescribed value of $\boldsymbol{g}_{sph} = 0.0001139$ is reached. Bond number in the simulations range from 0.14 to 1.5, with the droplet radii ranging between $1.77\,h$ and $5.85\,h$ or 0.63 and 2.09 mm. Surface inclinations are held constant throughout each simulation at angles ranging from 10 to 90° measured from the horizontal. This yields a total of 81 $Bo \cdot sin(\alpha)$ values for every static contact angle θ_0. In addition we also use three different values for the viscosity ($\mu_{sph} = 0.01, 0.03, 0.1$) to cover a feasible range of Reynolds numbers observed in water-rock systems. Depending on the contact angle, obtained Reynolds numbers range from $Re = 302 - 3908$ for $\mu = 0.01$, $Re = 67 - 1299$ for $\mu = 0.03$, and $Re = 15 - 387$ for $\mu = 0.1$. Droplet bulk velocities are measured as soon as the maximum velocity is reached. We track the droplet front position and evaluate $\Delta x / \Delta t$ where Δt is a time interval long enough to average out fluctuations in particles positions that may occur at the droplet front due to the dynamic wetting process. This behavior can be observed at low Bond numbers when body forces only partially exceed drag forces due to the slightly non-homogeneous density distribution of the wall particles. Figure 5.8 shows simulation results for two different droplet sizes $R_{eq} = 2.8\,h$ and $4.82\,h$ ($Bo = 0.34, 1.02$) at the same time for several viscosities, static contact angles at an inclination angle of $\alpha = 90°$. Note that the maximum velocity of some droplets at very low capillary numbers (e.g. for $s_{sf} = 0.01$, $\theta_0 = 110°$) occurs after crossing the x-direction periodic boundary. The shown simulation snapshots are taken before the droplets crossed the boundary and droplet shapes are mainly round or slightly cornered at this (early) time such that the force balance assumptions of PODGORSKI et al. (2001) are correct. However, de-

pending on capillary and Bond number, the scaling law is applied only to fully accelerated droplets, which show several effects that have to be considered for the interpretation of the results. As noted by PODGORSKI et al. (2001) the linear scaling fails above a certain capillary number in the pearling regime when droplets develop strong tails and emit smaller static droplets via a Rayleigh-like instability. Subsequent droplets that absorb such emitted droplets may experience a drag reduction when the emitted droplet size is big enough. Consequently, γ values determined in the laboratory experiment are slightly higher in this regime and cannot be determined independent of droplet size (i.e., Bond number). Furthermore, the scaling can only be applied to droplets with a radius smaller or on the order of the capillary length λ_c of the fluid, where

$$\lambda_c = \sqrt{\frac{\sigma}{\rho g}}, \tag{5.32}$$

which assumes values of $R = 56\,h$ (2.75 mm at average subsurface temperatures of 10 °C). For droplets that do not strongly deviate from the rounded or cornered shape, the velocities (or Ca) obtained from the SPH simulations agree with the Podgorski scaling (see Fig. 5.9). However, for hydrophobic surfaces (i.e., $\theta_0 = 110°$) the velocities obtained from the SPH model deviate from the linear scaling predicted by the theory of PODGORSKI et al. (2001). This disagreement can be explained by the fact that a droplet on a non-wetting surface and flowing down with high velocity may develop a rolling behavior that violates the force balance assumptions in the PODGORSKI et al. (2001) theory. We observe top view droplet shapes ranging from round to slightly cornered and strongly elongated for high static contact angles ($s_{sf} = 0.01,0.02$) (see Fig. 5.10). As a result, droplets above a certain Ca value experience a drag increase due to the higher contact area such that γ values (given by a slope of the linear part of the curves in Fig. 5.9) become lower (see for example the upper row, data points above dashed line). Due to the poor linear relationship in this Ca range the scaling depends on the areal extent of the droplet such that no common γ value can be determined

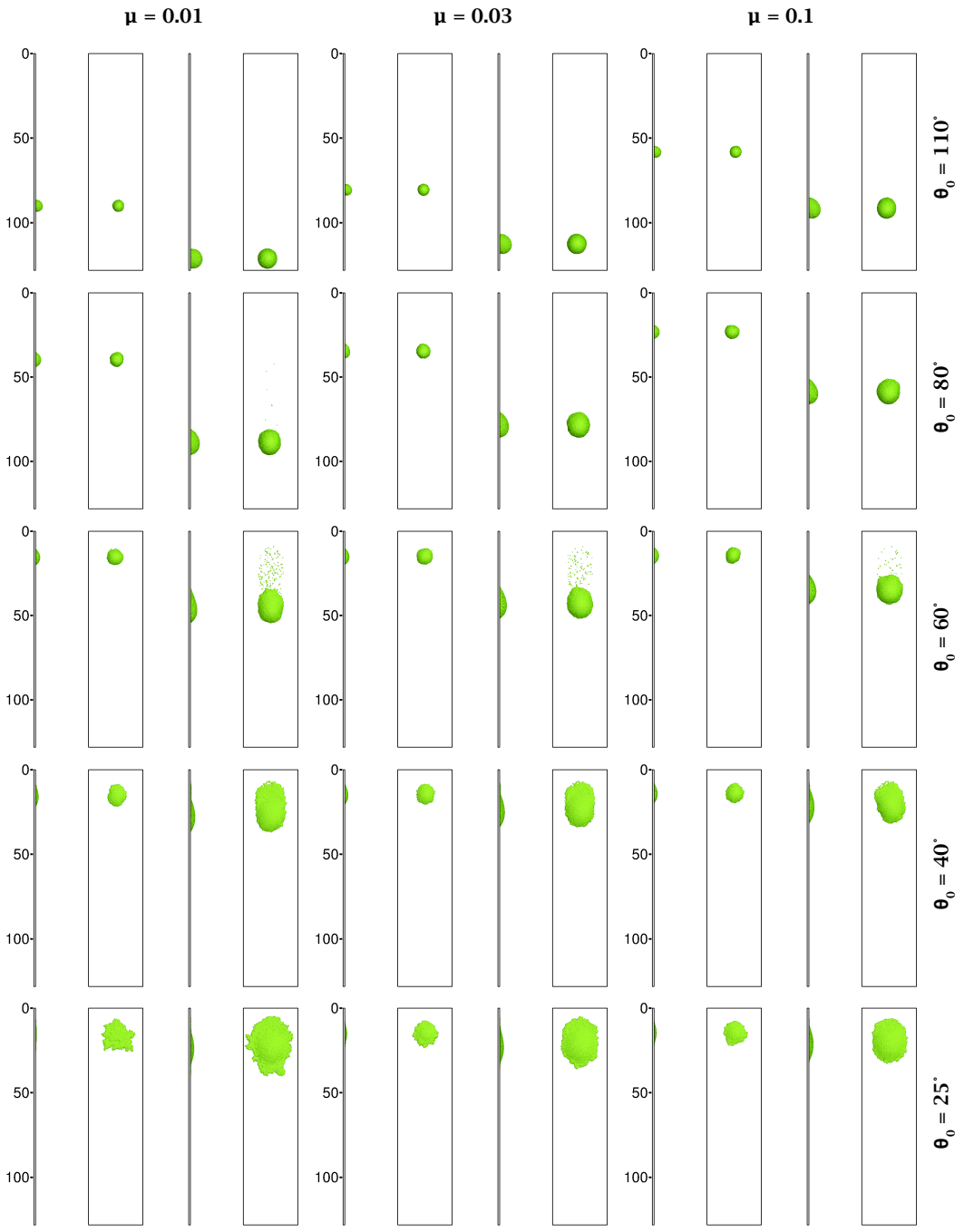

FIG. 5.8. Simulation results for two droplet sizes (R_{eq} = 2.28 h and R_{eq} = 4.82 h) at time step t = 1800 (116.25 ms) for three viscosities μ_{sph} = 0.01,0.03,0.1 and five interaction strengths s_{sf} = 0.01,0.02...0.05 (static contact angles from 25 to 100° at an inclination angle α = 90°. Note that all shown droplets have not yet crossed the mirror boundary at the shown time step. At later time steps faster droplets cross the x-direction mirror boundary several times.

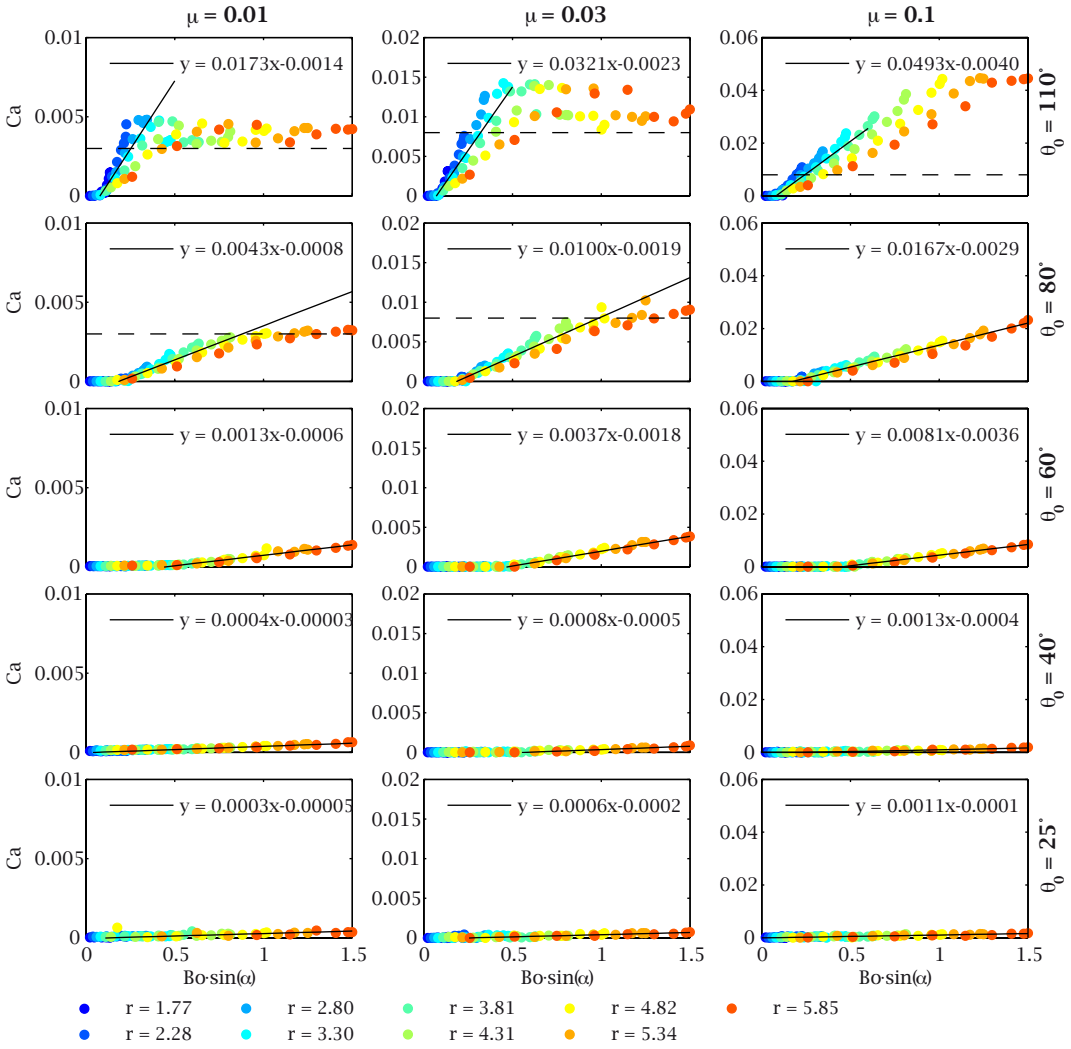

FIG. 5.9. Dimensionless scaling according to PODGORSKI et al. (2001) for three viscosities μ_{sph} = 0.01,0.03,0.1, five interaction strengths s_{sf} = 0.01,0.02...0.05 at several inclination angles α =25 to 100° and nine different droplet sizes (1.77 h and 5.85 h, 0.63 and 2.09 mm). Droplets above the dashed lines show a strong deviation from the rounded or spherical shape such that the linear scaling fails and are not included in the calculation of y and Δ_θ. Below a certain Ca value scaling parameters are partially difficult to determine due to sudden particle fluctuations and droplet front movement caused by strong interactions forces.

for all simulations. For lower static contact angles (s_{sf} = 0.03,0.04,0.05) droplets develop a trailing film of varying thickness which is only poorly developed for intermediate static contact angles (s_{sf} = 0.03, θ_0 = 60°) as can be seen in Fig. 5.11. Within the simulated timespan the change in droplet mass, i.e., the ratio of fluid volume in the film and in the droplet, is negligible such that the force balance of PODGORSKI et al. (2001) can still be applied. However, for longer simulations it is clear that droplet movement will slow down and finally stop when the droplet sizes are below the critical Bond number and the main fluid volume resides in the film. The formation of trailing droplets, as it has been observed by PODGORSKI et al. (2001), is present in our simulations, however, due to their small size (relative to h) the trailing droplets are resolved by only a few SPH particles and most likely do not behave quantitatively correct. Furthermore, the pronounced pearling regime described by PODGORSKI et al. (2001) occurs for Bond numbers above 1.5 (and static contact angles of about 50°), which we do not cover in our simulations. To our knowledge the occurrence of trailing films over such a range of wetting properties has not been quantified in laboratory experiments, therefore the influence of this on droplet flow is shown in the following section.

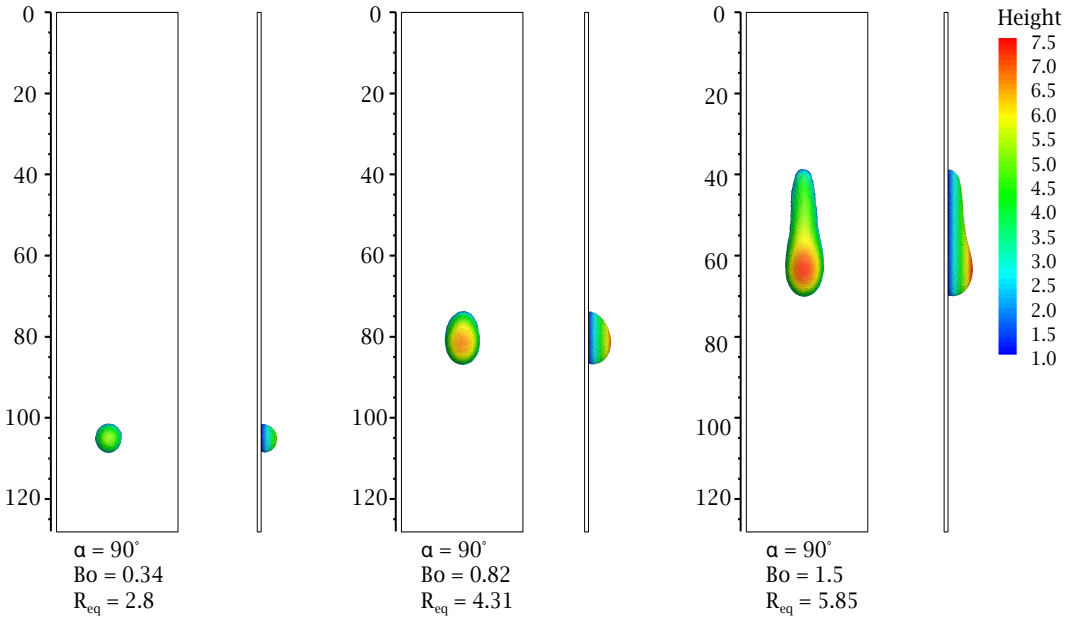

FIG. 5.10. Depending on capillary and Bond number droplet shapes range from round (left) to slightly cornered with a strong elongation (right). Time is $t = 4800$ (0.31 s) with $\mu_{sph} = 0.03$ and $s_{sf} = 0.01$ ($\theta_0 = 110°$).

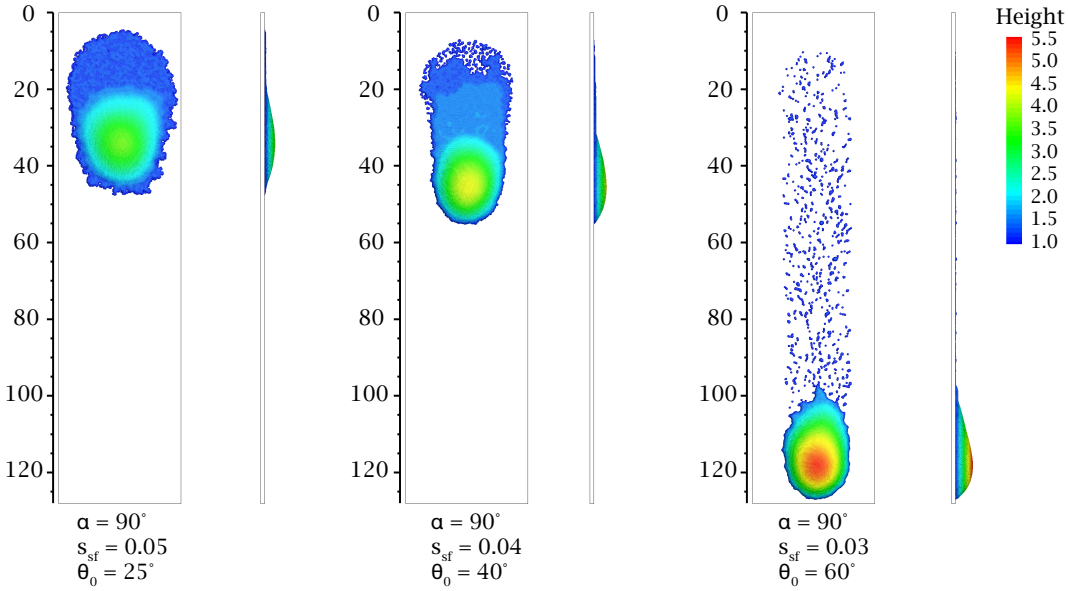

FIG. 5.11. Trailing films of droplets with $s_{sf} = 0.05$, $s_{sf} = 0.04$ and $s_{sf} = 0.03$ (from left to right). μ_{sph} is 0.03 and $t = 4800$ (0.31 s).

5.5 Droplet Flow on Inclined Wet Surfaces

We define a stationary moving droplet as a droplet whose mass and shape does not change as it flows down the surface. In the above section we observed that stationary moving droplets cannot be formed on a dry surface if the static contact angle is small. To study dynamics of stationary moving droplets with low static contact angles, we conduct a second set of simulations using a prewetted surface. The initial surface film thickness is determined by probing the film left behind in the simulations with initially dry conditions in order to find the appropriate average amount of particles. We assume that the thickness of trailing films in our simulations reflects the maximum fluid capacity kept as film for a given fluid-substrate combination and thus acts as a lubrification for droplets by enhancing the dynamic wetting and dewetting at the advancing and receding contact line. Furthermore, a stationary moving droplet develops at a maximum velocity. Even though droplets at intermediate static contact angles ($s_{sf} = 0.03$, $\theta_0 = 60°$) also leave behind partial films, it is impossible to create a prewetted surface as the initial films immediately break up via a Marangoni-like instability for $s_{sf} \leq 0.03$ (see Fig. 5.12). Consequently droplets will coalesce and their volume changes such that the force balance cannot be applied. Therefore we restrict the simulations with prewetted surfaces to static contact angles $\theta_0 = 25°$ and $\theta_0 = 40°$. Figure 5.13 shows droplets at maximum acceleration sliding on the prewetted surface. The film thickness varies between 0.3 and 0.5 h which corresponds to 107 to 178 µm. This is higher than what has been reported for example by Tokunaga & Wan (1997), Tokunaga et al. (2000) (2 to 70 µm) and Dragila & Weisbrod (2003) (0.9 to 40 µm) but of the right order of magnitude. However, as also noted by Tartakovsky & Meakin (2005b), depending on the chosen SPH resolution, simulations may become (1) computationally too expensive in order to cover such length scales and (2) hydrodynamics of thin adsorbed films may not be adequately represented by the Navier-Stokes approximations when chemical potentials dominate flow behavior (Lebeau & Konrad, 2010; Or & Tuller, 2000). Applying the dimensionless scaling to the prewetted simulations yields a

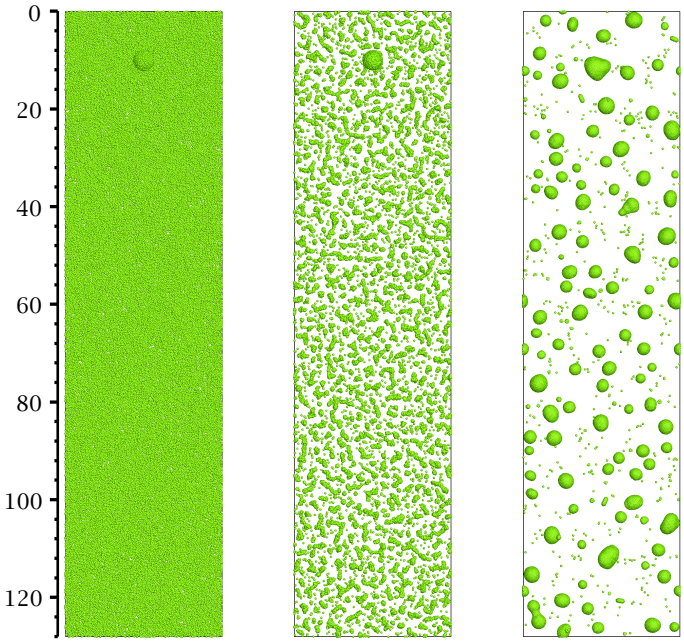

FIG. 5.12. Prewetted surfaces with $s_{sf} \leq 0.03$ exhibit a Marangoni-like breakup of films and are not used in the simulations. Shown example has an interaction force $s_{sf} = 0.01$ with $\mu_{sph} = 0.03$ and t=1, 10, 340 (0.64 ms, 21.9 ms.

general increase of γ values with droplet velocities being nearly tripled for a viscosity of $\mu_{sph} = 0.1$ (see Fig. 5.14). Figure 5.15 gives a comprehensive overview of the scaling parameter and shows that the velocity increase is less pronounced at lower viscosities ($\mu_{sph} = 0.01$,0.03). Partially, this might be caused by droplets still "loosing" SPH particles to the prewetted surface, especially during the initial placement of the droplets when the gravitation is slowly increased. We use only droplets with radii bigger than 4.31 h to determine the scaling, as smaller droplets below the critical Bond number are stuck on the surface but may still display some fluctuating movement induced by interaction with the film. Figure 5.16 shows the resulting maximum Reynolds numbers from our numerical experiments under dry and prewetted surface conditions for all tested static contact angles. Ranges for the occurrence of adsorbed films, which develop under dry surface conditions when droplets leave behind trails, are given as a function of s_{sf} and

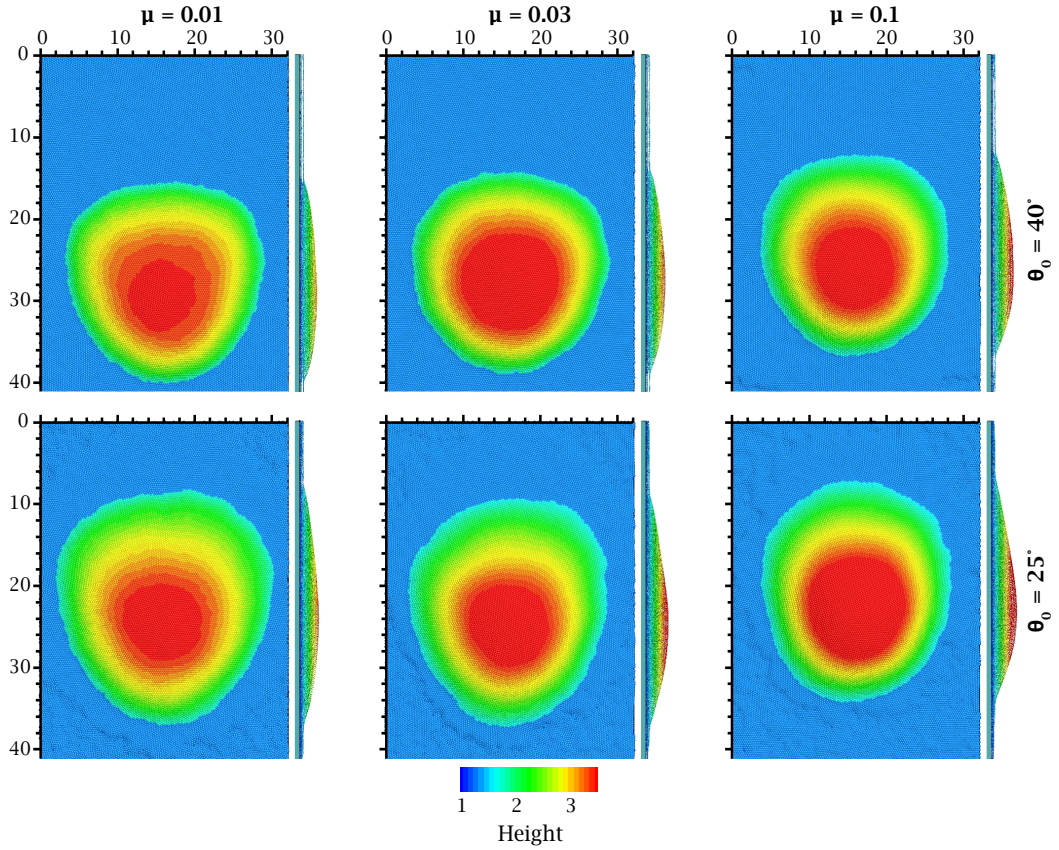

FIG. 5.13. Droplets sliding on a prewetted surface with equilibrated radius R_{eq} = 5.85 h at maximum acceleration (t=2670, 0.17 s). Maximum film thickness is about 0.3 to 0.5 h (107 to 178 µm).

Re where

$$Re = \frac{\rho v V^{(1/3)}}{\mu}. \tag{5.33}$$

In general two flow regimes can be distinguished: (1) droplets without trailing films and (2) droplets with trailing films of varying thickness. The former can be observed over the whole range of the modeled viscosities with a static contact angle of ~110° (s_{sf} = 0.01). At lower static contact angles (between 80° and 60°) only droplets with a viscosity of μ = 0.1, i.e., lower Reynolds numbers, are free of trailing films. Droplets with a static contact

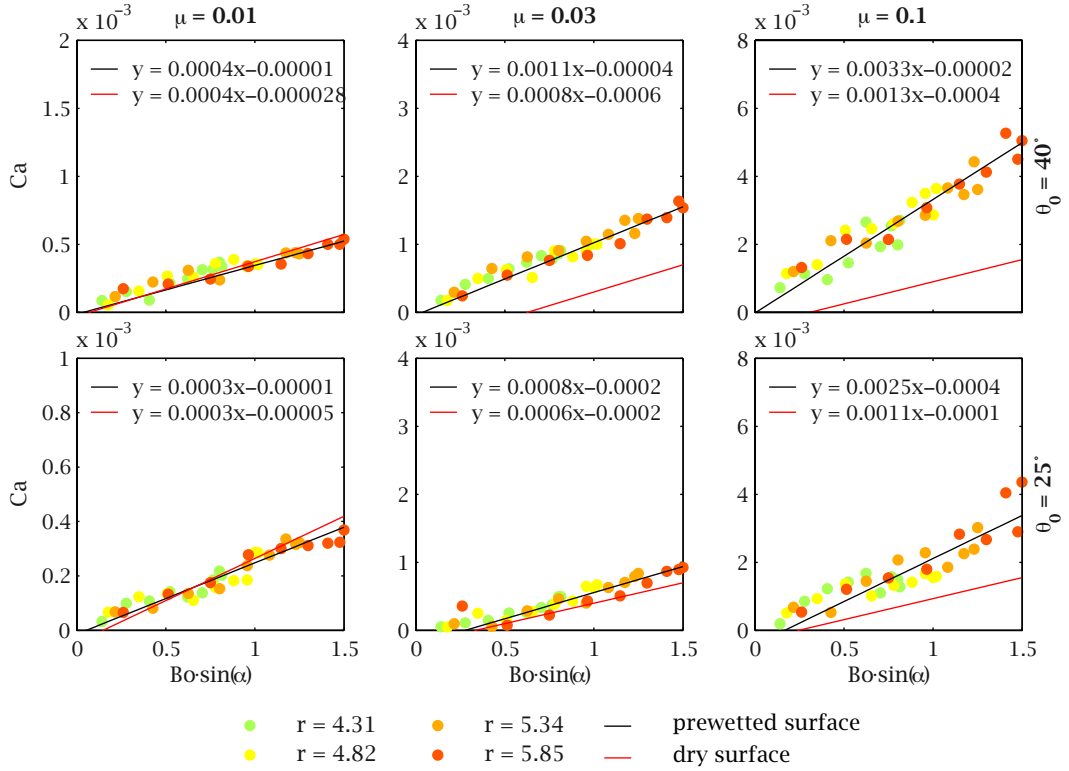

FIG. 5.14. Dimensionless scaling for three viscosities μ_{sph} = 0.01,0.03,0.1 and two interaction strengths s_{sf} = 0.04 and s_{sf} = 0.05 with a prewetted surface. Scaling parameter of the dry surface are shown for comparison. Note that droplets with radius $R_{eq} < 4.31$ h are not moving but exhibit spreading effects and sudden particle fluctuations and are thus not included in the calculation.

angle smaller ~80° (s_{sf} = 0.02) and $\mu \leq 0.03$ all leave trailing films where the film thickness is higher for lower viscosities and/or lower static contact angles. This observation can be attributed to the fact that both lower viscosity and lower static contact angle (corresponds to small ratio s_{ff}/s_{sf}) facilitate the fluid spreading along the surface. The calculated Reynolds numbers and the range of static contact angles are in agreement with the ranges reported in literature. For example, the highest Reynolds number obtained in our simulations is of the same order obtained in a laboratory experiment for a similar microscale system (DRAGILA & WEISBROD, 2004b). Static contact angles reported in experiments range from 23 to 70° (e.g.

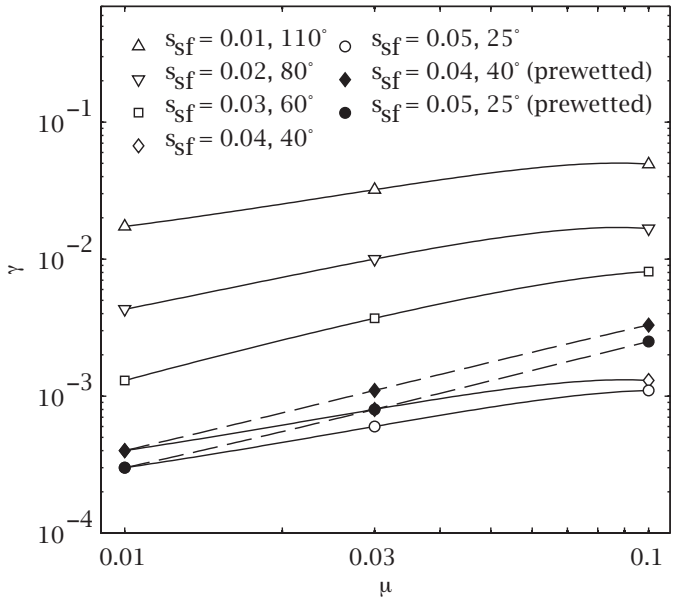

FIG. 5.15. Scaling parameter γ as defined by GHEZZEHEI (2004) vs. viscosity μ_{sph} for all investigated static contact angles under dry and prewetted surface conditions. Droplets on prewetted surfaces display increased velocities by a factor of up to three ($\mu_{sph} = 0.1$).

SOBOLEV et al., 2000; SU et al., 2001; SU et al., 1999; TOKUNAGA & WAN, 2001) and are also within the range of angles produced by our SPH model. Therefore, the presented simulation results give a comprehensive overview of the flow dynamics that could be expected under experimental and most common field conditions.

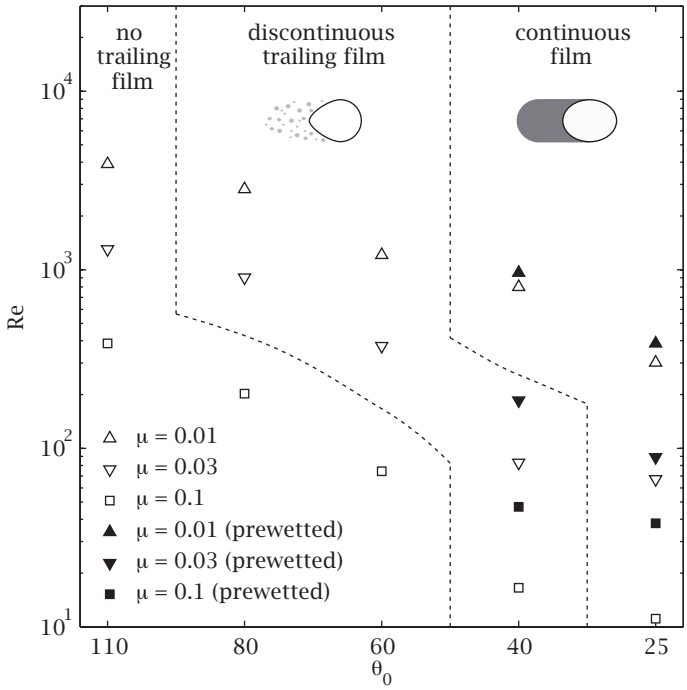

FIG. 5.16. Maximum Reynolds numbers for all investigated static contact angles and viscosities for dry and prewetted surfaces. Trailing films vary in volume and appear more pronounced at higher Reynolds numbers and static contact angles. Regime transitions have been approximated based on simulation data.

5.6 Droplet Flow on Rough Surfaces

Here we study the effect of surface roughness on the droplet flow. The simulation setup now consists of surfaces with a self-affine fractal geometry (MANDELBROT, 1982) described by the Hurst exponent ζ (BOUCHAUD et al., 1990), which has a nearly constant value of about 0.8 ± 0.05 independent of the material (BOUCHAUD, 1997; PONSON et al., 2006). The domain size for the simulations is the same as in section 5.4.2. We employ three surfaces with a Hurst exponent of $\zeta = 0.75,\ 0.50,\ 0.25$ (see Fig. 5.17). The viscosity is set to $\mu = 0.03$ and the droplet radius is 5.85 h. The surface inclination is set to 90° and 45° and solid-fluid interaction forces are $s_{sf} = 0.01, 0.02, 0.03$ (θ_0 =110°, 80°, 60°). Figure 5.18 shows the resulting Reynolds numbers (i.e.,

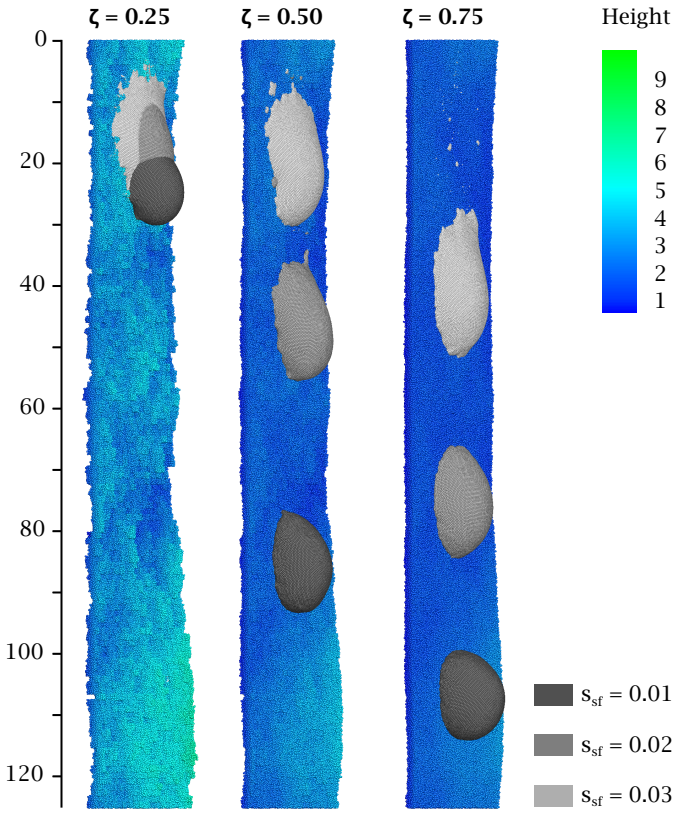

FIG. 5.17. Advancing droplets on rough surfaces with Hurst coefficients ζ = 0.25, 0.5 and 0.75 at time t=2000 (0.13 s). Results are shown for droplets with μ_{sph} = 0.03 and a solid-fluid interaction strength of s_{sf} = 0.01, 0.02 and 0.03. The equilibrium radius of the droplets is R_{eq} = 5.85.

dimensionless velocity) for the surfaces with different roughnesses and the smooth surface. Our results shows that surface roughnes decreases the velocity of droplets. For $\theta_0 = 110^\circ$ and 80° we observe the velocity decrease between 33 % and 37 %for a roughness coefficient $\zeta = 0.75$ in comparison with the smooth surface. These results are independent of the surface inclination. For $\theta_0 = 60^\circ$, the velocity decreases by as much as 80 % for an inclination angle of 90° and 98 % for in inclination angle of 45°. For lower Hurst exponents, i.e., "rougher" surfaces, droplets with static contact angle of 60° barely move, while for higher contact angles the velocity is almost linearly proportional to ζ, i.e., the velocity decreases linearly with decreasing

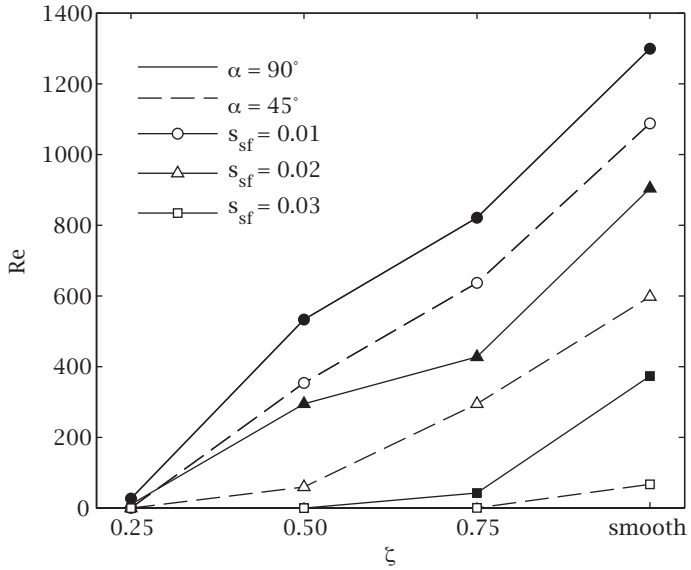

FIG. 5.18. Reynolds numbers for three roughness coefficients, three static contact angles (110°, 80°, 60°) and two inclination angles.

Hurst exponent. Our simulations suggest that, for low contact angles, little pits and depressions created by the roughness cause an additional capillary suction which prevents the movement of droplets.

5.7 Conclusion

We employed a three-dimensional multiphase SPH model to simulate gravity-driven free-surface flow dominated by the effects of surface tension. The model uses pair-wise interaction forces to represent fluid-fluid and fluid-solid interactions and allows modeling a wide range of wetting conditions. Various flow conditions have been investigated and the model ability to simulate (1) wetting and non-wetting droplet flow on dry surfaces and (2) flow on surfaces prewetted with adsorbed films has been demonstrated. Static contact angles of sessile droplets are shown to be independent of the chosen resolution, i.e., computation time can be saved while still preserving physically correct model behavior. The dynamic contact angle hysteresis for droplets at the verge of movement, i.e., at the critical state, matches empirical experiments of ElSherbini & Jacobi (2004). Droplets with higher

Bond numbers (that is, low static contact angles and higher inclination angles at a critical state) exhibit a slightly higher $\theta_{min}/\theta_{max}$ ratio which is believed to be a result of an insufficient resolution of droplet wedges. In order to further verify our model for transient flow conditions we have shown that it can reproduce the linear scaling proposed by PODGORSKI et al. (2001). We have demonstrated that Ca, Re, and contact angles agree with those reported in laboratory experiments for water-rock systems for a wide range of Bo. We have also shown that the SPH model can be used to estimate the scaling parameter γ as a function of the static contact angle in the model of GHEZZEHEI (2004). Our simulations show that the linear scaling fails as soon as droplet shapes strongly deviate from a rounded or cornered shape. This is in accordance with the observations of PODGORSKI et al. (2001). We found that droplets on dry surfaces leave behind trailing films for small static contact angles and initially dry surfaces. These results agree with experimental observations of TOKUNAGA & WAN (1997) and OR & TULLER (2000). Prewetted surfaces are shown to increase droplets velocities by enhancing the wetting and dewetting dynamics processes and thus, despite their relatively slow velocities ($3 \times 10^{-7}\,\mathrm{m\,s^{-1}}$, TOKUNAGA et al., 2000) can be an important part of flow dynamics even if gravity-driven flow prevails. Our simulations show that fluid films are stable for static contact angles below ~40°. These results indicate that flow regime (droplets leaving behind a dry surface versus droplets leaving behind discontinuous or continuous films) and droplet velocity (Reynolds number) depend on the static contact angle and initial wetting condition of the fracture wall (dry versus prewetted). Therefore, a flow regime may affect the average flux in the fracture and should be accounted for in an effective model. We considered the effect of "macroscale" roughness on the drop dynamics and demonstrated that it affects traveling distance and transversal movement. We define a macroscale roughness when the following conditions are satisfied: (1) the ratio of characteristic roughness length scale d_r to average interparticle distance d_p is on the order of one or higher; and (2) the characteristic roughness length is much smaller than the capillary length λ_c. Microscale roughness (i.e., $d_r/d_p << 1$ and $d_r/\lambda_c << 1$) may result in more com-

plex phenomena such as the lotus effect (HUANG et al., 2009; MARMUR, 2004) and apparent contact angles (CASSIE, 1948). However, studying the effect of the microroughness is outside of the scope of this work as simulation of such phenomena would require exascale computations with the number of SPH particles on the order of 10^7 to 10^9. The following topics deserve more attention for further model applications: (1) the critical transitions between different flow regimes, e.g. forced wetting transitions such as Landau-Levich films which occur for very low contact angles LE GRAND et al. (2005); (2) shape transitions from oval to corner and cusps which involve field singularities; and (3) transitions to rivulets and falling films. Given that the application of our model is aimed towards fractured media we defined a lower scale that we believe is a proper starting point for model development and allows realistic computation times. Further model improvements might cover implementation of more realistic boundary conditions, however, for rough surfaces this is still an open question MONAGHAN (2005). The presented simulations cover a wide spectrum of the possible flow regimes and boundary conditions encountered in natural fractured aquifers. Furthermore, these simulations demonstrate that SPH is a versatile method and can be easily extended to simulate more complex systems, allowing for a unified characterization of the flow and possibly transport processes across the matrix-fracture interface in partial fracture networks on a centimeter to meter scale, which is the scope of future work.

Acknowledgments

The authors would like to thank four anonymous reviewers. This work was partially supported by the DAAD (German Academic Exchange Service) providing J. Kordilla with an international research scholarship at the Pacific Northwest National Laboratory (PNNL), USA. A.M. Tartakovsky was supported by the Department of Energy's Office of Advanced Scientific Computing Research Program and at Pacific Northwest National Laboratory (PNNL). PNNL is operated by Battelle for the U.S. Department of Energy.

5.8 References

ALLEN, M. & TILDESLEY, D. (1989): *Computer Simulation of Liquids*. Clarendon Press, Oxford: p. 404 (cit. on pp. 120, 122).

BIKERMAN, J. (1950): 'Sliding of drops from surfaces of different roughnesses'. *Journal of Colloid Science*, vol. **5**(4): pp. 349–359 (cit. on p. 126).

BOUCHAUD, E. (1997): 'Scaling properties of cracks'. *Journal of Physics: Condensed Matter*, vol. **9**(21): pp. 4319–4344 (cit. on p. 141).

BOUCHAUD, E., LAPASSET, G. & PLANES, J. (1990): 'Fractal dimension of fractured surfaces: a universal value?' *Europhys. Lett.* Vol. **73**(13): pp. 73–79 (cit. on p. 141).

BRACKBILL, J., KOTHE, D. & ZEMACH, C. (1992): 'A continuum method for modeling surface tension'. *Journal of Computational Physics*, vol. **100**(2): pp. 335–354 (cit. on p. 119).

CASSIE, A. (1948): 'Contact angles'. *Discussions of the Faraday Society*, vol. **3**: pp. 11–16 (cit. on p. 145).

DOE, T. (2001): 'What do drops do? Surface wetting and network geometry effects on vadose-zone fracture flow'. *Conceptual models of flow and transport in the fractured vadose zone*. Washington D.C.: National Academy Press. Chap. 8: pp. 243–270 (cit. on p. 112).

DRAGILA, M. I. & WEISBROD, N. (2004a): 'Flow in Menisci Corners of Capillary Rivulets'. *Vadose Zone Journal*, vol. **3**: pp. 1439–1442 (cit. on p. 112).

– (2004b): 'Fluid motion through an unsaturated fracture junction'. *Water Resources Research*, vol. **40**: pp. 1–11 (cit. on pp. 112, 139).

– (2003): 'Parameters affecting maximum fluid transport in large aperture fractures'. *Advances in Water Resources*, vol. **26**: pp. 1219–1228 (cit. on pp. 112, 136).

DUSSAN, E. B. & CHOW, R. T.-P. (1983): 'On the ability of drops or bubbles to stick to non-horizontal surfaces of solids'. *Journal of Fluid Mechanics*, vol. **137**: pp. 1–29 (cit. on p. 126).

ELSHERBINI, A. I. & JACOBI, A. M. (2004): 'Liquid drops on vertical and inclined surfaces; I. An experimental study of drop geometry.' *Journal of*

Colloid and Interface Science, vol. **273**(2): pp. 556–65 (cit. on pp. 114, 126–128, 143).

– (2006): 'Retention forces and contact angles for critical liquid drops on non-horizontal surfaces.' *Journal of Colloid and Interface Science*, vol. **299**(2): pp. 841–9 (cit. on pp. 115, 126, 127).

Evans, D. D. & Rasmussen, T. C. (1991): *Unsaturated Flow and Transport Through Fractured Rock Related to High-level Waste Repositories: Final Report–phase III*. Tech. rep. Washington: Office of Nuclear Regulatory Research (cit. on p. 112).

Evans, D. D., Rasmussen, T. C., Todd, C. & J., N. T. (2001): 'Flow and Transport Through Unsaturated Fractured Rock'. *Geophysical Monograph Series*, vol. **42**: p. 201 (cit. on p. 112).

Furmidge, C. (1962): 'Studies at phase interfaces. I. The sliding of liquid drops on solid surfaces and a theory for spray retention'. *Journal of Colloid Science*, vol. **17**(4): pp. 309–324 (cit. on p. 126).

Gennes, P. de (1985): 'Wetting: statics and dynamics'. *Reviews of Modern Physics*, vol. **57**(3): pp. 827–863 (cit. on p. 117).

Genuchten, M. T. van (1980): 'A Closed-form Equation for Predicting the Hydraulic Conductivity of Unsaturated Soils'. *Soil Science Society of America Journal*, vol. **44**(5): pp. 892–898 (cit. on p. 112).

Germann, P. F., Helbling, A. & Vadilonga, T. (2007): 'Rivulet Approach to Rates of Preferential Infiltration'. *Vadose Zone Journal*, vol. **6**(2): pp. 207–220 (cit. on p. 112).

Ghezzehei, T. A. (2004): 'Constraints for flow regimes on smooth fracture surfaces'. *Water Resources Research*, vol. **40**: pp. 1–14 (cit. on pp. 112, 113, 129, 140, 144).

Gingold, R. A. & Monaghan, J. J. (1982): 'Kernel estimates as a basis for general particle methods in hydrodynamics'. *Journal of Computational Physics*, vol. **46**(3): pp. 429–453 (cit. on p. 117).

Gingold, R. A. & Monaghan, J. J. (1977): 'Smoothed particle hydrodynamics: theory and application to non-spherical stars'. *Mon. Not. R. Astron. Soc.* Vol. **181**: pp. 375–389 (cit. on p. 113).

HIRT, C. & NICHOLS, B. (1981): 'Volume of Fluid (VOF) Method for the Dynamics of Free Boundaries'. *Journal of Computational Physics*, vol. **39**: pp. 201–225 (cit. on p. 113).

HOLMES, D., WILLIAMS, J. & TILKE, P. (2011): 'Smooth particle hydrodynamics simulations of low Reynolds number flows through porous media'. *International Journal for Numerical and Analytical Methods in Geomechanics*, vol. **35**: pp. 419–437 (cit. on p. 114).

HOLMES, D., WILLIAMS, J., TILKE, P. & LEONARDI, C. (2000): 'Characterizing flow in oil reservoir rock using SPH: Absolute permeability'. *International Journal for Numerical and Analytical Methods in Geomechanics*, vol. **61**(7): pp. 1–22 (cit. on p. 114).

HOOVER, W. G., PIERCE, T. G., HOOVER, C. G., SHUGART, J. O., STEIN, C. M. & EDWARDS, A. L. (1994): 'Molecular Dynamics , Smoothed-Particle Applied Mechanics , and Irreversibility'. *Computers & Mathematics with Applications*, vol. **28**(10): pp. 155–174 (cit. on p. 114).

HUANG, H. & MEAKIN, P. (2008): 'Three-dimensional simulation of liquid drop dynamics within unsaturated vertical Hele-Shaw cells'. *Water Resources Research*, vol. **44**(3): W03411 (cit. on p. 113).

HUANG, J. J., SHU, C. & CHEW, Y. T. (2009): 'Lattice Boltzmann study of droplet motion inside a grooved channel'. *Physics of Fluids*, vol. **21**: pp. 1–11 (cit. on pp. 126, 145).

HUH, C. & SCRIVEN, L. (1971): 'Hydrodynamic model of steady movement of a solid/liquid/fluid contact line'. *Journal of Colloid and Interface Science*, vol. **35**(1): pp. 85–101 (cit. on p. 117).

JIANG, T., OUYANG, J., YANG, B. & REN, J. (2010): 'The SPH method for simulating a viscoelastic drop impact and spreading on an inclined plate'. *Computational Mechanics*, vol. **45**(6): pp. 573–583 (cit. on p. 126).

KWOK, D. Y., GIETZELT, T., GRUNDKE, K., JACOBASCH, H.-J. & NEUMANN, A. W. (1997): 'Contact Angle Measurements and Contact Angle Interpretation. 1. Contact Angle Measurements by Axisymmetric Drop Shape Analysis and a Goniometer Sessile Drop Technique'. *Langmuir*, vol. **13**(10): pp. 2880–2894 (cit. on p. 124).

Le Grand, N., Daerr, A. & Limat, L. (2005): 'Shape and motion of drops sliding down an inclined plane'. *Journal of Fluid Mechanics*, vol. **541**: p. 293 (cit. on pp. 126, 145).

Lebeau, M. & Konrad, J.-M. (2010): 'A new capillary and thin film flow model for predicting the hydraulic conductivity of unsaturated porous media'. *Water Resources Research*, vol. **46**(12): pp. 1–15 (cit. on p. 136).

Liu, M., Meakin, P. & Huang, H. (2006): 'Dissipative particle dynamics with attractive and repulsive particle-particle interactions'. *Physics of Fluids*, vol. **18**(1): p. 017101 (cit. on pp. 118, 119).

Lucy, L. B. (1977): 'A numerical approach to the testing of the fission hypothesis'. *Astronomical Journal*, vol. **82**(12): pp. 1013–1024 (cit. on p. 114).

Macdougall, G. & Ockrent, C. (1942): 'Surface Energy Relations in Liquid/-Solid Systems. I. The Adhesion of Liquids to Solids and a New Method of Determining the Surface Tension of Liquids'. *Proceedings of the Royal Society A*, vol. **180**: p. 151 (cit. on p. 127).

Mandelbrot, B. (1982): *The fractal geometry of nature* (cit. on p. 141).

Marmur, A. (2004): 'The Lotus Effect : Superhydrophobicity and Metastability'. *Langmuir*, vol. (20): pp. 3517–3519 (cit. on p. 145).

Mclaren, R. G., Forsyth, P. A., Sudicky, E. A., Vanderkwaak, J. E., Schwartz, F. W. & Kessler, J. H. (2000): 'Flow and transport in fractured tuff at Yucca Mountain: numerical experiments on fast preferential flow mechanisms'. *Journal of Contaminant Hydrology*, vol. **43**: pp. 211–238 (cit. on p. 112).

Meakin, P. & Tartakovsky, A. (2009): 'Modeling and simulation of pore-scale multiphase fluid flow and reactive transport in fractured and porous media'. *Reviews of Geophysics*, vol. (47): pp. 1–47 (cit. on p. 114).

Mognetti, B., Kusumaatmaja, H. & Yeomans, J. (2010): 'Drop dynamics on hydrophobic and superhydrophobic surfaces'. *Faraday Discuss.* Vol. **146**: pp. 153–165 (cit. on p. 126).

Monaghan, J. J. (2005): 'Smoothed particle hydrodynamics'. *Reports on Progress in Physics*, vol. **68**(8): pp. 1703–1759 (cit. on p. 145).

Monaghan, J. J. (1982): 'Why particle methods work'. *SIAM: SIAM Journal on Scientific Computing*, vol. **3**(4): pp. 422–433 (cit. on p. 115).

Morris, J. P. (1997): 'Modeling Low Reynolds Number Incompressible Flows Using SPH'. *Journal of Computational Physics*, vol. **136**(1): pp. 214–226 (cit. on p. 117).

Mualem, Y. (1976): 'A new model for predicting the hydraulic conductivity of unsaturated porous media'. *Water Resources Research*, vol. **12**(3): pp. 513–522 (cit. on p. 112).

Or, D. & Tuller, M. (2000): 'Flow in unsaturated fractured porous media: Hydraulic conductivity of rough surfaces'. *Water Resources Research*, vol. **36**(5): pp. 1165–1177 (cit. on pp. 136, 144).

Podgorski, T., Flesselles, J.-M. & Limat, L. (2001): 'Corners, Cusps, and Pearls in Running Drops'. *Physical Review Letters*, vol. **87**(3): p. 036102 (cit. on pp. 113, 115, 126, 128–131, 133, 134, 144).

Ponson, L., Bonamy, D. & Bouchaud, E. (2006): 'Two-Dimensional Scaling Properties of Experimental Fracture Surfaces'. *Physical Review Letters*, vol. **96**(3): p. 035506 (cit. on p. 141).

Singhal, B. B. & Gupta, R. P. (2010): *Applied Hydrogeology of Fractured Rocks*. Springer: p. 408 (cit. on p. 112).

Sobolev, V. D., Churaev, N. V., Velarde, M. G. & Zorin, Z. M. (2000): 'Surface Tension and Dynamic Contact Angle of Water in Thin Quartz Capillaries'. *Journal of Colloid and Interface Science*, vol. **222**(1): pp. 51–54 (cit. on p. 139).

Su, G. W., Geller, J. T., Pruess, K. & Hunt, J. R. (2001): 'Solute transport along preferential flow paths in unsaturated fractures'. *Water Resources Research*, vol. **37**(10): pp. 2481–2491 (cit. on pp. 112, 140).

Su, G. W., Geller, J. T., Hunt, J. R. & Pruess, K. (2004): 'Small-Scale Features of Gravity-Driven Flow in Unsaturated Fractures'. *Vadose Zone Journal*, vol. **3**(2): pp. 592–601 (cit. on p. 112).

Su, G. W., Geller, J. T., Pruess, K. & Wen, F. (1999): 'Experimental studies of water seepage and intermittent flow in unsaturated, rough-walled fractures'. *Water Resources Research*, vol. **35**(4): p. 1019 (cit. on p. 140).

TANNER, L. (1979): 'The spreading of silicone oil drops on horizontal surfaces'. *Journal of Physics D: Applied Physics*, vol. **12**(9): pp. 1473–1485 (cit. on p. 117).

TARTAKOVSKY, A., FERRIS, K.F. & MEAKIN, P. (2009a): 'Lagrangian particle model for multiphase flows'. *Computer Physics Communications*, vol. **180**(10): pp. 1874–1881 (cit. on pp. 114, 122).

TARTAKOVSKY, A. & MEAKIN, P. (2005a): 'A smoothed particle hydrodynamics model for miscible flow in three-dimensional fractures and the two-dimensional Rayleigh-Taylor instability'. *Journal of Computational Physics*, vol. **207**: pp. 610–624 (cit. on p. 116).

– (2005b): 'Modeling of surface tension and contact angles with smoothed particle hydrodynamics'. *Physical Review E*, vol. **72**: p. 026301 (cit. on pp. 114, 115, 117–120, 122, 136).

– (2006): 'Pore scale modeling of immiscible and miscible fluid flows using smoothed particle hydrodynamics'. *Advances in Water Resources*, vol. **29**(10): pp. 1464–1478 (cit. on p. 114).

– (2005c): 'Simulation of Unsaturated Flow in Complex Fractures Using Smoothed Particle Hydrodynamics'. *Vadose Zone Journal*, vol. **4**(3): pp. 848–855 (cit. on p. 114).

TARTAKOVSKY, A., TARTAKOVSKY, G. & SCHEIBE, T. (2009b): 'Effects of incomplete mixing on multicomponent reactive transport'. *Advances in Water Resources*, vol. **32**(11): pp. 1674–1679 (cit. on p. 114).

TARTAKOVSKY, A., WARD, A.L. & MEAKIN, P. (2007): 'Pore-scale simulations of drainage of heterogeneous and anisotropic porous media'. *Physics of Fluids*, vol. **19**(10): p. 103301 (cit. on p. 114).

TOKUNAGA, T.K. & WAN, J. (2001): 'Surface-zone flow along unsaturated rock fractures'. *Water Resources Research*, vol. **37**(2): p. 287 (cit. on p. 140).

– (1997): 'Water film flow along fracture surfaces of porous rock'. *Water Resources Research*, vol. **33**(6): p. 1287 (cit. on pp. 112, 136, 144).

TOKUNAGA, T.K., WAN, J. & SUTTON, S.R. (2000): 'Transient film flow on rough fracture surfaces'. *Water Resources Research*, vol. **36**(7): pp. 1737–1746 (cit. on pp. 112, 136, 144).

TSUKADA, T., HOZAWA, M., IMAISHI, N. & FUJIKAWA, K. (1982): 'Static drop formation on an inclined flat plate'. *Journal of Chemical Engineering of Japan*, vol. **15**: pp. 412–426 (cit. on p. 127).

6 | Smoothed particle hydrodynamics model for Landau-Lifshitz Navier-Stokes and advection-diffusion equations*

Kordilla, J.[1], Tartakovsky, A.M.[2,3], Pan, W.[2]

[1]Geoscientific Centre, University of Göttingen, Göttingen, Germany

[2]Computational Mathematics Group, Pacific Northwest National Laboratory, Richland, USA

[3]School of Geosciences, Dept. of Mathematics and Statistics, University of South Florida, Tampa, USA

* Kordilla, J., Tartakovsky, A.M. & Pan, W., (2014): Smoothed particle hydrodynamics model for Landau-Lifshitz Navier-Stokes and advection-diffusion equations. *Submitted to a peer reviewed journal.*

Abstract. We propose a novel Smoothed Particle Hydrodynamics (SPH) discretization of the fully-coupled Landau-Lifshitz-Navier-Stokes (LLNS) and advection-diffusion equations. The accuracy of the SPH solution of the LLNS equations is demonstrated by comparing the scaling of velocity variance and self-diffusion coefficient with kinetic temperature and particle mass obtained from the SPH simulations and analytical solutions. The spatial covariance of pressure and velocity fluctuations are found to be in a good agreement with theoretical models. To validate the accuracy of the SPH method for the coupled LLNS and advection-diffusion equations, we simulate the interface between two miscible fluids. We study the formation of the so-called giant fluctuations of the front between light and heavy fluids with and without gravity, where the light fluid lays on the top of the heavy fluid. We find that the power spectra of the simulated concentration field is in good agreement with the experiments and analytical solutions. In the absence of gravity the the power spectra decays as the power -4 of the wave number except for small wave numbers which diverge from this power law behavior due to the effect of finite domain size. Gravity suppresses the fluctuations resulting in the much weaker dependence of the power spectra on the wave number. Finally the model is used to study the effect of thermal fluctuation on the Rayleigh-Taylor instability, an unstable dynamics of the front between a heavy fluid overlying a light fluid. The front dynamics is shown to agree well with the analytical solutions.

6.1 Introduction

In the presence of a macroscopic concentration gradient (e.g. the concentration gradient across the front separating two miscible fluids), non-equilibrium systems are known to relax to an equilibrated state via diffusion (Bear, 1972; Cussler, 1997). On macroscopic scales diffusion is often approximated by Fick's law (Fick, 1855). However, on mesoscopic or molecular scales thermal fluctuations become a significant part of the hydrodynamics and greatly influence mixing. Thermal fluctuations may have a significant impact on miscible fluids close to a hydrodynamic instability such as Rayleigh-Taylor and Kelvin-Helmholtz instabilities. Fluctuations may also have significant qualitative impact even on hydrodynamically stable miscible systems. For example, thermal fluctuations produce anomalously large fluctuations of the front separating two miscible fluids (with a light fluid overlaying a heavy fluid). Such fluctuations are often called "giant fluctuations" to emphasize the fact that they can be observed by the naked eye (Brogioli et al., 2000; Croccolo et al., 2007; Vailati & Giglio, 1997).

The fluctuations of thermodynamic quantities have been extensively studied in the context of Brownian motion. Einstein (1905) and von Smoluchowski (1906) demonstrated that diffusion resulting from the thermal fluctuations and random movement of a particle in a fluid has the same origin as the dissipative drag forces that are exerted on the particle by the fluid. Later, this relationship was quantitatively described by the fluctuation-dissipation theorem (Callen & Welton, 1951).

To capture the effect of thermal fluctuations on the fluid flow on the hydrodynamic scale, Landau & Lifshitz (1987) proposed a stochastic form of the Navier-Stokes equations that is commonly referred to as the Landau-Lifshitz-Navier-Stokes (LLNS) equations. In the LLNS equations, a random stress is added to the Navier-Stokes equations, and the strength of the random stress is related to the viscous stress via the fluctuation-dissipation theorem. Similarly, a random mass flux is added into the advection-diffusion equation to consistently include the effect of thermal fluctuations on Fick-

ian diffusion. The most common numerical techniques for directly solving the LLNS and stochastic diffusion equations are based on the finite-volume method (Bell et al., 2007; Donev & Vanden-Eijnden, 2010; Donev et al., 2011a; Serrano & Español, 2001). Stochastic Lattice-Boltzmann models (Ladd, 1993) and smoothed dissipative particle dynamics (SDPD) (Español & Revenga, 2003; Español et al., 1999) have been used to model fluid flow in the presence of fluctuations, but these method have not been derived via the direct discretization of the LLNS equations. For example, SDPD is obtained by adding a random force into the SPH discretization of the (deterministic) NS equations, and relating the magnitude of the random force to the viscous SPH force via the GENERIC framework (Grmela & Öttinger, 1997; Öttinger & Grmela, 1997; Serrano et al., 2002). Moreover, these methods have not been used to solve stochastic diffusion equations coupled with the LLNS equations.

Here we use the SPH method to solve stochastic partial differential equations including the LLNS and advection-diffusion equations. With regard to the LLNS equations, the SPH discretization provides an alternative to SDPD for introducing fluctuations in the SPH flow equations. It also provides a consistent framework for discretizing other stochastic conservation equations. We demonstrate the accuracy of the SPH solution of the LLNS equations by comparing statistics of the fluctuations of pressure and velocity with the analytical solutions. The accuracy of the solution of the stochastic diffusion equation is verified by comparing moments of a conservative tracer with the analytical solution. Finally, we use the coupled LLNS and advection-diffusion equations to study the effect of fluctuations on the diffusive front in the absence and presence of gravity. We analyze the spatial correlation of the diffusive front geometry and compare the results with the theoretical predictions. Furthermore the classical Rayleigh-Taylor instability is simulated to verify the accuracy of the stochastic SPH model.

6.2 Stochastic flow and transport equations

We study the isothermal stochastic Navier-Stokes equations including the continuity equation

$$\frac{D\rho}{Dt} = -\rho\left(\boldsymbol{\nabla}\cdot\boldsymbol{v}\right), \tag{6.1}$$

the momentum conservation equation

$$\frac{D\boldsymbol{v}}{Dt} = -\frac{1}{\rho}\boldsymbol{\nabla}P + \frac{1}{\rho}\boldsymbol{\nabla}\cdot\boldsymbol{\tau} + \boldsymbol{g} + \frac{1}{\rho}\boldsymbol{\nabla}\cdot\boldsymbol{s} \tag{6.2}$$

and the stochastic advection-diffusion equation

$$\frac{DC}{Dt} = \frac{1}{\rho}\boldsymbol{\nabla}\cdot\left(\rho D^F\boldsymbol{\nabla}C\right) + \frac{1}{\rho}\boldsymbol{\nabla}\cdot\boldsymbol{J}. \tag{6.3}$$

Here $D/Dt = \partial/\partial t + \boldsymbol{v}\cdot\boldsymbol{\nabla}$ is the total derivative and ρ, $\boldsymbol{v}$, P and $\boldsymbol{g}$ are the density, velocity, pressure and body force, and D^F is the Fickian diffusion coefficient. The components of the viscous stress $\boldsymbol{\tau}$ are given by

$$\tau^{ik} = \mu\left(\frac{\partial v^i}{\partial x^k} + \frac{\partial v^k}{\partial x^i}\right), \tag{6.4}$$

where μ is the (shear) viscosity and the bulk viscosity is assumed to be equal to $\frac{2}{3}\mu$. $C = \widetilde{C}/C_{max}$ is the normalized mass fraction of solute varying from zero to one ($\widetilde{C}$ is the mass fraction and C_{max} is the maximum mass fraction). In the following, we refer to C as concentration. The fluctuations in velocity and concentration are caused by the random stress tensor

$$\boldsymbol{s} = \sigma\boldsymbol{\xi} \tag{6.5}$$

and random flux vector

$$\boldsymbol{J} = \tilde{\sigma}\tilde{\boldsymbol{\xi}}, \tag{6.6}$$

where $\boldsymbol{\xi}$ is a random symmetric tensor and $\tilde{\boldsymbol{\xi}}$ is a random vector (whose components are random Gaussian variables), and σ and $\tilde{\sigma}$ are the strengths of the corresponding noises. The random stress is related to the viscous stress by the fluctuation-dissipation theorem (LANDAU & LIFSHITZ, 1987). For incompressible and low-compressible fluids, the covariance of the stress components is:

$$\overline{s^{ik}(\mathbf{r_1},t_1)s^{lm}(\mathbf{r_2},t_2)} = \sigma^2\delta(\mathbf{r}_1-\mathbf{r}_2)\delta(t_1-t_2) \quad \sigma^2 = 2\mu k_B T\delta^{im}\delta^{kl}, \tag{6.7}$$

where k_B is the Boltzmann constant, T denotes the temperature, $\delta(z)$ is the Dirac delta function and δ^{ij} is the Kronecker delta function. The fluctuation-dissipation theorem is also used to relate the random flux $\boldsymbol{J}$ to the diffusion term (DONEV et al., 2011b)

$$\overline{J^i(\mathbf{r_1},t_1)J^j(\mathbf{r_2},t_2)} = \tilde{\sigma}^2\delta(\mathbf{r}_1-\mathbf{r}_2)\delta(t_1-t_2) \quad \tilde{\sigma}^2 = 2m_m DC(1-C)\rho\delta^{ij}, \tag{6.8}$$

where m_m is the mass of a single solvent molecule. In general, the density and viscosity of the fluid are functions of the solute concentration C.

6.3 SPH discretization

Numerical discretization of the stochastic partial differential equations using SPH is based on the following identity for a continuous field $f(\boldsymbol{r})$ defined on a domain Ω:

$$f(\boldsymbol{r}) = \int_\Omega f(\boldsymbol{r}')\delta(\boldsymbol{r}-\boldsymbol{r}')d\boldsymbol{r}'. \tag{6.9}$$

To construct a numerical scheme, the δ function is approximated with a smooth kernel function W yielding the *integral* approximation of $f(\boldsymbol{r})$ (MONAGHAN, 1982):

$$\langle f(\boldsymbol{r})\rangle = \int_\Omega f(\boldsymbol{r}')W(|\boldsymbol{r}-\boldsymbol{r}'|,h)d\boldsymbol{r}'. \tag{6.10}$$

The kernel $W(|\boldsymbol{r}-\boldsymbol{r}'|,h)$ satisfies: (1) the normalization condition

$$\int_\Omega W(|\boldsymbol{r}-\boldsymbol{r}'|,h)d\boldsymbol{r}' = 1; \tag{6.11}$$

(2) has compact support h, $W(r > h,h) = 0$; and (3) in the limit of $h \to 0$, W approaches the Dirac delta function

$$\lim_{h\to 0} W(|\boldsymbol{r}-\boldsymbol{r}'|,h) = \delta(\boldsymbol{r}-\boldsymbol{r}'). \tag{6.12}$$

In this work we use a fourth-order weighting function to describe W (TARTAKOVSKY & MEAKIN, 2005a):

$$W(|\boldsymbol{r}|,h) = \frac{\alpha_k}{h^3}\begin{cases} (3q)^5 - 6\,(2q)^5 + 15\,(q)^5 & 0 \le |\boldsymbol{r}| < \frac{1}{3}\ h \\ (3q)^5 - 6\,(2q)^5 & \frac{1}{3}h \le |\boldsymbol{r}| < \frac{2}{3}\ h \\ (3q)^5 & \frac{2}{3}h \le |\boldsymbol{r}| < h \\ 0 & |\boldsymbol{r}| > h, \end{cases} \tag{6.13}$$

where $\alpha_k = 81/(359\pi)$ is the normalization constant and $q = 1-3|\boldsymbol{r}|/(qh)$.

Next, Ω is discretized with N points (that are usually referred to as particles) with positions $\boldsymbol{r}_j$ ($j = 1,\ldots,N$) and the integral in Eq. (6.10) is approximated as a sum to obtain the *discrete* approximation $\langle\langle f(\boldsymbol{r})\rangle\rangle$ of $f(\boldsymbol{r})$:

$$\langle\langle f(\boldsymbol{r})\rangle\rangle = \sum_{j=1}^{N} f_j W(|\boldsymbol{r}-\boldsymbol{r}_j|,h)\Delta V_j = \sum_{j=1}^{N} \frac{1}{n_j} f_j W(|\boldsymbol{r}-\boldsymbol{r}_j|,h), \tag{6.14}$$

where $f(\boldsymbol{r}_j) = f_j$, $\Delta V_j = \frac{m_j}{\rho_j}$ is the volume associated with particle j, m_j is the prescribed mass of particle j, ρ_j is the mass density of the fluid at position $\boldsymbol{r}_j$ and $n_j = \frac{\rho_j}{m_j}$ is the number density. Equation (6.14) allows to

compute spatial derivatives of $\langle\langle f(\boldsymbol{r})\rangle\rangle$ exactly as

$$\boldsymbol{\nabla}\langle\langle f(\boldsymbol{r})\rangle\rangle = \sum_{j=1}^{N} \frac{f_j}{n_j} \boldsymbol{\nabla} W(|\boldsymbol{r}-\boldsymbol{r}_j|,h), \tag{6.15}$$

where $\boldsymbol{\nabla} W(|\boldsymbol{r}-\boldsymbol{r}_j|,h)$ can be found analytically.

If the particles are uniformly distributed (e.g. located on a regular lattice with the lattice size Δ), then the particle number density can be found exactly as $n_j = \Delta^{-d}$, where d is the number of spatial dimensions. In the Lagrangian SPH framework, the particles are advected with the fluid velocity and become disordered. For a non-uniform particle distribution, the particle number density can be approximately found from Eq. (6.14) with $f_i = n_i$ as

$$\langle\langle n_i\rangle\rangle = \sum_{j=1}^{N} W(|\boldsymbol{r}-\boldsymbol{r}_j|,h), \tag{6.16}$$

Alternatively, $n_i = \rho_i/m_i$ can be found from the continuity equation. To simplify the notation, we will drop double brackets in the following derivations.

Using Eqs. (6.14-6.15), an SPH discretization of the Navier-Stokes Eqs. (6.1) and (6.2) can be obtained as (GINGOLD & MONAGHAN, 1982; LANDAU & LIFSHITZ, 1987; MONAGHAN, 2005):

$$\frac{D(m_i \mathbf{v}_i)}{Dt} = \boldsymbol{F}_i \tag{6.17}$$

$$\begin{aligned} \boldsymbol{F}_i = & -\sum_{j=1}^{N} \left(\frac{P_j}{n_j^2} + \frac{P_i}{n_i^2} \right) \frac{\mathbf{r}_{ij}}{r_{ij}} \frac{dW(r_{ij},h)}{dr_{ij}} \\ & + \sum_{j=1}^{N} \frac{5(\mu_i+\mu_j)}{n_i n_j} \frac{(\mathbf{v}_{ij}\cdot\mathbf{r}_{ij})}{r_{ij}^2} \frac{\mathbf{r}_{ij}}{r_{ij}} \frac{dW(r_{ij},h)}{dr_{ij}} + m_i \boldsymbol{g} \\ & + \sum_{j=1}^{N} \left(\frac{\boldsymbol{s}_j}{n_j^2} + \frac{\boldsymbol{s}_i}{n_i^2} \right) \cdot \frac{\mathbf{r}_{ij}}{r_{ij}} \frac{dW(r_{ij},h)}{dr_{ij}}. \end{aligned} \tag{6.18}$$

Following TARTAKOVSKY & MEAKIN (2005a) and ZHU & FOX (2002) a numerical discretization of the convection-diffusion equation is obtained as

$$\frac{D(m_i C_i)}{Dt} = \sum_{j=1}^{N} \frac{(D_i^F m_i n_i + D_j^F m_j n_j)(C_i - C_j)}{n_i n_j} \left(\frac{1}{r_{ij}} \frac{dW(r_{ij},h)}{dr_{ij}} \right) + \sum_{j=1}^{N} \left(\frac{\boldsymbol{J}_j}{n_j^2} + \frac{\boldsymbol{J}_i}{n_i^2} \right) \cdot \frac{\mathbf{r}_{ij}}{r_{ij}} \frac{dW(r_{ij},h)}{dr_{ij}}. \tag{6.19}$$

The particle positions are evolved in time according to

$$\frac{d\boldsymbol{r}_i}{dt} = \boldsymbol{v}_i. \tag{6.20}$$

Here, $\boldsymbol{v}_i$ is the velocity of particle i, t is time, P_i is the fluid pressure at $\boldsymbol{r}_i$, $\boldsymbol{s}_i$ is the random stress at $\boldsymbol{r}_i$, $r_{ij} = |\boldsymbol{r}_{ij}|$, $\boldsymbol{r}_{ij} = \boldsymbol{r}_i - \boldsymbol{r}_j$, and $\boldsymbol{v}_{ij} = \boldsymbol{v}_i - \boldsymbol{v}_j$. For computational efficiency, we set h to unity and locate particles within the interaction range using a common link-list approach with an underlying cubic-lattice of size $h = 1.0$.

To close the system of SPH equations we employ a common equation of state (EOS) in the form

$$P_i = c^2 m_i n_i, \tag{6.21}$$

where c is the artificial speed of sound, which is chosen such that the desired compressibility of the system is obtained. Depending on application, this EOS is often applied to incompressible systems (KORDILLA et al., 2013; MORRIS, 1997; TARTAKOVSKY & MEAKIN, 2005b), where a choice of c, based on dimensionless analysis (MONAGHAN, 1992; MORRIS, 1997), can yield the quasi-incompressible approximation of an incompressible fluid.

In general, m_i and μ_i depend on C_i. In SPH, the mass fraction can be defined as $\widetilde{C}_i = m_i^s / m_i = m_i^s / (m_i^0 + m_i^s)$, where m_i is the total mass of particle i (mass of the solution carried by particle i), m_i^s is the mass of solute, and m_i^0 is the mass of solvent carried by particle i. Then, the dependence

of m_i on C_i can be expressed as

$$m_i = m_i^0 + m_i \widetilde{C}_i = m_i^0 + m_i C_{max} C_i. \tag{6.22}$$

In the following we assume that m_i^0 is constant (i.e. does not change as result of diffusion), $\widetilde{C} << 1$ (dilute solution), the mass of solute carried by particle i is $m_i^s = m_i^0 \widetilde{C}_i$ and

$$m_i = m_i^0 + \kappa C_i \tag{6.23}$$

where $\kappa = m_i^0 C_{max}$ is a constant. Then Eq. (6.19) can be linearized as

$$\begin{aligned} \frac{DC_i}{Dt} &= G_i \\ G_i &= \frac{1}{m_i^0} \sum_{j=1}^{N} \frac{(D_i^F m_i n_i + D_j^F m_j n_j)(C_i - C_j)}{n_i n_j} \left(\frac{1}{r_{ij}} \frac{dW(r_{ij},h)}{dr_{ij}} \right) \\ &\quad + \frac{1}{m_i^0} \sum_{j=1}^{N} \left(\frac{\boldsymbol{J}_j}{n_j^2} + \frac{\boldsymbol{J}_i}{n_i^2} \right) \cdot \frac{\mathbf{r}_{ij}}{r_{ij}} \frac{dW(r_{ij},h)}{dr_{ij}}. \end{aligned} \tag{6.24}$$

For the sake of simplicity we neglect the dependence of the viscosity on the fluid compositions.

In SPH, the fluid domain is discretized with fluid particles with volume $\Delta V_i = 1/n_i$ and time integration is done with time step Δt. Therefore, we can write the lm-component of the random stress tensor at $\boldsymbol{r}_i$ as:

$$s_i^{lm} = \sqrt{\frac{2\mu k_B T \delta^{lm}}{\Delta V_i \Delta t}} \xi_i^{lm} = \sqrt{\frac{2\mu k_B T \delta^{lm} n_i}{\Delta t}} \xi_i^{lm}, \tag{6.25}$$

where ξ_i^{lm} is a unitless random number from a uniform or normal distribution with a unit variance. No summation over repeating indices is assumed in Eq. (6.25). Similarly, the l-component of the random flux can be written

as

$$J_i^l = \sqrt{\frac{2m_m D^F C(1-C)\rho_i}{\Delta V_i \Delta t}}\tilde{\xi}_i^l = \sqrt{\frac{2m_m m_i D^F C(1-C)n_i^2}{\Delta t}}\tilde{\xi}_i^l, \tag{6.26}$$

where $\tilde{\xi}_i^l$ is a unitless random number from a uniform or normal distribution with a unit variance.

In order to maintain the kinetic energy of the modeled system independent of resolution (number of particles), and to recover the appropriate scaling behavior of velocity fluctuations with temperature, we follow the work of FÜCHSLIN et al. (2007) and introduce scaling of the Boltzmann constant, k_B. Consider a fluid system modeled with two different resolutions corresponding to N^* and N number of particles, respectively, where N^* is the number of particles in the referenced model. We assume that the Boltzmann constant in the system with N^* particles is k_B, and in the system with N particles is $\tilde{k}_B$. Equating the total kinetic energy of the models with these two resolutions leads to $\frac{3}{2}N^* k_B T = \frac{3}{2}N\tilde{k}_B T$. Noting that the average volume of particles is inversely proportional to the number of particles we arrive to the scaling law

$$\widetilde{k}_B = \frac{V}{V^*}k_B, \tag{6.27}$$

where V is the average volume of particles in the system with N particles and V^* is the average volume of particles in the system with N^* particles. Next, we rewrite Eq. (6.25) as

$$s_i^{lm} = \sqrt{\frac{2\mu V^* \widetilde{k}_B T \delta^{lm} n_i}{V_i \Delta t}}\xi_i^{lm}, \tag{6.28}$$

where we replace V with $V_i = 1/n_i$, the volume of particle i. We numerically determined that the correct hydrodynamics is obtained with $V^* = 2h^3$.

Therefore, we set the expression for stress to:

$$s_i^{lm} = \sqrt{\frac{4h^3\mu T^* \delta^{lm} n_i^2}{\Delta t}}\xi_i^{lm}, \tag{6.29}$$

where $T^* = \widetilde{k}_B T$.

To integrate the SPH Eqs. (6.17) and (6.20), an explicit "velocity-Verlet" algorithm (Allen & Tildesley, 1989) with adaptive time stepping is employed:

$$\begin{aligned}
\boldsymbol{r}_i(t+\Delta t) &= \boldsymbol{r}_i(t) + \Delta t \boldsymbol{v}_i(t) + 0.5\Delta t^2 \boldsymbol{F}_i(t)/m_i && (6.30)\\
C_i(t+\Delta t) &= C_i(t) + 0.5\Delta t\,[G_i(t) + G_i(t+\Delta t)] && (6.31)\\
m_i(t+\Delta t) &= m_i^s + \kappa C_i(t+\Delta t) && (6.32)\\
\boldsymbol{v}_i(t+\Delta t) &= \frac{m_i(t)\boldsymbol{v}_i(t) + 0.5\Delta t\left[\boldsymbol{F}_i(t) + \boldsymbol{F}_i(t+\Delta t)\right]}{m_i(t+\Delta t)}, && (6.33)
\end{aligned}$$

where $\boldsymbol{F}_i(t+\Delta t)$ is computed as a function of $\boldsymbol{r}_j(t+\Delta t)$ and $\boldsymbol{v}_j(t)$ $(j = 1,...,N)$. At each time step stability of the solution is ensured by satisfying the time step constraints (Morris, 1997; Tartakovsky & Meakin, 2005b):

$$\Delta t = \min\left[\varepsilon \min_i \frac{h}{3|\boldsymbol{v}_i|}, \quad \varepsilon \min_i \sqrt{\frac{h}{3|\boldsymbol{a}_i|}}, \quad \varepsilon \min_i \frac{\rho_i h^2}{9\mu}, \quad \varepsilon \min_i \frac{h^2}{9D}\right], \tag{6.34}$$

where $|\cdot|$ is the magnitude of a vector, $\Delta t = (\Delta t_k + \Delta t_{k-1})/2$ with subscript k denotes the current and previous time step, ε is a factor (in general less then one) needed to ensure proper convergence behavior in the mesoscopic SPH model and $a_i = d\boldsymbol{v}_i/dt$.

6.4 Smoothed Dissipative Particle Hydrodynamics

In the SDPD method, the stochastic flow equation is obtained by applying the fluctuation-dissipation theorem directly to the discretized momentum

conservation equation:

$$\begin{aligned}\frac{D(m_i\mathbf{v}_i)}{Dt} &= -\sum_{j=1}^{N}\left(\frac{P_j}{n_j^2}+\frac{P_i}{n_i^2}\right)\frac{\mathbf{r}_{ij}}{r_{ij}}\frac{dW(r_{ij},h)}{dr_{ij}} \\ &\quad+\sum_{j=1}^{N}\frac{5(\mu_i+\mu_j)}{n_i n_j}\frac{(\mathbf{v}_{ij}\cdot\mathbf{r}_{ij})}{r_{ij}^2}\frac{\mathbf{r}_{ij}}{r_{ij}}\frac{dW(r_{ij},h)}{dr_{ij}}+m_i\boldsymbol{g} \\ &\quad+\sum_{j=1}^{N}\mathbf{F}_{ij}^{S} \end{aligned} \tag{6.35}$$

Specifically, the fluctuation dissipation theorem is used to relate the stochastic force $\mathbf{F}_{ij}^{S}$ to the viscous (dissipative) force

$$\boldsymbol{F}_{ij}^{(visc)} = \frac{5(\mu_i+\mu_j)}{n_i n_j}\frac{(\mathbf{v}_{ij}\cdot\mathbf{r}_{ij})}{r_{ij}^2}\frac{\mathbf{r}_{ij}}{r_{ij}}\frac{dW(r_{ij},h)}{dr_{ij}} \tag{6.36}$$

as

$$F_{ij}^{S,l} = B_{ij}\frac{r_{ij}^{l}}{|r_{ij}|}\frac{\tilde{\xi}_{ij}^{l}}{\sqrt{dt}}, \tag{6.37}$$

where

$$B_{ij} = \sqrt{-2\widetilde{k}_B T\frac{5(\mu_i+\mu_j)}{n_i n_j}\frac{1}{r_{ij}}\frac{dW(r_{ij},h)}{dr_{ij}}} \tag{6.38}$$

and $\tilde{\zeta}_{ij}^{l}=\tilde{\zeta}_{ji}^{l}$ is a random number from a Gaussian distribution with zero mean and unity variance, and superscript l denotes the l-component of the vectors.

6.5 Validation of the SPH method for LLNS equations

We study the accuracy of the SPH solution of the LLNS equations by comparing thermodynamic quantities such as kinetic temperature and velocity variance obtained from the SPH simulations and analytical solutions.

6.5.1 Convergence of SPH solution of the LLNS equations

First, we study the convergence behavior of the SPH solution of the stochastic NS equations with respect to time step and spatial resolution.

Figure 6.1 shows the dependence of T^*_{kin}/T^* on the time step. The normalized kinetic temperature $T^*_{kin} = \widetilde{k}_B T_{kin}$ is computed as

$$T^*_{kin} = \frac{1}{3}\sum_{i=1}^{N} m_i(\delta v^2_{x,i} + \delta v^2_{y,i} + \delta v^2_{z,i}), \tag{6.39}$$

where $\delta v_{k,i} = v_{k,i} - \langle v_k \rangle$ ($k = x,y,z$) are the fluctuations of k-component of the velocity of particle i around the mean velocity in k-direction, $\langle v_k \rangle = \frac{1}{N}\sum_{i=1}^{N} v_{k,i}$. In our simulations there are no sources of energy other than random fluctuations and the kinetic temperature of the system should theoretically be equal to the temperature that is prescribed in Eq. (6.7), i.e. T^*_{kin}/T^* should be equal to one. In the simulations shown in Fig. 6.1, the model domain has the size $L_x = L_y = L_z = 8\,h$ and is periodic in all

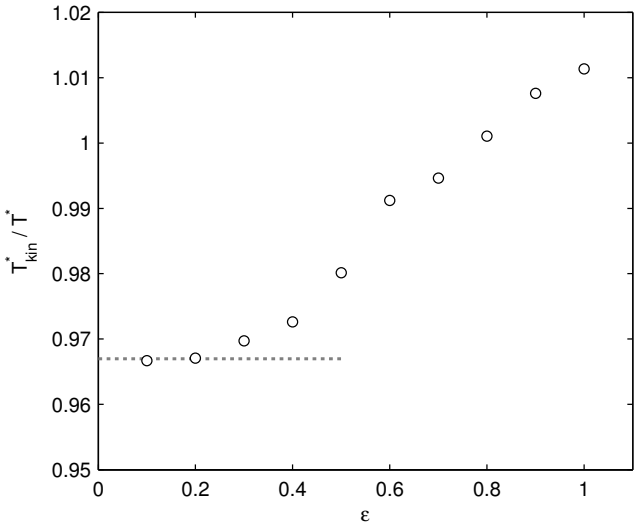

FIG. 6.1. Effect of time step reduction factor ε on the deviation of the system temperature from the prescribed temperature. $T^* = 0.01$, $n_{eq} = 20$, $\rho_0 = 30$, $m = 1.5$ and $\mu = 10$. Convergence is reached for $\varepsilon \leq 0.25$.

three directions. The prescribed temperature is $T^* = 0.01$, number density $n_{eq} = 20$, mass density of $\rho_{eq} = n_{eq} m_0 = 30$, mass $m_i = m_0 = 1.5$ and viscosity $\mu = 10$. We found domain size effects to be negligible when $L_x = L_y = L_z \geq 8\,h$. Convergence is reached at about $\varepsilon = 0.25$ using the time step criteria Eq. (6.34). In order to keep computation times lower, we set $\varepsilon = 0.5$ in all of the following simulations which yields a difference of about 1% compared to $\varepsilon = 0.25$. We should note that the kinetic temperature is proportional to the velocity variance. Therefore, Fig. 6.1 also illustrates that for sufficiently small Δt, the SPH model correctly predicts the velocity variance. Next, we study the effect of resolution (i.e. n_{eq}) on the accuracy of the SPH model. In Fig. 6.2 we plot T^*_{kin}/T^* versus the equilibrium density n_{eq}. In the simulations shown in this figure, the equilibrium mass density is kept constant ($\rho_{eq} = 30$) and the mass of the particles is set to $m_i = m_0 = \rho_{eq}/n_{eq}$. It is important to note that the speed of sound

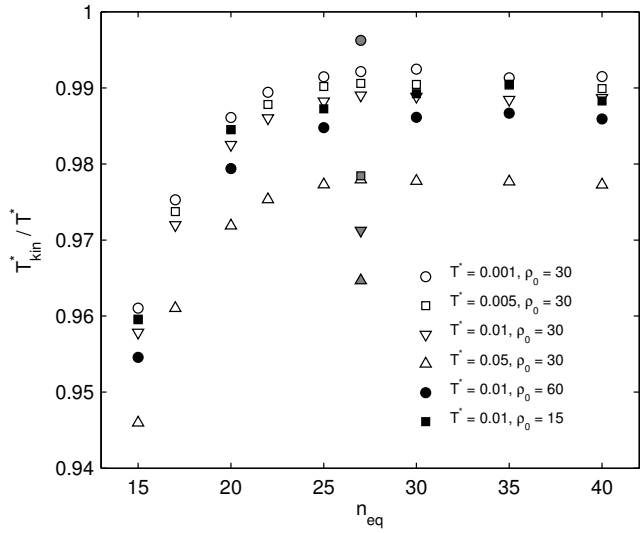

FIG. 6.2. Scaling of kinetic system temperature with changes in resolution and changes of the mass density ρ_0. Here $\mu = 10$ and $\varepsilon = 0.5$. Convergence is reached for $n_{eq} \geq 20$. Gray markers correspond to the kinetic temperatures for the SDPD implementation of the stochastic stress at $n_{eq} = 27$.

should scale with mass as

$$c \sim \sqrt{\frac{\widetilde{k}_B T}{m_0}} = \sqrt{\frac{2h^3 \rho_{eq} T^*}{m_0^2}}. \tag{6.40}$$

To obtain this scaling in the SPH model, we start with the expression for the pressure variance derived in LANDAU & LIFSHITZ (1987):

$$\langle \delta P^2 \rangle = \frac{\rho_{eq} k_B T c^2}{\Delta V}, \tag{6.41}$$

where δP is the fluctuation of pressure around the mean pressure. Noting that in the above equation $\Delta V = 1/n_{eq}$, $\delta P = c^2 m_i \delta n$ (δn is the fluctuation of density around n_{eq}) and $\rho_{eq} = m_i n_{eq}$ and replacing k_B with $\widetilde{k}_B$ we obtain the scaling law for the speed of sound

$$c = \beta \sqrt{\frac{2h^3 \rho_{eq} T^*}{m_0^2}}, \tag{6.42}$$

where β is the inverse of the coefficient of variation of the particle number density,

$$\beta = \frac{n_{eq}}{\sqrt{\langle \delta n^2 \rangle}}. \tag{6.43}$$

This results in the EOS

$$P_i = T^* 2h^3 n_{eq} n_i \beta. \tag{6.44}$$

We numerically determined that to recover the correct hydrodynamic behavior, β should be approximately equal to 5.5. A significantly smaller β results in a high compressibility of the fluid and may lead to numerical instability. For higher β (i.e. for less compressible fluids), the thermodynamic variables become dependent on the speed of sound. Therefore, in all our simulations we set $\beta = 5.5$. Figure 6.2 shows T^*_{kin}/T^* for

$T^* = 0.001, 0.005, 0.01, 0.05$. For all considered temperatures, convergence is reached at a number density of about $n_{eq} = 20$ with the error being less than 2%. Kinetic temperatures obtained from simulations using an SDPD implementation of the stochastic force are slightly higher with a maximum error of about 4%.

It follows from Eq. (6.39) that for all SPH particles having the same masses $m_i = \rho_0/n_{eq}$, the velocity variance $\sigma_v^2 = \frac{1}{3}\sum_{i=1}^{N}(\delta v_{x,i}^2 + \delta v_{y,i}^2 + \delta v_{z,i}^2)$ should scale as

$$\sigma_v^2 = \frac{T^*}{m_0} = \frac{n_{eq}T^*}{\rho_0}, \tag{6.45}$$

i.e. that for a fluid with a given mass density ρ_0, the velocity variance is inversley proportional to the mass of the SPH particles or linearly proportional to the resolution n_{eq}.

6.5.2 Spatial statistics of hydrodynamics variables

Here we further validate the SPH model for the LLNS equations by comparing statistics of pressure and velocity obtained from the SPH simulations and analytical solutions.

Combining Eqs. (6.40) and (6.41) leads to the scaling law for the pressure variance:

$$\langle \delta P^2 \rangle \sim \frac{h^3 \rho_{eq}^3 T^{*2}}{m_0^3}\beta = h^3 n_{eq}^3 T^{*2}\beta. \tag{6.46}$$

Figure 6.3 plots $\langle \delta P^2 \rangle = \frac{1}{N}\sum_{i=1}^{N}(P_i - \langle P \rangle)^2$ (where $\langle P \rangle = \frac{1}{N}\sum_{i=1}^{N} P_i$) as a function of n_{eq} and for all prescribed T^*. It can be seen that $\langle \delta P^2 \rangle$ correctly scales as n^3 (or $1/m_0^3$) for the considered range of number densities and temperatures. Figure 6.4 shows the correlation function of the pressure fluctuations, $\langle \delta P(\mathbf{r}_i)\delta P(\mathbf{r}_j)\rangle / \langle \delta P^2 \rangle$, as a function of $r_{ij} = |\mathbf{r}_i - \mathbf{r}_j|$, obtained from the SPH simulations. The computed pressure correlation function agrees well with the theoretical expression (Bell et al., 2007):

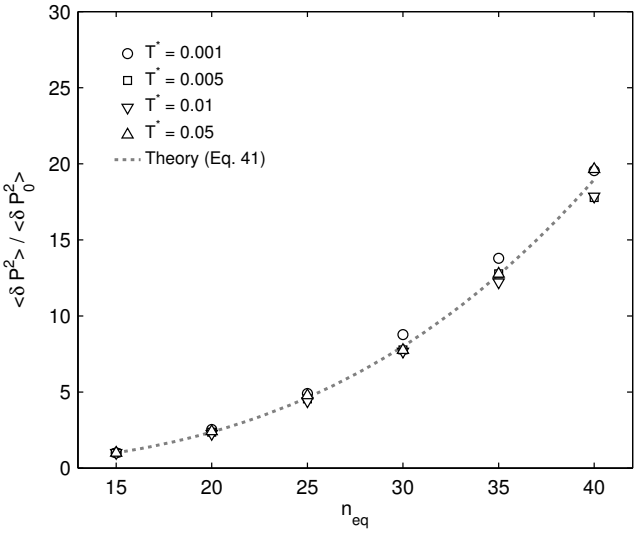

FIG. 6.3. Scaling of the pressure variance. $< \delta P_0^2 >$ is obtained at $n_{eq} = 15$.

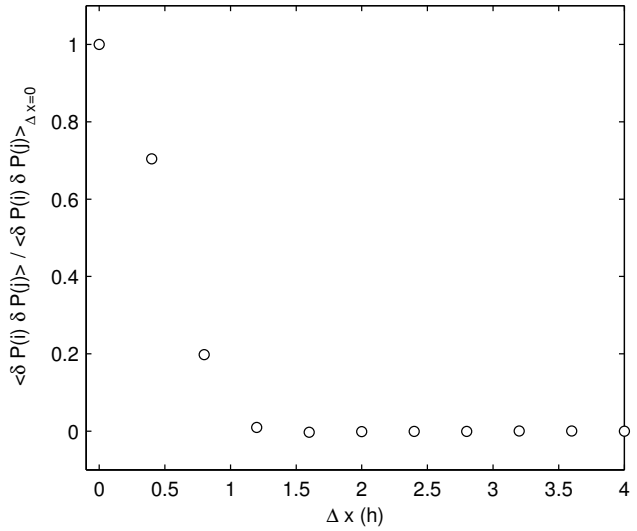

FIG. 6.4. Spatial correlation of pressure fluctuations. $T^* = 0.05$, $n_{eq} = 27$, $\rho_0 = 30$.

$$\frac{\langle \delta P(\mathbf{r}_i) \delta P(\mathbf{r}_j) \rangle}{\langle \delta P^2 \rangle} = \delta_{ij}. \tag{6.47}$$

Due to the smooth SPH interpolation, the unit peak in the correlation

function at $r_{ij} = 0$ is diffused over the $0 \leq r_{ij} \leq h$ region, however, the correlation function correctly vanishes for $r_{ij} > h$. The theoretical form of the velocity correlation and cross-correlation functions is given by BELL et al. (2007) as:

$$\langle \delta v_k(\mathbf{r}_i) \delta v_k(\mathbf{r}_j) \rangle = \langle \delta v_k^2 \rangle \delta_{ij} \tag{6.48}$$

and

$$\langle \delta v_k(\mathbf{r}_i) \delta v_l(\mathbf{r}_j) \rangle = 0 \quad k \neq l, \tag{6.49}$$

where v_k (k = 1,2,3) is the k-component of the velocity vector. Figure 6.5 shows the spatial cross-correlation function of the velocity components v_x and v_y, which behave entirely uncorrelated as expected from Eq. (6.49). The spatial correlation function of velocity $\langle \delta v_x(\mathbf{r}_i) \delta v_x(\mathbf{r}_j) \rangle$ shown in Fig. 6.6 exhibits the same behavior as the pressure correlation function, i.e. we obtain a correct peak value for $r_{ij} = 0$ and a vanishing correlation function for $r_{ij} > h$, h. Though not shown here, the correlation function of the y and z components of velocity have the same correct behavior as shown in

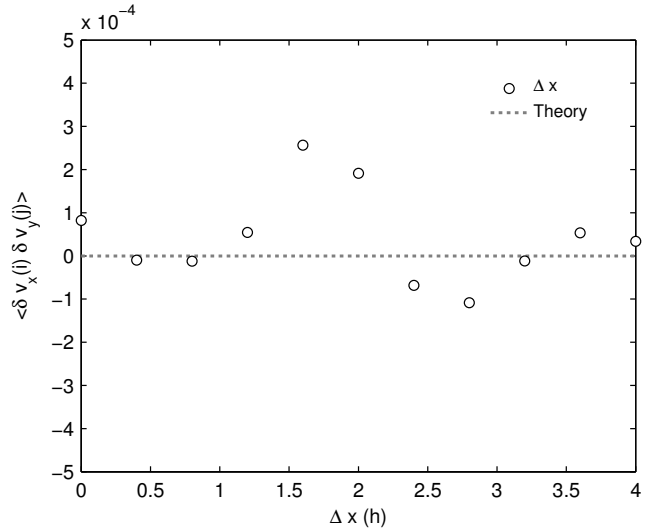

FIG. 6.5. Correlation of velocity components v_x and v_y.

Fig. 6.6.

6.5.3 Self-diffusion coefficient

The coefficient of mechanical diffusion (describing the "diffusion" of the SPH particles), i.e. the self-diffusion coefficient has a similar scaling behavior as the velocity variance. For example, for an SDPD model with a slightly different discretization of the viscous force than used in this work, the self-diffusion coefficient was obtained as (LITVINOV et al., 2009):

$$D = \frac{\tau k_B T}{3} = \zeta \frac{n_{eq} h^2 k_B T}{\mu}, \tag{6.50}$$

with $\zeta = \frac{1}{12}$. For our SPH model, we numerically determined the value of $\zeta = 0.045$.

To validate the scaling of D, we compute the diffusion coefficient from SPH simulations over the same range of number densities and temperatures as in the previous example. The principal components of the diffusion

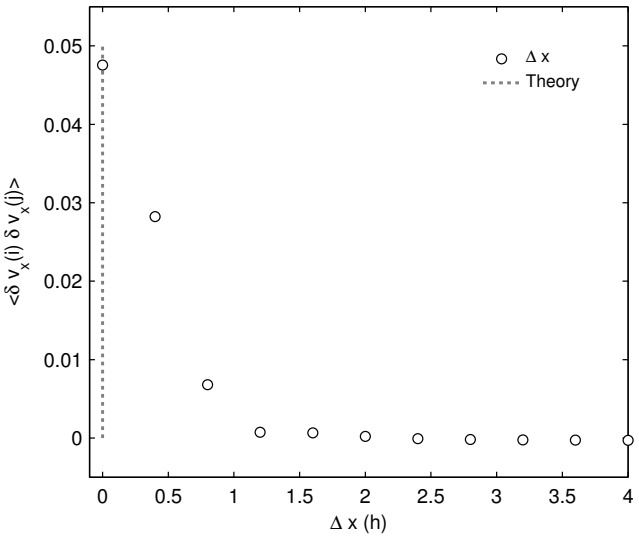

FIG. 6.6. Spatial correlation of velocity fluctuations.

tensor D_{ll}, $l = 1,2,3$ are obtained from the expression

$$\frac{dI_{ll}}{dt} = 2D_{ll} \tag{6.51}$$

and the diffusion coefficient is calculated as:

$$D = \frac{1}{3}\sum_{l=1}^{3} D_{ll}. \tag{6.52}$$

Here the first and second moments of the particle displacements in l direction are computed as

$$I_l(t) = \sum_{i}^{N} (x_{l,i} - x_{l,i}^0)/N \tag{6.53}$$

and

$$I_{ll}(t) = \sum_{i}^{N} I_{ll} - (x_{l,i} - x_{l,i}^0)^2/N, \tag{6.54}$$

where N is the total number of particles and x^0 denotes the initial particle position.

Figure 6.7 shows the resulting scaling of the diffusion coefficients with changing resolution, which agrees with Eq. (6.50).

The same correct linear scaling for the diffusion coefficient is obtained for the whole temperature range considered in the simulations (see Fig. 6.8).

The corresponding Schmidt numbers for all simulations are shown in Fig. 6.9.

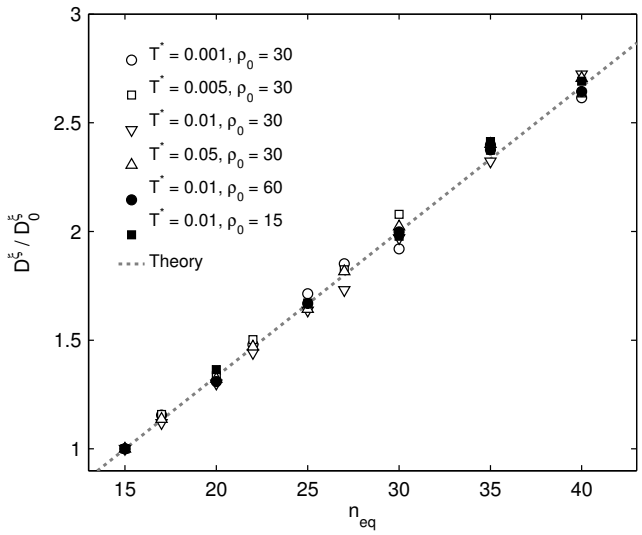

FIG. 6.7. Scaling of the stochastic diffusion coefficient with increasing resolution, where D_0^ξ is the diffusion coefficient at $n_{eq} = 15$ for each temperature T^*. D^ξ is obtained by linear regression of MSD/Δt where MSD $> 1.0\,h$.

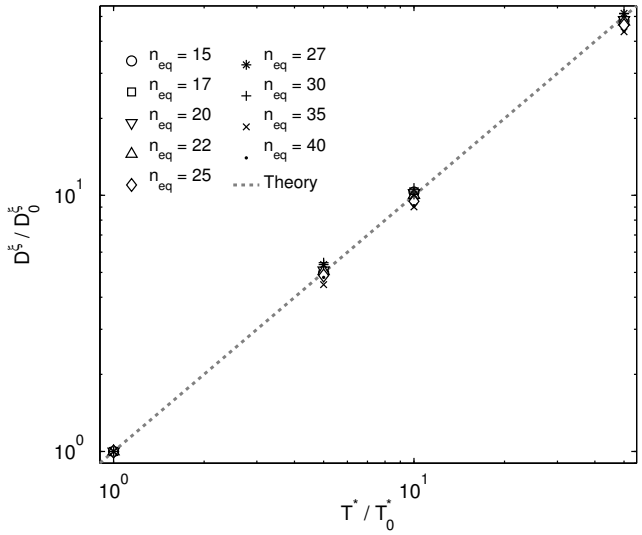

FIG. 6.8. Scaling of the stochastic diffusion coefficient with increasing temperature T^*. Here $T^* = 0.001, 0.005, 0.01, 0.05$ ($T_0^* = 0.001$) and D_0^ξ corresponds to the diffusion coefficient at $T^* = 0.001$ for each number density n_{eq}. The diffusion coefficient D^ξ is obtained by linear regression of MSD/Δt where MSD $> 1.0\,h$.

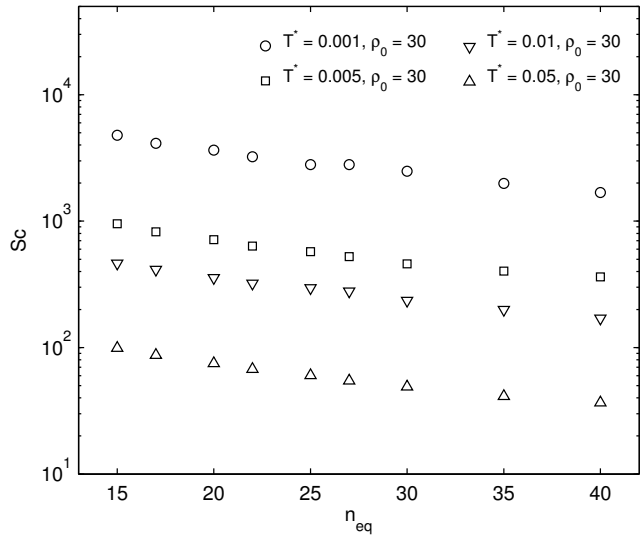

FIG. 6.9. Schmidt numbers *Sc* determined from the simulations.

6.6 SPH model for highly diluted solutions

Here we study the enhancement of Fickian diffusion by thermal fluctuations in non-equilibrium systems. In this section we study highly diluted solutions, i.e. we assume that the density of the solution (and, hence, the mass of the SPH particles) does not depend on the concentration (mass fraction) of the solution, C. To isolate the effect of stochastic fluxes in Eq. (6.3) we assume that the advection velocity is zero and only solve Eq. (6.3). As shown numerically in (Donev et al., 2011a; Donev et al., 2011b), the effective diffusion coefficient D^{eff} consists of a deterministic Fickian part D^F and a stochastic contribution D^ξ: $D^{eff} = D^F + D^\xi$. In turn, D^ξ is a result of the random advection (which is characterized by the self-diffusion coefficient in Eq. 6.50) and the random flux $\boldsymbol{J}$ in the stochastic advection-diffusion equation.

In order to study the effect of diffusion enhancement we simulate a spherical plume with radius $3\,h$ and an initial uniform concentration $C_0 = 1.0$ surrounded by a solution with zero concentration. A periodic domain with the dimensions $L_x = L_y = L_z = 16\,h$, is used in this study. The SPH particles are initially placed on a regular grid. The initial number density in these simulations is $n_{eq} = 27$, the viscosity is $\mu = 10$, and the mass density of the solvent is $\rho_0 = 30.0$, such that the mass of solvent carried by particle i is $m_i = \rho_0/n_{eq} = 1.11$. We run the simulations with four different temperatures ($T^* = 0.001, 0.005, 0.01$ and 0.05), the ratio D^F/D^ξ ranging from $2-10$ and the value of D^ξ is estimated from Eq. (6.50).

The resulting diffusion coefficient is determined from simulations as $D = \frac{1}{3}(D_{11} + D_{22} + D_{33})$, where D_{ll} is found as

$$\frac{dI_{ll}}{dt} = 2D_{ll}. \tag{6.55}$$

The second moments of the plume in l direction are calculated as

$$I_{ll} = \frac{1}{M}\sum_i (x_{l,i} - I_l)^2 C_i m_i, \tag{6.56}$$

the first moments are found as

$$I_l = \frac{1}{M} \sum_i x_{l,i} C_i m_i, \tag{6.57}$$

and the total mass of the solute is

$$M = \sum_i C_i m_i. \tag{6.58}$$

In order to study the accuracy of the SPH solution of the stochastic and deterministic advection-diffusion equations we solve: (1) the deterministic diffusion equation in the absence of advection; (2) the coupled LLNS and stochastic advection equation ($D^F = 0$); and (3) the coupled LLNS and stochastic advection-diffusion equations. In the first case we compute the resulting diffusion coefficient and compare it with the prescribed Fickian diffusion coefficient. In the second case we numerically compute D^ξ. Once

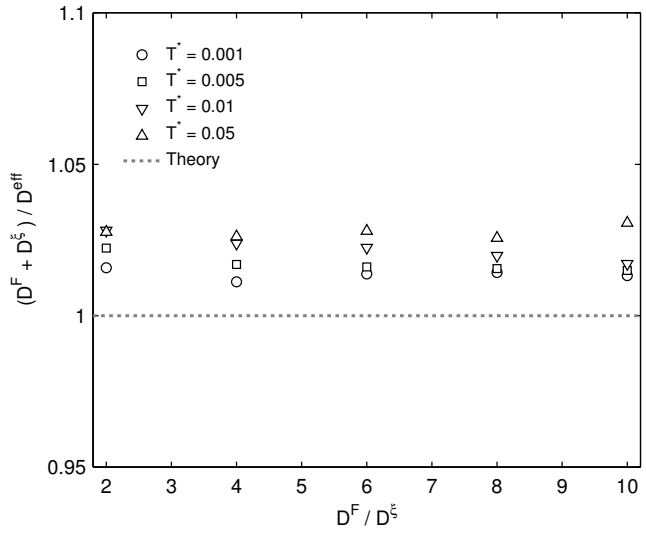

FIG. 6.10. Accuracy of the diffusion enhancement for different ratios of D^F/D^ξ. Diffusion coefficients $D^\xi + D^F$ are obtained from simulations where only Fickian diffusion is active or where only thermal fluctuations occur and then compared to simulations where both are present.

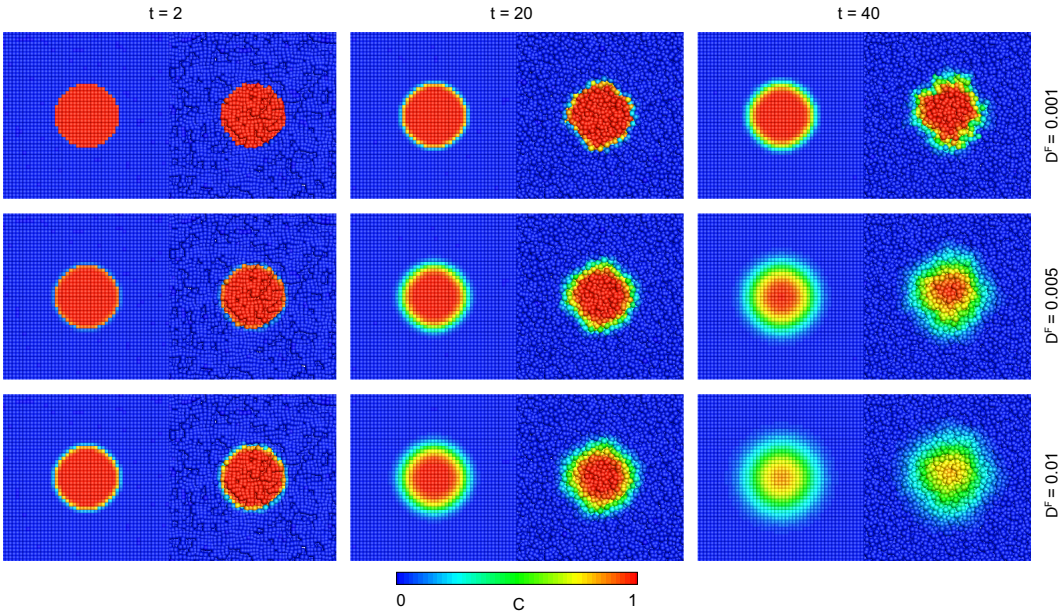

FIG. 6.11. Cross-section of spherical plumes at times $t = 2{,}20{,}40$ at a temperature of $T^* = 0.01$. Left picture at each time corresponds to pure Fickian diffusion, right side to Fickian diffusion enhanced by thermal fluctuations at the given temperature. $D^F/D^\xi = 2{,}4{,}8$ for $D^F = 0.001, 0.005, 0.01$, i.e. the impact of thermal fluctuations on the concentration field decreases from top to bottom. Cubic domain with edge size $16\,h$ with an initial plume diameter of $6\,h$.

the deterministic solution is verified and D^ξ is evaluated, we compute the effective diffusion coefficient in the third simulation as

$$D^{eff} = D^\xi + D^F \tag{6.59}$$

and compare this value with the effective diffusion coefficient obtained from the SPH solution of the LLNS and stochastic diffusion equation with the corresponding D^F and T^*.

The results of the simulations indicate a very good agreement between D^{eff} obtained from Eq. (6.59) and the solution of the full stochastic diffusion equation (see Fig. 6.10). The relative errors are between 0.8% and 2.5%.

Figure 6.11 shows a cross section of the spherical plume for three different ratios of $D^F/D^\xi = 2,4,8$ at time $t = 2,20,40$ and a temperature of $T^* = 0.01$. Results demonstrate that for rather high ratios of D^ξ/D^F, that is, a mesoscopic scale where the microscopic effects begin to dominate the transport description, the concentration front is characterized by clear fluctuations (e.g. upper right picture in Fig. 6.11). In contrast, for a lower ratio of D^ξ/D^F this effect is less pronounced as the time evolution of the concentration front is controlled by the Fickian description of diffusive transport.

6.7 SPH solution of the coupled LLNS and stochastic diffusion equations

Here we use the coupled stochastic SPH model to study the effect of gravity on thermally enhanced diffusive transport. Specifically, we study perturbations of a front between two miscible fluids due to random stresses and fluxes in the momentum and advection-diffusion equations. In the coupled model we solve the LLNS and stochastic advection-diffusion equations with the mass of SPH particles (and density of the solution) depending on C according to Eq. (6.23).

We simulate a three-dimensional domain filled with the solution of a conservative species C. We consider two cases: (1) initial C is zero in the upper half of the domain and one in the lower half of the domain; and (2) initial C is one in the upper half of the domain and zero in the lower half of the domain. In the first case, the fluid configuration is stable, i.e. the initially sharp front widens due to molecular diffusion and perturbs due to random fluctuations in fluid velocity and diffusive fluxes. In this case we use the SPH model to study how gravity suppresses perturbations of the front (also known as giant fluctuations). In the second case, the flow configuration is unstable as the heavy fluid on top tries to replace the light fluid on the bottom, a phenomenon known as the Rayleigh-Taylor instability. In this case we use the stochastic SPH model to study the effect of random stresses and diffusive fluxes on the development of the Rayleigh-Taylor instability.

In both study cases, the domain size is $L_x = L_y = 16\,h$ and $L_z = 8\,h$. The upper and lower horizontal boundaries are assumed to be impermeable

and all the vertical boundaries are treated as periodic. To impose no-flow boundary conditions at the bottom of the domain we set a layer of immobile particles with the thickness $\Delta L_z = 1\,h$. Particles in this layer contribute to the density evolution and forces in the LLNS equations (i.e. the summations in Eqs. (6.17) and (6.16) are over all fluid and boundary particles). In addition, a bounce-back condition is used to implement the no-flow boundary condition. The bounce-back boundary condition is implemented by inverting the velocity vector of particles crossing the impermeable boundary ($z_i < 1\,h$ or $z_i > 16\,h$) and returning these particle into the fluid domain along their "exit" trajectories. The zero-flux boundary condition for the stochastic advection-diffusion equation is imposed by including only fluid particles in the summations in Eq. (6.24). The solvent mass for all particles is set to $m_i^0 = m_0 = 1$ and m_i is computed according to Eq. (6.23). The parameter κ in Eq. (6.23) is related to the Atwood number, A, via

$$A = \frac{m(C=1) - m(C=0)}{m(C=1) + m(C=0)} = \frac{\kappa}{2m^0 + \kappa}, \tag{6.60}$$

where $m(C=1)$ and $m(C=0)$ are the masses of particles with $C=1$ and $C=0$, respectively.

6.7.1 Giant fluctuations

Here we consider two scenarios: (1) with gravity; and (2) in the absence of gravity. In both scenarios, the solution with $C=0$ ("light fluid") lies on top of the solution with $C=1$ ("heavy fluid"), the Atwood number is $At = 0.83$ ($\kappa = 10$) and the temperature is set to $T^* = 0.001$. In the first scenario, the system is initially equilibrated, i.e. brought to hydrostatic condition by solving only the NS equations. $C=0$ and 1 are maintained in the upper and lower part of the domain, respectively, during the equilibration process. In the absence of gravity, there is no need to pre-equilibrate the particle system in the simulations of the second scenario. For each scenario we conduct three simulations: (1) no Fickian diffusion, i.e., $D^F = 0.0$; (2) $D^F = 0.001$; and (3) $D^F = 0.005$.

Figure 6.12 shows the cross-sections of the resulting concentrations at

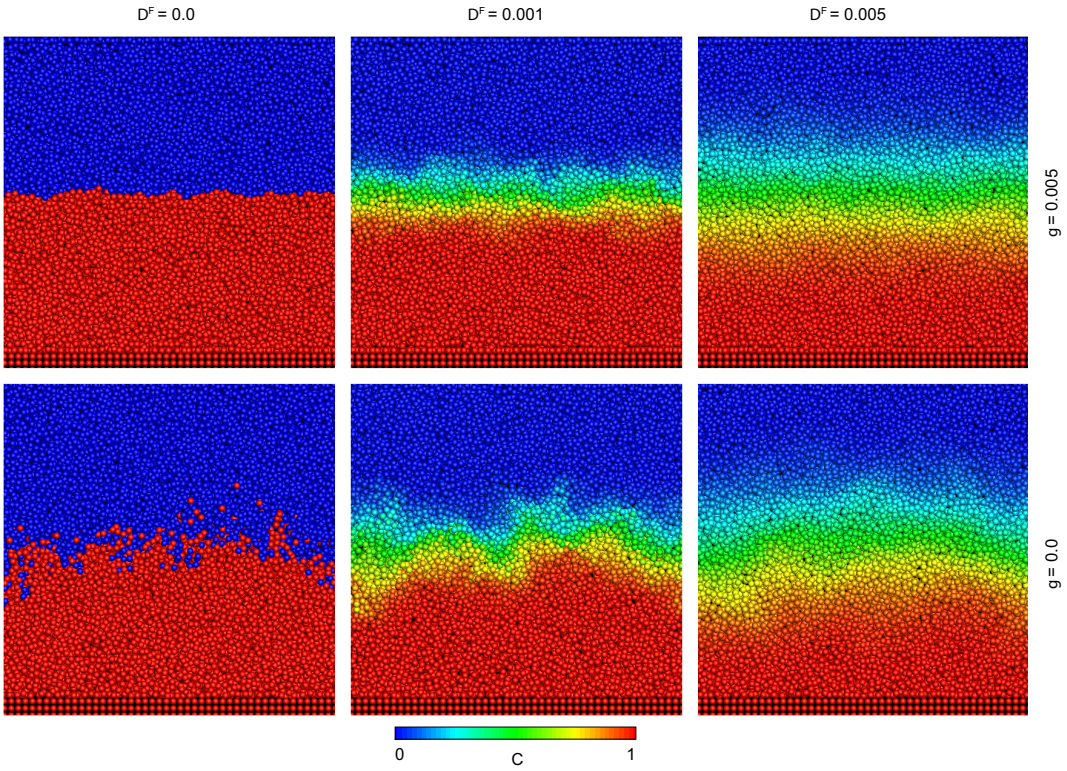

FIG. 6.12. Cross-section of the interface between a heavy fluid and a light fluid on top at time $t = 414$. Temperature is $T^* = 0.001$, $\kappa = 10$, $\mu = 10$. (Upper row) In the presence of gravity with same increase of Fickian diffusion from left to right. (Lower row) Without gravity and increasing Fickian diffusion from left to right.

time $t = 414$ for each of the six simulations described above. Subfigures in the top row show the distribution of C obtained from the simulations in the absence of gravity, where one can clearly see the presence of giant fluctuations or perturbations of the front. Subfigures in the bottom row show the distribution of C obtained from the simulations with gravity. It can be seen that gravity significantly reduces front perturbations for all considered values of D^F, but the effect of gravity becomes less pronounced with increasing D^F. As D^F becomes significantly larger than D^ξ (or when $T^* \to 0$), the stochastic diffusion reduces to a deterministic diffusion and thus fluctuations completely disappear.

Structure factor

In order to analyze the diffusive interface we decompose the two-dimensional concentration field into its Fourier modes and wave vectors q to obtain a one-dimensional, radially averaged, static power spectrum $\boldsymbol{S}(q)$ (REDIES et al., 2007). We remap the original particle data onto a regular grid with $L_xR \times L_yR$ cells by averaging the particle concentration $\boldsymbol{C}(x,y,z)$ of all particles in each cell over the depth L_z, excluding the lower boundaries, to create a two-dimensional concentration field $\boldsymbol{C}(x,y)$ normal to z (see Fig. 6.14). Here $R = 1$ is chosen to minimize interpolation errors due to the resampling and $L_xR = L_yR = N_x = N_y = N$. The averaging of the particle concentrations can be understood as a numerical equivalent of the common experimental shadowgraphy technique (BROGIOLI et al., 2000; VAILATI et al., 2006). We follow the work of BROGIOLI et al. (2000) and VAILATI et al. (2011) and obtain the static power spectrum from the relative concentration $\boldsymbol{C}^*(x,y) = \left[\boldsymbol{C}(x,y) - \boldsymbol{C}_0(x,y)\right] / \boldsymbol{C}_0(x,y)$, where $\boldsymbol{C}_0(x,y)$ denotes the initial concentration. To convert the two-dimensional Fourier transform

$$\boldsymbol{F}(q_x,q_y) = \sum_{x=0}^{N_x-1} \sum_{y=0}^{N_y-1} \boldsymbol{C}^*(x,y) e^{-i2\pi(q_x x/N_x + q_y y/N_y)} \tag{6.61}$$

and its complex result $\boldsymbol{F}(q_x,q_y)$ into a one-dimensional equivalent we first construct a two-dimensional power spectrum $\boldsymbol{S}(q_x,q_y) = \left|\mathrm{Re}\left[\boldsymbol{F}(q_x,q_y)\right]\right|^2$, where Re denotes the real parts of $\boldsymbol{F}$ and the first and third (second and fourth) quadrants of the field $\boldsymbol{F}$ have been swapped to relocate the lowest spatial frequencies q_x and q_y to the center.

We then rotate a sampling profile line with endpoints $\boldsymbol{P}_a$ and $\boldsymbol{P}_b$ about the center coordinate $\boldsymbol{P_a} = (N/2 = 0, N/2 = 0)$ in one degree increments, where

$$\boldsymbol{P_b} = \frac{N}{2}(1 + \boldsymbol{u}) \qquad \boldsymbol{u} = (cos(\theta), sin(\theta)), \tag{6.62}$$

and compute power spectrum profiles $\boldsymbol{S}^{\theta}_{ab}(q) = q$ between $\boldsymbol{P}_a$ and $\boldsymbol{P}_b$

to obtain the one-dimensional radially averaged power spectrum $\boldsymbol{S}(q) = \frac{1}{360}\sum_{\theta=0}^{\theta=2\pi} \boldsymbol{S}_{ab}$. In the absence of gravity, the nonequilibrium concentration fluctuations are known to exhibit a characteristic q^{-4} decay of the power-spectrum (KIRKPATRICK et al., 1982). However, this can only be observed over a limited range of wavenumbers due to several effects that relax the fluctuations and eliminate the scale-invariant character. At low wavenumbers the primary reason is a finite size of the domain (VAILATI et al., 2006). Gravity dampens the fluctuations leading to a much weaker dependence of the power spectrum on wavenumber (VAILATI et al., 2011).

We obtain the power spectrum $\boldsymbol{S}(q)$ from simulations similar to the ones described in Sec. 6.7 with the domain size $L_x = L_y = 32\,h$ and $L_z = 16\,h$, temperature $T^* = 0.003$ (which corresponds to a Schmidt number of $Sc \approx 1000$), $\kappa = 10$. In these simulations, the light fluid ($C = 0$) lies on top of the heavy fluid ($C = 1$). According to ORTIZ DE ZÁRATE et al. (2004) and VAILATI et al. (2011), in the absence of gravity the scale-invariant characteristics of the power spectrum are independent of the fluid configuration and concentration gradient and scale as

$$S(q)/S^{\infty} = (q^4 + Bq^2 + \Lambda^4)^{-1}. \tag{6.63}$$

Here $B = \Lambda \tanh(\Lambda/2)\,[2\Lambda \tanh(\Lambda/2) - 4]$ and Λ is a fitting constant. To normalize the data, the asymptotic value of $S^{\infty} = \lim_{q\to\infty} S(q)q^4$ is ob-

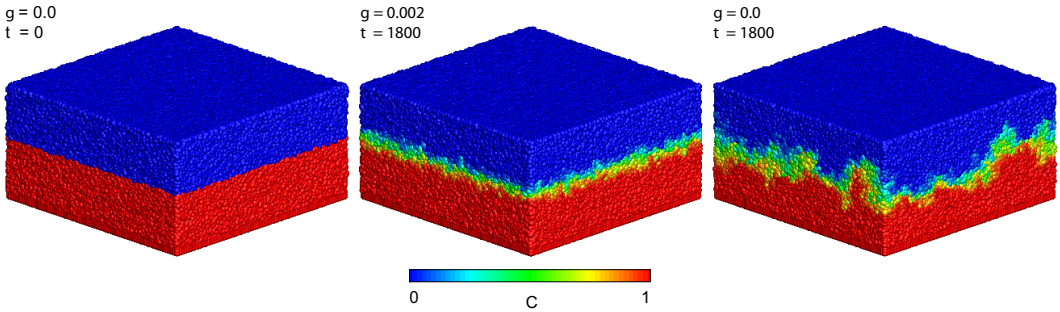

FIG. 6.13. Concentration fields $\boldsymbol{C}(x,y,z)$ at $t = 0$ and $t = 1800$ with gravity (middle) and without gravity (right) at a temperature of $T^* = 0.003$.

tained from a fit of the linear part of $S(q)q^4$ which corresponds to fitting a power-law function $S^{\infty}q^{-4}$ to $S(q)$. Figure 6.13a shows the initial concentration distribution and Figs. 6.13b and c show the concentration distribution at time $t = 1800$ with and without gravity, respectively. Figure 6.14 depicts the corresponding remapped two-dimensional concentration fields $\boldsymbol{C}^*(x,y)$ used to obtain the power spectra. Figure 6.15 shows the resulting power spectra scaled onto the universal curve according to Eq. (6.63) with $\Lambda = 2.33$ and the theoretical scaling for bounded and unbounded conditions. This confirms the scale-invariant nature of the fluctuation front and the saturation due to finite-size effects at low wave numbers. The power spectrum of the interface in the presence of gravity clearly shows the saturation of the divergence at low wave numbers. It should be noted, that even when gravity relaxes the interface fluctuations, the theory also predicts a q^{-4} divergence at very high wave numbers (VAILATI et al., 2011) which is only weakly visible in our simulations. It is believed that this is an effect of insufficient resolution and simulations with $n_{eq} > 27$ might be necessary to properly resolve the divergence.

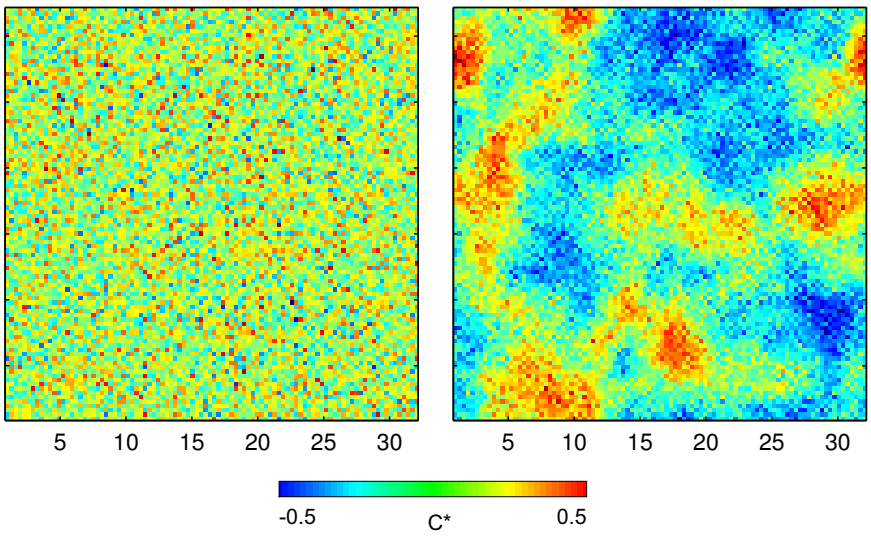

FIG. 6.14. Two-dimensional concentration fields $\boldsymbol{C}^*(x,y)$ with $R = n^{1/3}$ at $t = 1800$ with gravity (left) and without gravity (right).

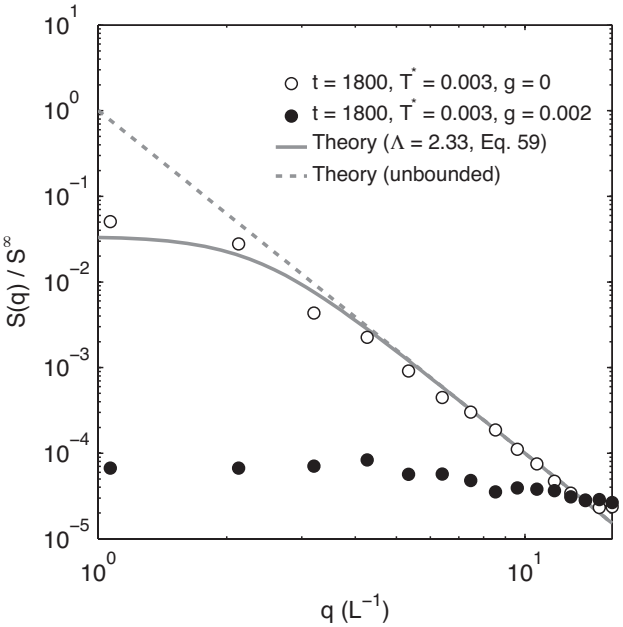

FIG. 6.15. Power spectra obtained from the remapped concentration fields at $t = 1800$ including the effect of gravity. Note that due to resolution limitations the simulations with gravity do not show a fully developed q^{-4} divergence, which would be expected only for very high wave numbers. Thus the value of S^{∞} is obtained from a fit of $S(q)q^4$ in the same range as for $g = 0.0$.

6.7.2 Rayleigh-Taylor instability

Here we study the effect of thermal fluctuations on the development of the Rayleigh-Taylor instability, an unstable displacement of a light (C=0) fluid with a heavy fluid (C=1) under the action of gravity. In the considered cases, the Atwood number is $A = 0.6$ ($\kappa = 3$), gravity is $g = 0.002$, viscosity is $\mu = 10$ and the number density is $n_{eq} = 27$. The domain size is $L_x = 16\,h$, $L_y = 8\,h$ and $L_z = 32\,h$. The no-flow boundary condition is imposed in the z direction by placing a layer of boundary particles at the bottom of the domain. Periodic boundary conditions are imposed in the x and y directions. To initiate the Rayleigh-Taylor instability we perturb the interface according to

$$z(x) = z_0 + cos(\pi x/L_x)\eta_0, \tag{6.64}$$

where $z_0 = 0.5L_z + 1$ with the initial amplitude $\eta_0 = 0.5$ and the wavelength $\lambda = 16\,h$.

This yields a pseudo-2D simulation setup. In order to bring the system to a hydrostatic equilibrium we solve the LLNS equations including thermal fluctuations (no Fickian diffusion) and constantly reassign the appropriate concentrations above and below the interface defined by Eq. (6.64). In the final simulations we investigate three cases with the same effective diffusion coefficient $D^{eff} = 0.00036$ ($Sc \approx 1000$): (1) $D^{\xi} = 0.00012$, $D^{F} = 0.00024$, (2) $D^{\xi} = 0$, $D^{F} = 0.00036$ and (3) $D^{\xi} = 0.00012$, $D^{F} = 0.00024$ (SDPD implementation of the stress tensor, see Eq. 6.37) to compare the time evolution of the diffusive interface.

After Duff et al. (1962) the amplitude of the interface has to satisfy:

$$\frac{d\eta}{dt} = \eta n(A,\nu,k), \tag{6.65}$$

where η is the amplitude of the diffusive interface, n is exponential growth coefficient given by Bellman & Pennington (1953), Duff et al. (1962), and Hide (1955)

$$n = \sqrt{A\frac{gk}{\psi(a,A) + \nu^2 k^4}} - (\nu + D^{eff})k^2. \tag{6.66}$$

Here, $\nu = (\mu_1+\mu_2)/(\rho_1+\rho_2)$ is the kinematic viscosity, k is the wave number of the perturbed interface, $a = (2k\sqrt{D^{eff}t})^{-1}$ and $\psi = 1 + \sqrt{2/\pi}a^{-1}$ for $a \geq 1$. Consequently the time dependent solution is:

$$\eta(t) = \eta_0 exp\left(t\left[\sqrt{A\frac{gk}{\psi(a,A)} + k^4\nu} - k^2\nu - D^{eff}k^2\right]\right). \tag{6.67}$$

A simpler form neglecting the effect of viscosity and diffusion is given as

(CHANDRASEKHAR, 1955; RAYLEIGH, 1883; TAYLOR, 1950):

$$\eta(t) = \eta_0 exp\left(t\sqrt{Agk}\right). \tag{6.68}$$

It should be noted that Eq. (6.67) and (6.68) are only valid at early times and/or small η because these equations have been derived from the linearized hydrodynamic equations (VANDERVOORT, 1961). At later times (when $\eta \approx \lambda/2\pi$; (ANUCHINA & KUCHERENKO, 1978)) departure from the exponential time dependence to a more complex quadratic time dependence (e.g. READ, 1984; YOUNGS, 1984)

$$\eta(t) = \alpha_q A g t^2 \tag{6.69}$$

and finally to a linear evolution of the diffusive front has been observed (e.g. BIRKHOFF & CARTER, 1957; GARABEDIAN, 1957; LAFAY et al., 2007; LAYZER, 1955).

Figure 6.16 shows the resulting evolution of the unstable front and Fig. 6.17 displays the corresponding interface amplitude for both the stochastic and deterministic cases. Note that the interface position at each time step has been approximated by averaging the lowest particle position that satisfies $(0.5 - C) \leq 0$ and $Lx/2 - 0.5\,h > x < Lx/2 + 0.5\,h$ between 0 and L_y with $\Delta y = 0.25\,h$. In general, both solutions agree well with the analytical solutions of CHANDRASEKHAR (1955) and DUFF et al. (1962) for early times ($t \lesssim 300$) and with the late time behavior given by YOUNGS (1984) ($t \gtrsim 300$), where $a_q = 0.035$. This is in agreement with the wide range of a_q values that have been reported in literature (GLIMM et al., 2001) and lie between 0.01 and 0.08. Figure 6.17 (right panel) shows that the front in the stochastic simulation propagates faster, especially at late times. The rate of the front perturbation growth is proportional to the concentration time. The coefficient of Fickian diffusion is smaller in the stochastic model ($D^F < D^{eff}$) than in the deterministic model ($D^F = D^{eff}$) and, as a result, the

concentration gradients across the interface are higher in the stochastic simulation than in the deterministic simulation, which can be seen in Fig. 6.16. Therefore, the front perturbation grows faster in the stochastic simulation than in the deterministic simulation. Simulations using the SDPD implementation display a slightly slower development of the front growth at late times compared to the LLNS-SPH simulations. This is most likely caused by the difference in kinetic temperatures (about 4%, see Fig. 6.2) as development of vortices rolled up along the tail is favored and thus leading to higher drag forces on the perturbation front at late times.

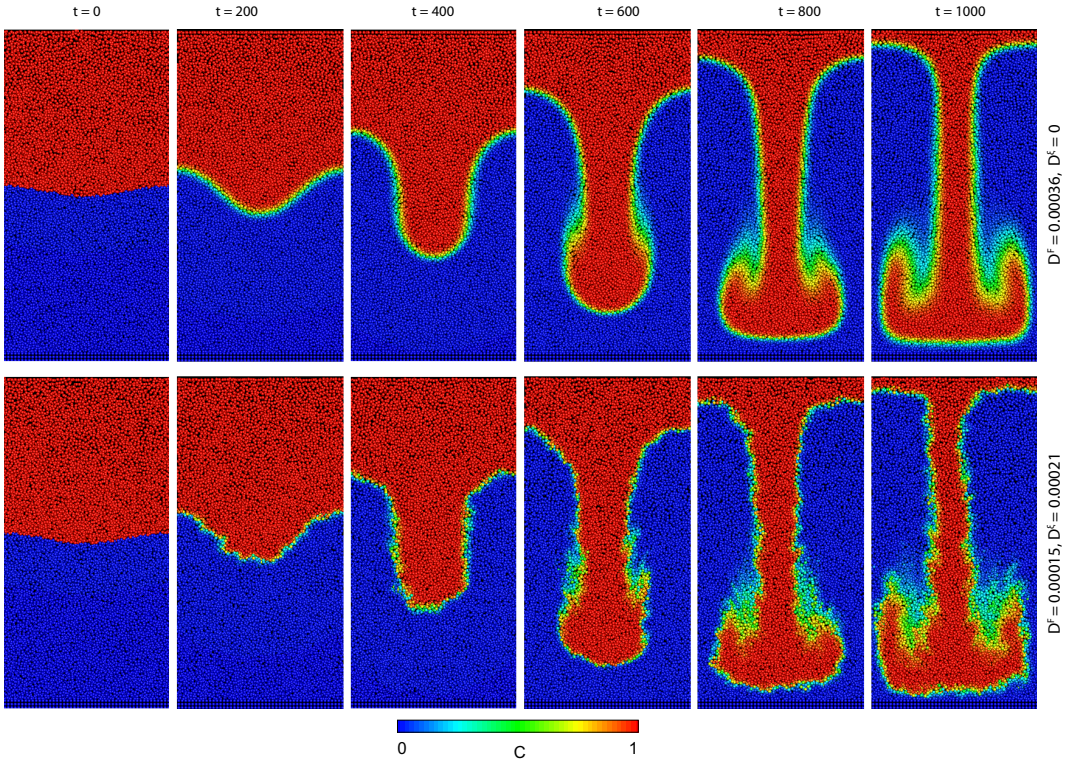

FIG. 6.16. Rayleigh-Taylor instability at a Schmidt number of $Sc \approx 1000$ ($D^{eff} = 0.00036$), $At = 0.6$ ($\kappa = 3$), gravity $g = 0.002$, viscosity $\mu = 10$ and number density $n_{eq} = 27$. Domain size is $L_x = 16\,h$, $L_y = 8\,h$ and $L_z = 32\,h$. (Upper row) Only fickian diffusion with $D^F = 0.00036$. (Lower row) $D^F = 0.00024$ and $D^\xi = 0.00012$, $T^* = 0.002$.

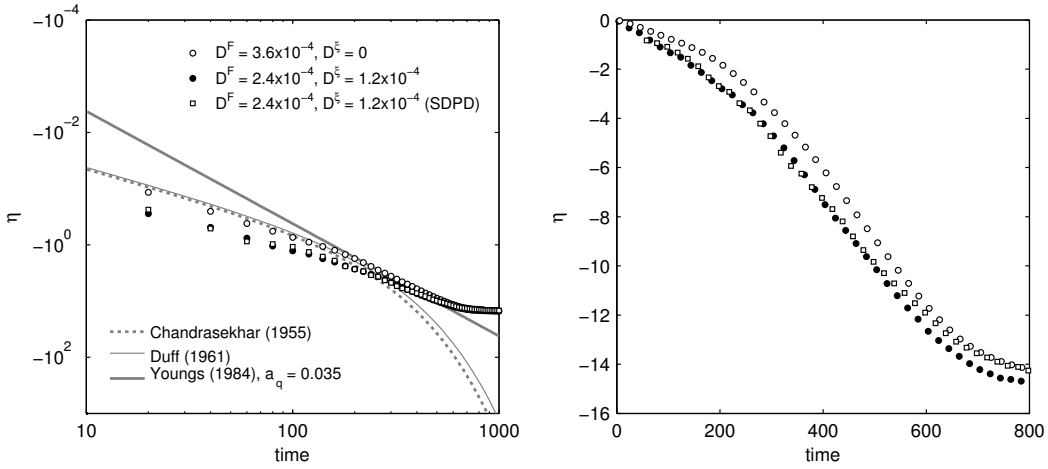

FIG. 6.17. (Left) Simulations of the Rayleigh-Taylor instability with same effective diffusion $D^{eff} = 0.00036$ at Schmidt number $Sc \approx 1000$ and $g = 0.002$ and the corresponding simulations using the SDPD implementation. The solution of CHANDRASEKHAR (1955) and DUFF et al. (1962) have been derived for early times. In contrast the analytical solution of YOUNGS (1984) is valid for late times and employs the α_q calibration parameter which has been reported by various lab and numerical experiments to lie in a range between 0.01 and 0.08 (GLIMM et al., 2001) (here $a_q = 0.035$). (Right) Same simulations plotted on linear scale.

6.8 Conclusion

We presented a novel, Smoothed Particle Hydrodynamics based, method for solving coupled LLNS and stochastic advection-diffusion equations. It is shown that the resulting stochastic SPH model produces a correct scaling behavior of thermodynamic quantities, such as velocity variance and self-diffusion coefficient, and the correct spatial correlation of pressure and velocities. We used the SPH model to investigate the effect of thermal fluctuations on diffusive mixing. First, we simulated diffusion of a plume and demonstrated the accuracy of the SPH model with an error of less than 2%. Then, the role of thermal fluctuations on the evolution of a diffusive interface between a light fluid lying on top of a heavy fluid has been demonstrated. In agreement with recent laboratory experiments and theoretical considerations, we demonstrated that in the absence of gravity

the SPH model recovers the characteristic q^{-4} divergence of the interface power spectrum and its scale-invariant nature. Also in agreement with previous studies, our results show that gravity reduces the perturbations of the miscible front. Lastly, we used the stochastic SPH model to study the effect of thermal fluctuations on the development of the Rayleigh-Taylor instability. We found that random thermal fluctuations slightly accelerate the development of the instability. In the stochastic SPH model, mixing of two miscible fluids results from mechanical mixing of two fluids due to random advection and diffusive mixing. In the standard deterministic description (based on the Navier-Stokes and advection-diffusion equation) the mixing is treated as an effective diffusion process. Therefore, the deterministic model produces smaller concentration gradients across the front separating two miscible fluids, which slows the development of the Rayleigh-Taylor instability. The evolution of the miscible front, obtained from the deterministic and stochastic models, agrees well with the analytical solutions, which demonstrated the accuracy of the SPH model.

Acknowledgment

This work was partially supported by the DAAD (German Academic Exchange Service) providing J. Kordilla with an international research scholarship at the Pacific Northwest National Laboratory (PNNL), USA. A.M. Tartakovsky was supported by the Department of Energy's Office of Advanced Scientific Computing Research Program and at Pacific Northwest National Laboratory (PNNL). PNNL is operated by Battelle for the U.S. Department of Energy. W. Pan was supported by the Applied Mathematics Program within the U.S. Department of Energy Office of Advanced Scientific Computing Research as part of the Collaboratory on Mathematics for Mesoscopic Modeling of Materials (CM4), under award number DE-SC0009247.

6.9 References

ALLEN, M. & TILDESLEY, D. (1989): *Computer Simulation of Liquids*. Clarendon Press, Oxford: p. 404 (cit. on p. 165).

ANUCHINA, N. & KUCHERENKO, Y. (1978): 'Turbulent mixing at an accelerating interface between liquids of different densities'. *Fluid Dynamics*, vol. **28**(6): pp. 157–160 (cit. on p. 188).

BEAR, J. (1972): *Dynamics of fluids in porous media*. Courier Dover Publications (cit. on p. 156).

BELL, J. B., GARCIA, A. & WILLIAMS, S. A. (2007): 'Numerical methods for the stochastic Landau-Lifshitz Navier-Stokes equations'. *Physical Review E*, vol. **76**(1): p. 016708 (cit. on pp. 157, 170, 172).

BELLMAN, R. & PENNINGTON, R. (1953): 'Effects of surface tension and viscosity on Taylor instability'. *Quarterly of Applied Mathematics*, vol. **12**: pp. 151–162 (cit. on p. 187).

BIRKHOFF, G. & CARTER, D. (1957): 'Rising plane bubbles'. *Journal of Rational Mechanics and Analysis*, vol. **6**(6): pp. 769–779 (cit. on p. 188).

BROGIOLI, D., VAILATI, A. & GIGLIO, M. (2000): 'Giant fluctuations in diffusion processes'. *Journal of Physics: Condensed Matter*, vol. **12**(8A): A39–A46 (cit. on pp. 156, 183).

CALLEN, H. & WELTON, T. (1951): 'Irreversibility and Generalized Noise'. *Physical Review*, vol. (cit. on p. 156).

CHANDRASEKHAR, S. (1955): 'The character of the equilibrium of an incompressible heavy viscous fluid of variable density'. *Mathematical Proceedings of the Cambridge Philosophical Society*, vol. **51**(01): p. 162 (cit. on pp. 188, 190).

CROCCOLO, F., BROGIOLI, D., VAILATI, A., GIGLIO, M. & CANNELL, D. S. (2007): 'Nondiffusive decay of gradient-driven fluctuations in a free-diffusion process'. *Physical Review E*, vol. **76**(4): p. 041112 (cit. on p. 156).

CUSSLER, E. (1997): *Diffusion: mass transfer in fluid systems*. Cambridge University Press (cit. on p. 156).

Donev, A. & Vanden-Eijnden, E. (2010): 'On the accuracy of finite-volume schemes for fluctuating hydrodynamics'. *Communications in Applied Mathematics and Computational Science*, vol. **5**(2) (cit. on p. 157).

Donev, A., Bell, J. B., Fuente, A. de la & Garcia, A. (2011a): 'Diffusive Transport by Thermal Velocity Fluctuations'. *Physical Review Letters*, vol. **106**(20): p. 204501 (cit. on pp. 157, 177).

Donev, A., Bell, J. B., Fuente, A. de la & Garcia, A. L. (2011b): 'Enhancement of diffusive transport by non-equilibrium thermal fluctuations'. *Journal of Statistical Mechanics: Theory and Experiment*, vol. **2011**(06): P06014 (cit. on pp. 159, 177).

Duff, R. E., Harlow, F. H. & Hirt, C. W. (1962): 'Effects of Diffusion on Interface Instability between Gases'. *Physics of Fluids*, vol. **5**(4): p. 417 (cit. on pp. 187, 188, 190).

Einstein, A. (1905): 'Über die von der molekularkinetischen Theorie der Wärme geforderte Bewegung von in ruhenden Flüssigkeiten suspendierten Teilchen'. *Annalen der Physik*, vol. **322**(8): pp. 549–560 (cit. on p. 156).

Español, P. & Revenga, M. (2003): 'Smoothed dissipative particle dynamics'. *Physical Review E*, vol. **67**(2): pp. 1–12 (cit. on p. 157).

Español, P., Serrano, M. & Öttinger, H. (1999): 'Thermodynamically Admissible Form for Discrete Hydrodynamics'. *Physical Review Letters*, vol. **83**(22): pp. 4542–4545 (cit. on p. 157).

Fick, A. (1855): 'Ueber Diffusion'. *Annalen der Physik*, vol. **170**(1): pp. 59–86 (cit. on p. 156).

Füchslin, R. M., Fellermann, H., Eriksson, A. & Ziock, H.-J. (2007): 'Coarse-Graining and Scaling in Dissipative Particle Dynamics'. *The Journal of Chemical Physics*, vol.: p. 8 (cit. on p. 164).

Garabedian, P. (1957): 'On steady-state bubbles generated by Taylor instability'. *Proceedings of the Royal Society of London. Series A. Mathematical and Physical Sciences*, vol. **241**(1226): pp. 423–431 (cit. on p. 188).

Gingold, R. A. & Monaghan, J. J. (1982): 'Kernel estimates as a basis for general particle methods in hydrodynamics'. *Journal of Computational Physics*, vol. **46**(3): pp. 429–453 (cit. on p. 161).

Glimm, J., Grove, J., Li, X., Oh, W. & Sharp, D. (2001): 'A Critical Analysis of RayleighTaylor Growth Rates'. *Journal of Computational Physics*, vol. **169**(2): pp. 652–677 (cit. on pp. 188, 190).

Grmela, M. & Öttinger, H. (1997): 'Dynamics and thermodynamics of complex fluids. I. Development of a general formalism'. *Physical Review E*, vol. **56**(6): p. 6620 (cit. on p. 157).

Hide, R. (1955): 'Waves in a heavy, viscous, incompressible, electrically conducting fluid of variable density, in the presence of a magnetic field'. *Proceedings of the Royal Society of London. Series A. Mathematical and Physical Sciences*, vol. (cit. on p. 187).

Kirkpatrick, T., Cohen, E. & Dorfman, J. (1982): 'Light scattering by a fluid in a nonequilibrium steady state. II. Large gradients'. *Physical Review A*, vol. **26**(2) (cit. on p. 184).

Kordilla, J., Tartakovsky, A. & Geyer, T. (2013): 'A Smoothed Particle Hydrodynamics model for droplet and film flow on smooth and rough fracture surfaces'. *Advances in Water Resources*, vol. **59**: pp. 1–14 (cit. on p. 162).

Ladd, A. (1993): 'Short-time motion of colloidal particles: Numerical simulation via a fluctuating lattice-Boltzmann equation'. *Physical Review Letters*, vol. **70**(9): pp. 1339–1342 (cit. on p. 157).

Lafay, M.-A., Le Creurer, B. & Gauthier, S. (2007): 'Compressibility effects on the Rayleigh-Taylor instability between miscible fluids'. *Europhysics Letters (EPL)*, vol. **79**(6): p. 64002 (cit. on p. 188).

Landau, L. D. & Lifshitz, E. M. (1987): *Fluid Mechanics: Volume 6 (Course Of Theoretical Physics)*. Butterworth-Heinemann (cit. on pp. 156, 159, 161, 169).

Layzer, D. (1955): 'On the Instability of Superposed Fluids in a Gravitational Field'. *The Astrophysical Journal*, vol. **122**(1): pp. 1–12 (cit. on p. 188).

Litvinov, S., Ellero, M., Hu, X. & Adams, N. A. (2009): 'Self-diffusion coefficient in smoothed dissipative particle dynamics.' *The Journal of chemical physics*, vol. **130**(2): p. 021101 (cit. on p. 173).

Monaghan, J. J. (1992): 'Smoothed particle hydrodynamics'. *Annual Review of Astronomy and Astrophysics*, vol. **68**: pp. 543–574 (cit. on p. 162).

– (2005): 'Smoothed particle hydrodynamics'. *Reports on Progress in Physics*, vol. **68**(8): pp. 1703–1759 (cit. on p. 161).
– (1982): 'Why particle methods work'. *SIAM: SIAM Journal on Scientific Computing*, vol. **3**(4): pp. 422–433 (cit. on p. 159).
Morris, J. P. (1997): 'Modeling Low Reynolds Number Incompressible Flows Using SPH'. *Journal of Computational Physics*, vol. **136**(1): pp. 214–226 (cit. on pp. 162, 165).
Ortiz de Zárate, J. M., Peluso, F. & Sengers, J. V. (2004): 'Nonequilibrium fluctuations in the Rayleigh-Benard problem for binary fluid mixtures.' *The European physical journal. E, Soft matter*, vol. **15**(3): pp. 319–33 (cit. on p. 184).
Öttinger, H. & Grmela, M. (1997): 'Dynamics and thermodynamics of complex fluids. II. Illustrations of a general formalism'. *Physical Review E*, vol. **56**(6): p. 6633 (cit. on p. 157).
Rayleigh, L. (1883): 'Investigation of the character of the equilibrium of an incompressible heavy fluid of variable density'. *Proceedings of the London Mathematical Society*, vol. **14**: pp. 170–177 (cit. on p. 188).
Read, K. (1984): 'Experimental investigation of turbulent mixing by Rayleigh-Taylor instability'. *Physica D: Nonlinear Phenomena*, vol. **12**(1-3): pp. 45–58 (cit. on p. 188).
Redies, C., Hasenstein, J. & Denzler, J. (2007): 'Fractal-like image statistics in visual art: similarity to natural scenes.' *Spatial vision*, vol. **21**(1-2): pp. 137–48 (cit. on p. 183).
Serrano, M. & Español, P. (2001): 'Thermodynamically consistent mesoscopic fluid particle model'. *Physical Review E*, vol. **64**(4): p. 046115 (cit. on p. 157).
Serrano, M., Fabritiis, G., Español, P., Flekkøy, E. & Coveney, P. (2002): 'Mesoscopic dynamics of Voronoi fluid particles'. *Journal of Physics A: Mathematical and General*, vol. **35**: p. 1605 (cit. on p. 157).
Smoluchowski, M. von (1906): 'Zur kinetischen Theorie der Brownschen Molekularbewegung und der Suspensionen'. *Annalen der Physik*, vol. **326**(14): pp. 756–780 (cit. on p. 156).

Tartakovsky, A. & Meakin, P. (2005a): 'A smoothed particle hydrodynamics model for miscible flow in three-dimensional fractures and the two-dimensional Rayleigh-Taylor instability'. *Journal of Computational Physics*, vol. **207**: pp. 610–624 (cit. on pp. 160, 162).

– (2005b): 'Modeling of surface tension and contact angles with smoothed particle hydrodynamics'. *Physical Review E*, vol. **72**: p. 026301 (cit. on pp. 162, 165).

Taylor, G. (1950): 'The instability of liquid surfaces when accelerated in a direction perpendicular to their planes. I'. *Proceedings of the Royal Society of London. Series A. Mathematical and Physical Sciences*, vol. **201**(1065): pp. 192–196 (cit. on p. 188).

Vailati, A., Cerbino, R., Mazzoni, S., Giglio, M., Nikolaenko, G., Takacs, C. J., Cannell, D. S., Meyer, W. V. & Smart, A. E. (2006): 'Gradient-driven fluctuations experiment: fluid fluctuations in microgravity.' *Applied optics*, vol. **45**(10): pp. 2155–65 (cit. on pp. 183, 184).

Vailati, A., Cerbino, R., Mazzoni, S., Takacs, C. J., Cannell, D. S. & Giglio, M. (2011): 'Fractal fronts of diffusion in microgravity.' *Nature communications*, vol. **2**: p. 290 (cit. on pp. 183–185).

Vailati, A. & Giglio, M. (1997): 'Giant fluctuations in a free diffusion process'. *Nature*, vol. **390**(November): pp. 4–7 (cit. on p. 156).

Vandervoort, P. (1961): 'The character of the equilibrium of a compressible inviscid fluid of varying density'. *The Astrophysical Journal*, vol. **134**: p. 699 (cit. on p. 188).

Youngs, D. L. (1984): 'Numerical simulation of turbulent mixing by Rayleigh-Taylor instability'. *Physica D: Nonlinear Phenomena*, vol. **12**(1-3): pp. 32–44 (cit. on pp. 188, 190).

Zhu, Y. I. & Fox, P. J. (2002): 'Simulation of Pore-Scale Dispersion in Periodic Porous Media Using Smoothed Particle Hydrodynamics'. *Journal of Computational Physics*, vol. **182**(2): pp. 622–645 (cit. on p. 162).

7 | General Conclusion

Despite the strong interest of the gas, oil and fracking industry for flow and transport in fractured aquifers, and the recent stimulation of research related to the characterization of nuclear waste disposal sites located below fractured rock bodies in Yucca mountain, the understanding of flow and transport mechanisms in unsaturated fractures is still far from maturity. This applies to all areas of research such as small-scale characterization, upscaling procedures and field-scale modeling of unsaturated fracture flow. Only in recent years the importance of free-surface flow modes such as adsorbed films has been acknowledged by the research community and models have been developed to account for some of these flow phenomena (Lebeau & Konrad, 2010; Nimmo, 2010). Due to a number of simplifying assumptions regarding the flow complexity (only adsorbed laminar film flow is considered) these models can be employed for predictive modeling purposes, however, it is not surprising that especially in highly heterogeneous systems the travel time distribution are unlikely to be correctly obtained from such models.

Probably one of the biggest issues for the adequate characterization of small scale fracture flow and transport has been the lack of numerical models that can deal with the complex flow dynamics on a discrete level. Approaches such as discrete single fracture models (Lomize, 1951) (parallel plate model) or extended models that take into account microroughness (Tsang & Tsang, 1987) can successfully simulate flow and transport dynamics in saturated systems but are not able to capture flow in unsaturated gravity-driven systems.

The two main objects of this thesis are (1) the assessment of the double-continuum approach to simulate unsaturated flow in fractured aquifers and (2) the development of a discrete particle-based model for state of the art small-scale flow and transport simulations.

7.1 Double continuum modeling of unsaturated fractured aquifers

Following SAUTER (1992) a double-continuum model has been employed to simulate the spring discharge of a fractured karst aquifer. The transient two-dimensional model takes into account saturated and unsaturated flow according to the Richards equation and dynamic hydraulic properties are obtained from classical van Genuchten relationships. The primary fractured porous matrix system and the secondary conduit continuum are coupled by a linear exchange term.

- In order to account for rapid vertical flow processes in the unsaturated conduit continuum the fast recharge component is applied to the bottom of the model domain, essentially creating a bypass, under the assumption that no exchange occurs between unsaturated matrix and conduits.
- The matrix porosity as well as the matrix van Genuchten parameters exhibit the highest sensitivity as they mainly control the head dependent inter-continuum water transfer.
- An extensive multidimensional sensitivity analysis is performed on single parameters, as well as parameter combinations for feasible parameter ranges. For combined parameter variations belonging to different continua as well as for combinations involving the exchange parameter non-linear dependencies over the sensitivity parameter space could be identified. This indicates a certain ambiguity of the model results.
- The simulation of unsaturated flow with the Richards equation and the van Genuchten parameter set in aquifers with highly localized flow features in the unsaturated zone is critically discussed.

7.2 SPH modeling of free surface fracture flow

In order to provide an innovative numerical tool for the investigation of rapid recharge in fractured aquifers an SPH model for free-surface flow including the effects of surface tension based on the model of TARTAKOVSKY & MEAKIN (2005) has been developed and applied to simulate droplet flow on dry and wet fracture surfaces. The model allows to simulate transient flow dynamics over a wide range of wettings conditions and Reynolds numbers without the need of explicitly resolving the airphase, thus resulting in a tremendous computational advantage, especially under near dry conditions.

- The model has been successfully employed to obtain a comprehensive dimensionless parameter set, which can serve as an input for semi-analytical upscaled models, such as that of GHEZZEHEI (2004).
- The accuracy of the model has been verified by comparison to semi-analytical solutions and laboratory experiments. Transient droplet dynamics can reproduce the characteristic linear scaling of Capillary and Bond number (PODGORSKI et al., 2001) and advancing and receding contact angles at the onset of motion follow the empirical relationships established by ELSHERBINI & JACOBI (2006).
- Due to the recent development of unsaturated flow models including the effect of adsorbed films (NIMMO, 2010) the model has been used to investigate their dynamic creation on initially dry fracture surfaces. Based on Reynolds number and Bond numbers the occurrence of adsorbed films has been delineated, giving further insight into the complex dynamics.
- To study the effect of adsorbed films on droplet dynamics, surfaces have been covered by films with thickness corresponding to the dynamically created film thickness under initially dry conditions. The coexistence of droplets and adsorbed films led to an increase of droplet velocities up to a factor of three.
- The effect of a macroscale roughness on droplet velocities has been

studied by creating fracture surfaces with a self-affine fractal geometry. For a common fracture roughness a drop in velocities of up to 70 % was demonstrated.

7.3 Mesoscopic model for advection-diffusion processes

Despite their excellent ability to resolve discrete small-scale flow and transport dynamics, common SPH models rely on a macroscopic Navier-Stokes continuum description of the flow field possibly coupled with an advection-diffusion equation governed by Fickian transport. However, on mesoscopic scales, that is, on scales where these macroscopic descriptions begin to break down, flow and transport equations in particle models have to incorporate the fluctuating dynamics of the underlying atomistic system. For the flow and transport in unsaturated fractures mesoscopic dynamics generally become important when the system is characterized by a low Peclet number, indicating a regime dominated by molecular diffusion. This can be the case for (1) slow surface flow, e.g., in nearly horizontal fractures, (2) flow in the adjacent porous matrix and (3) a combination of both cases, i.e., flow across the matrix-fracture interface.

- A novel discretization of the fully-coupled Landau-Lifshitz-Navier-Stokes and advection-diffusion equations has been proposed.
- The model satisfies the fluctuation-dissipation theorem and prescribed temperatures match the kinetic temperature obtained by means of kinetic theory.
- Velocity variance and self-diffusion coefficients correctly scale with kinetic temperature and particle mass, thus the model can dynamically adapt to the simulated system scale and resolution.
- Spatial covariances of pressure and velocity fluctuations are in good agreement with analytical solutions.
- In order to study the accuracy of the coupled LLNS and advection-diffusion equations the interface between two miscible fluids under various dynamic and stationary conditions is studied.

- A moment analysis is used to compare effective diffusion coefficients (i.e., the coefficient that describes the combined effect of the molecular and macroscopic theory) for different ratios of molecular (thermal) and macrosopic (Fickian) diffusion and are found to be in good agreement with theory.
- A flat interface between two miscible fluids with a heavy fluid on the bottom is simulated with and without the influence of gravitation. Static power spectra of the two-dimensional concentration field obtained via Fourier analysis are shown to (1) reproduce the characteristic q^{-4} wavenumber divergence in the absence of gravity and (2) the interface relaxation and power spectrum dampening by gravitation reported in literature (VAILATI et al., 2011).
- The dynamic interface development is studied by simulating a heavy fluid lying on top of a heavy fluid, which results in a classical Rayleigh-Taylor instability. The interface height is shown to develop in time according to experimental and analytical solutions and thermal fluctuations are shown to slightly increase the velocity of the interface.

7.4 Suggestions for further research

Double-continuum model

The simulation of karst spring dynamics with a double-continuum model and the ambiguous results due to the limitations in process description provided the impetus for the development of adequate discrete flow and transport models in this thesis. It is obvious that the latter models can currently only serve as a numerical tool to provide insight into the small-scale dynamics and help to improve upscaled continuum approaches or discrete fracture models. Growing computational resources might allow the simulation of whole fracture networks on catchment scale with SPH in the future. Nevertheless, double-continuum (and multi-continuum) models in many cases provide the right amount of physical abstraction, as the field data density usually does not allow to simulate more complex systems. In order to enhance the double-continuum approach to simulate unsaturated

flow and transport in fractured (karstic) aquifers the following research is suggested:

1. *Implementation of alternative van Genuchten type relationships.* As demonstrated by SAUTER (1992) and in this thesis (see Chapter 4) the double continuum approach is suitable to simulate saturated flow in the presence of a highly localized conduit system, but cannot adequately describe the underlying physical processes of preferential flow dynamics in the unsaturated zone with the van Genuchten relationships. In general this applies to aquifer systems with highly heterogeneous flow features such as dissolution shafts, wide aperture fractures or fault zones, which prevent or complicate the definition of an REV. One straight-forward approach would be to adopt newer forms of van Genuchten like relationships which incorporate, at least partially, surface flow regimes (LEBEAU & KONRAD, 2010) and thus could be used to simulate unsaturated flow in the secondary continuum.
2. *Implementation of a suitable bypass function.* Another approach would be to entirely drop the description of flow by the Richards equation in any medium for which no REV can be defined (i.e., in this work the conduit continuum) and replace it with an integral approach such as a source-responsive film flow model (NIMMO, 2010). This would require to limit the exchange between both continua to the interface defined by the vertical extent of the conduit continuum and bypass the unsaturated zone to apply recharge directly at the water table of the conduit continuum. A similar bypass approach has been successfully applied by DOUMMAR et al. (2012) for a distributive model.

Free-surface SPH model

In its current state the free-surface model is capable of simulating all types of flow modes (droplets, rivulets, films) encountered in fractures. However, one of the key aspects of unsaturated flow in wide aperture fractures, and still one of the most difficult to assess parameters, is the transient switching of flow modes as a reaction to dynamic recharge. A deeper understand-

ing of these processes will be necessary to enhance volume-effective models that rely on water retention curves in oder to predict hydraulic conductivities. The distribution of these modes on a single fracture surface depends on dynamic properties such as

- the spatial distribution of recharge along the fracture entry,
- the strength and periodicity of the recharge,
- the wetting properties, i.e., the properties of the matrix interface

and static properties of the fracture such as

- the fracture roughness and
- the fracture orientation.

Future research should therefore focus on several main aspects:

1. *The verification of the transient dynamics and switching of flow modes on smooth and rough surfaces.* This includes a more rigorous investigation of the onset of dynamic wetting on initially dry surfaces by Landau-Levich films, forming of rivulets by droplet merging and the dynamics of free-surface waves. In order to find the right level of coarse-graining and save computational resources, but at the same time preserve all important flow dynamics, resolution studies including a suitable objective function will be required.
2. *The investigation of flow in fracture networks.* Especially the dynamic properties are likely to be influenced by the network geometry and feedback effects are expected to control the distribution of flow modes.
3. *Extension of the droplet simulations on rough fracture surfaces.* The dimensionless scaling of PODGORSKI et al. (2001) has been derived from experimental results on smooth surfaces Chapter 5. It is likely that also for the case of a macroroughness, and even for fractures with a surface tortuosity (given a certain minimum traveling distance), a linear scaling can be extracted from the simulation data to serve as an input function for upscaled models.

4. *Parallelization of the model for HPC systems.* From a computational point of view the current free-surface model is not able to simulate flow in fracture networks on meter scales. A parallelized model will be necessary to achieve this, also bearing in mind, that transient wetting and drying cycles will require longer simulation times.

Stochastic SPH model

As the free-surface code and stochastic code have been developed on the same codebase it is simple to merge them for the future application to simulate flow in complex fracture networks. Even though the stochastic code has already been parallelized, it would be advisable to implement both codes in an existing high-performance code such as that employed by PAN et al. (2012). Their code is based on the MD codes of PLIMPTON (1995), which have been exclusively developed for HPC systems, and thus exhibit an excellent scaling performance. The stochastic code has so far only been used to study interfaces in the absence of any complex geometries. Aimed towards the simulation of flow in geological media future research should address the following topics:

1. *Simulation of interface dynamics in discrete pore spaces.* Even though particle models provide an excellent tool to investigate pore-scale flow and transport dynamics, large-scale simulations will have to rely on computationally more efficient Darcy-scale techniques. Therefore it would be advisable to compare stochastic pore-scale simulations with Darcy-scale approaches in order to validate the latter ones. A similar procedure has been carried out for example by TARTAKOVSKY et al. (2009) to compare an reactive SPH transport model with a corresponding Darcy-scale model.
2. *Simulation of transport dynamics on fracture surfaces and across matrix-fracture interfaces.* This will require merging of both codes. Depending on the investigated scale the stochastic code can also be employed to simulate transport on macrosopic scales via conservative Fickian diffusion, i.e., fluctuating hydrodynamical effects can simply

be turned off. The characterization of matrix-fracture interface dynamics is closely linked to the recession and transport dynamics in karst aquifers. Mixing of old and young water as indicated by $\delta^{18}O$ analyses has been attributed to the release of old water stored in the matrix system during recession periods (GEYER et al., 2008; SAUTER, 1992). The developed methods provide an excellent tool to investigate this behavior and provide a small-scale demonstration for such dynamics.

7.5 References

DOUMMAR, J., SAUTER, M. & GEYER, T. (2012): 'Simulation of flow processes in a large scale karst system with an integrated catchment model (Mike She) Identification of relevant parameters influencing spring discharge'. *Journal of Hydrology*, vol. **426-427**: pp. 112–123 (cit. on p. 202).

ELSHERBINI, A. I. & JACOBI, A. M. (2006): 'Retention forces and contact angles for critical liquid drops on non-horizontal surfaces.' *Journal of Colloid and Interface Science*, vol. **299**(2): pp. 841–9 (cit. on p. 199).

GEYER, T., BIRK, S., LIEDL, R. & SAUTER, M. (2008): 'Quantification of temporal distribution of recharge in karst systems from spring hydrographs'. *Journal of Hydrology*, vol. **348**(3-4): pp. 452–463 (cit. on p. 205).

GHEZZEHEI, T. A. (2004): 'Constraints for flow regimes on smooth fracture surfaces'. *Water Resources Research*, vol. **40**: pp. 1–14 (cit. on p. 199).

LEBEAU, M. & KONRAD, J.-M. (2010): 'A new capillary and thin film flow model for predicting the hydraulic conductivity of unsaturated porous media'. *Water Resources Research*, vol. **46**(12): pp. 1–15 (cit. on pp. 197, 202).

LOMIZE, G. (1951): 'Flow in fractured rocks'. *Gosenergoizdat, Moscow*, vol. **127** (cit. on p. 197).

NIMMO, J. R. (2010): 'Theory for Source-Responsive and Free-Surface Film Modeling of Unsaturated Flow'. *Vadose Zone Journal*, vol. **9**(2): p. 295 (cit. on pp. 197, 199, 202).

PAN, W., TARTAKOVSKY, A. & MONAGHAN, J. J. (2012): 'A smoothed-particle hydrodynamics model for ice-sheet and ice-shelf dynamics'. *Journal of Glaciology*, vol. **58**(208): pp. 216–222 (cit. on p. 204).

PLIMPTON, S. (1995): 'Fast parallel algorithms for short-range molecular dynamics'. *Journal of Computational Physics*, vol. **117**(1): pp. 1–19 (cit. on p. 204).

PODGORSKI, T., FLESSELLES, J.-M. & LIMAT, L. (2001): 'Corners, Cusps, and Pearls in Running Drops'. *Physical Review Letters*, vol. **87**(3): p. 036102 (cit. on pp. 199, 203).

SAUTER, M. (1992): *Quantification and Forecasting of Regional Groundwater Flow and Transport in a Karst Aquifer (Gallusquelle, Malm, SW. Germany)*. Tübinger Geowissenschaftliche Arbeiten: p. 150 (cit. on pp. 198, 202, 205).

TARTAKOVSKY, A. & MEAKIN, P. (2005): 'Modeling of surface tension and contact angles with smoothed particle hydrodynamics'. *Physical Review E*, vol. **72**: p. 026301 (cit. on p. 199).

TARTAKOVSKY, A., TARTAKOVSKY, G. & SCHEIBE, T. (2009): 'Effects of incomplete mixing on multicomponent reactive transport'. *Advances in Water Resources*, vol. **32**(11): pp. 1674–1679 (cit. on p. 204).

TSANG, Y. & TSANG, C. (1987): 'Channel model of flow through fractured media'. *Water Resources Research*, vol. (cit. on p. 197).

VAILATI, A., CERBINO, R., MAZZONI, S., TAKACS, C. J., CANNELL, D. S. & GIGLIO, M. (2011): 'Fractal fronts of diffusion in microgravity.' *Nature communications*, vol. **2**: p. 290 (cit. on p. 201).